FROM DEVELOPMENT OF SEMI-EMPIRICAL ATOMISTIC POTENTIALS TO APPLICATIONS OF CORRELATION CONSISTENT BASIS SETS

Joshua S. Gibson

Dissertation Prepared for the Degree of

DOCTOR OF PHILOSOPHY

UNIVERSITY OF NORTH TEXAS

May 2014

APPROVED:

Angela K. Wilson, Major Professor
Thomas R. Cundari, Committee Member
Martin Schwartz, Committee Member
Jincheng Du, Committee Member
William Acree, Jr. Chair of the Department of Chemistry
Mark Wardell, Dean of the Toulouse Graduate School

Gibson, Joshua S., From Development of Semi-Empirical Atomistic Potentials to Applications of Correlation Consistent Basis Sets. Doctor of Philosophy (Chemistry - Physical Chemistry), May 2014, 305 pp., 85 tables, 53 figures, 259 equations, 183 numbered references.

The development of the semi-empirical atomistic potential called the embedded atom method (EAM) has allowed for the efficient modeling of solid-state environments, at a lower computational cost than afforded by density functional theory (DFT). This offers the capability of EAM to model the energetics of solid-state phases of varying coordination, including defects, such as vacancies and self-interstitials. This dissertation highlights the development and application of two EAMs: a Ti potential constructed with the multi-state modified embedded atom method (MS-MEAM), and a Ni potential constructed with the fragment Hamiltonian (FH) method. Both potentials exhibit flexibility in the description of different solid-states phases and applications.

This dissertation also outlines two applications of DFT. First, a study of structure and stability for solid-state forms of Ni_xC_y (in which *x* and *y* are integers) is investigated using plane-wave DFT. A ground state phase for Ni_2C is elucidated and compared to known and hypothesized forms of Ni_xC_y. Also, a set of correlation consistent basis sets, previously constructed using the B3LYP and BLYP density functionals, are studied. They are compared to the well-known to the correlation consistent basis sets that were constructed with higher-level ab initio methodologies through computations of enthalpies of formation and combustion enthalpies. The computational accuracy with regard to experiment is reported.

ACKNOWLEDGEMENTS

First, I would like to acknowledge the Lord Jesus Christ, the Messiah and Savior of the world, the mediator between the LORD God and mankind (Luke 1:32). I look to Him as a cornerstone of strength and a source of renewing spirit. As the writer of the book of Hebrews wrote, “let us run with endurance the race that is set before us, looking to Jesus, the founder and perfecter of our faith…” (Hebrews 12:1-2).

I would also like to acknowledge my dear and loving wife, Danielle. When I prayed for the LORD to lead me to a good woman, He led me to Danielle. Having attended graduate school in Denton allowed me to meet Danielle and marry her. She has the heart of a servant, a gentle spirit, and a strong love of and relationship with my Lord Jesus. Further, she has been very supportive of me through graduate school. I anticipate starting a family with my wife, knowing that my children will have a mother, on whom the LORD smiles.

I want to recognize my mother (Gavona), her husband (Sean), my father (Eddie), my maternal grandparents (Larry and Deanna), and my parents-in-law (Hadley and Marilyn). Also, I would like to acknowledge the Wilson group, and, in particular, Brian Prascher, Andrew Mahler, Charles Peterson, Michael Zhou, and Andrew Ding. Finally, I would like to acknowledge Dr. Srinivasan Srivilliputhur, Dr. Michael Baskes, and Dr. Jincheng Du for their assistance in my research

Finally, I would like to recognize my research advisor, Angela Wilson. I have been very blessed to have an advisor that has allowed me to conduct my research freely.

TABLE OF CONTENTS

Page

ACKNOWLEDGEMENTS i

LIST OF TABLES viii

LIST OF FIGURES xv

Chapters

1 INTRODUCTION 1

2 AN OVERVIEW OF QUANTUM MECHINCAL AB INTIO METHODOLOGIES 4

2.1 The Schrödinger Equation 4

2.2 Hartree-Fock Approximation 9

2.3 Many-Body Perturbation Theory 14

2.4 Configuration Interaction 17

2.5 Coupled Cluster Theory 19

2.6 Complete Active Space Self-Consistent Field Theory 21

2.7 Density Functional Theory 23

2.8 Basis Functions 28

3 AN OVERVIEW OF SOLID STATE PHYSICS 33

3.1 Crystal Structures 34

3.2 The Reciprocal Lattice 35

3.3 Electronic Structure Theory 40

3.4 Chemical Bonding 44

3.5 K-point Sampling 47

3.6 Pseudopotentials 49

4 FIRST PRINCIPLE STUDY OF STRUCTURE AND STABILITY OF NICKEL CARBIDES 60
4.1 Introduction 60
4.2 Computational Methods 62
4.3 Results and Discussion 63
4.3.1 Structures 63
4.3.1.1 NiC 63
4.3.1.2 Ni_2C 64
4.3.1.3 Ni_3C 65
4.3.1.4 Ni_2C Defects 65
4.3.2 Thermodynamics 66
4.3.3 Electronic Properties 68
4.4 Conclusions 69
5 BENCHMARKS OF CORRELATION CONSISTENT BASIS SETS OPTIMIZED FOR DENSITY FUNCTIONAL THEORY 77
5.1 Introduction 77
5.2 Methodology 80
5.3 Results and Discussion 83
5.3.1 Atomic Energetics 83
5.3.2 Molecular Energetics 85
5.3.3 Enthalpies of Formation and Computational Efficiencies 88
5.3.4 Energetics and Computational Efficiency Comparisons in Fullerene Computations 91

5.4 Conclusions 93
6 THE FRAGMENT HAMILTONIAN METHOD 128
6.1 Introduction 128
6.2 The Fragment Hamiltonian Method 131
6.2.1 Foundation 131
6.2.2 The Embedding Functional 140
6.2.3 Derivation of the Two-Electron Hopping Energy 144
6.3 The Fragment Hamiltonian Method applied to Ni 149
6.4 Conclusions 154
7 THE MULTI-STATE MODIFIED EMBEDDED ATOM METHOD 161
7.1 Background – Potential Development 161
7.2 Methodology 166
7.3 Determination of MS-MEAM Functions 172
7.4 Results 179
7.4.1 MS-MEAM Functions 179
7.4.2 Comparison of EAM Potentials with DFT 181
7.4.2.1 Binding Curves 181
7.4.2.2 Equilibrium Curves 184
7.4.2.3 Transformation Pathways 186
7.4.2.4 Structural, Elastic, and Deformation Energetics 187
7.5 Conclusions 190
8 CONCLUDING REMARKS 209

APPENDIX A: SUPPLEMENTAL MATERIAL FOR THE CORRELATION CONSISTENT BASIS SETS OPTIMIZED FOR DENSITY FUNCTIONAL THEORY 212
APPENDIX B: TRANSFORMATION PATHWAYS FOR THE MULTI-STATE MODIFIED EMBEDDED ATOM METHOD 286
REFERENCES..... 295

LIST OF TABLES

Page

Table 2.1: CSFs for a set of n electrons in n orbitals, denoted by CASSCF[n,n] 32

Table 4.1: Computed Ni_2C structures 72

Table 4.2: Formation energies of late 3*d* binary transition metal carbide M_2C (M = Fe, Co, and Ni). 73

Table 5.1: A comparison of the number of primitive (parentheses) and contracted [brackets] functions of the cc-pV*n*Z, cc-pV*n*Z[rc](tr), reoptimized cc-pV*n*Z, and pc-*n* basis sets..... 95

Table 5.2: The atomic energies (E_h) of the B3LYP/cc-pVnZ and their calculated complete basis set limits, followed by the differences (mE_h) of the cc-pV*n*Z[rc](tr) and reoptimized basis sets with respect to B3LYP/cc-pV*n*Z atomic energies (E_h) and their calculated complete basis set limits..... 96

Table 5.3: The atomic energies (E_h) of the BLYP/cc-pVnZ and their calculated complete basis set limits, followed by the differences (mE_h) of the cc-pV*n*Z[rc](tr) and reoptimized basis sets with respect to BLYP/cc-pV*n*Z atomic energies (E_h) and their calculated complete basis set limits..... 97

Table 5.4: Combustion enthalpies at 298 K (kcal/mol) computed with B3LYP and the cc-pV*n*Z, cc-pV*n*Z[rc](tr), and reoptimized basis sets 98

Table 5.5: Combustion enthalpies at 298 K (kcal/mol) extrapolated from B3LYP and the cc-pV*n*Z, cc-pV*n*Z[rc](tr), and reoptimized basis sets 99

Table 5.6: Combustion enthalpies at 298 K (kcal/mol) extrapolated from B3LYP and the cc-pV*n*Z, cc-pV*n*Z[rc](tr), and reoptimized basis sets 100

Table 5.7: Combustion enthalpies at 298 K (kcal/mol) computed with BLYP and the cc-pV*n*Z, cc-pV*n*Z[rc](tr), and reoptimized basis sets 101

Table 5.8: The 86 molecules for which enthalpies of formation at 298K were computed 102

Table 5.9: The differences for total energies (in mE_h) of the cc-pV*n*Z[rc](*tr*) and reoptimized basis sets with respect to B3LYP/cc-pVnZ and BLYP/cc-pV*n*Z. The energies were computed with fixed B3LYP/cc-pVTZ geometries 103

Table 5.10: B3LYP enthalpies of formation (kcal/mol) computed with the cc-pV*n*Z basis sets at geometries optimized with B3LYP/cc-pVTZ and experimental values. MADs and MSDs are also listed. Zero-point energies and thermal corrections were taken from the B3LYP/cc-pVTZ frequencies. 104

Table 5.11: B3LYP CBS-extrapolated enthalpies of formation (kcal/mol) computed with the cc-pV*n*Z, cc-pV*n*Z[rc](tr) , and cc-pV*n*Z-B3LYP basis sets at geometries optimized with B3LYP/cc-pVTZ. MADs and MSDs from experiment are also listed. Zero-point energies and thermal corrections were taken from the B3LYP/cc-pVTZ frequencies 108

Table 5.12: BLYP enthalpies of formation (kcal/mol) computed with the cc-pV*n*Z basis sets at geometries optimized with B3LYP/cc-pVTZ and experimental values. MADs and MSDs are also listed. Zero-point energies and thermal corrections were taken from the B3LYP/cc-pVTZ frequencies. 112

Table 5.13: BLYP CBS-extrapolated enthalpies of formation (kcal/mol) computed with the cc-pV*n*Z, cc-pV*n*Z[rc](tr) , and cc-pV*n*Z-B3LYP basis sets at geometries optimized with B3LYP/cc-pVTZ. MADs and MSDs from experiment are also listed.

Zero-point energies and thermal corrections were taken from the B3LYP/cc-pVTZ frequencies 116

Table 5.14: The mean CPU savings of single point B3LYP calculations on the 86 molecule set for the cc-pVnZ(rc)(tr) and reoptimized basis sets as a percentage of the B3LYP/cc-pVnZ calculation CPU requirements at each basis set level.. 120

Table 5.15: The mean CPU savings of single point BLYP calculations on the 86 molecule set for the cc-pVnZ(rc)(tr) and reoptimized basis sets as a percentage of the BLYP/cc-pVnZ calculation CPU requirements at each basis set level.... 121

Table 5.16: The atomization energies for fullerenes using B3LYP and BLYP/cc-pVnZ (in kcal/mol), and the differences of the cc-pVnZ[rc](tr) and reoptimized basis sets with respect to the corresponding method, and experimental values..... 122

Table 5.17: CPU time savings relative to the standard cc-pVnZ basis sets in computing total energies using the recontracted and reoptimized cc-pVnZ basis sets 123

Table 6.1: Fitted variables for the GSF curve obtained from VASP 156

Table 6.2: Fitted and VASP GSF energies in mJ/m^2 156

Table 6.3: Fitted Rose EOS parameters for the reference crystal structures..... 156

Table 6.4: Fitted parameters for the FH method 157

Table 6.5: Elastic constants (in GPa) determined with VASP, FH, and Expt.; 157

Table 7.1: Symmetry factors 192

Table 7.2: Selected reference structures and transformation pathways that correspond to the MEAM functions 193

Table 7.3: Scaled equilibrium energies and nearest neighbor distances for selected structures 193

Table 7.4: Computations of lattice and elastic constants from selected EAMs, DFT, and experiment. 194

Table 7.5: Computations of surface and stacking fault energies from selected EAMs, DFT, and experiment. 194

Table 7.6: Computations of vacancy and self-interstitial energies from selected EAMs, DFT, and experiment. 196

Table A.1: Comparisons between B3LYP total energies (E_h) computed with the cc-pV*n*Z, cc-pV*n*Z[rc](tr), and cc-pV*n*Z-B3LYP basis sets at geometries optimized with B3LYP/cc-pVTZ 213

Table A.2: Comparisons between B3LYP complete basis set limit energies (E_h) computed with the cc-pV*n*Z, cc-pV*n*Z[rc](tr), and cc-pV*n*Z-B3LYP basis sets at fixed geometries optimized with B3LYP/cc-pVTZ 217

Table A.3: Comparisons between BLYP total energies (E_h) computed with the cc-pV*n*Z, cc-pV*n*Z[rc](tr), and cc-pV*n*Z-BLYP basis sets at fixed geometries optimized with B3LYP/cc-pVTZ 221

Table A.4: Comparisons between BLYP complete basis set limit energies (E_h) computed with the cc-pV*n*Z, cc-pV*n*Z[rc](tr), and cc-pV*n*Z-BLYP basis sets at fixed geometries optimized with B3LYP/cc-pVTZ 225

Table A.5: Comparisons of CPU savings for B3LYP total energy calculations computed with the cc-pV*n*Z[rc](tr) and cc-pV*n*Z-B3LYP basis sets as a percent

ratio of the cc-pV*n*Z basis sets, using fixed geometries optimized with B3LYP/cc-pVTZ..... 229

Table A.6: Comparisons of CPU savings for BLYP total energy calculations computed with the cc-pV*n*Z[rc](tr) and cc-pV*n*Z-B3LYP basis sets as a percent ratio of the cc-pV*n*Z basis sets, using fixed geometries optimized with B3LYP/cc-pVTZ..... 233

Table A.7: Hydrogen cc-pVDZ-B3LYP 236

Table A.8: Hydrogen cc-pVTZ-B3LYP 236

Table A.9: Hydrogen cc-pVQZ-B3LYP 237

Table A.10: Hydrogen cc-pV5Z-B3LYP 238

Table A.11: Hydrogen cc-pVDZ-BLYP 239

Table A.12: Hydrogen cc-pVTZ-BLYP 239

Table A.13: Hydrogen cc-pVQZ-BLYP 240

Table A.14: Hydrogen cc-pV5Z-BLYP 241

Table A.15: Boron cc-pVDZ-B3LYP 242

Table A.16: Boron cc-pVTZ-B3LYP 243

Table A.17: Boron cc-pVQZ-B3LYP 244

Table A.18: Boron cc-pV5Z-B3LYP 245

Table A.19: Boron cc-pVDZ-BLYP 246

Table A.20: Boron cc-pVTZ-BLYP 247

Table A.21: Boron cc-pVQZ-BLYP 248

Table A.22: Boron cc-pV5Z-BLYP 249

Table A.23: Carbon cc-pVDZ-B3LYP 250

Table A.24: Carbon cc-pVTZ-B3LYP 251
Table A.25: Carbon cc-pVQZ-B3LYP 252
Table A.26: Carbon cc-pV5Z-B3LYP 253
Table A.27: Carbon cc-pVDZ-BLYP 255
Table A.28: Carbon cc-pVTZ-BLYP 256
Table A.29: Carbon cc-pVQZ-BLYP 257
Table A.30: Carbon cc-pV5Z-BLYP 258
Table A.31: Nitrogen cc-pVDZ-B3LYP 259
Table A.32: Nitrogen cc-pVTZ-B3LYP 260
Table A.33: Nitrogen cc-pVQZ-B3LYP 261
Table A.34: Nitrogen cc-pV5Z-B3LYP 262
Table A.35: Nitrogen cc-pVDZ-B3LYP 263
Table A.36: Nitrogen cc-pVTZ-B3LYP 264
Table A.37: Nitrogen cc-pVQZ-B3LYP 265
Table A.38: Nitrogen cc-pV5Z-B3LYP 266
Table A.39: Oxygen cc-pVDZ-B3LYP 268
Table A.40: Oxygen cc-pVTZ-B3LYP 269
Table A.41: Oxygen cc-pVQZ-B3LYP 270
Table A.42: Oxygen cc-pV5Z-B3LYP 271
Table A.43: Oxygen cc-pVDZ-BLYP 272
Table A.44: Oxygen cc-pVTZ-BLYP 273
Table A.45: Oxygen cc-pVQZ-BLYP 274
Table A.46: Oxygen cc-pV5Z-BLYP 275

Table A.47: Fluorine cc-pVDZ-B3LYP 276

Table A.48: Fluorine cc-pVTZ-B3LYP 277

Table A.49: Fluorine cc-pVQZ-B3LYP 278

Table A.50: Fluorine cc-pV5Z-B3LYP 279

Table A.51: Fluorine cc-pVDZ-BLYP 281

Table A.52: Fluorine cc-pVTZ-BLYP 282

Table A.53: Fluorine cc-pVQZ-BLYP 283

Table A.54: Fluorine cc-pV5Z-BLYP 284

LIST OF FIGURES

Page

Figure 3.1: Seven crystal lattices types (horizontal) of fourteen different crystal structures (simple, body centered, face centered, and end centered) 51

Figure 3.2: The First Brillouin Zone 52

Figure 3.3: Band structure corresponding to p_x and p_y orbital interactions 53

Figure 3.4: Band structure (left) and DOS (right) of ReO_5 54

Figure 3.5: The first Brillouin zone and corresponding wavevectors of a simple cubic lattice 55

Figure 3.6: The first Brillouin zone and corresponding wavevectors of a simple orthorhombic lattice 56

Figure 3.7: Band structures of (a) an insulator or semiconductor, (b) a semimetal, and (c) a metal 57

Figure 3.8: Construction of the valence and conduction band energies of NaCl 58

Figure 3.9: Energy bands as a function of the bonding interaction in Group 4 tetrahedral solids 59

Figure 3.10: The DOS, $g(\varepsilon)$, and that multiplied by Fermi-Dirac function, $g(\varepsilon)S0(\varepsilon-E_F)$, that represents DOS that are occupied by electrons 59

Figure 4.1: Illustrations of computed structures (single unit cell shown) for (a) P_{nnm} and (b) P_{bcn} orthorhombic forms of Ni_2C. Ni = blue; C = gray 73

Figure 4.2: Illustrations of computed structures (single unit cells) for defect carbides: (a) Ni_4C, (b) Ni_3C_2, and (c) Ni_7C_4 73

Figure 4.3: Formation energies of Ni-carbides (kcal mol^{-1}) 74

Figure 4.4: Band structure of (a) NiC (rocksalt, B1), (b) Ni_2C (orthorhombic, P_{nnm}), and (c) Ni_3C (hexagonal) 75

Figure 4.5: Band structures of (a) Ni_3C_2, (b) Ni_7C_4, and (c) Ni_4C. All are in orthorhombic symmetry 76

Figure 5.1: Basis set convergence graphs of CHF_3 computed with B3LYP with the cc-pV*n*Z (top), cc-pV*n*Z[rc](tr) (middle) , and cc-pV*n*Z-B3LYP (bottom) 124

Figure 5.2: Basis set convergence graphs of C_2F_4 computed with BLYP with the cc-pV*n*Z (top), cc-pV*n*Z[rc](tr) (middle) , and cc-pV*n*Z-BLYP (bottom) 125

Figure 5.3: Basis set convergence graphs of HCOCOH computed with B3LYP with the cc-pV*n*Z (top), cc-pV*n*Z[rc](tr) (middle), and cc-pV*n*Z-B3LYP (bottom) 126

Figure 5.4: Basis set convergence graphs of HCOCOH computed with BLYP with the cc-pV*n*Z (top), cc-pV*n*Z[rc](tr) (middle) , and cc-pV*n*Z-BLYP (bottom) 127

Figure 6.1: Fitted (red) and VASP (blue) GSF pathways 157

Figure 6.2: VASP total energy differences between fcc and the sc, 2d square, and 1d linear chain structures 158

Figure 6.3: The FH embedding functional, the one-electron hopping energy, the pair potential, and the fcc background density 158

Figure 6.4: Ni binding curves for the fcc, sc, 2d square, and 1d chain structures 159

Figure 6.5: The (100) and (111) surface energies as a function of surface displacement 159

Figure 6.6: The GSF pathway as a function of the (111) planar displacement along the <112> direction 160

Figure 7.1: The screening ellipse 197

Figure 7.2: The symmetric and angular densities 197
Figure 7.3: Logarithmic plots for the partial positive and negative densities 198
Figure 7.4: The screening functions 199
Figure 7.5: The fcc binding curves computed with VASP, MS-MEAM, and the Zhou and Ackland EAMs 199
Figure 7.6: The hcp binding curves computed with VASP, MS-MEAM, and the Zhou and Ackland EAMs 200
Figure 7.7: The bcc binding curves computed with VASP, MS-MEAM, and the Zhou and Ackland EAMs 200
Figure 7.8 The oDC10 binding curves computed with VASP, MS-MEAM, and the Zhou and Ackland EAMs 201
Figure 7.9: The SC binding curves computed with VASP, MS-MEAM, and the Zhou and Ackland EAMs 201
Figure 7.10: The 2D-hex binding curves computed with VASP, MS-MEAM, and the Zhou and Ackland EAMs 202
Figure 7.11: The 2D-sq binding curves computed with VASP, MS-MEAM, and the Zhou and Ackland EAMs 202
Figure 7.12: The DC binding curves computed with VASP, MS-MEAM, and the Zhou and Ackland EAMs 203
Figure 7.13: The graphene binding curves computed with VASP, MS-MEAM, and the Zhou and Ackland EAMs 203
Figure 7.14: The zigzag binding curves computed with VASP, MS-MEAM, and the Zhou and Ackland EAMs 204

Figure 7.15: The beam binding curves computed with VASP, MS-MEAM, and the Zhou and Ackland EAMs 204
Figure 7.16: The line binding curves computed with VASP, MS-MEAM, and the Zhou and Ackland EAMs 205
Figure 7.17: The dimer binding curves computed with VASP, MS-MEAM, and the Zhou and Ackland EAMs 205
Figure 7.18: The Bain transformation pathway computed with VASP, MS-MEAM, and the Zhou and Ackland EAMs 206
Figure 7.19: The Trigonal transformation pathway computed with VASP, MS-MEAM, and the Zhou and Ackland EAMs 206
Figure 7.20: The 2D transformation pathway computed with VASP, MS-MEAM, and the Zhou and Ackland EAMs 207
Figure 7.21: The Zigzag transformation pathway computed with VASP, MS-MEAM, and the Zhou and Ackland EAMs 207
Figure 7.22: The oDC transformation pathway computed with VASP, MS-MEAM, and the Zhou and Ackland EAMs 208
Figure B.1: The Bain transformation pathway 292
Figure B.2: The 2D transformation pathway 293
Figure B.3: The Trigonal transformation pathway 293
Figure B.4: The screening parameters for Bain, Trigonal, and 2D pathways 294
Figure B.5: The oDC10 structure 294
Figure B.6: The Zigzag pathway 295

CHAPTER 1

INTRODUCTION

The formulation of Erwin Schrödinger's differential wave equation in the mid-1920's, along with Werner Heisenberg's approach to describing quantum mechanics, utilizing Heisenberg and Born's matrix mechanics, was the beginning of the means to describe the quantum state of a molecular system, be it at the atomic and molecular scale or higher. Such a quantum state incorporated the motions of the nuclei and electrons. However, it could be said that quantum chemistry itself was born in the 1930s with the application of the Born-Oppenheimer approximation in describing a molecular system. Keeping constant the nuclear motions, relative to those of the electrons, being much faster, the nuclear wavefunction could be multiplicatively separated from the electronic wavefunction. The nuclear-electronic interactions could thus be approximated as a constant. This made solving for the energy eigenvalue of the wavefunction more feasible for a many-body system. This approach to solving for the electronic wavefunction and the total electronic energy eigenvalue of a molecular system would, over the following seventy years, lead to the birth of numerous methodological approaches to understand the electronic phenomenology of molecular systems.

This dissertation is divided into nine chapters, this chapter, being the first, stands as an introduction. From here, the principles concerning the Schrödinger equation, including the Born-Oppenheimer approximation, the Pauli-Exclusion principle, spatial and spin orbitals, and Slater determinants is explored in chapter 2. In addition, numerous quantum mechanical ab initio methodologies are briefly introduced, including Hartree-Fock (HF) theory, many-body perturbation theory (MBPT), configuration

interaction (CI), coupled cluster (CC) theory, complete active space self-consistent field (CASSCF) theory, and density functional theory (DFT). Then, chapter 3 introduces topics in solid-state physics, including periodic boundary conditions within crystal structures, the corresponding reciprocal lattice, and various topics of electronic structure theory in crystal structures.

The focus of chapters 4 and 5 is geared towards direct application of quantum mechanical ab initio methodologies. Chapter 4 highlights a DFT investigation of the ground state for solid-state phases of Ni_2C; further, formation energies of Ni_2C, the experimentally established Ni_3C, and other possible forms of Ni_xC_y are computed and compared. Chapter 5 concerns the development of correlation consistent basis sets optimized with DFT functionals. These sets and the regular correlation consistent basis sets are used to compute total energies, enthalpies of formation, and combustion enthalpies, all of which are compared to known experimental values to assess performance and accuracy.

Chapters 6 and 7 introduce semi-empirical approaches that afford the computation of total energies for physical systems containing upwards of 10,000 atoms. Such large systems cannot be computationally managed by the previously listed ab initio methodologies because of the computational costs in terms of CPU and memory. Therefore, semi-empiricism itself allows for construction of very useful methods, when parameterized with regard to molecular systems or crystals of importance. The content of chapters 6 and 7 has theoretical foundation in the semi-empirical atomistic potential called the embedded atom method (EAM). This method has allowed for the efficient modeling of solid-state environments, at much lower computational cost than that

afforded by DFT. This enables modeling the energetics of solid-state phases of high coordination, and defects, including vacancies and self-interstitials. Modifications to the EAM, which successively yielded the modified embedded atom method (MEAM) allowed for more accurate modeling of bulk defects by better describing environments of low coordination. Consequently, more accurate modeling of bulk defects, as well as surfaces, alloys, and liquid phase transitions was feasible. Chapter 6 illustrates the development of an atomistic potential, called the fragment Hamiltonian (FH) method in collaboration with Dr. Steve Valone from Los Alamos National Laboratory, is discussed in this dissertation. The FH method is shown to be formulated using a wavefunction-based perspective, unlike EAM, which is based upon the second moment approximation to tight-binding theory. Finally, the development and application of a Ti potential constructed with the multi-state modified embedded atom method (MS-MEAM) is investigated in chapter 7. For this atomistic potential, DFT potential energy curves of various Ti solid-state phases are *implemented as functions* in MS-MEAM; in contrast, MEAM fits to potential energy curves through *variation of parameters*.

CHAPTER 2

AN OVERVIEW OF QUANTUM MECHANICAL AB INTIO METHODOLOGIES

2.1 The Schrödinger Equation

The main purpose of quantum mechanics is to describe a molecular system through computation of the energy eigenvalue of an eigenstate, known at the wavefunction. This is accomplished by solving the non-relativistic time-independent Schrödinger Equation:[1]

$$\widehat{\mathcal{H}}|\Psi\rangle = E|\Psi\rangle \qquad [2.1]$$

From the left of Equation [2.1], the Hamiltonian operator, $\widehat{\mathcal{H}}$, operates on the wavefunction, Ψ, of the molecular system, which is shown to equal the product of a total energy constant, E, and the wavefunction. The Hamiltonian contains information of the component nuclei and electrons:

$$\widehat{\mathcal{H}} = -\sum_{i=1}^{N}\frac{1}{2}\nabla_i^2 - \sum_{A=1}^{N}\frac{1}{2}\nabla_A^2 - \sum_{i=1}^{N}\sum_{A=1}^{N}\frac{Z_A}{r_{iA}} + \sum_{i=1}^{N}\sum_{j>i}^{N}\frac{1}{r_{ij}} + \sum_{A=1}^{N}\sum_{B>A}^{N}\frac{Z_A Z_B}{r_{AB}} \qquad [2.2]$$

In [2.2], the terms on the right-hand side account for the kinetic energies of *N* electrons (*i*), the kinetic energies of *N* nuclei (*A*), the nuclear-electron interactions, nuclear-nuclear interactions, and electron-electron interactions. The ∇_i^2 and ∇_A^2 involve the sum of second derivatives for the spatial coordinates of electrons and nuclei, *Z* is the nuclear charge, and *r* is the distance between a nucleus and electron (r_{iA}), two electrons (r_{ij}), and two nuclei (r_{AB}).

Foundational to quantum chemistry is the Born-Oppenheimer approximation,[2] which states that since the nuclei are much heavier than the electrons in a molecular system, and the electrons have much faster motions than the nuclei. Consequently, this

permits abandonment of the nuclear kinetic energies and nuclear-nuclear interactions in [2.2]:

$$\widehat{\mathcal{H}}_{elec} = -\sum_{i=1}^{N}\frac{1}{2}\nabla_i^2 - \sum_{i=1}^{N}\sum_{A=1}^{N}\frac{Z_A}{r_{iA}} + \sum_{i=1}^{N}\sum_{j>i}^{N}\frac{1}{r_{ij}} \quad [2.3]$$

The resulting electronic Hamiltonian only accounts for variable electronic motions while keeping constant the nuclear positions. As a result of this approximation, the total energy computation of a molecule is reduced comparative to that of a geometric optimization (in which the nuclear coordinates change). The Born-Oppenheimer approximation also has a stunning effect on the Schrödinger Equation. The Hamiltonian operator, $\widehat{\mathcal{H}}_{total}$, can be additively separated into a sum of electronic and nuclear Hamiltonians, $\widehat{\mathcal{H}}_{elec}$ and $\widehat{\mathcal{H}}_{nuc}$, respectively. For consistency, the nuclear and electronic wavefunctions, Ψ_{elec} and Ψ_{nuc}, respectively, and can be multiplicatively separated between the total wavefunction, Ψ_{total}, as well, because they are independent of each other. Therefore, the Schrödinger equation can be written as:

$$\begin{aligned}\widehat{\mathcal{H}}_{total}\Psi_{total} &= \left(\widehat{\mathcal{H}}_{elec} + \widehat{\mathcal{H}}_{nuc}\right)\Psi_{elec}\Psi_{nuc} = (E_{elec} + E_{nuc})\Psi_{elec}\Psi_{nuc} \\ &= E_{total}\Psi_{total}\end{aligned} \quad [2.4]$$

The electronic energy and the nuclear energy are denoted as E_{elec} and E_{nuc}. It is noted that the nuclear Hamiltonian accounts for the nuclear-nuclear interactions, which are constant for a fixed molecular geometry. The electronic and nuclear Schrödinger equations are thus written as:

$$\widehat{\mathcal{H}}_{elec}\Psi_{elec} = E_{elec}\Psi_{elec} \quad [2.5]$$

$$\widehat{\mathcal{H}}_{nuc}\Psi_{nuc} = E_{nuc}\Psi_{nuc} \quad [2.6]$$

Even though the electronic and nuclear wavefunctions are both dependent on electronic and nuclear coordinates, consistency between the two types of Hamiltonians and wavefunctions must be exercised to produce either the nuclear or electronic total energy, whichever is desired.

The electronic Hamiltonian has been identified, but now the electronic wavefunction must be described. As it is not only a function of the nuclear coordinates, but it is also dependent on the electron coordinates and the electron spin. Electrons have half-integral spins and follow the Pauli exclusion principle.[3] This principle dictates that no two electrons of same spin can occupy the same quantum state. Therefore, only two electrons, each of which having a ½ and -½ integral spins can be near each other. This antisymmetrical behavior has the effect in an electronic wavefunction. An example of this is given in the following four-electron wavefunction, ψ, in which r_i is the coordinate position, $r_i = r(x_i, y_i, z_i)$, for electron *i*:

$$\psi(r_1, r_2, r_3, r_4) = -\psi(r_2, r_1, r_3, r_4) \qquad [2.7]$$

Given the coordinate exchange for electrons 1 and 2, the wavefunction changes sign. Any electronic wavefunction for a molecular system exhibits this phenomenon.

Equation [2.7] contains spatial information of the electrons because it is implicitly a function of spatial orbitals. Spatial orbitals, denoted as $\varphi(r)$, are one-electron wavefunctions, such that that probability, *P*, of finding an electron within the range *dr* is:

$$P = \int |\varphi(r)|^2 dr \qquad [2.8]$$

It is noted that spatial orbitals are orthonormal, such that:

$$\int \varphi_i(r)\varphi_j(r)dr = \delta_{ij} \qquad [2.9]$$

For the same orbitals in Equation [2.9], $i = j$, δ_{ij}= 1; otherwise, Equation [2.9] yields δ_{ij}=0. For a molecular system to be described exactly by a set of spatial orbitals, a complete set of a linear combination of atomic orbitals (LCAO) is required:

$$\psi_a^{LCAO}(r) = \sum_{i=1}^{N} c_{ia}\varphi_i(r) \text{ such that } a = 1,2,3 \ldots N \qquad [2.10]$$

In [2.10], c_{ai} are fitted constants specific for the molecule. For orthonormality, the sum of $| c_{ai} |^2 = 1$. In reality, the set of *i* spatial orbitals would span to infinity for a complete set; therefore, the set of *i* is truncated to a constant number of orbitals for computational efficiency.

The remainder of the chapter uses an alternative notation for integration called "bra-ket" notation. This is illustrated using [2.11]:

$$\langle \varphi_i(r) | \varphi_j(r) \rangle = \delta_{ij} \qquad [2.11]$$

The electron spin within a spatial orbital requires a spin function, designated here as $\alpha(\zeta)$ and $\beta(\zeta)$ for up-spin and down-spin, respectively, dependent on a "spin coordinate", ζ. These spin functions also behave orthonormally, in [2.9]. Combining a spin function multiplicatively with a spatial orbital produces a "spin orbital":

$$\phi_i(x) = \begin{cases} \varphi_i(r)\,\alpha(\zeta) \\ \varphi_i(r)\,\beta(\zeta) \end{cases} \qquad [2.12]$$

The coordinate, *x*, denotes the spatial and spin coordinates, *r* and ζ, in [2.12]. On the left-hand side, the subscript specifies the electron number (assumed to exist within a set of electrons) and, if necessary, a superscript specifes the electron spin for either case on the right-hand side.

From here, an example of a many-electron wavefunction is briefly studied. Take a system with two electrons composed of two spin orbitals having unspecified spins.

Like with [2.5] and [2.6], the possible wavefunctions would be composed of a product of two spin orbitals:

$$\psi_{ij} = \phi_i(x_1)\phi_j(x_2) \qquad [2.13]$$

However, this wavefunction does not account for antisymmetry because permutation of the coordinate positions give the negative of the wavefunction, and therefore does not fully describe the system. Equation [2.13] needs to be expanded to account for antisymmetry. This can be illustrated as:

$$\psi_{ij} = \frac{1}{\sqrt{2}}\Big(\phi_i(x_1)\phi_j(x_2) - \phi_i(x_2)\phi_j(x_1)\Big) = -\psi_{ji} \qquad [2.14]$$

With permutations of the spatial coordinates in [2.14], the wavefunction maintains the given form on the right-hand side. Also, this wavefunction is orthonormal in that applying [2.14] within [2.11] yields unity. Equation [2.14] is called a Slater determinant,[4] and can be illustrated as a determinant:

$$\psi_{ij} = \frac{1}{\sqrt{2}}\begin{vmatrix}\phi_i(x_1) & \phi_j(x_1)\\ \phi_i(x_2) & \phi_j(x_2)\end{vmatrix} \qquad [2.15]$$

This example describes a system with two electrons, yielding the determinant of a *2*x*2* matrix, with the normalization constant of 1/√2. In fact, a Slater determinant for a system with *N* electrons involves, as expected, an *N*x*N* matrix:

$$\psi_N = \frac{1}{\sqrt{N!}}\begin{vmatrix}\phi_1(x_1) & \phi_2(x_1) & \cdots & \phi_N(x_1)\\ \phi_1(x_2) & \phi_2(x_2) & \cdots & \phi_N(x_2)\\ \vdots & \vdots & \ddots & \vdots\\ \phi_1(x_N) & \phi_2(x_N) & \cdots & \phi_N(x_N)\end{vmatrix} \qquad [2.16]$$

The Slater determinant has two fundamental properties. First, permutation of the coordinate positions of two electrons between two rows maintains antisymmetry within the wavefunction, therefore keeping constant the overall form. For the spin orbitals, this accounts for exchange correlation, which is the behavior of electrons with same spin.

However, this does not account for correlation between electrons of different spins. Second, specifying two electrons as occupying the same space by having two identical columns causes the Slater determinant to collapse to zero.

The last thing to be introduced in this section is the variational principle,[5] which states that the computed total energy from a trial wavefunction will always be an upper bound to the true total energy. Essentially, given a set of computed total energies, the lowest total energy will be closest to the "true energy," E_o. The general equation for solving for the total energy is:

$$\frac{\langle\psi|\hat{\mathcal{H}}|\psi\rangle}{\langle\psi|\psi\rangle} = \frac{\langle\psi|E|\psi\rangle}{\langle\psi|\psi\rangle} \geq E_o \qquad [2.17]$$

In the numerator, operation of the Hamiltonian on the wavefunction within the first part of Equation [2.17] yields a constant total energy. Undistributing the total energy outside the integral yields the probability function, which divides by itself in the denominator, thus isolating the total energy. If the wavefunction has been orthonormalized, then the denominator equals unity.

2.2 Hartree-Fock Approximation

The main goal of quantum chemistry has been finding ways to use the Schrödinger equation for a many-electron system to describe its chemical and physical phenomenology. The well-known starting point for this endeavor is the Hartree-Fock (HF) approximation.[6-8] To obtain the orbital set that behaves like a Slater determinant, the coefficients of a basis set containing molecular orbitals (similar to [2.10]) are optimized iteratively with regard to each electron. Thus, as the optimization process

iterates between each electron, the method implicitly demands that current electron view all other electrons as an overall average, or a “field,” of neighboring electrons.

The HF total energy is given as a sum of the electron and nuclear total energies:

$$E^{HF} = E^{HF}_{nuc} + E^{HF}_{elec} \quad [2.18]$$

The nuclear total energy by computing the nuclear-nuclear interactions:

$$E^{HF}_{nuc} = \sum_{A=1}^{N} \sum_{B>A}^{N} \frac{Z_A Z_B}{r_{AB}} \quad [2.19]$$

The HF Hamiltonian, which is a sum of one-electron Fock operators that operate on the number of electrons, *N*, in the molecular system, is introduced:

$$\hat{\mathcal{H}}^{HF}_{elec} = \sum_{i=1}^{N} \hat{f}(r_i) \quad [2.20]$$

The Fock operator, $\hat{f}(r_i)$, is a function of the one-electron kinetic energy operator, the one-electron potential energy operator, as well as the two-electron coulomb operator and two-electron exchange operator:

$$\hat{f}(r_i) = \left[-\frac{1}{2}\nabla_i^2 + \sum_{i=A}^{N} \frac{Z_A}{r_{iA}} \right] + \sum_{j=1}^{N} \left[2\hat{J}_{ij}(r_i) - \hat{K}_{ij}(r_i) \right] \quad [2.21]$$

Both operators are a function of the r_{ij}^{-1} operator, which accounts for two-electron interactions. The two-electron coulomb operator accounts for the repulsive interactions between electrons and has the form:

$$\hat{J}_{ij}(r_i) = \left\langle \varphi_j(r_j) \middle| r_{ij}^{-1} \middle| \varphi_j(r_j) \right\rangle \quad [2.22]$$

The antisymmetric nature of electrons (Equations [2.14]-[2.16]) and the corresponding effect on the total energy is accounted within HF approximation through the two-electron exchange operator:

$$\hat{K}_{ij}(r_i) = \langle \varphi_j(r_j) | r_{ij}^{-1} | \varphi_i(r_j) \rangle \quad [2.23]$$

With the given operators, the electronic total energy is obtained through means of the Self-Consistent Field (SCF) procedure. To further explore the SCF procedure and two-electron operators, Equation [2.17] is applied. Assuming the molecular basis set has unoptimized coefficients, and using spatial orbitals, φ:

$$\hat{f}(r_1) \sum_{i=1}^{N} c_{ia} |\phi_i(r_1)\rangle = \sum_{i=1}^{N} c_{ia} \left[\hat{h}(r_1) + \sum_{j=1}^{N} 2\hat{J}_{ij}(r_1) + \hat{K}_{ij}(r_1) \right] |\phi_i(r_1)\rangle \quad [2.24]$$

The one-electron operator, $\hat{h}(r_1)$, is given in the bracketed terms in Equation [2.21]. If the both sides are multiplied by $\langle \varphi_i(r_1)|$, then, using Equation [2.22], the two electron Coulombic integral is:

$$J_{ij}(r_1) = 2\langle \varphi_i(r_1)\varphi_j(r_2) | r_{ij}^{-1} | \varphi_j(r_2)\varphi_i(r_1) \rangle \quad [2.25]$$

and, using Equation [2.23], the two-electron exchange integral is:

$$K_{ij}(r_1) = \langle \varphi_i(r_1)\varphi_j(r_2) | r_{ij}^{-1} | \varphi_i(r_2)\varphi_j(r_1) \rangle \quad [2.26]$$

Comparison of the coulomb and exchange integrals illustrates a permutation of coordinates between spatial orbitals φ_i and φ_j in the latter half of the integral, thus illustrating electron exchange. However, this exchange only concerns same-spin electrons, and therefore HF cannot account for the exchange correlation between two electrons that differ in spin. Also, in [2.17], the negative sign precedes the exchange operator. This is necessary because exchange between two same-spin electrons has the stabilizing effect, thus decreasing the orbital energy.

Continuing with [2.24], the operation of the Fock operator on the right-hand side is executed on $|\varphi_i(r_1)\rangle$, to produce the orbital energy, and then $\langle \varphi_j(r_1)|$ is multiplied on

the left of both sides of the equality. With the left-hand side rewritten as the molecular basis set, the following is given:

$$\sum_{i=1}^{N} c_{ia}\langle\varphi_j(r_1)|\hat{f}(r_1)|\varphi_i(r_1)\rangle = \varepsilon_a \sum_{i=1}^{N} c_{ia}\langle\varphi_j(r_1)|\varphi_i(r_1)\rangle \quad [2.27]$$

The above equality can be written in matrix form, known as the Roothan-Hall equations:[9,10]

$$\mathbf{FC} = \mathbf{SC\varepsilon} \quad [2.28]$$

In Equation [2.28], **F** is the *M* by *M* Fock matrix of *M* orbitals containing elements $\mathrm{F}_{ji} = \langle\varphi_j(r_1)|\hat{f}(r_i)|\varphi_i(r_1)\rangle$; **S** is an *M* by *M* overlap matrix containing overlapping orbitals of elements $S_{ji} = \langle\phi_j(r_1)|\phi_i(r_1)\rangle$; **C** is an *M* by *M* matrix containing the molecular orbital expansion coefficients, c_{ia}; and $\boldsymbol{\varepsilon}$ is an *M* by *M* matrix containing the orbital energies along the diagonal.

Finally, the SCF procedure requires solving the *secular equation*:

$$\sum_{i=1}^{N} c_{ia}\left(F_{ji} - \varepsilon_a S_{ji}\right) = 0 \quad [2.29]$$

Assuming that one iteration of the SCF procedure has been executed between [2.20] and [2.29], a new iteration is executed with the expansion coefficients computed from the first iteration to build a new Fock matrix in [2.24]. Then the difference between the electronic total energies from the first and second iterations is taken and compared to an energy difference threshold (for example, $\Delta E_{th} = 1x10^{-8}$ Hartree). Assuming that difference threshold is not met, then the newly computed expansion coefficients are used to compute another new Fock matrix, and another electronic energy difference between the current and previous iteration is compared to energy difference threshold.

After some number of iterations, the electronic total energy is computed that satisfies the energy difference threshold. This will be very much dependent on repeated computations of the expansion coefficients, which are functionally representative of charge density and bonding involved within a molecular geometry. To illustrate this, with [2.10], probability of finding an electron, also known as the total charge density, is inserted into [2.8], the molecular orbital basis set:

$$P = \sum_{a} \left| \sum_{i=1}^{N} c_{ia} \varphi_i(r) \right|^2 \qquad [2.30]$$

The integral from [2.8] has been removed in place of the more approximate summation over all *a* molecular orbitals. Reorganization of the right-hand side, and noting the absolute square behaves as $|\psi|^2 = \psi^* \psi$, gives:

$$P = \sum_{i=1}^{N} \sum_{j>i}^{N} \sum_{a} c_{ja}^* c_{ia} \, \varphi_j^*(r) \varphi_i(r) \qquad [2.31]$$

The electron density matrix for a molecular orbital basis set:

$$D_{ij} = \sum_{a} c_{ia}^* c_{ja} \qquad [2.32]$$

The coefficients in the density matrix are the very same involved in the SCF procedure. It can therefore be said that minimization of the HF electronic energy optimizes the electron density.

As previously noted, HF is an approximation towards solving the total energy in the Schrödinger equation. However, improvements are necessary because HF fails to describe electron correlation between electrons of different spin. It treats electron interactions in an average field of electrons. As a result, HF recovers approximately 99% of the true energy, E_o. Therefore, this chapter briefly overviews some *ab initio*

methodologies that use the HF solution, and attempt to recover the 1% that describes electron correlation.

2.3 Many-Body Perturbation Theory

An ab initio methodology that is able to account for more electron correlation energy is many-body perturbation theory (MBPT).[11] Like HF, MBPT is size-consistent in that the total energy scales linearly with the number of electrons in a molecular system. However, MPBT is not variational. In this method, a perturbation operator, $\hat{\mathcal{V}}$, is added to the zero-order Hamiltonian, $\hat{\mathcal{H}}_o$. Therefore, the perturbed Hamiltonian has the form:

$$\hat{\mathcal{H}} = \hat{\mathcal{H}}_o + \lambda\hat{\mathcal{V}} \qquad [2.33]$$

The perturbed Hamiltonian is applied to the zero-order wavefunction, which is an eigenfunction of the zero-order Hamiltonian, to produce a λ-order perturbation energy correction (in which λ is an integer) to the zero-order total energy.

As an example, the first- and second-order energies are solved. The wavefunctions and energies are expanded, respectively, as a function of an order parameter, λ:

$$\mathcal{E}_i = E_i^{(0)} + \lambda E_i^{(1)} + \lambda^2 E_i^{(2)} + \cdots \qquad [2.34]$$

$$|\Phi_i\rangle = \left|\Psi_i^{(0)}\right\rangle + \lambda\left|\Psi_i^{(1)}\right\rangle + \lambda^2\left|\Psi_i^{(2)}\right\rangle + \cdots \qquad [2.35]$$

In [2.34] and [2.35], the superscripts define the order of perturbation, and the subscript, *i,* relates the expansions to the wavefunction, $|\Phi_i\rangle$. The perturbed Hamiltonian [2.33] is applied to [2.35] and equal to the product of [2.34] and [2.35]:

$$\left(\hat{\mathcal{H}}_o + \lambda\hat{\mathcal{V}}\right)\left(\left|\Psi_i^{(0)}\right\rangle + \lambda\left|\Psi_i^{(1)}\right\rangle + \lambda^2\left|\Psi_i^{(2)}\right\rangle + \cdots\right)$$
$$= \left(E_i^0 + \lambda E_i^{(1)} + \lambda^2 E_i^{(2)} + \cdots\right)\left(\left|\Psi_i^{(0)}\right\rangle + \lambda\left|\Psi_i^{(1)}\right\rangle + \lambda^2\left|\Psi_i^{(2)}\right\rangle + \cdots\right) \quad [2.36]$$

Given that the λ-order eigenfunctions in [2.35] are orthonormal to each other, the zero-order wavefunction is multiplied across [2.33] on the left and terms are isolated by the order of λ:

$$E_i^{(0)} = \left\langle\Psi_i^{(0)}\middle|\hat{\mathcal{H}}_o\middle|\Psi_i^{(0)}\right\rangle \quad [2.37]$$

$$E_i^{(1)} = \left\langle\Psi_i^{(0)}\middle|\hat{\mathcal{V}}\middle|\Psi_i^{(0)}\right\rangle \quad [2.38]$$

$$E_i^{(2)} = \left\langle\Psi_i^{(0)}\middle|\hat{\mathcal{V}}\middle|\Psi_i^{(1)}\right\rangle \quad [2.39]$$

These are the zero-, first-, and second-order energies. The second-order energy in [2.39] is a function of the first-order wavefunction, but it can be rewritten as a function of the zero-order energies and wavefunctions. This first requires expansion of the first-order wavefunction in terms of eigenfunctions of the zero-order Hamiltonian:

$$\left|\Psi_i^{(1)}\right\rangle = \sum_n \left|\Psi^{(n)}\right\rangle\left\langle\Psi^{(n)}\middle|\Psi_i^{(1)}\right\rangle \quad [2.40]$$

Next, equitable terms relating to the first-order parameter using [2.36] are extracted to create the relation:

$$\left(E_i^{(0)} - \hat{\mathcal{H}}_o\right)\left|\Psi_i^{(1)}\right\rangle = \left(\hat{\mathcal{V}} - E_i^{(1)}\right)\left|\Psi_i^{(0)}\right\rangle \quad [2.41]$$

Multiplying across from the left by $\left\langle\Psi^{(n)}\right|$ and keeping in mind that the zero-order eigenfunctions are orthogonal $\left(\text{i. e.}\left\langle\Psi^{(n)}\middle|\Psi_i^{(0)}\right\rangle = 0\right)$, the following is obtained:

$$\left(E_i^{(0)} - E_n^{(0)}\right)\left\langle\Psi^{(n)}\middle|\Psi_i^{(1)}\right\rangle = \left\langle\Psi^{(n)}\middle|\hat{\mathcal{V}}\middle|\Psi_i^{(0)}\right\rangle \quad [2.42]$$

Applying [2.40] within [2.39] gives:

$$E_i^{(2)} = \sum_n \left\langle \Psi_i^{(0)} \middle| \hat{\mathcal{V}} \middle| \Psi^{(n)} \right\rangle \left\langle \Psi^{(n)} \middle| \Psi_i^{(1)} \right\rangle \quad [2.43]$$

Finally, rearranging [2.42] and substituting the result into [2.43] yields:

$$E_i^{(2)} = \sum_n \frac{\left| \left\langle \Psi^{(n)} \middle| \hat{\mathcal{V}} \middle| \Psi_i^{(0)} \right\rangle \right|^2}{\left(E_i^{(0)} - E_n^{(0)} \right)} \quad [2.44]$$

This is the second-order energy. Over all, the second-order total energy is given as:

$$E_{total} = E_i^{(0)} + E_i^{(1)} + E_i^{(2)} \quad [2.45]$$

It is noted that the if the HF Hamiltonian is used as the zero-order Hamiltonian, then the sum of the zero- and first-order total energies account give the HF total energy. The zero-order energy accounts for the one-electron orbital energies. The first-order energy, determined by $\hat{\mathcal{V}}$, accounts for the two-electron interactions, $\hat{J}_{ij}(r_i)$ and $\hat{K}_{ij}(r_i)$.

Assuming that $\left| \Psi_i^{(0)} \right\rangle$ is the HF ground state Slater determinant, then, according to Brillouin's theorem, the projection of $\left| \Psi_i^{(0)} \right\rangle$ onto the first excited state determinant yields no interaction. So, for *n* = 1, $\left\langle \Psi^{(n)} \middle| \mathcal{V} \middle| \Psi_i^{(0)} \right\rangle = 0$, so no correlation energy is obtained from the first order correction. However, Equation [2.44] can be rewritten to account for second-order (or double) excitations;

$$E_{ij}^{(2)} = \sum_{ab} \frac{\left| \left\langle \Psi^{(ab)} \middle| r_{12}^{-1} \middle| \Psi_{xy}^{(0)} \right\rangle - \left\langle \Psi^{(ab)} \middle| r_{12}^{-1} \middle| \Psi_{yx}^{(0)} \right\rangle \right|^2}{\left(\varepsilon_x + \varepsilon_y - \varepsilon_a - \varepsilon_b \right)} \quad [2.46]$$

Now, the total energy as a function of double excitations of electrons from the *x* and *y* orbitals into excited *a* and *b* orbitals are computed. This is the second-order Møller-Plesset (MP2)[12] correction. Substituting [2.46] into [2.45], having used the HF

Hamiltonian, yields the MP2 total energy. Higher order λ corrections can be computed as well, in which $n < 2$. However, MP2 is the most popular of the perturbative corrections because of the higher computational requirements, the non-variational behavior, and possible divergent behavior of the higher-level corrections.

2.4 Configuration Interaction

This ab initio method, called configuration interaction (CI),[13] is conceptually straightforward method in that all possible electron configurations of a Slater determinant are considered, and the corresponding wavefunction forms the basis of the *N*-electron wavefunction. Thus, the CI wavefunction has the form:

$$|\Phi_{CI}\rangle = C|\Psi_o\rangle + C_i^a|\Psi_i^a\rangle + C_{ij}^{ab}\left|\Psi_{ij}^{ab}\right\rangle + C_{ijk}^{abc}\left|\Psi_{ijk}^{abc}\right\rangle + C_{ijkl}^{abcd}\left|\Psi_{ijkl}^{abcd}\right\rangle + \cdots \qquad [2.47]$$

The wavefunction accounts for the ground state and excited state wavefunctions, and the associated expansion coefficients. For example, the first excitation involves promotion of an electron from orbitals *i* to *a*; the second excitation involves promotion of two electrons, one from orbitals *i* to *a*, and another from orbitals *j* to *b*; the third involves three electron excitations, and so forth. Thus, $|\Psi_o\rangle$ is the ground state wavefunction, $|\Psi_i^a\rangle$ is the first exited state, $\left|\Psi_{ij}^{ab}\right\rangle$ is the second excited state, $\left|\Psi_{ijk}^{abc}\right\rangle$ is the third excited state, and so forth. Computing the "Full CI" wavefunction[14] requires solving the exact energy of a molecular system using an *N*-electron Hamiltonian, $\mathcal{H}$, formed in the basis of a complete CI wavefunction. This process is very computationally expensive and feasible mainly for small molecules and atoms, including H_2 and He.

In the formation of the CI matrix, a few observations are noted. First, Brillouin's theorem applies with CI, in that the singly excited wavefunction does not mix with the

ground state wavefunction, thus $\langle \Psi_o | \mathcal{H} | \Psi_i^a \rangle = 0$. Also, no mixing occurs between the ground state and third, or higher, excited- state wavefunctions; this occurs because the Hamiltonian accounts for only, at most, two-electron interactions between two coupled one-electron wavefunctions. Therefore, if the coupled CI matrix element differs by an order of more than two, then it equals zero. For example, $\langle \Psi_o | \widehat{\mathcal{H}} | \Psi_{ij}^{ab} \rangle \neq 0$, but $\langle \Psi_o | \widehat{\mathcal{H}} | \Psi_{ijk}^{abc} \rangle = 0$.

Given these facts, and the computational expense of a full CI computation, the CI wavefunction can be truncated to consider a limited scope of excitations. Applying Brillouin's theorem, the CI wavefunction is truncated to the second-order excitation, and first-order excitations are removed by setting $C_i^a = 0$. This is called configuration interaction with doubles excitations (CID). Another form of CI, called configuration interaction with singles and doubles excitations (CISD) includes singles and doubles excitations. Despite Brillouin's theorem, the first-order and second-order excited wavefunctions do mix, such that $\langle \Psi_i^a | \mathcal{H} | \Psi_{ij}^{ab} \rangle \neq 0$. This incorporation of singles is important for an accurate computation of one-electron properties, including the dipole moment, and charge and spin densities, but not so for the total energy. Indeed, contributions of excitations toward the total energy result from the ability of the excited wavefunction to mix with the ground-state wavefunction. Therefore, decreasing the magnitude of truncation on the CI wavefunction, starting with second-order excited wavefunction, and adding the third- (CISDT), fourth- (CISDTQ), and higher, causes CI to recover progressively more and more of the electron correlation energy, towards a Full CI wavefunction, that HF fails to account. But, this progression demands more computational effort. Truncation of the CI wavefunction does increase the computational

efficiency, but the drawback is that it removes size-consistency in the computation of a molecule. A known solution for this is Davidson correction,[15] which estimates higher order interaction energies from a truncated CI expansion. The correction, ΔE_Q, is computed from the CISD total energy, and the coefficient of the ground-state wavefunction, *C*:

$$\Delta E_Q = (1 - C^2) E_{CISD} \quad [2.48]$$

Overall, the foundation of the CI wavefunction is very straightforward, but it is very limited in its computation feasibility.

2.5 Coupled Cluster Theory

Another *ab initio* method is briefly introduced, which also can recover electron correlation energy, is the coupled cluster method.[16-19] The form of the coupled cluster wavefunction is given in the following:

$$|\Phi_{CI}\rangle = e^{\hat{T}} |\Psi_o\rangle \quad [2.49]$$

In [2.49], the wavefunction, $|\Psi_o\rangle$, is the ground state HF wavefunction, which is a Slater determinant, and the exponential contains the cluster operator, $\hat{T}$, that accounts for single, double, triple, quadruple, and more excited states through the promotion of clusters of one, two, three, four, and more clusters of electrons, respectively. This is illustrated though a Taylor series expansion of the exponential:

$$e^{\hat{T}} = 1 + \hat{T} + \frac{\hat{T}^2}{2!} + \frac{\hat{T}^3}{3!} + \frac{\hat{T}^4}{4!} + \cdots + \frac{\hat{T}^N}{N!} \quad [2.50]$$

In [2.50], the cluster operator is defined as:

$$\hat{T} = \hat{T}_1 + \hat{T}_2 + \hat{T}_3 + \hat{T}_4 + \cdots + \hat{T}_N \quad [2.51]$$

As examples of the cluster operator, the single and double excited states are produced using the first- and second-order cluster operators, respectively:

$$\hat{T}_1|\Psi_o\rangle = \sum_a t^a|\Psi^a\rangle \qquad [2.52]$$

$$\hat{T}_2|\Psi_o\rangle = \sum_{ab} t^{ab}|\Psi^{ab}\rangle \qquad [2.53]$$

In the above, $|\Psi^a\rangle$ and $|\Psi^{ab}\rangle$ are the first- and second-order excited states, and t^a and t^{ab} are cluster coefficients, the values of which are determined through variation of the wavefunction to solve for the total energy, as displayed in [2.17]. One interesting point to note is that, with the form of [2.50], given $\hat{T}^n$, it is possible to have groups of excited clusters operate on the ground state wavefunction. For example, using $\hat{T}^2$in [2.51], the applicable cluster operators include $\hat{T}_1^2$, $\hat{T}_2^2$, $\hat{T}_3^2$, $\hat{T}_4^2$, and the cross terms. These multiplicative cluster operators are uncoupled excitations; for example, $\hat{T}_1^2$ accounts for two uncoupled excitations of two single electrons. In contrast, $\hat{T}_2$ accounts for the coupled excitation of two electrons. Operation of $\hat{T}_1^2$ on the ground-state wavefunction yields two cluster coefficients for each excited electron:

$$\hat{T}_1^2|\Psi_o\rangle = \hat{T}_1\hat{T}_1|\Psi_o\rangle = \hat{T}_1\sum_a t^a|\Psi^a\rangle = \sum_a t^a\hat{T}_1|\Psi^{a_1}\rangle = \sum_{ab} t^a t^b|\Psi^{ab}\rangle \qquad [2.54]$$

These excitations are analogous to those performed in full CI. However, coupled cluster also performs uncoupled excitations to contribute to the total energy.

Like with full CI, the cluster operator can be truncated such that only double excitations apply; with that, the cluster operator becomes $\hat{T} = \hat{T}_2$. This form of coupled cluster is called coupled cluster doubles (CCD). If the cluster operator becomes $\hat{T} = \hat{T}_1 + \hat{T}_2$, then the corresponding form of coupled cluster is coupled cluster singles

and doubles (CCSD). Also, for $\hat{T} = \hat{T}_1 + \hat{T}_2 + \hat{T}_3$, this is called coupled cluster singles, doubles, and triples (CCSDT). This last method is quite accurate in recovering the electron correlation energy (~99%), but it is expeditious only for small molecules. Therefore, a more feasible approach, for increasing number of atoms in a molecule, is to use CCSD and add triples excitations as a perturbation. This form of coupled cluster is called CCSD(T), in which the parentheses denote the triples excitations as a perturbation. In all truncations of the cluster operator, a size-consistent wavefunction is maintained, due to the exponentiation of the cluster operator, which permits uncoupled excitations unlike with a truncated CI wavefunction.

2.6 Complete Active Space Self-Consistent Field Theory

At this point in the chapter, only methods that require a single-reference wavefunction have been examined. However, transition metals are known for low-lying degenerate excited states, so a single-reference method is not adequate in describing the corresponding electronic structure associated with this static correlation. For clarification, static correlation takes account of the possible combinations of electron occupation in orbitals. Therefore, a method that can describe the molecule or reaction using a multi-reference wavefunction-based approach is required. A well-known multi-reference approach is the complete active space self-consistent field (CASSCF) method.[20] The CASSCF wavefunction has the form:

$$|\Phi_{CASSCF}\rangle = \sum_{l} C_l |\mathrm{X}_l\rangle \qquad [2.55]$$

In which:

$$|\mathrm{X}_l\rangle = G \sum_{k \in l} |\Psi_k\rangle \qquad [2.56]$$

And:

$$|\Psi_k\rangle = \sum_{\nu} P_{\nu k} |\Omega_\nu\rangle \qquad [2.57]$$

Essentially, the CASSCF wavefunction can be expanded as a sum of l configuration state functions (CSFs), $|\mathrm{X}_l\rangle$, which is a symmetry-adapted linear combination of Slater determinants, $|\Psi_k\rangle$, and configuration coefficients, C_l. Also, G is a normalization constant. These CSFs are symmetry-adapted because all contributing Slater determinants are all eigenfunctions of the angular momentum and spin operators, L^2 and S^2, and the corresponding projections along the z-axis, L_z^2 and S_z^2, for linear molecules. The Slater determinants are further composed of molecular orbitals,$|\Omega_\nu\rangle$, and the corresponding coefficients, $P_{\nu k}$.

Solving for the CASSCF wavefunction of a molecule is completely dependent on the electronic active-space that is composed of all possible electron configurations that populate the set of molecular orbitals. The orbitals are divided into the inactive and active orbitals. The inactive orbitals are doubly occupied and do not contribute to any electron correlation, but all other electrons are in active orbitals, which are correlated amongst each other and therefore contribute to the determination of all C_l and $P_{\nu k}$. The number of electrons and molecular orbitals must be chosen for a molecular computation. Typically, the valence electrons and the resident orbitals are selected. The magnitude of a computation grows with the number of electrons and orbitals because they determine

the how many CSFs compose the CASSCF wavefunction. The number of CSFs can be determined by the Weyl-Robinson Formula:[21]

$$n_{CSFs} = \frac{2S+1}{m+1}\binom{m+1}{m-0.5N-S}\binom{m+1}{0.5N-S} \quad [2.58]$$

In [2.57], *m* is the number of active orbitals, *N* is the total number of active electrons, and *S* is the total spin. The difficulty of a CASSCF wavefunction can be illustrated with the large possible number of CSFs, using [2.57], as illustrated in Table 1.1. The number of CSFs can increase, as shown by Table 1.1, with the factorial number of the electrons, thereby heavily increasing the computational expense for solving the CASSCF wavefunction. With quantization of all possible CSFs, CASSCF is able to describe the static correlation of electrons, by typifying all possible states, including near-degenerate ones. Although, CASSCF fails in describing the dynamic correlation of electrons; that is, the instantaneous interactions of electrons with other proximal electrons. The scenario is similar to single-reference SCF, in which each electron sees all other electrons in an "averaged field," and the molecular orbital coefficients are optimized accordingly, among all possible configurations. There are multi-reference methods that recover dynamic correlation, using the CASSCF wavefunction and total energy as an initial guess. They include such methods as complete active space perturbation theory of order 2 or 3 (CASPT2,[22] CASPT3[23]), multi-reference configuration interaction (MRCI),[24-26] and multi-reference coupled-cluster (MRCC).[27] However, these methods are beyond the scope of this dissertation, and consequently is not reviewed here.

2.7 Density Functional Theory

The complexity of solving the electronic wavefunction for a molecular system of *N* electrons with 3*N* spatial and *N* spin components is the fact that the electronic Hamiltonian can handle only one- and two- electron interactions. This accounts for, at most, six spatial components. Therefore, a method that could account for electron interactions term of fewer variables could provide much more computational efficiency and mathematical elegance would be very attractive. This is the theme of density functional theory (DFT),[28] in that the complexity of the multi-component electronic wavefunction is reduced to an electron density.

The Hohenberg-Kohn theorems[28] lays the foundation for DFT; the first theorem states that a single-reference (thus, nondegenerate) electron density uniquely determines the ground state total energy, the molecular wavefunction, and any electronic properties for a molecular system. The electron density is computed by taking the absolute-square of the normalized electron density and integrating it over all space and spin:

$$\rho = \int_0^N \left[\sum_{all\ m_s} \int \dots \int |\psi(r, r_2 \cdots r_n)|^2 dr_2 \cdots dr_n \right] dr \qquad [2.59]$$

In [2.59], m_s specifies the spin of all *N* electrons. In light of this theorem, the total energy can be written as a functional of the electron density:

$$E = E[\rho] = T[\rho] + V_{Ne}[\rho] + V_{ee}[\rho]$$

$$= \left\langle \psi(r, r_2 \cdots r_n) \middle| -\sum_{i=1}^{N} \frac{1}{2} \nabla_i^2 - \sum_{i=1}^{N} \sum_{A=1}^{N} \frac{Z_A}{r_{iA}} + \sum_{i=1}^{N} \sum_{j>i}^{N} \frac{1}{r_{ij}} \middle| \psi(r, r_2 \cdots r_n) \right\rangle \qquad [2.60]$$

The above expression relates the total energy as a sum, on the right-hand side, of the kinetic energy functional:

$$T[\rho] = \left\langle \psi(r, r_2 \cdots r_n) \right| = -\sum_{i=1}^{N} \frac{1}{2} \nabla_i^2 \left| \psi(r, r_2 \cdots r_n) \right\rangle \qquad [2.61]$$

Along with the nuclear-attraction potential energy functional:

$$V_{Ne}[\rho] = \left\langle \psi(r, r_2 \cdots r_n) \right| \sum_{i=1}^{N} \sum_{A=1}^{N} \frac{Z_A}{r_{iA}} \left| \psi(r, r_2 \cdots r_n) \right\rangle = \int \upsilon(r) \rho(r)\, dr \qquad [2.62]$$

And the two-electron interaction energy functional:

$$V_{ee}[\rho] = \left\langle \psi(r, r_2 \cdots r_n) \right| \sum_{i=1}^{N} \sum_{j>i}^{N} \frac{1}{r_{ij}} \left| \psi(r, r_2 \cdots r_n) \right\rangle \qquad [2.63]$$

The second Hohenberg-Kohn Theorem states that the ground state electron density minimizes the total energy functional. Hence, it links DFT to the Variational principle associated with [2.17] for the electron density.

A practical means of determining the electron density and then the total energy was formulated by Kohn and Sham, now known as the Kohn-Sham method.[29] They applied a "fictitious reference system of *N* noninteracting electrons that each experience the same external potential energy function, $\upsilon(r)$."[30] Therefore, the Hamiltonian of this reference system is:

$$H = \sum_{i=1}^{N} h_i^{KS} = \sum_{i=1}^{N} \frac{1}{2} \nabla_i^2 + \upsilon(r_i) \qquad [2.64]$$

Also, the Kohn-Sham one-electron wavefunction is a Slater determinant of spin orbitals that are eigenfunctions of [2.64].

In addition, Kohn and Sham rewrote the total energy functional. First, the kinetic energy functional can be rewritten as a difference of kinetic energy functionals of the real molecular system and the fictitious system:

$$\Delta T[\rho] = T[\rho] - T_s[\rho] \qquad [2.65]$$

In [2.65], the subscript *s* denotes the fictitious system. Also, a difference equation for the electron-electron interactions is given:

$$\Delta V_{ee}[\rho] = V_{ee}[\rho] - \frac{1}{2}\iint \frac{\rho(r_1)\rho(r_2)}{r_{12}} dr_1 dr_2 \qquad [2.66]$$

The second term on the right-hand side accounts for electronic charge interaction by smearing the electron densities over all space; the ½ coefficient accounts for double-counting after integration of the two-electron interactions. Next, substituting [2.65] and [2.66] into [2.60] yields:

$$E[\rho] = T_s[\rho] + \int v(r)\rho(r)\, dr + \frac{1}{2}\iint \frac{\rho(r_1)\rho(r_2)}{r_{12}} dr_1 dr_2 + \Delta T[\rho] + \Delta V_{ee}[\rho] \qquad [2.67]$$

At this point, the energy functional of a real molecular system is composed of a sum of a kinetic energy, potential energy, and electron-electron interaction functionals that describe a fictitious reference system, and two difference functionals that bridge the gap in the descriptions of the real and fictitious systems. The sum of these last two functionals are known to describe electron exchange and correlation. This is the exchange-correlation (XC) functional:

$$E_{XC}[\rho] = \Delta T[\rho] + \Delta V_{ee}[\rho] \qquad [2.68]$$

So, now the total energy functional, in its final form, is given as:

$$E[\rho] = T_s[\rho] + \int v(r)\rho(r)\, dr + \frac{1}{2}\iint \frac{\rho(r_1)\rho(r_2)}{r_{12}} dr_1 dr_2 + E_{XC}[\rho] \qquad [2.69]$$

The XC functional is an energy term that can be expanded as a sum of the exchange and correlation energies:

$$E_{XC}[\rho] = E_X[\rho] + E_C[\rho] \qquad [2.70]$$

The exchange energy accounts for the energy associated with the antisymmetry requirement of electrons; also, the correlation energy accounts for the energy associated with the Coulombic repulsions, which cause electrons to avoid each other.

The exact form of the XC functional is unknown, and many forms of which have been produced to improve DFT applications for molecular and solid-state computations. For this overview of DFT, three classes of XC functionals are briefly mentioned. To begin, the local density approximation (LDA)[31,32] describes an electron density with a slowly varying gradient. Hohenberg and Kohn illustrated that this XC functional can be written as:

$$E_{XC}^{LDA}[\rho] = \int \rho(r)\varepsilon_{XC}(\rho)dr \qquad [2.71]$$

The LDA XC functional describes a "jellium," in which interacting electrons and positive charges, associated with nuclei, are both uniformly distributed throughout space. This model is known to work very well for models requiring the conduction of electrons though a solid-state network. Also, to account for spin, the local spin density approximation (LSDA) constructs a jellium for electron densities of different spin, both up (α) and down (β):

$$E_{XC}^{LSDA}[\rho_\alpha, \rho_\beta] = \int \rho(r)\varepsilon_{XC}(\rho_\alpha, \rho_\beta)dr \qquad [2.72]$$

To account for electron densities with larger gradients, a generalized gradient approximation (GGA) is constructed, which has the general functional form:

$$E_{XC}^{GGA}[\rho_\alpha, \rho_\beta] = \int f(\rho_\alpha, \rho_\beta, \nabla\rho_\alpha, \nabla\rho_\beta)dr \qquad [2.73]$$

Some examples of GGA functionals include the Perdew-Wang 91 (PW91) XC functional[33,34] and the Perdew-Burke-Ernzerhof (PBE) XC functional,[35,36] both of which are vastly applied to solid-state computations.

The last class of XC functional to be mentioned in this section is the hybrid functional. These contain a parameterized mixture of HF exchange energy (see [2.26]) and gradient-corrected exchange and correlation energy terms from other functionals. A well-known example is the B3LYP XC functional,[37] in which the "3" signifies the three parameter contribution:

$$E_{XC}^{B3LYP} = (1 - a_o - a_x)E_X^{LSDA} + a_o E_X^{HF} + a_x E_X^{B88} + (1 - a_x)E_C^{VWN} + a_C E_C^{LYP} \quad [2.74]$$

Specifically, the LSDA, HF, and Becke88 (B88)[38] exchange functionals, and the Vosko-Wilk-Nusair (VWN)[39] and Lee-Yang-Parr (LYP)[40] correlation functionals all contribute to the B3LYP XC functional. The B3LYP parameters, a_o= 0.20, a_x= 0.72, and a_c= 0.81, were fitted to a set of atomization energies. It is noted that the B3LYP XC functional is among the most popular functional for computations of molecular properties, including atomization and reaction enthalpies, ionization potentials, and geometry optimizations.

2.8 Basis Functions

This last section elaborates on the right-hand side of atomic orbital basis set, [2.10], called the basis functions. There are two common types of basis functions: Slater-type orbitals (STOs)[41] and Gaussian-type orbitals (GTOs).[42] An STO that is centered on an atom *a* is written as:

$$\varphi_a^{STO}(r) = N r_a^{n-1} e^{-\zeta r_a} Y_l^m(\theta_a, \phi_a) \quad [2.75]$$

In [2.75], *N* is the normalization constant, $r_a^{n-1}e^{-\zeta r_a}$ is the radial component that depends on the principal quantum number, *n*, and $Y_l^m(\theta_a, \phi_a)$ is the spherical harmonic

component that depends on the azimuthal and magnetic quantum numbers, *l* and *m*, respectively. The radial component was derived by Slater to describe the hydrogenic-like one-electron orbital. However, for polyatomic molecules, much difficulty occurs for the two-electron integral, Equations [2.25] and [2.26], when integral accounts for three or four atomic centers. In a nutshell, for a basis set containing *b* basis functions, $\varphi_1^{STO}(r), \varphi_2^{STO}(r), \ldots, \varphi_b^{STO}(r)$, there are *b* possible permutations of $\langle \varphi_i \varphi_j | \varphi_k \varphi_l \rangle$ four-centered integrals (in which *i*, *j*, *k*, and *l* are atomic centers) and thusly $b^4/8$ electron interaction integrals to compute.[30]

To reduce the number of electron interaction integrals, and thereby increase the computational efficiency, GTOs are used in place of STOs:

$$\varphi_{ijk}^{GTO}(r) = N x_a^i y_a^j z_a^k e^{-\zeta r_a^2} Y_l^m(\theta_a, \phi_a) \qquad [2.76]$$

The two differences between [2.75] and [2.76] include the replacement of interior functions in the exponential from *r* to r^2 and of the exterior function r^{n-1} to $x^i y^k z^j$. The increase in the efficiency of GTOs stems from the fact that a product of two one-centered GTOs produces a two-centered GTO. The resulting two-electron integrals allow for faster computations. Also, the $x^i y^k z^j$ component are functions along the *x*, *y*, and *z* axes (assuming, of course that $r = r(x, y, z)$). When $i + j + k = 0$ (in which *i*, *j*, and *k* are all zero), an *s*-type GTO is produced; when $i + j + k = 1$ (in which *i*, *j*, or *k*=1), an *p*-type GTO is produced. A *d*-type GTO is formed when $i + j + k = 2$ (in which $i = j = 1$ and $k = 0$, or $i = k = 1$ and $j = 0$, or $j = k = 1$ and $i = 0$). Basically, the combinations of *i*, *j*, and *k* can produce any l-type GTO, where *l* = *s, p, d, f, g, h,* and beyond.

In the application of GTOs for a molecular basis set, it is standard practice to use a normalized linear combination, called *contractions,* of GTOs, called *primitives*:

$$\chi_a(r) = \sum_{i=1}^{N} c_{ai}\varphi_i(r) \qquad [2.77]$$

In the above, $\chi_a(r)$ is a contraction composed of *N* primitives, $\varphi_i(r)$, and *N* normalized contraction coefficients, c_{ai}. The simplest type of basis set is a *minimal basis set*, which is composed of a contraction of three GTOs to simulate an STO (STO-3G) for every *l*-type orbital. Taking the C atom as an example, the corresponding minimal basis set contains five basis functions, made from two *s*-type functions (for the 1*s* and 2*s* atomic orbitals) and three *p*-type functions (for the $2p_x$, $2p_y$, and $2p_z$ atomic orbitals). A total energy computation that employs a minimal basis set involves the simplest means of recovering correlation energy, with regard to basis set selection. However, a minimal basis set does not allow for variation of orbitals with changes in the molecular environment, such as changes in the number of electrons, protonation of electronegative atom, or expansion and contraction of atomic distances. One modification to the basis set to allow for better simulation of the molecular environment is to use a *split-valence* basis set. Since the valence orbitals are primarily responsible for bonding for molecules, then the description of the valence orbitals can be improved by splitting the valence orbitals between the inner and outer parts using two sets of GTO contractions. The inner GTO contraction maintains a selected ζ within each primitive, which is different from the ζ employed by the outer GTO contraction. Since two different ζ values are employed, then this split-valence basis set is a double-ζ basis set; that is, there are twice as many basis functions present compared to the corresponding minimal basis set, and the second set of functions have a different value for ζ (see the exponential in [2.76]). *Polarization functions* are also used to improve a

basis set. These include functions of higher *l*-type description beyond the core and valence *l*-type functions. The purpose of polarization functions is to improve the bonding description by allowing for a more spherically asymmetric description of electronic behavior within the valence orbitals. For example, polarization functions allow for computed molecular shape of ammonia (NH_3) to be trigonal pyramidal; without polarization functions, NH_3 would be predicted to have a trigonal planar shape. Finally, *diffuse* functions are another correction for basis sets. These are GTOs that have very small ζ values, compared to those employed within core and valence orbitals and polarization functions. Diffuse functions are employed in molecular computations to better describe anionic behavior.

At this point, the correlation consistent basis sets[43] are introduced. They are split-valence basis sets of varying ζ qualities as well as polarization functions to account for correlation energy. The cc-basis sets are denoted as cc-pVnZ, in which n= D (double), T (triple), Q (quadruple), and beyond. The "Z" denotes ζ, and "n" denotes the ζ quality. The "V" in cc-pVDZ specifies the valence set of basis functions; specifically, since, "VDZ" is specified, then the DZ rule applies only for the valence basis functions. Finally, the "cc-p" specifies correlation consistent polarization functions that recover the correlation energy. For example, the cc-pVDZ basis set for Carbon (the acronym "cc-pVDZ" is explained shortly) requires a set of nine *s*-type GTO primitives, four *p*-type GTO primitives, and one *d*-type GTO primitive, all of which recover an approximately consistent amount of correlation energy. The nine *s*-type GTO primitives are organized in three *s*-type GTO contractions, the four *p*-type GTO primitives are organized in two *p*-type GTO contractions, and the one *d*-type GTO primitive stands alone as one *d*-type

GTO contraction. This primitive/contraction combination is denoted by (9*s*4*p*1*d*)/[3*s*2*p*1*d*]. Similarly, triple-zeta (TZ) basis sets contain three times as many basis functions present compared to the corresponding minimal basis set, and all three sets of functions have different values for ζ. To show some examples, the 1*d* primitive is the correlation/polarization for the cc-pVDZ set, the 2*d*1*f* is the correlation/polarization for the cc-pVTZ set, and the 3*d*2*f*1*g* is the correlation/polarization for the cc-pVQZ set. The cc-basis sets can be augmented to better describe long-range effects and polarizabilities of charges species by diffuse functions. In the cc-basis sets, this augmentation[44] is noted with the prefix "aug-"; as an example, the aug-cc-pVDZ set increases each set of *l*-type contraction in the cc-pVDZ set by one diffuse GTO primitive. Therefore, the cc-pVDZ set with (9*s*4*p*1*d*)/[3*s*2*p*1*d*] becomes the aug-cc-pVDZ basis set with (10*s*5*p*2*d*)/[3*s*2*p*1*d*].

Table 2.1: CSFs for a set of *n* electrons in *n* orbitals, denoted by CASSCF[n,n]

CASSCF[n,n]	CSFs
[2,2]	3
[4,4]	20
[6,6]	175
[8,8]	1764
[10,10]	19404
[12,12]	226512
[14,14]	2760615
[16,16]	34763300
[18,18]	449141836
[20,20]	5924217936

CHAPTER 3

AN OVERVIEW OF SOLID-STATE PHYSICS

Solid-state physics is concerned with the atomic structure, properties, and applications of atoms that exist in the solid phase. Elements across the Periodic Table form macroscopic structures in the solid phase at room temperature (298.15 K) and pressure (1.0 atm), called crystals that contain repeated atomic arrangements. Such monoatomic and polyatomic crystals are essentially a three dimensional network of atoms in which electrons may conduct, depending on the atoms that form the crystal, bonding types (ionic, covalent, and metallic), temperature, and pressure to which the crystal is exposed. For example, the electronic structures of semiconductors, such as Si and Ge, have energy gaps, which are significant breaks of 1.1 eV and 0.7 eV at 300 K[45] between electronically occupied states and electronically unoccupied states. Energy gaps of these magnitudes allow for the moderated conduction of electrons with varying temperatures, pressures, and external magnetic fields and, therefore, are the foundation of electronic devices, such as radios, computers, diodes, solar cells, and transistors. Crystals made solely from alkali, alkaline earth, and transition metals lack energy gaps and thus have higher conductivities that generally do not benefit such electronic applications. Instead, solid solutions of elements, or alloys, have other applications. For example, stainless steel (Fe_3C) has a high resistance to corrosion and oxidation and is necessary in the production of cookware, buildings, surgical equipment, and firearms.[46] Also, Alnico, which is primarily composed of aluminum, nickel, and cobalt, acts as a permanent magnet; in fact, it has a Curie point of 860 ^{o}C, above which the aligned magnetic moments are disordered, thus transforming Alnico© from a paramagnet into a

ferromagnet.[47] Alnico is used in the manufacture of devices, such as electric motors, loudspeakers, and magnetrons.[48]

In this chapter, fundamental topics of solid–state physics are introduced. An overview of basic crystal structures, formed by the sum of repeated atoms and the lattice spacing in which they exist, which have been experimentally determined, are presented. Next, the reciprocal lattice is discussed; this is a lattice that can be formed from a corresponding crystal structure and is the space in which the electron density of a crystal structure is analyzed. The solution to the wavefunctions of a crystal structure, assembled through Bloch's theorem, is investigated. Following that, resources for evaluating the electronic structure, mainly through band structure theory and density of states (DOS), is also to be discussed. Chemical bonding within crystal structures from various sections of the periodic table is surveyed. Finally, brief synopses of k-point sampling, a resource that is implemented in calculating accurate electronic energies, and pseudopotentials and pseudowavefunctions are presented.

3.1 Crystal Structures

The combination of a set volume of space and the arrangement of the constituent atoms may be defined as a crystal structure. The space of the crystal structure can be defined as a 'lattice' and the set of atoms can be defined as a basis. The lattice is described by three primitive translational vectors, $\boldsymbol{a_1}$, $\boldsymbol{a_2}$, and $\boldsymbol{a_3}$ that are translationally symmetric throughout the crystal, and are thus primitive. They may be written as function of *x*, *y*, and *z* coordinates, all of which may have corresponding *i*, *j*, and *k* vectors, respectively:

$$\boldsymbol{a_1} = x_1\boldsymbol{i} + y_1\boldsymbol{j} + z_1\boldsymbol{k} \quad [3.1]$$

$$\boldsymbol{a_2} = x_2\boldsymbol{i} + y_2\boldsymbol{j} + z_2\boldsymbol{k} \quad [3.2]$$

$$\boldsymbol{a_3} = x_3\boldsymbol{i} + y_3\boldsymbol{j} + z_3\boldsymbol{k} \quad [3.3]$$

The angles between $\boldsymbol{a_1}$ and $\boldsymbol{a_2}$, $\boldsymbol{a_2}$ and $\boldsymbol{a_3}$, and $\boldsymbol{a_3}$ and $\boldsymbol{a_1}$, all of which may be labeled as α, β, and γ, respectively, may vary from 90^o, as illustrated in Figure 3.1. The position of each atom may be noted with a vector, defined as a 'basis vector,' All of these basis vectors exist within the volume of the crystal lattice, V_{xl}:

$$V_{xl} = |\boldsymbol{a_1} \cdot \boldsymbol{a_2} \times \boldsymbol{a_3}| \quad [3.4]$$

The crystal structure is produced by combining the lattice translational vectors and the set of basis vectors.

3.2 The Reciprocal Lattice

Unlike crystal structures, which are not just mathematical constructions but rather have been experimentally observed, a 'reciprocal lattice' is solely a mathematical construction, derived from a corresponding crystal structure, in which the electron density throughout the crystal structure may be analyzed. To find the reciprocal lattice, the translational invariance of the electron density must be taken into account.

$$\boldsymbol{T} = u_1\boldsymbol{a_1} + u_2\boldsymbol{a_2} + u_3\boldsymbol{a_3} \quad [3.5]$$

Equation [3.5] is a translation vector, $\boldsymbol{T}$, in which $\boldsymbol{a_1}$, $\boldsymbol{a_2}$, and $\boldsymbol{a_3}$ are the primitive translational vectors of the crystal lattice and u_1, u_2, and u_3 are integers. An arbitrary point located at $\boldsymbol{r} = w_1\boldsymbol{a_1} + w_2\boldsymbol{a_2} + w_3\boldsymbol{a_3}$ within one crystal structure may be translated to proximal crystal structures using [3.5].

$$\boldsymbol{r} + \boldsymbol{T} = (u_1 + w_1)\boldsymbol{a_1} + (u_2 + w_2)\boldsymbol{a_2} + (u_3 + w_3)\boldsymbol{a_3} = u_1\boldsymbol{a_1} + u_2\boldsymbol{a_2} + u_3\boldsymbol{a_3} \quad [3.6]$$

The initial and final points within both crystal structures have identical environments. Therefore, movement between the crystal structures by ***T*** results in translational invariance. With the electron density defined as *n(r),* this translational invariance is shown by the following:

$$n(\boldsymbol{r}) = n(\boldsymbol{r} + \boldsymbol{T}) \quad [3.7]$$

The electron density is defined as the absolute square of the wavefunction for the crystal structure.

$$n(\boldsymbol{r}) = |\Psi(\boldsymbol{r})|^2 \quad [3.8]$$

Unlike the electron density, the wavefunction is not translationally invariant; in fact, translation of the wavefunction produces a phase factor, μ, such that the absolute square of this phase factor is unity:

$$\Psi(\boldsymbol{r}) = \Psi(\boldsymbol{r} + \boldsymbol{T}) = \mu\Psi(\boldsymbol{r}) \quad [3.9]$$

$$|\mu\Psi(\boldsymbol{r})|^2 = \mu\Psi(\boldsymbol{r}) \cdot \mu\Psi(\boldsymbol{r}) = (\mu \cdot \mu)\big(\Psi(\boldsymbol{r}) \cdot \Psi(\boldsymbol{r})\big) = (1)|\Psi(\boldsymbol{r})|^2 = n(\boldsymbol{r}) \quad [3.10]$$

The phase factor is a plane wave:

$$\mu = exp(i\boldsymbol{G} \cdot \boldsymbol{r}) \quad [3.11]$$

Thus, μ is a complex exponential function, which is a function of the position vector, **r**, and a reciprocal lattice vector, ***G***, which has the form:

$$\boldsymbol{G} = v_1\boldsymbol{b_1} + v_2\boldsymbol{b_2} + v_3\boldsymbol{b_3} \quad [3.12]$$

The reciprocal lattice vector is a function of primitive reciprocal vectors, $\boldsymbol{b_1}$, $\boldsymbol{b_2}$, and $\boldsymbol{b_3}$, all of which have units of inverse length, and v_1, v_2 and v_3 are integers. The primitive reciprocal vectors can be constructed using the primitive translational vectors of the crystal structures:

$$\boldsymbol{b_1} = 2\pi \frac{\boldsymbol{a_2} \times \boldsymbol{a_3}}{|\boldsymbol{a_1} \cdot \boldsymbol{a_2} \times \boldsymbol{a_3}|} \quad [3.13]$$

$$\boldsymbol{b_2} = 2\pi \frac{\boldsymbol{a_3} \times \boldsymbol{a_1}}{|\boldsymbol{a_1} \cdot \boldsymbol{a_2} \times \boldsymbol{a_3}|} \quad [3.14]$$

$$\boldsymbol{b_3} = 2\pi \frac{\boldsymbol{a_1} \times \boldsymbol{a_2}}{|\boldsymbol{a_1} \cdot \boldsymbol{a_2} \times \boldsymbol{a_3}|} \quad [3.15]$$

Each primitive translational vector is orthogonal to its corresponding primitive reciprocal:

$$\boldsymbol{b_n} \cdot \boldsymbol{a_n} = 2\pi\delta_{nm} \quad [3.16]$$

where δ_{nm} is the Kronocker delta function.

Like crystal structures, reciprocal lattices have the property of translational invariance. Therefore, only one reciprocal lattice needs to be constructed that contains all information necessary for the analysis of electronic structure. This reciprocal lattice is calculated using [3.13] through [3.15] to calculate the reciprocal lattice vectors. A square lattice, as a simple two-dimensional example, can be constructed using reciprocal lattice vectors that may be obtained using [3.13] through [3.15]. Figure 3.2 illustrates a segment of points that have been produced from the repetition of reciprocal lattice vectors, $\boldsymbol{b_1}$ and $\boldsymbol{b_2}$. All lattice points are conceptually joined to each other by vertical, horizontal, and diagonal lines. This results in lines that bisect other lines (or planes if in three dimensional space) halfway between lattice points. The lowest area encapsulation of each lattice point results in construction of Wigner-Seitz cells; these cells are also called Brillouin zones. On the right part of Figure 3.2, the lowest area (shaded) is produced using horizontal and vertical (non-diagonal) lines, thus illustrating the first Brillouin zone. Only this zone is needed because, similarly to the other Brillouin zones, it contains all the necessary electronic structure information. A translation through the Brillouin zone is actually a change in the wavevector, $\boldsymbol{k}$, having units of reciprocal length,

of an electron that is described as a plane wave, $exp(i\boldsymbol{k}\cdot\boldsymbol{r})$. This translation is particularly important in the analysis of band structures and are explored later.

$$\hat{H} = \hat{K} + \hat{V} \quad [3.17]$$

Given $f(\boldsymbol{r})$, an arbitrary wavefunction, E_K is the kinetic energy eigenvalue and $V(\boldsymbol{r})$ is the potential energy eigenvalue, both of which correspond to $f(\boldsymbol{r})$, and so:

$$\left[\hat{T}_T, \hat{H}\right] f(\boldsymbol{r}) = \left[\hat{T}_T, \hat{K}\right] f(\boldsymbol{r}) + \left[\hat{T}_T, \hat{V}\right] f(\boldsymbol{r}) \quad [3.18]$$

$$\left[\hat{T}_T, \hat{K}\right] f(\boldsymbol{r}) = \hat{T}_T \hat{K} f(\boldsymbol{r}) + \hat{K}\hat{T}_T f(\boldsymbol{r}) = E_K \hat{T}_T f(\boldsymbol{r}) - \hat{K} f(\boldsymbol{r} + \boldsymbol{T}) \quad [3.19]$$

$$= E_K f(\boldsymbol{r} + \boldsymbol{T}) - E_K f(\boldsymbol{r} + \boldsymbol{T}) = 0$$

$$\left[\hat{T}_T, \hat{V}\right] f(\boldsymbol{r}) = \left[\hat{T}_T, V(\boldsymbol{r})\right] f(\boldsymbol{r}) = \hat{T}_T V(\boldsymbol{r}) f(\boldsymbol{r}) + V(\boldsymbol{r})\hat{T}_T f(\boldsymbol{r}) \quad [3.20]$$

$$= \hat{T}_T V(\boldsymbol{r}) f(\boldsymbol{r}) - V(\boldsymbol{r}) f(\boldsymbol{r} + \boldsymbol{T}) = V(\boldsymbol{r} + \boldsymbol{T}) f(\boldsymbol{r} + \boldsymbol{T}) - V(\boldsymbol{r}) f(\boldsymbol{r} + \boldsymbol{T}) = 0$$

in which:

$$V(\boldsymbol{r} + \boldsymbol{T}) - V(\boldsymbol{r}) = 0 \quad [3.21]$$

Equation [3.21] is applicable since the crystal structure is repeated with respect to the translation vector, $\boldsymbol{T}$. Therefore, [3.18] through [3.20] all equal zero, and all crystal structures throughout the crystalline material have a common set of wavefunctions and eigenvalues. As a result, all computations for a crystalline material are executed by using *only* the translational vectors and atomic basis vectors of a repeated crystal structure.

The Translation operator may be used on [3.9], which is expanded below as a plane wave basis set:

$$\hat{T}_T|\Psi\rangle = \hat{T}_T \sum_{\boldsymbol{k+G}} C_{\boldsymbol{k+G}} exp(i(\boldsymbol{k}+\boldsymbol{G})\cdot\boldsymbol{r})$$

$$= \sum_{\boldsymbol{k+G}} C_{\boldsymbol{k+G}} exp(i(\boldsymbol{k}+\boldsymbol{G})\cdot\boldsymbol{r}) exp(i(\boldsymbol{k}+\boldsymbol{G})\cdot\boldsymbol{T})$$

$$= exp(i(\boldsymbol{k})\cdot\boldsymbol{T}) \sum_{\boldsymbol{k+G}} C_{\boldsymbol{k+G}} exp(i(\boldsymbol{k}+\boldsymbol{G})\cdot\boldsymbol{r}) exp(i(\boldsymbol{G})\cdot\boldsymbol{T}) \quad [3.22]$$

$$= t_T \sum_{\boldsymbol{k+G}} C_{\boldsymbol{k+G}} exp(i(\boldsymbol{k}+\boldsymbol{G})\cdot\boldsymbol{r}) exp(i(\boldsymbol{G})\cdot\boldsymbol{T})$$

$$= t_T \sum_{\boldsymbol{G}} C_{\boldsymbol{k+G}} exp(i(\boldsymbol{k}+\boldsymbol{G})\cdot\boldsymbol{r}) exp(i2\pi n)$$

$$= t_T \sum_{\boldsymbol{G}} C_{\boldsymbol{k+G}} exp(i(\boldsymbol{k}+\boldsymbol{G})\cdot\boldsymbol{r})$$

In [3.22], $C_{\boldsymbol{k+G}}$ are the plane wave coefficients and $t_{\boldsymbol{T}}$ is the eigenvalue of the Translation operator with respect to the plane wave set. It is noted that [3.22] requires the use of [3.5], [3.12], and [3.16]. The plane wave basis set is taken with respect to all possible ***k*+*G*** wavevectors, all of which are equivalent to all possible ***k***; thus, ***k*=*k*+*G***. Therefore, $t_{\boldsymbol{T}}=exp(i\boldsymbol{k}\cdot\boldsymbol{T})$ is degenerate for all ***k*+*G***. With this boundary condition, the associated wavefunction as a plane wave basis set can be written:

$$|\Psi_k\rangle = \sum_{\boldsymbol{k+G}} C_{\boldsymbol{k+G}} exp(i(\boldsymbol{k}+\boldsymbol{G})\cdot\boldsymbol{r}) = exp(i(\boldsymbol{k})\cdot\boldsymbol{r}) \sum_{\boldsymbol{k+G}} C_{\boldsymbol{k+G}} exp(i\boldsymbol{G}\cdot\boldsymbol{r}) \quad [3.23]$$

$$= u_k(\boldsymbol{r}) exp(i(\boldsymbol{k})\cdot\boldsymbol{r})$$

It is a product of a plane wave with a wavevector, ***k***, and the periodic potential that is composed of the atomic potentials within the reciprocal lattice. The periodic potential, $u_{\boldsymbol{k}}(\boldsymbol{r})$, may be written as a Fourier sum and has the property of translational invariance. This is illustrated using the translation vector from [3.4]:

$$u_k(\boldsymbol{r}+\boldsymbol{T}) = \sum_{\boldsymbol{k}+\boldsymbol{G}} C_{\boldsymbol{k}+\boldsymbol{G}} exp\big(i(\boldsymbol{G})\cdot(\boldsymbol{r}+\boldsymbol{T})\big) = \sum_{\boldsymbol{k}+\boldsymbol{G}} C_{\boldsymbol{k}+\boldsymbol{G}} exp(i\boldsymbol{G}\cdot\boldsymbol{r})\, exp(i\boldsymbol{G}\cdot\boldsymbol{T})$$
$$= \sum_{\boldsymbol{k}+\boldsymbol{G}} C_{\boldsymbol{k}+\boldsymbol{G}} exp(i\boldsymbol{G}\cdot\boldsymbol{r}) = u_k(\boldsymbol{r}) \qquad [3.24]$$

Equation [3.24] is a one-electron form of a Bloch function. The Bloch function for all electrons within a crystal structure can be written as a complete set of plane waves with all possible wavevectors:

$$|\Psi\rangle = \sum_k |\Psi_k\rangle = \sum_{\boldsymbol{k}} u_k(\boldsymbol{r}) exp(i\boldsymbol{k}\cdot\boldsymbol{r}) \qquad [3.25]$$

As the form of [3.25] might suggest, the complete set of one-electron Bloch functions represents all electrons that propagate throughout the crystal structure. The freedom with which all these electrons may propagate depends not only on the identity of the nuclei, but also the proximity of the electrons to the nuclei.

3.3 Electronic Structure Theory

It was noted that analysis of the electronic structure of a crystal structure may be executed within the first Brillouin zone. This is because the first Brillouin zone exists within reciprocal space, which, like plane waves that describe electron wave behavior, is a function of the wavevector, ***k***. Therefore, atomic orbital interactions can be observed within the first Brillouin zone.

For a plane wave, the norm of the wavevector, ***k***, is related to the wavelength, λ, by the following:

$$\lambda = \frac{2\pi}{\|\boldsymbol{k}\|} \qquad [3.26]$$

Within a crystal structure, atomic orbitals interact according to the electronic wavefunction (Equation [3.25]). To better understand this, it is helpful to introduce such interactions using a one-dimensional linear chain of six atoms, all of which are separated by a lattice constant, *a*, equipped with s orbitals, and a wavefunction dependent upon a non-integer variable wavenumber, *k*, also referred to as a k-point (it should be noted that since this chain of atoms is one-dimensional, then the wavevector is actually a wavenumber). If *k = 0*, then, by [3.26], the wavefunction has an infinitely long wavelength and thus contains no nodes between the *s* orbitals. Therefore, complete in-phase bonding between these s orbitals is achieved. As the wavevector increases, the wavelength decreases, thus causing nodal behavior in the wavefunction. The wavenumber is also defined another way, which can provide a better illustration:

$$k = \pm\frac{2\pi p}{Na} \in -\frac{\pi}{a} < k < \frac{\pi}{a} \qquad [3.27]$$

In [3.27], *a* is the lattice constant (in this example, for the linear chain of six atoms), N is the number of atoms in the system (in this example, *N*=6), and *p* has integer values that result in the given range. For the linear chain of six atoms, *k* has the values:

$$k_{6-chain} = 0, \pm\frac{\pi}{3a}, \pm\frac{2\pi}{3}, \pm\frac{\pi}{a} \qquad [3.28]$$

The boundaries of the one-dimensional first Brillouin zone are between *-π/a* and *π/a,* beyond which translational invariance causes an environmental repetition of the first Brillouin zone. Energy values are associated with all six wavenumbers. Therefore, if these energies are plotted with respect to the varying wavenumbers in [3.28], then a band of energies is produced. Orbital energies within a crystal structure are commonly illustrated as a band that depends on the electron wavevector through the reciprocal lattice.

The *n*-dimensional wavevector that has components that are all zero is called the gamma (Γ) point. Depending on the shape of the orbital (*s*, p_x, p_y, p_z, etc), the energy at the gamma point may or may not be the lowest energy of the band. The Figure 3.3 illustrates this condition in two dimensions. Two 3 x 3 atomic grids, all of which contain p_x and p_y orbitals, are illustrated in Figure 3.3; the electronic interactions throughout the p_x orbitals and p_y orbitals as a function of a two-dimensional wavevector can be examined. This example allows the use of Equation [3.28] to plot a p_x and p_y band, also illustrated in Figure 3.3. Each band starts at the Γ point ($\boldsymbol{k} = 0\boldsymbol{i} + 0\boldsymbol{j}$). As illustrated in Figure 3.3, the p_x and p_y both have σ antibonding and π bonding interactions. Because of the antibonding interactions, the energy at the Γ point for both orbital sets is not the lowest energy in the band structure of Figure 3.3. The band between the Γ point and the X point ($\boldsymbol{k} = \pi/a\boldsymbol{i} + 0\boldsymbol{j}$) is constructed using positive values of [3.28]. Obviously, the fine curvature of the band illustrated in Figure 3.3 contains more than three points and can thus be constructed through spectroscopy or computation through k-point sampling, a process that are examined in a later section. At the X point, the p_x orbitals have σ and π bonding interactions and the p_y orbitals have σ and π antibonding interactions; as a result, the p_x and p_y energies at the X point are highly split, in which the latter energy is much higher than the former energy. The band between the X point and the M point ($\boldsymbol{k} = \pi/a\boldsymbol{i} + \pi/a\boldsymbol{j}$) may also be constructed using positive values of [3.28]. At the M point, the p_x and p_y orbitals have σ bonding and π antibonding interactions; as a result, the p_x and p_y energies at the X point are degenerate, which results low energies along both bands. Finally, the band between the M point and the Γ point causes a rise in band energies, back to the initial condition.

Another useful resource for understanding three-dimensional electronic structures is called the density of states (DOS). An example of this is the right portion of Figure 3.4, which is the DOS of ReO_3 (it is conventional to show the DOS alongside the band structure to show the relationship between both figures). The DOS is useful in plotting the total number of states, which is the sum of degenerate energy points (which may be a function of different wavevectors) from the band structure. Further, the Fermi energy (E_F) through the Band Structure and DOS, Figure 3.4, illustrates the energy separation of the occupied states (shaded DOS) and unoccupied states (unshaded DOS). Because a band gap does not exist at E_F, electrons may be promoted to excited states with little change in energy. States below E_F are called the valence states and states above E_F are called conduction states (similarly, bands below E_F are called the valence bands and above the Fermi energy are called conduction bands). In Figure 3.4, the band structure of ReO_3 has an E_F that crosses the lower portion of the Re *5d* bands. With little change in energy (by photo or thermal excitation), electrons may be promoted to the conduction bands, allowing electrons to conduct throughout the material. Materials that exhibit this facile excitation are called metals; this is illustrated in Figure 3.7c. If the DOS and band structure for a given material have a band gap through which the Fermi energy crosses, then the material is a semiconductor or an insulator. The difference between the types of materials depends on the energy width of the band gap, which directly affects the required energy to excite electrons into the conduction bands. The formal definition for band gap width varies throughout solid-state texts, all of which classify semiconductors as having maximum band gap widths no more than 2.00 to 3.00 eV. Materials having band gaps widths beyond this range are called insulators, as

shown in Figure 3.7a. Finally, a material lacking a band gap, but having one or more of the highest energy valence bands being higher in energy than the one or more of the lowest conduction bands in various regions of reciprocal space is called a semimetal; this is illustrated in Figure 3.7b. Conduction may be initiated with a change in the wavevector or a lattice vibration; as a result, conduction of electrons can theoretically occur at 0 K. Semimetals have conduction properties between those of a metal and semiconductor. Typical semimetals include crystalline metalloids, such as Sn, As, Sb, and Bi, and HgTe.

3.4 Chemical Bonding

The electronic structure of various crystal structures may be formed through three main types of chemical bonding: ionic, covalent, and metallic. All three bonding mechanisms are briefly explored in this section. Ionic bonding involving atoms from the far left and far right of the periodic table within a solid produce a DOS that is composed of valence states from the anions and conduction states from the cations (Figure 3.8 illustrates the bonding mechanism of NaCl as an example), thus the latter are higher in energy than the former. This is different in comparison to the gas phase illustration, which shows that the anions are higher in energy than the cations. A Madelung potential in the solid phase causes this difference, which is the electrostatic charge that ions experience as a result of being surrounded by other ions of opposite charge. Such an arrangement results in a periodicity, ... CACACACA ..., of cations (C) and anions (A), in three dimensions. The Madelung potential is a function of the Madelung constant, which takes into account not only the Coulombic charge from nearest-neighbor cations and anions, but also form long-range cationic and anionic Coulombic charge. This effect

produces a wide band gap compared to that between the same ions in the gas phase. In addition, polarization energy takes into account the movement of an electron through the solid and causes the wide band gap to decrease somewhat. Finally, the overlap of orbitals from nearest-neighboring ions results in a broadening of valence states into a band of anionic states (observed in a DOS) and a broadening of conduction states into a band of cationic states. This results in a large decrease in the band gap, but most ionic solids are insulators and thus may easily have band gaps larger than 3.00 eV. The bandwidths, which are the range of energies that conduction or valence states span, depend on the orbital character of the cations and anions, respectively.

Conduction electrons in cations, from the first, second, or third column of the periodic table, experience a much lower effective nuclear charge than valence electrons in anions from the far right of the periodic table. As a result, orbitals of cations are more diffuse than those of anion and participate more in orbital overlap. Thus, it is expected that conduction bandwidths are much larger than valence bandwidths. The mechanism of chemical bonding between atoms in Groups 4, 5, and 6 of the periodic table is quite different than the bonding of ionic solids because these atoms have similar energies. Thus, covalent bonding is the primary bonding mechanism. These atoms have electrons that experience effective nuclear charges midway between those experienced by electrons in atoms from the far left or right of the periodic table.

The orbital character of Groups 4, 5, and 6 are proportionally midway as well. The differences in the bonding character of covalent solids may be observed by comparing elements down the periodic table: *p* orbital diffusivity decreases, due 1) to the presence of nodes, as the principle quantum number increases, and 2) due to

relativistic effects experienced by the valence electrons for atoms beginning in the third row of the periodic table. Consequently, orbital overlap in covalent solids decreases going down the periodic table, causing a proportional decrease in the width of the band gap. Figure 3.9 shows this behavior for Group 4 tetrahedral solids. This trend has been observed in homogeneous covalent solids, such as C (diamond), Si, Ge, and Sn, and in heterogeneous covalent solids, such as BN, AlP, GaAs, and InSb. These structures are four coordinate structures due to the covalent bonding.

Simple metals are formed with atoms from Groups 1 - 3 of the periodic table. Such atoms are electron deficient, compared to atoms in Group 4 - 8, and unable to attain stable bonding. Close packed structures are, therefore, formed in simple metals, in which high coordination numbers, around six, yield structural stability. Also, Groups 1 - 3 atoms contain diffuse orbitals, which allow for large orbital overlap, yielding the formation of a large band, which is a continuum of states that could be seen in a DOS plot and lacking a band gap. Further, the large diffusivity results in a band in which the valence electrons are only marginally affected by nuclear charge, allowing for facile conduction of electrons near the valence states with minimal excitation: this model is called the “nearly free-electron model.” This model cannot apply to transition metals because the *d* orbitals are more contracted, due to relativistic effects and higher effective nuclear charges. Consequently, the bandwidth associated with *d* orbital overlap is much smaller than the bandwidth associated with *s* orbital overlap.

3.5 K-point Sampling

A large number of atoms in three dimensions are required for the formation of a macroscopic material. For approximately one mole of a monoatomic crystal, the number of atoms, N, along each dimension, *x, y,* and *z,* is equivalent to the following:

$$N_x N_y N_z = 1x10^{23}\text{atoms} \quad [3.29]$$

To obtain band energies, including the Fermi energy and the free energy of a crystal lattice, using a plane wave basis set, a set of k-points within the first Brillouin zone must be chosen. The first Brillouin zone contains an extremely large number of k-points. This may be illustrated by rewriting [3.27] for each coordinate axis:

$$k_i = \pm\frac{2\pi p_i}{N_i a} \in -\frac{\pi}{a} < k_i < \frac{\pi}{a} \text{ for } i = x, y, z \quad [3.30]$$

Since *N* along each coordinate axis is large, then the number of integers, *p*, required for all k-points is likely to be large as well. Therefore, it is more computationally convenient to sample the first Brillouin zone by inputting a number of points along each component axis. For example, if an 8 x 8 x 8 k-point grid is used, then the number of k-points in the first Brillouin zone, which would be used to calculate all necessary energies is 8 x 8 x 8 = 83 = 512 k-points. Depending on the trial structure, the trial basis vectors (the number and types of atoms) and the trial lattice constants, choosing a k-point grid that produces the desired computational accuracy within acceptable computational cost requires trial-and-error.

Since the energy of the crystal lattice is a function of the electron density within the first Brillouin zone, then the electron density over the filled bands must be integrated as a function of the k-points:[49]

$$E = \frac{1}{\Omega_{FBZ}} \sum_{n} \int_{\Omega_{FBZ}} \varepsilon_{n\boldsymbol{k}} \Theta(\varepsilon_{n\boldsymbol{k}} - E_F)\, d\boldsymbol{k} \qquad [3.31]$$

In [3.31], n specifies the electrons, $\varepsilon_{n\boldsymbol{k}}$ specifies the band energies, Ω_{FBZ} is the reciprocal volume of the first Brillouin zone, E_F is the Fermi energy, and Θ is the Dirac step function, which yields $\Theta=1$ when $\varepsilon_{n\boldsymbol{k}} < E_F$ and $\Theta=0$ when $\varepsilon_{n\boldsymbol{k}} > E_F$. Since a limited number of k-points is used, then the integral in [3.31] becomes a discrete sum:

$$E = \frac{1}{\Omega_{FBZ}} \sum_{n} \sum_{\boldsymbol{k}} \varepsilon_{n\boldsymbol{k}} \Theta(\varepsilon_{n\boldsymbol{k}} - E_F) \qquad [3.32]$$

Convergence of the electronic energy may become slow since Θ transforms from 1 to 0 as the Fermi energy is crossed. Therefore, smoother functions should substitute Θ for computational efficiency and produce partial electron occupancies near the Fermi energy, thus causing electron smearing.

The Fermi-Dirac function can be used to provide smooth electron smearing:

$$S(E) = \left[\exp\left(\frac{E - E_F}{k_b T}\right) + 1\right]^{-1} \qquad [3.33]$$

In [1.35], k_b is Boltzmann's constant, T is the temperature in K, and $S(E)$ can be used to describe electron occupation as a function of energy. An undefined electron occupancy, however, results when computations are performed at 0 K; therefore, a value of T near 0 K must be specified. Methfessel and Paxton[50] observed a limitation to electron smearing via the Fermi-Dirac function. Figure 3.10 illustrates the available DOS, $g(\varepsilon)$, of a chemical system and the electron smearing of the DOS by the Fermi-Dirac function, $g(\varepsilon)S_0(\varepsilon\text{-}EF)$, which accounts for DOS that are occupied by electrons.

The lined area to the left of E_F are unoccupied DOS and the lined area to the right of E_F are DOS that are occupied by electrons. Given these electrons were energetically

promoted from the left lined area to the right lined area, both lined areas should be equal. However, it is apparent in Figure 3.8 that both lined areas are not equal. Therefore, the Fermi-Dirac function does not accurately model electron occupation around the Fermi energy for metals, which unlike insulators and semiconductors, lack band gaps; semiconductors and insulators have zero charge density. Thus, Methfessel and Paxton formulated another electron smearing model:[50]

$$S(E) = \frac{1}{2}\big(1 - erf(x)\big) + \sum_{n=1}^{N} \frac{(-1)^n}{n!\, 4^n \sqrt{\pi}} H_{2n-1}(x) exp(-x^2) \qquad [3.34]$$

In Equation [3.34], *erf(x)* is the error function and $H_{2n-1}(x)$ is a Hermite polynomial of degree 2*n*-1.

3.6 Pseudopotentials

For an atom within a crystal lattice, the region may be divided into two parts: the core region, which contains the core electrons and atomic charge, and the valence region, which contains the valence electrons that may conduct through the material upon excitation. In the core region, use of a plane wave basis set to model the all-electron wavefunction, which describes the charge density in the core states, would be computationally expensive. This is because the core wave character exhibits strong oscillations requiring numerous plane waves to be equivalent to an atomic wavefunction. On the other hand, the valence states contain a much lower charge density, thus resulting in smoother wave character. However, since valence and conduction electrons dominate the electronic structure of crystals and the core electrons remain essentially unperturbed, then approximating the core potential and wavefunction may reduce computational expense:

$$V_{PS} = V_{true} - \sum_{c} (E_{true} - E_c)|c\rangle\langle c| \qquad [3.35]$$

Equation [3.35] is a pseudopotential formed by the difference between the true potential and the valence energy projected on the core states. The pseudopotential is smooth and may converge toward the nucleus. The corresponding pseudowavefunction, also referred as an auxiliary wavefunction, approximates the behavior of all-electron wavefunctions, but the former lack strong oscillatory wave character of the latter.

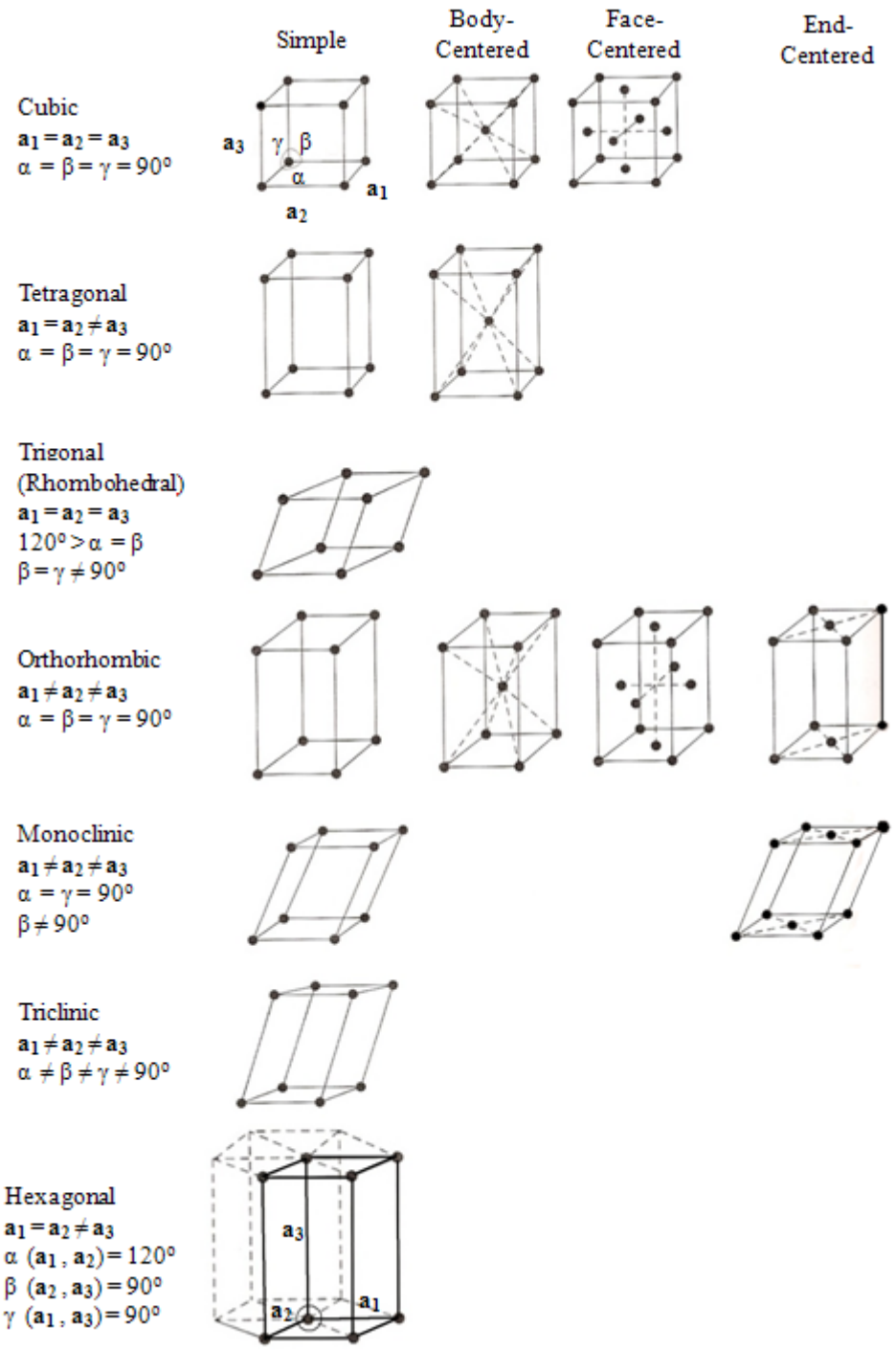

Figure 3.1: Seven crystal lattices types (horizontal) of fourteen different crystal structures (simple, body centered, face centered, and end centered). Figure is taken from Ref [51].

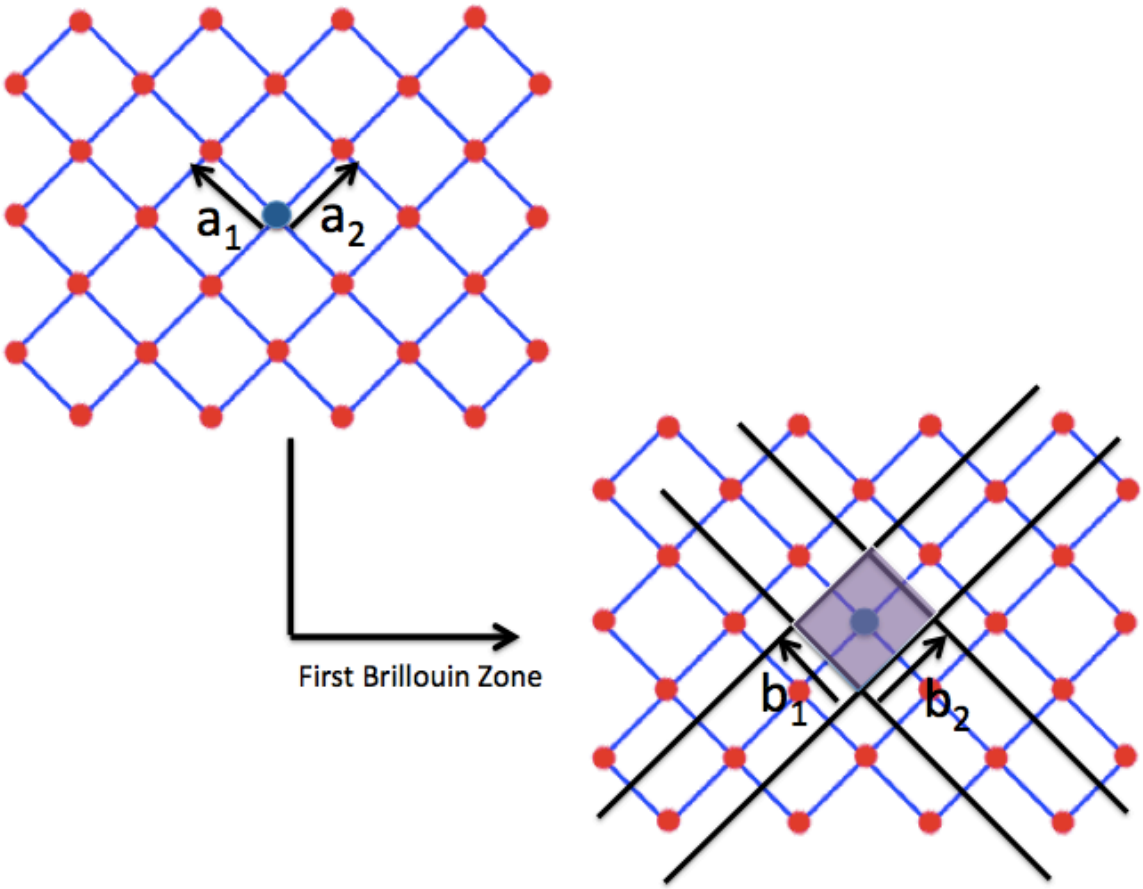

Figure 3.2: Top-left: Square lattice in real space with lattice vectors $\mathbf{a_1}$ and $\mathbf{a_2}$. Bottom-right: Construction of the first Brillouin zone (shaded) with Bragg planes. Figure is taken from Ref. [52]

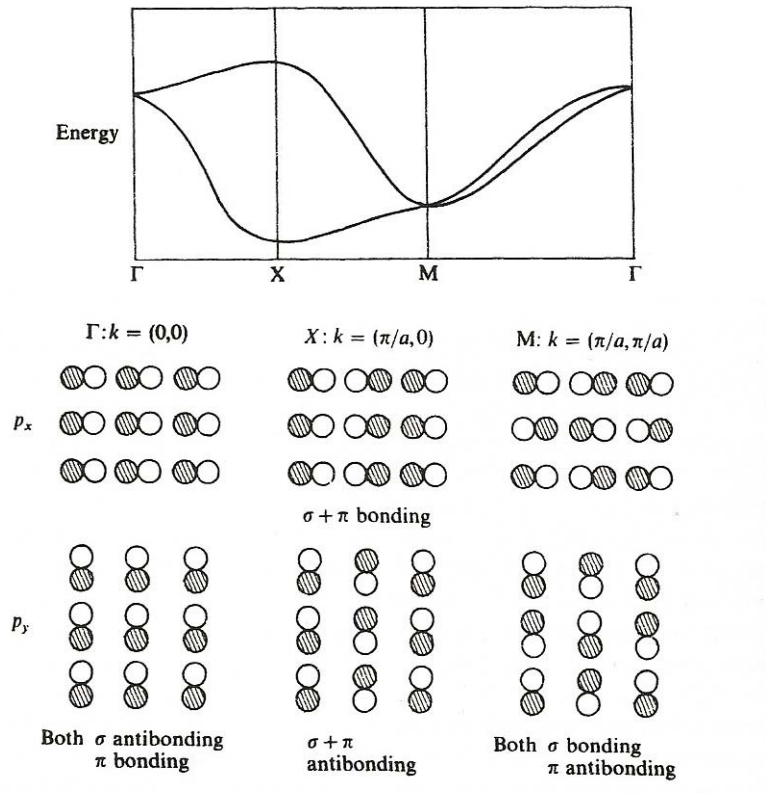

Figure 3.3: Band structure corresponding to p_x and p_y orbital interactions. Figure is taken from Ref. [45]

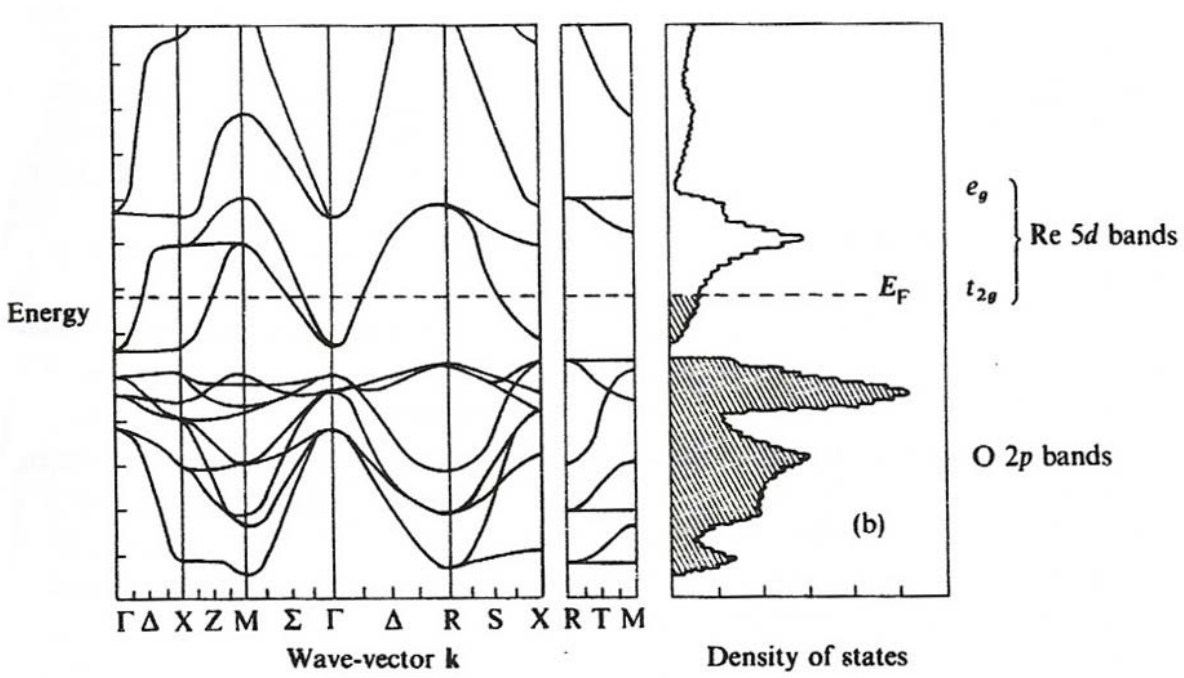

Figure 3.4: Band structure (left) and DOS (right) of ReO_5. Figure is taken from Ref. [45].

Simple cubic

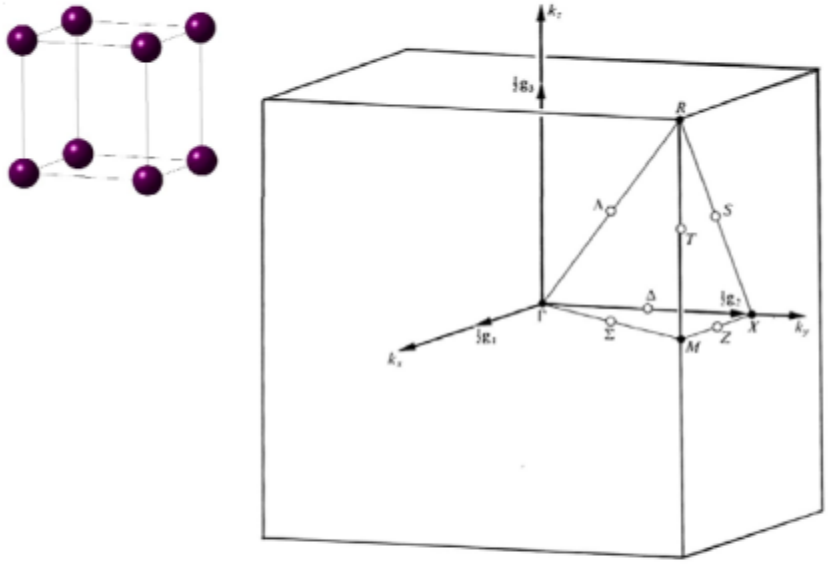

Label	Coordinates (g_1, g_2, g_3)
Γ	0 0 0
X	$0\ \frac{1}{2}\ 0$
M	$\frac{1}{2}\ \frac{1}{2}\ 0$
R	$\frac{1}{2}\ \frac{1}{2}\ \frac{1}{2}$

Figure 3.5: The first Brillouin zone and corresponding wavevectors of a simple cubic lattice. Figure is taken from Ref. [53].

Simple orthorhombic

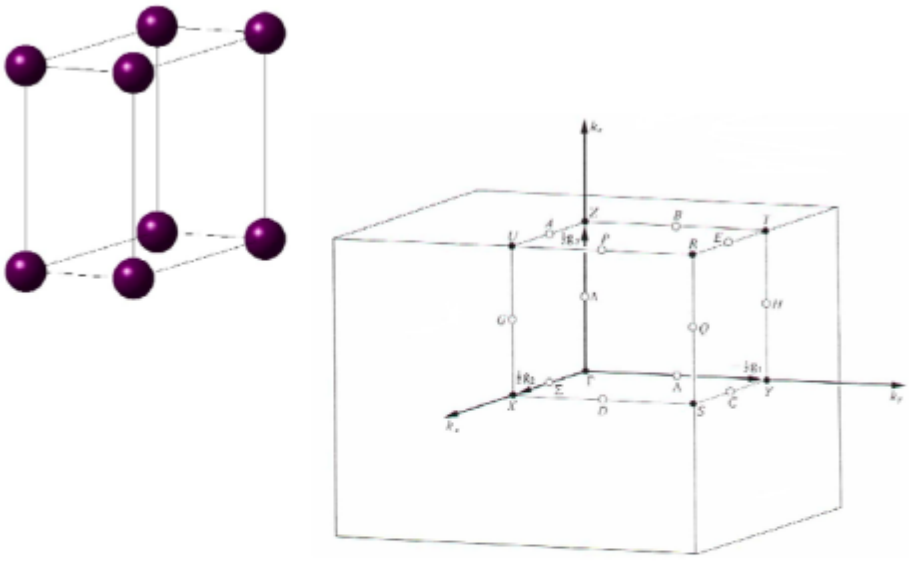

Label	Coordinates (g_1, g_2, g_3)
Γ	0 0 0
Y	$-\frac{1}{2}$ 0 0
X	0 $\frac{1}{2}$ 0
Z	0 0 $\frac{1}{2}$
U	0 $\frac{1}{2}$ $\frac{1}{2}$
T	$-\frac{1}{2}$ 0 $\frac{1}{2}$
S	$-\frac{1}{2}$ $\frac{1}{2}$ 0
R	$-\frac{1}{2}$ $\frac{1}{2}$ $\frac{1}{2}$

Figure 3.6: The first Brillouin zone and corresponding wavevectors of a simple orthorhombic lattice. Figure is taken from Ref. [53].

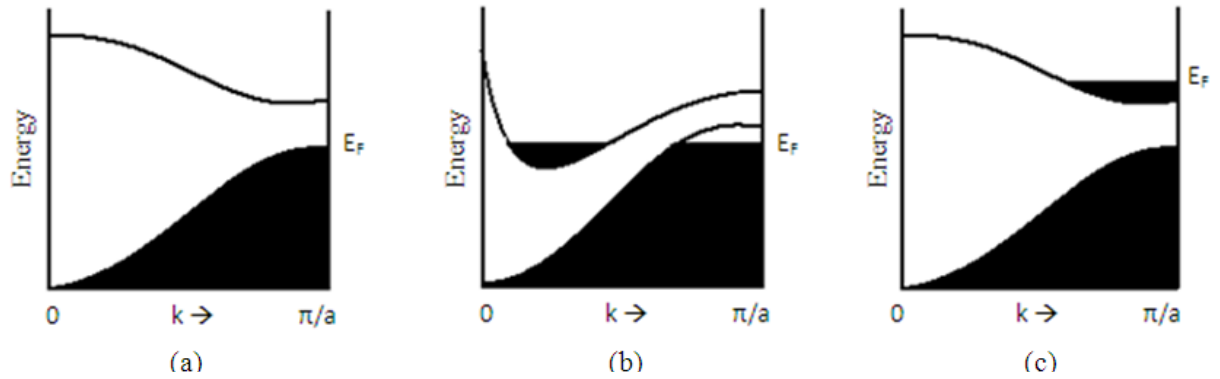

Figure 3.7: Band structures of (a) an insulator or semiconductor, (b) a semimetal, and (c) a metal. Illustration (a) is has electron occupancy (shading) that is below the band gap and Fermi energy at the lowest edge of the band gap. Illustrations (b) and (c) show a semimetal and metal, respectively, with regard to electron occupancy (shading). Although (c) has a band gap, the Fermi energy lies higher in energy than the band gap. Figure is taken from Ref. [54].

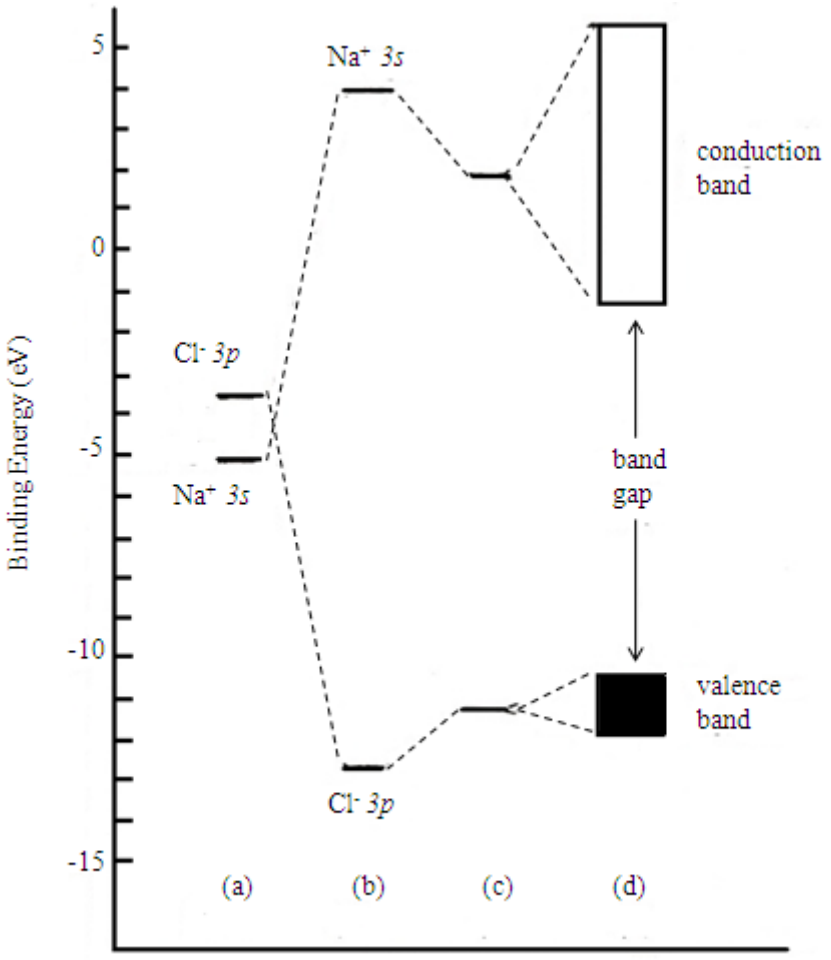

Figure 3.8: Construction of the valence and conduction band energies of NaCl; (a) the free ions, (b) Madelung Potential, (c) electrostatic polarization from electron transfer through the solid, and (d) orbital overlap of nearest-neighboring ions. Figure is taken from Ref. [45].

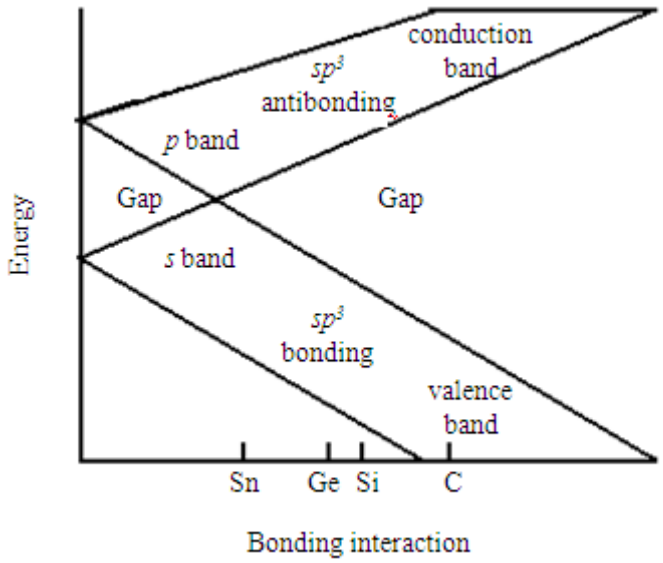

Figure 3.9: Energy bands as a function of the bonding interaction in Group 4 tetrahedral solids. Figure is taken from Ref. [45].

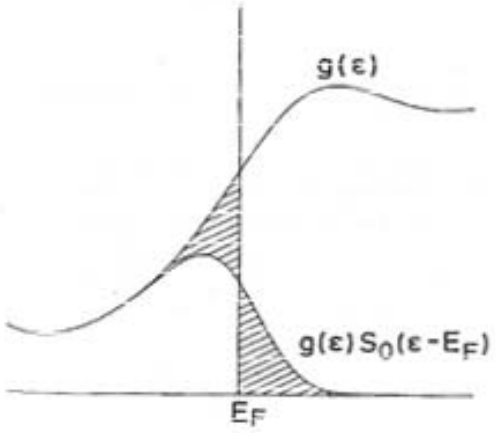

Figure 3.10: The DOS, *g(ε),* and that multiplied by Fermi-Dirac function, *g(ε)S0(ε-E_F)*, that represents DOS that are occupied by electrons. DOS to the left and right of E_F are occupied and unoccupied by electrons, respectively. Further, the lined area to the left of E_F are unoccupied DOS and the lined are to the right are occupied DOS. Figure is taken from Ref. [50].

CHAPTER 4

FIRST PRINCPLE STUDY OF STRUCTURE AND STABILITY OF NICKEL CARBIDES

4.1 Introduction

The interaction between nickel and carbon has received increased attention in recent years due to applications in carbon nanotube growth. In part, this interest has been driven by the desire to understand the growth mechanisms of carbon nanotubes (CNTs) and carbon nanofibers (CNFs) on Ni nanocatalysts.[55-60] The chemical and physical properties of carbides of late 3*d* metals have also garnered considerable attention. For example, iron–carbon compounds have been well studied due to their role in steel formation.[61,62] A number of studies of hemicarbides of iron (Fe_2C) and cobalt (Co_2C) have been reported.[61,63-66]

Among many possible stoichiometries, NiC, Ni_2C and Ni_3C are the three most prominent nickel carbides. Ni_3C has received much attention due to controversy about its structural characterization, which was deduced to be hexagonal.[64,67-71] However, structural analysis of this carbide was clouded for quite some time due to the similarity of its lattice constants and diffraction patterns to hexagonal close-packed (hcp) Ni. However, formation of hexagonal Ni_3C was confirmed later.[72] To the authors' knowledge, there is no experimental crystal structure for NiC published in the literature. Paduani[73] has published a study of crystalline NiC (rocksalt, B1 structure) along with FeC and CoC using full-potential linearized augmented-plane wave (FP-LAPW) methods in conjunction with the generalized gradient approximation (GGA) density functional theory (DFT). A lattice constant of NiC (a = 3.89 Å) and bulk modulus (B) of 367 GPA were computed. Note that an earlier linear muffin-tin orbital (LMTO) study by Haglund et al.

estimated a lattice constant of 3.98 Å for NiC.[74,75] Cheng-Bin et al., using Gaussian-based periodic DFT methods, calculated a lattice constant of 3.99 Å and B = 311 GPa using the Vinet equation of state for NiC (rocksalt).[76] A similar lattice constant to that of Cheng- Bin et al. was reported by Zhang et al. using Gaussian-based periodic DFT computations.[77]

To the authors' knowledge, there were no experimental studies reported in the literature for Ni_2C. In a recent experimental study by Banerjee and co-workers,[78] the mixing of Ni and CNTs to make functionally graded materials was interpreted via high resolution tunneling electron microscopy (HRTEM) to lead to the formation of a hexagonal crystalline material with lattice constants, a ~ 2.6 Å and c ~ 4.3 Å. Analysis of the elemental composition via 3D atom probe experiments suggested a Ni-carbide with a stoichiometry between that of Ni_2C and Ni_3C. However, no definitive conclusions could be drawn from this experiment. Few computational studies have been performed on this material. For example, an earlier study by Guillermet and Grimvall[79] estimated an enthalpy of formation of +13 ± 5 kJ mol^{-1} for Ni_2C.

Nickel is the primary component of most aerospace superalloys and, therefore, is an attractive target for fabrication of ultra-strength materials with CNTs and other alloys and composites. Therefore, a systematic theoretical investigation of the nickel carbides warrants attention. A first principles study of Ni-carbides was reported with an emphasis on Ni_2C structures. Plausible structures were explored and the properties compared to previous research on other Ni-carbide stoichiometries (NiC and Ni_3C). Implications for the bonding in late 3d metal carbides were also discussed.

4.2 Computational methods

All computations were performed using density functional theory (DFT). They were performed with the Vienna *Ab initio* simulation package (VASP, version 4.6),[80-83] implementing the projector augmented wave (PAW) method.[84] Exchange-correlation was treated using the generalized gradient approximation (GGA), as parameterized by the Perdew–Burke–Ernzerhof (PBE) functional.[35,36] The PAW potentials correspond to $3d^8\ 4s^2$ and $2s^2\ 2p^2$ valence electron configurations of nickel and carbon, respectively. We use a k-points mesh of 8 × 8 × 8 for the most stable crystal structures. The energy cutoff was set to 650 eV. Optimizations were done by simultaneous relaxation of the ions within the unit cell and the lattice constants. Magnetic effects were assessed by performing spin polarized computations. Non spin-polarized methods were used throughout this manuscript for the carbides as no difference is found between spin polarized and spin non-polarized geometry optimizations. Besides different nickel carbides, computations were also performed on fcc-Ni and C (diamond) to calculate the formation energies of the carbides.

We focused on the diamond allotrope of carbon for energy.[85] For the cubic unit cell ($Fd\bar{3}m$) of diamond calculation (15 × 15 × 15, ENCUT = 650 eV) yields an optimized a = 3.57 Å, identical to the value reported by Wyckoff.[86]

Crystallographic analyses of fcc-Ni (a = 3.52 Å) have been reported as far back as 1917.[87] An a = 3.52 Å (15×15×15 mesh, ENCUT = 650 eV) is obtained, identical to experiment. Similar optimized lattice constants (a < 0.01 Å, E < 0.01 eV) were obtained with spin polarized and non spin-polarized simulations. We have also calculated the structure of metastable hcp-Ni using the same computational scheme as for fcc-Ni. The

calculated lattice parameters of *a* = 2.49 Å and *c* = 4.09 Å, using spin-polarized methods, are commensurate with experiment.[88-90] The computations indicate hcp-Ni > fcc-Ni by 0.02 eV atom^{-1}.

The heat of formation of each carbide phase, with formula Ni_xC_y , is calculated using:

$$\Delta H_f \approx \Delta E_f = E_{tot}(Ni_xC_y) - xE_{tot}(fcc - \mathrm{Ni}) - yE_{tot}(diamond) - 0.025\ eV \quad [4.1]$$

For this study, *H* is approximated as *E* because the *pV* term is extremely small for relaxed solid structures at ambient pressure. The calorimetrically determined enthalpy difference, 0.025 eV, between diamond and graphite is added in the above equation. Note that in [4.1], the total energy corresponding to a ferromagnetic solution of fcc- nickel is used. Diamond is used as the reference structure because conventional local or semi-local functionals are found to give unreasonable results for van der Waals type interactions in the graphite structure. Thermal and entropic corrections were not incorporated in these computations. It is also noted that the absence of phonon computations might include a few structures that are not minima. Preliminary computations of elastic constants suggest that the lowest energy orthorhombic Ni_2C satisfies the conditions of mechanical stability.

4.3 Results and discussion

4.3.1 Structures

4.3.1.1 NiC

A rocksalt (B1) structure is assumed for NiC as in previous studies. A lattice constant of 4.077 Å is calculated. This value is comparable to previously reported

simulations: 4.193 Å (Zhang et al.; Gaussian-based periodic DFT[77]), 3.894 Å (Paduani, FP-LAPW/GGA[73]), and 4.08 A˚ (Xiao et al., GGA-DFT[60]).

4.3.1.2 Ni_2C

A comprehensive structural search is performed using twenty eight (28) distinct structures. Table 4.1 summarizes the optimized lattice parameters and relative energies of all calculated Ni_2C structures. Six distinct structures within the orthorhombic family were analyzed. Space group #58 (P_{nnm}) has been established by crystallography[91,92] for the related hemicarbides, Fe_2C and Co_2C. Hence, it is reasonable that this is a stable geometry for the Ni congener. Several other transition metal hemicarbides crystallize in space group #60 (P_{bcn}), namely V_2C, Mo_2C andW_2C. The P_{nnm} and P_{bcn} structures, Figure 4.1, are essentially degenerate with each other at the level of theory employed here, as well as $Pa\bar{3}$ (trigonal, space group #162, β-V_2N prototype) and $P4_{2/mnm}$ (tetragonal, space group #136, rutile prototype) Ni_2C structures. Inspection of the unit cell lattice constants, Table 4.1, shows structural similarity between the $P4_{2/mnm}$ and P_{bcn} polymorphs of Ni_2C, the latter being slightly less symmetric, as expected from the lower crystal symmetry. Not surprisingly, Ni-C and Ni-Ni distances within the unit cell are similar for these two structures. Optimized lattice constants for P_{nnm} Ni_2C are a = 4.72 Å, b = 4.17 Å, c = 2.92 Å ; $\alpha = \beta = \gamma = 90^o$. Optimized lattice constants for P_{bcn} Ni_2C are a = 4.19 Å, b = 5.51 Å, c = 4.94 Å; $\alpha = \beta = \gamma = 90^o$.The P_{nnm} and P_{bcn} structures are essentially degenerate, utilizing the computational methods employed in this research.

4.3.1.3 Ni_3C

This stoichiometry has been well studied within the Ni-C system.[63,71,72,93-97] To the authors' knowledge, two polymorphs have been proposed for Ni_3C: orthorhombic (cementite) and hexagonal/rhombohedral (bainite) structures. Our survey of A_3B structures predicts the cementite and hexagonal structures as the most stable structures for Ni_3C. For the cementite structure, the optimized lattice parameters are found to be a = 4.95 Å, b = 6.79 Å, and c = 4.47 Å, which are nearly identical to those calculated by Shein et al.: a = 4.97 Å, b = 6.81 Å, and c = 4.47 Å.[98] Optimized lattice constants are $a = \sqrt{3}a_h$ = 4.59 Å, $c = 3c_h$ = 13.02 Å for the hexagonal super-lattice. These correspond to a_h = 2.65 Å, c_h = 4.34 Å for the unit cell, and are thus in very good agreement with Electron Diffraction and X-ray Diffraction results.[69-71] The present computations predict that the cementite structure is 0.14 eV/formula-unit. higher in energy than the bainite structure.

4.3.1.4 Ni_2C Defects

The P_{nnm} Ni_2C stoichiometry is subject to defect computations in which each Ni and C atom in the unit cell, see Figure 4.1a, is individually removed and the resulting crystal structure is relaxed to a ground state. Removal of each Ni atom from P_{nnm} Ni_2C—yielding Ni_3C_2 stoichiometry— followed by geometry optimization results in an orthorhombic lattice (Figure 4.2a) and an electronic energy per formula unit of −16.11 eV. Removal of each C from P_{nnm} Ni_2C— yielding Ni_4C stoichiometry—followed by geometry optimization also results in an orthorhombic lattice (Figure 4.2b) and an electronic energy per formula unit of −15.43 eV. No magnetic ordering is observed in

the defect carbide structures.

The geometry optimization of the Ni_3C_2 stoichiometry in Figure 4.2b results in a sawhorse configuration of Ni atoms surrounding a central C. The nearest Ni–Ni and Ni–C distances are 2.60 Å and 1.84 Å , respectively, which are a slight increase in Ni–Ni and a decrease in Ni–C distances compared to P_{nnm} Ni_2C. The Ni_7C_4 stoichiometry results in cell that contains an octahedral configuration along with a 'rectangular' pyramidal configuration of atoms, both of which have a central C atom that is surrounded by Ni atoms. The octahedral configuration is slightly distorted, thus resulting in nearest Ni-Ni distances within the range of 2.49–2.91 and Ni–C distances of 1.91–1.94 Å. Also, the rectangular pyramidal configuration results in Ni–Ni distances within the range of 2.41–2.91 Å and Ni–C distances within the range of 1.89–1.93 Å. The optimization of the Ni_4C stoichiometry in Figure 4.2b results in an octahedral configuration of Ni atoms surrounding a lattice vacancy, in which a C would exist for Ni_2C. The nearest Ni–Ni and Ni–C distances are 2.53–2.55 Å and 1.83–1.85 Å, respectively. This marks a subtle change in Ni-Ni distances and a decrease in Ni-C distances compared to the Ni_2C.

4.3.2 Thermodynamics

The formation energies are determined for three Ni-carbide stoichiometries using the most stable structures identified for each—NiC ($Fm\bar{3}m$), Ni_2C (P_{nnm}) and Ni_3C ($P6_322$). Given the difficulties in modeling graphite with DFT methods, the diamond form of C is used as the standard and then corrected for the experimental energy difference between diamond and graphite (see section 4.2).[62] Note that phonon computations are

not performed to incorporate enthalpic and entropic corrections. The calculated energetic data are graphically presented in Figure 4.3. To gain more insight into the stability of these Ni-carbides, the formation energies of defect Ni- carbides, specifically Ni_3C_2, Ni_4C, and Ni_7C_4, were calculated and included in Figure 4.3. As illustrated, the formation energy of Ni_4C is between those of Ni_2C and Ni_3C, each of which has 66% (atom %) or more Ni. Alternatively, NiC, Ni_3C_2, and Ni_7C_4 have much higher formation energies than Ni_3C_2, Ni_4C, and Ni_7C_4, possibly due to the increased concentration of C.

Several points are found to be interesting in Figure 4.3. First, NiC is by far less stable than Ni_3C and Ni_2C, with a formation energy of +48.6 kcal mol^{-1}. Second, the calculated formation energies for Ni_3C are in reasonable agreement with experimental estimates.[79,98] Third and most interestingly, the Ni_2C stoichiometry is only 1.5 kcal mol^{-1} (0.1 eV) less stable than the Ni_3C carbide. Hence, while most previous computational and experimental studies of Ni-carbides have focused on NiC and Ni_3C stoichiometries, the present computations suggest a metastable hemicarbide stoichiometry is also plausible. This would bring Ni more in line with its Fe and Co neighbors both of which form M_2C and M_3C stoichiometries. Finally, it is speculated that such metastable, more C rich species such as Ni_2C may explain the enhanced supersaturation of C in Ni seen in splat quenching[99] and related experiments.[67,68] These results indicate that stoichiometric nickel carbides Ni_3C as well as Ni_2C may exist in solid state environments such as composites.

Table 4.2 lists the calculated formation energies of Co_2C, Fe_2C, and Ni_2C at identical levels of theory. It should be noted that the formation energy of Ni_2C is within ±4.0 kcal mol^{-1} of those for Co_2C and Fe_2C. Ni_2C is calculated to be more stable than

Fe_2C, but marginally (by 3.4 kcal mol^{-1}) less stable than Co_2C. Given that the latter two species have been experimentally characterized,[91,92] it may be possible to observe P_{nnm} Ni_2C as well using the calculated lattice parameters in Table 4.1 as a guide.

4.3.3 Electronic Properties

To elucidate the electronic structure of NiC, Ni_2C and Ni_3C, the band structures of these materials are calculated at their most stable geometry. As can be seen in Figure 4.4, NiC and Ni_2C show a semimetallic behavior and Ni_3C shows metallic behavior. As shown in the Ni_2C band structure, Figure 4.4, the highest valence band (dotted line) rises above the Fermi level (dark horizontal line, Figure 4.4) between the Y and Γ points and between the Z and Γ points. As shown by the two dashed lines, the lowest conduction bands fall below the Fermi energy at the Z point. Visual inspection of the band structures shows a greater similarity for NiC → diamond and Ni_2C → Ni_3C, and a greater disparity between the former and latter pair.

The band structures of Ni_3C_2, Ni_7C_4, and Ni_4C (Figures 4.5a through 4.5c) were calculated and can be compared to that of Ni_2C (Figure 4.4b). All defect structures maintain the semimetallic behavior around the Fermi level (0.00 eV), as illustrated by the dashed bands. However, this semimetallic behavior is less prevalent in Ni_3C_2, increases with Ni_7C_4, and is even more in Ni_4C. In fact, in the Ni_3C_2 band structure, a gap appears to form around the Fermi energy between the dashed bands, except where they converge (between the T and Y points, at the Γ point, and between the X and U points). This is consistent with an increased covalent character in Ni_3C_2 with respect to Ni_2C. Conversely, the band structure of Ni_4C illustrates the most metallic character of

the defect carbides because the apparent gap between the dashed bands is the smallest and the highest dashed band copiously overlaps the Fermi level, as compared to the band structures of Ni_2C and Ni_2C_3, Figure 4.5. Therefore, analysis of the band structures for the various Ni-carbide stoichiometries shows a systematic progression from metallic to semimetallic to covalent behavior as the carbon concentration increases.

4.4 Conclusions

A first principles study of Ni-carbides is presented here. Several significant conclusions have resulted from the simulations, the most important of which are summarized here. Given a disparity of computational and experimental results in the literature, as well as the different methods used in previous theoretical studies, the present research illustrates for the first time a consistent set of simulations for an entire range of NiC compositions at a single level of theory: C (diamond), NiC (rocksalt), Ni_2C and Ni_3C and Ni (fcc and hcp). Our computations indicate that orthorhombic (cementite-like) and hexagonal (bainite-like) structures are the two most stable forms of Ni_3C. The hexagonal structure is calculated to be more stable than the orthorhombic structure using the methods employed in this research.

The stoichiometry Ni_2C is calculated to be much more stable and marginally less stable, respectively, than the well-studied NiC and Ni_3C. Moreover, its calculated formation energy is commensurate with known hemicarbides, Fe_2C and Co_2C. Improvements to the computational scheme are needed for more accurate thermodynamics of Ni_2C phases. For example, calculation of the phonon modes would be of interest to calculate thermodynamics at finite temperatures. Although none of the

low energy Ni_2C phases have lattice constants similar to those measured by HRTEM by Banerjee and co- workers,[78] our thermodynamic data clearly indicates that stoichiometric nickel carbides such as Ni_3C and Ni_2C have a high possibility of formation as a metastable phase in favorable solid state environments such as composites.

Although we have considered the Ni-carbide structures based on prototypes from well-known databases, it is possible that other structures exist outside those considered here. A *de novo* structural search may help locate such structures. Due to the importance of these materials, we believe that future work on metal carbides utilizing genetic algorithm or random structural search methods would be an important undertaking.

The combination of structural and energetic data, combined with band structure analyses, paint an interesting picture of Ni-carbides as one traverses toward more carbon rich stoichiometries. Calculated properties show a marked divergence upon going from Ni_2C to NiC and a similarity from Ni to Ni_3C to Ni_2C. For example, the calculated band structures of the stable forms of Ni_2C and Ni_3C display semimetallic behavior, and a discrete separation between C 2*s* and C 2*p* states, unlike the band structure for NiC. Also, a systematic progression from metallic to semimetallic to covalent behavior is observed for the defect carbides Ni_4C to Ni_7C_4, to Ni_3C_2. Additionally, the Ni-Ni distances in the low energy metastable Ni_2C and Ni_3C phases are not far from Ni-Ni distances in metallic Ni. In conjunction with this, Ni-C nearest distances correspond to single bond lengths. On the other hand, upon going from Ni_2C to NiC, one sees a marked increase in both Ni-Ni and Ni-C distances beyond typical covalent norms. Hence, metallic Ni-Ni bonding within the lattice is maintained for both

Ni_2C and Ni_3C (albeit reduced versus the metal), with concomitant stabilization from Ni-C bonding, keeping the formation energies of these stoichiometries only slightly positive. The closeness in energy of the various forms of Ni_3C and Ni_2C, combined with the diversity of structures they can energetically access, is consistent with the rapid diffusion of C through Ni that has been evidenced by several researchers[100] and which has been proposed to be significant to the formation of carbon nanotubes and carbon nanofibers.

Table 4.1: Computed Ni_2C structures; lattice constants are in Å; volumes per formula unit, *V(f.u.),* are in $Å^3$; energy per f.u., *E(f.u.)*, are in eV, *Z* is the number of f.u. in the unit cell. The structures with the lowest energy are italicized.

	Point Group	*a*	*b*	*c*	*Z*	*E* (f.u.)	*V* (f.u.)
				Cubic prototypes			
Be_2C	225	4.80	4.80	4.80	4	− 19.29	27.61
Ag_2O	224	4.13	4.13	4.13	2	− 18.03	35.13
a-Fe_2S	*205*	*4.79*	*4.79*	*4.79*	*4*	*− 19.63*	*27.45*
				Hexagonal prototypes			
Mo_2S	*194*	*2.69*	*2.69*	*8.91*	*2*	*− 19.49*	*27.99*
Cu_2Te	191	3.79	3.79	4.89	2	− 17.51	30.43
Fe_2P	189	5.29	5.29	3.27	3	− 19.21	26.42
β-SiO_2	180	4.68	4.68	6.52	3	− 18.23	41.18
				Trigonal prototypes			
$NiTe_2$	164	2.90	2.90	3.98	1	− 19.40	28.97
β-*V_2N*	*162*	*4.87*	*4.87*	*4.15*	*3*	*− 19.80*	*28.40*
α-*SiO_2*	154	4.51	4.51	4.87	3	− 19.06	28.57
Fe_2P	150	5.10	5.10	3.70	3	− 19.44	27.76
				Tetragonal prototypes			
Anatase	141	3.79	3.79	8.77	4	− 19.55	31.50
Al_2Cu	140	4.78	4.78	4.62	4	− 18.85	27.24
Ca_2As	139	3.26	3.26	10.24	4	− 18.84	27.24
Rutile	*136*	*4.48*	*4.48*	*2.91*	*2*	*− 19.78*	*29.17*
Ni_2B	130	4.79	4.79	4.60	4	− 18.85	26.35
Cu_2Sb	129	3.30	3.30	4.99	2	− 19.20	27.22
CaF_2	123	3.37	3.37	2.46	1	− 18.80	27.94
				Orthorhombic prototypes			
Co_2Si	60	5.45	6.09	3.15	4	− 19.24	26.13
V_2C, W_2C, Mo_2C	*62*	*4.19*	*5.51*	*4.94*	*4*	*− 19.82*	*28.4*
Fe_2C, Co_2C	*58*	*4.72*	*4.17*	*2.92*	*2*	*− 19.81*	*28.77*
CaF_2	47	2.46	3.40	3.33	1	− 18.76	27.80
Nb_2C	33	9.75	2.91	4.06	4	− 19.61	28.86
ZrO_2	29	4.69	4.86	4.77	4	− 19.67	27.14
				Monoclinic prototypes			
ZrO_2	*14*	*4.80*	*4.83*	*4.94*	*4*	*− 19.66*	*27.94*
SiO_2	9	5.27	8.41	5.00	8	− 19.43	27.69
$AuTe_2$	7	6.40	2.91	7.89	4	− 19.39	28.91
SiO_2	6	4.83	5.88	3.84	4	− 19.39	27.24

Table 4.2: Formation energies of late 3*d* binary transition metal carbide M_2C (M = Fe, Co, and Ni). The above uses diamond as the C reference state and are thus corrected for the experimental free energy difference between diamond and graphite.

Reaction	ΔE_{rxn} (kcal mol^{-1})
C + 2 Fe (bcc) → Fe_2C	+9.0
C + 2 Co (hcp) → Co_2C	+4.5
C + 2 Ni (fcc) → Ni_2C	+7.9

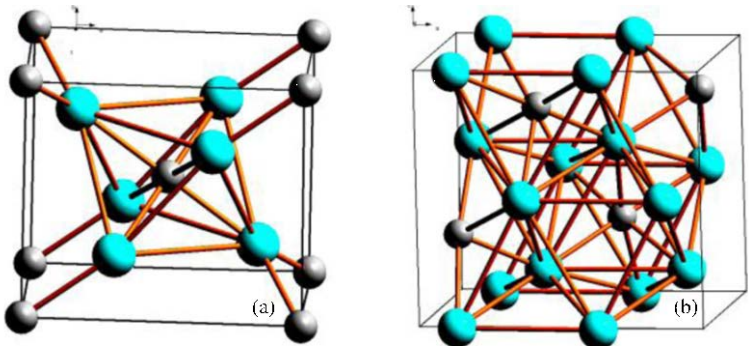

Figure 4.1: Illustrations of computed structures (single unit cell shown) for (a) P_{nnm} and (b) P_{bcn} orthorhombic forms of Ni_2C. Ni = blue; C = gray.

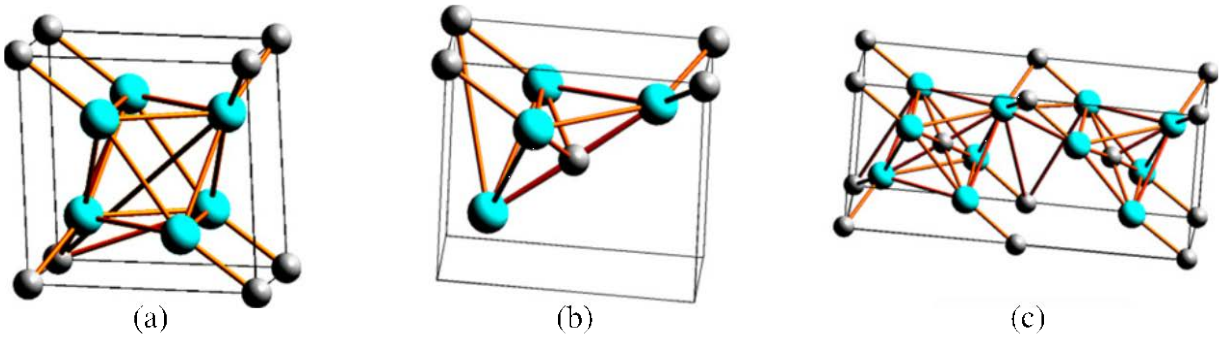

Figure 4.2: Illustrations of computed structures (single unit cells) for defect carbides: (a) Ni_4C, (b) Ni_3C_2, and (c) Ni_7C_4

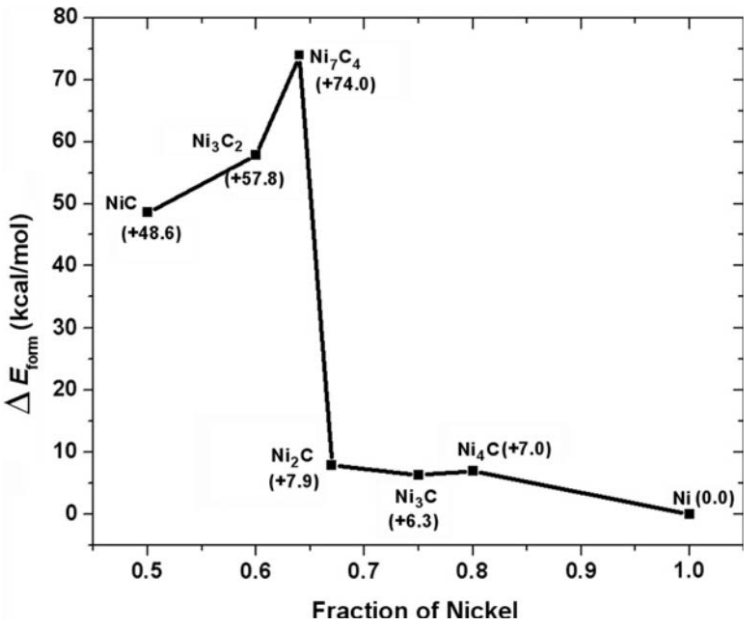

Figure 4.3: Formation energies of Ni-carbides (kcal mol^{-1}); computed with respect to diamond as the C reference state and corrected for the experimental free energy difference between diamond and graphite.

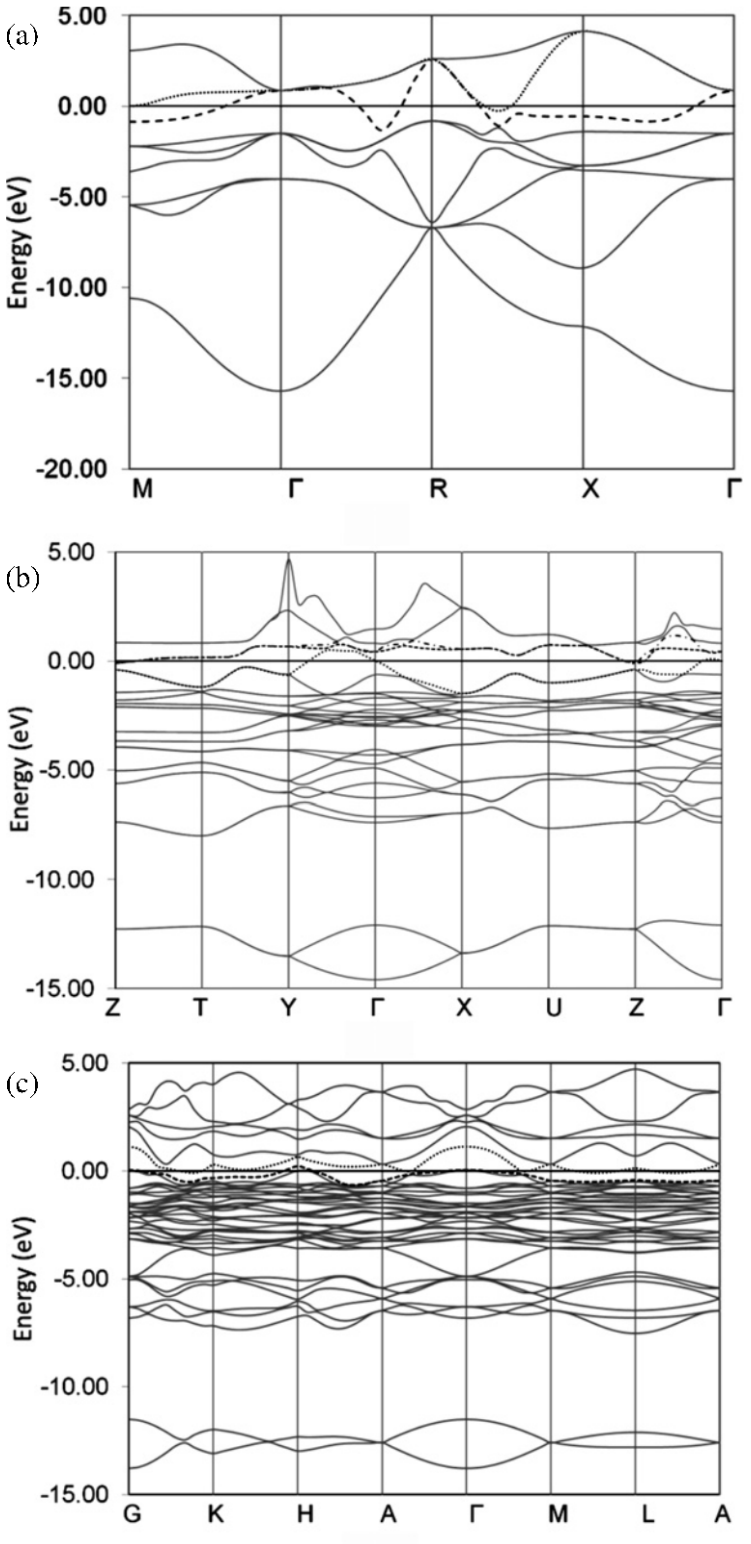

Figure 4.4: Band structure of (a) NiC (rocksalt, B1), (b) Ni_2C (orthorhombic, P_{nnm}), and (c) Ni_3C (hexagonal).

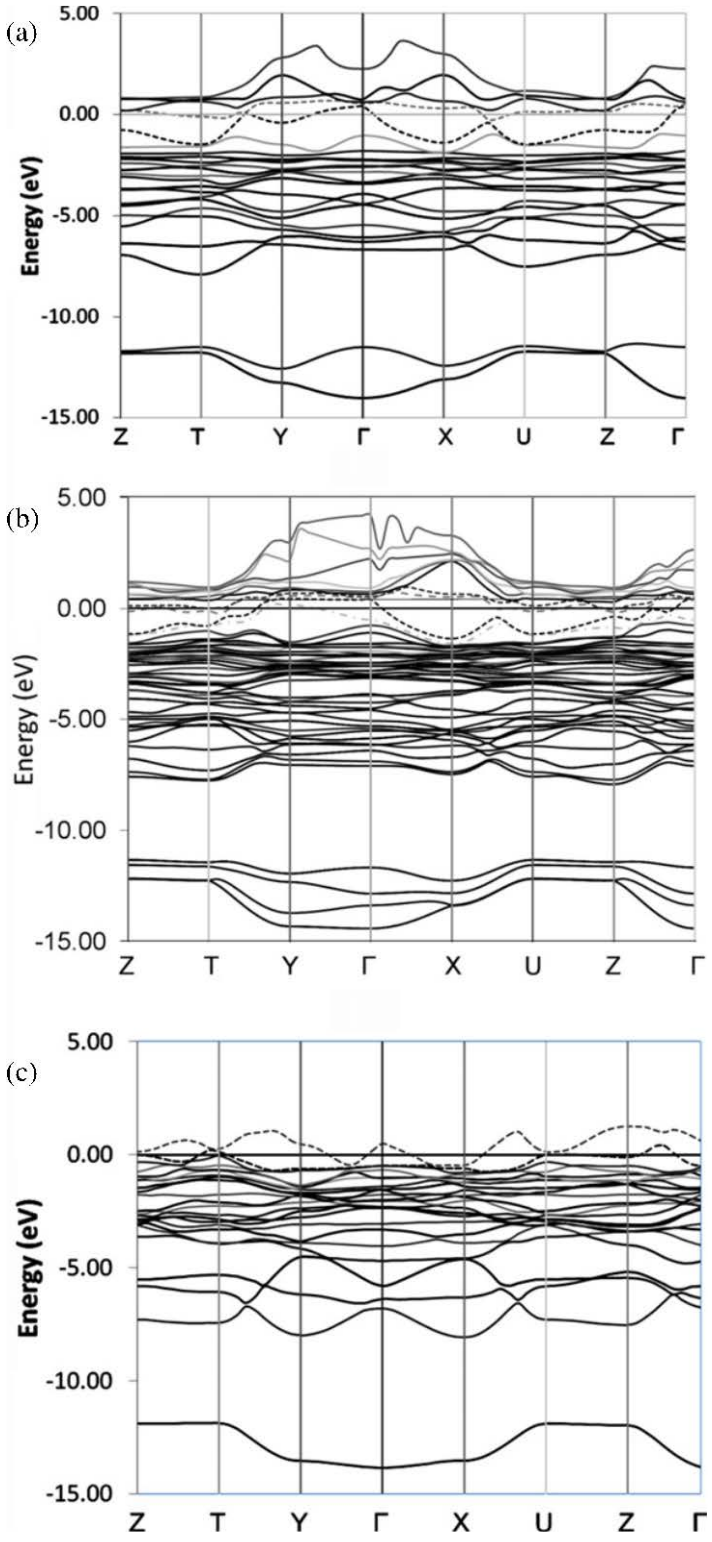

Figure 4.5: Band structures of (a) Ni_3C_2, (b) Ni_7C_4, and (c) Ni_4C. All are in orthorhombic symmetry.

CHAPTER 5

BENCHMARKS OF CORRELATION CONSISTENT BASIS SETS OPTIMIZED FOR DENSITY FUNCTIONAL THEORY

5.1 Introduction

Density functional theory (DFT)[101-103] is a widely used computational method known for providing molecular property prediction without the computational cost common to post-Hartree-Fock methods.[102] A major problem with DFT is that the exact energy functional is not known, and, because of this, many approximate exchange, correlation, and kinetic energy functionals have been developed. A resulting challenge, therefore, is the selection of an appropriate density functional for computing properties of interest. While numerous studies have enabled a much greater understanding of functional performance for specific properties and classes of molecules -- this knowledge has helped to enable a hierarchy of functionals to emerge -- the hierarchy is not yet as established as that which has evolved for ab initio correlated methods. This is unsurprising, as the explosion of the use of density functional theory in chemistry is much younger than for ab initio correlated methods, functional development is progressing at a rapid rate, and, as of yet, an *a priori* method as to how well a density functional might perform for a given chemical property is not firmly established. Additionally, unlike ab initio methods, it is not always clear how to systematically improve a density functional, though, indeed, significant developments continue to be made.

Kohn-Sham (KS) DFT[104,105] circumvents the lack of an exact kinetic energy functional by assuming an independent particle model, similar to that of Hartree-Fock

theory, computing the kinetic energy using orbitals instead of exclusively using the electron density. It is because of the introduction of orbitals that the need for a one-particle basis set arises in KS-DFT. Basis sets can offer a way of gauging the *intrinsic* accuracy of a given method. For example, the unique architecture of the correlation consistent polarized valence basis sets, denoted 'cc-pV*n*Z' (*n* is the ζ-level of the set, e.g. *n* = D is double-ζ, *n* = T is triple-ζ, etc.), results in monotonic convergence of energetic properties (e.g. enthalpies of formation, binding energies) with respect to the increase in the ζ-level for a given ab initio method.[106-110] The convergent behavior enables the complete basis set (CBS) limit – the limit at which no further improvements in the basis set affect the energy -- to be ascertained. Knowledge of the CBS limit provides a gauge for how well an ab initio method performs (i.e. relative to experiment) independent of the basis set, as the error arising from basis set incompleteness is effectively eliminated, and only the intrinsic error in the method remains. This approach has helped to develop a hierarchy of performance for ab initio methods. However, the question arises as to whether or not the use of a systematic series of basis sets is portable to KS-DFT, and if it is, it would provide a means of assessing the intrinsic accuracy of a given density functional.

Wang and Wilson[111-115] and Prascher et al.[116-118] have examined the behavior of KS energies computed with the cc-pV*n*Z basis sets using several density functionals. It was demonstrated that monotonic behavior in the energy is not always observed with respect to increasing basis set size, and should not necessarily be expected, as the basis sets were not optimized for KS-DFT, but rather for *ab initio* methods. Further, when the contractions of the cc-pV*n*Z basis sets were revisited by Prascher and

Wilson,[117] it was shown that recontraction did not remedy the non-monotonic behavior in molecular energetics, specifically for the atomization energies. Therefore, in this paper the next logical step is considered: explicit reoptimization of the primitive basis functions in the cc-pV*n*Z basis sets with respect to specific density functionals.

Optimization of basis sets for specific density functionals is not a common practice; the recontraction scheme just discussed is one form of basis set optimization. Jensen has introduced a family of *polarization consistent* (pc-*n*, where *n* is the ζ-level – e.g. *n* = 1 is double-ζ, *n* = 2 is triple-ζ, etc.) basis sets that were explicitly optimized using Becke exchange and Lee-Yang-Parr correlation (BLYP).[119-123] Recently, Jensen also produced an energy-optimized Gaussian basis set for diamond-like C and Si for DFT using the BLYP functional.[124] Also recently, Lehtola et al. produced electron momentum density-optimized one electron basis sets for atoms in rows 1-5, excluding the 3*d* atoms, using second order Møller-Plesset Perturbation Theory.[125] In this work, B3LYP and BLYP functionals were chosen because of the variety of properties that have been measured, including excitation energies,[126-128] radical energies,[129-131] enthalpies of formations,[132-134] and hydrogen-bonded systems,[135-137] with both functionals. The cc-pV*n*Z basis sets have been shown by Wang and Wilson to perform as well as the pc-*n* basis sets in computing optimized geometries and enthalpies of formation, but at a lower computational cost owing to fewer basis functions beyond the double-ζ level (see Table 5.1).[111,114] This fact, led Prascher et al. to investigate the necessity of high angular momentum functions in the basis set in KS-DFT calculations, in which they demonstrated that only *s*, *p*, *d*, and *f* functions need be retained in the cc-pV*n*Z basis sets to obtain optimized geometries within 0.01 Å and atomic and molecular

energetics (e.g. ionization potentials, electron affinities, and atomization energies) within 1.0 kcal/mol of the full (non-truncated) cc-pV*n*Z basis sets.[118] They examined the energetics of first-row atoms, diatomics, CH_4, NH_3, H_2O, SiH_4, PH_3, and H_2S. Further, systematic removal of the angular functions $l > 3$ resulted in dramatic reductions in the computational cost, on the order of 70%-90%. In this chapter, the truncation of *g* and *h* angular momentum functions were coupled with explicit reoptimization of the cc-pV*n*Z primitives to develop new, compact cc-pV*n*Z basis sets for KS-DFT calculations. These reoptimized basis sets were first introduced by Prascher.[116] The enthalpies of formation for 86 molecules, combustion enthalpies of 20 molecules, and atomization energies of six fullerenes are computed with these reoptimized basis sets and compared to those obtained with truncated forms of the previously introduced recontracted basis sets and the Dunning cc-pV*n*Z basis sets. It is noted that Michael Zhou, a former Texas Academy of Mathematics and Science (TAMS) student,[138] and the author of this chapter were responsible for all enthalpy and atomization energy computations.

5.2 Methodology

The BLYP density functional is employed here and compared with calculations utilizing the B3LYP.[37,38,118,139] The third parameterization of the Vosko-Wilk-Nusair local correlation functional (VWN-3) has been utilized in all B3LYP calculations.[140] We have chosen these two density functionals due to their well-established use in the literature and to provide two comparative examples. Although we have chosen to examine only two density functionals in this investigation, our proposed basis set methodology is portable to other density functionals.

The details for systematic truncation and recontraction of the cc-pV*n*Z basis sets for BLYP and B3LYP have been described previously.[117,118] In summary, any *g* and *h* functions are removed from the quadruple- and quintuple-ζ basis sets and the *s* and *p* contractions are optimized for BLYP or B3LYP specifically. These modifications give rise to a smaller, more compact family of basis sets denoted cc-pV*n*Z[rc](tr), where *n* = D, T, Q, and 5, *rc* stands for *recontracted*, and *tr* indicates which functions have been truncated. For example, the double- and triple-ζ basis sets are not truncated in any way, so they are denoted 'cc-pVDZ[rc]' and 'cc-pVTZ[rc]', respectively, but the quadruple- and quintuple-ζ basis sets are both recontracted and truncated, so they are denoted 'cc-pVQZ[rc](-1*g*)' and 'cc-pV5Z[rc](-2*g*1*h*)', respectively.

The *s*, *p*, *d*, and *f* primitives of the cc-pV*n*Z basis sets have been reoptimized in logarithmic space with respect to minimization of the BLYP and B3LYP atomic energies using the Broyden-Fletcher-Goldfarb-Shanno (BFGS) algorithm.[141] The tolerance for energy minimization was 10^{-9} E_h. We have removed all *g* and *h* functions from the cc-pV*n*Z sets, following the conclusions of Prascher et al.[118] Each basis set was optimized using the ground state electronic configuration of the respective atoms, except for hydrogen, which was optimized using H_2 as a model. This optimization model is entirely analogous to the model used to develop the original cc-pV*n*Z basis sets.[104] The new sets of optimized primitives were contracted using the same general contraction scheme utilized by the cc-pV*n*Z basis sets (*cf.* Table 5.1). These reoptimized basis sets are denoted 'cc-pV*n*Z-BLYP' for the BLYP-optimized primitives and 'cc-pV*n*Z-B3LYP' for the B3LYP-optimized primitives.

To approximate the KS limit (analogous to the CBS limit for *ab initio* methodology), three extrapolation schemes commonly used in assessing CBS limits were employed: the Peterson extrapolation scheme (P),[106,109]

$$E_n = E_{KS} + Ae^{-(n+1)} + Be^{-(n+1)^2} \quad [5.1]$$

the inverse cubic formula of Schwartz (S3),[142]

$$E_n = E_{KS} + \frac{A}{l_{max}^3} \quad [5.2]$$

and the inverse quartic formula for Schwartz (S4),[142]

$$E_n = E_{KS} + \frac{A}{l_{max}^4} \quad [5.3]$$

In each extrapolation scheme, E_n denotes the nth ζ-level energy (or property), E_{KS} denotes the KS limit of that energy (or property), and A and B are variable parameters fit to three or four energy points, using a least squares approach. We have avoided computing the KS limits of energy differences such as atomization energies, formation enthalpies, and reaction enthalpies. For example, the atomization energy equation, *AE* = *E*(products) – *E*(reactants), involves an energy difference in which *E*(products) does not necessarily converge at a similar rate as *E*(reactants). (It is assumed that *E*(products) and *E*(reactants) converge monotonically with respect to a given sequence of cc-pV*n*Z basis sets.) As a result of the different convergence rates of energies, energy differences often do not necessarily display smooth, monotonic behavior, despite having used a series of cc-pV*n*Z basis sets to obtain them. Attempting to extrapolate energy differences, therefore, occasionally leads to the erroneous conclusion that any observed non-monotonic behavior points to a problem with the

choice of basis sets. However, first extrapolating the individual energy components to their respective KS limits, then taking the difference of those KS limits yields an estimate of the asymptotic behavior of the energetic property.[107,111-115,117,118] In later sections of this paper, where thermodynamic values are computed, this approach has been followed. Energy calculations reported herein were computed using the Molpro 2006.1[143] software suite. Geometry optimizations were converged to 0.001 mE_h in energy gradients, while zero-point energies and thermal corrections were computed from the harmonic frequencies of energy-minimized structures (unless otherwise noted).

5.3 Results and Discussion

In the following subsections, the performance of optimized basis sets are compared with that of the cc-pV*n*Z and cc-pV*n*Z[rc](*tr*) basis sets. The impact of basis set choice upon total atomic energy for the atoms H, B, C, N, O, and F, as well as for the enthalpy of formation for 86 molecules comprised of these atoms, varying from two to 14 atoms was examined. An analysis of percentage of CPU savings that can be achieved with the modified basis sets is also reported. Also, the atomization energies and percentage of CPU savings for a set of fullerenes computed with the modified basis sets are reported.

5.3.1 Atomic Energetics

Atomic energies computed with the reoptimized correlation consistent basis sets were compared with the atomic energies of the cc-pV*n*Z and cc-pV*n*Z[rc](*tr*) basis sets utilizing each density functional. These energies are listed in Table 5.2 and 5.3. Explicit

reoptimization of the Gaussian primitives in the cc-pV*n*Z basis sets has a larger impact than recontraction on not only the double-ζ energies, but also the triple- and quadruple-ζ energies. For example, compared with the cc-pV*n*Z basis sets, the nitrogen, oxygen, and fluorine recontracted B3LYP atomic energies are lowered by 2.7, 3.1, and 3.6 mE_h, respectively, at the double-ζ level, and are lowered all by 0.7 mE_h, respectively, at the triple-ζ level. In contrast to this, the nitrogen, oxygen, and fluorine reoptimized B3LYP atomic energies are lowered by 3.5, 4.3, and 5.3 mE_h, respectively, at the double-ζ level, and are lowered by 1.0, 1.3, and 1.6 mE_h, respectively, at the triple-ζ level. The impact of recontraction is more pronounced for the BLYP atomic energies, impacting both the double- and triple-ζ energies. Reoptimization, again, makes a larger impact on total atomic energies than recontraction alone. Examining fluorine, it is observed that the total energy is lowered by 8.8, 2.8, 1.7, and 0.3 mE_h at the double-, triple-, quadruple-, and quintuple-ζ levels, respectively, relative to the original cc-pV*n*Z basis sets. However, despite the larger impact by reoptimization in BLYP atomic energies, the calculated KS limits are somewhat resilient. For all six atoms, each of the three extrapolation schemes yields a KS limit that is no larger than 1.4 mE_h lower than that computed from the cc-pV*n*Z energies. The energy lowering for all six atoms, for both methods using the modified quintuple sets, is no larger than 0.4 mE_h. Therefore, the quintuple total energies, in combination with the extrapolation schemes, defines the point at which saturation of the electron density occurs for these modified basis sets.

5.3.2 Molecular Energetics

To assess the impact of recontraction and reoptimization of the correlation consistent basis sets upon reaction enthalpies, 20 combustion reactions were considered. The calculated combustion enthalpies of reaction for both B3LYP and BLYP are listed in Tables 5.4 through 5.7. Examining the MADs for computed B3LYP and BLYP enthalpies in Table 5.4 and the extrapolated enthalpies in Table 5.5, it is again observed that the double-ζ level values are most affected by recontraction of the basis sets, compared with the standard cc-pV*n*Z basis sets. For example, in Table 5.4, methane, ethane, propane, and butane have combustion enthalpies that are affected by 2.8, 8.2, 12.0, and 15.8 kcal/mol, respectively, when the cc-pVDZ[rc](*tr*) basis set is employed versus the cc-pVDZ basis set. When the reoptimized sets are employed, the B3LYP-calculated combustion enthalpies of methane, ethane, propane, and butane results in changes of 4.2, 14.3, 20.4, and 26.6 kcal/mol, respectively, at the double-ζ level, compared with the cc-pVDZ values. Despite the large changes in combustion enthalpies at the double-ζ level arising from recontraction, there are no significant changes (i.e. > 1.0 kcal/mol) in the B3LYP enthalpies at the higher ζ-levels. However, reoptimizing the cc-pV*n*Z basis sets specifically for B3LYP does have larger impact on the combustion enthalpies. For methane and ethyne (the smallest two molecules in Table 5.4), the triple-ζ enthalpies results in changes of 1.9 and 1.0 kcal/mol, respectively, while the quadruple-ζ enthalpies results in changes of 1.1 and 1.0 kcal/mol, respectively. For spiropentane and benzene (the largest two molecules in Table 5.4), the triple-ζ enthalpies change by 5.3 and 3.9 kcal/mol, respectively, while the quadruple-ζ enthalpies change by 4.0 and 3.1 kcal/mol, respectively. In fact, the differences

between the cc-pV*n*Z and cc-pV*n*Z-B3LYP P, S3, and S4 KS limits, in Table 5.5, for the combustion enthalpies of spiropentane are 1.1, 1.8, and 2.7 kcal/mol, and for benzene are 0.1, 1.0, and 1.9 kcal/mol, respectively. All of the B3LYP enthalpies are closer to experiment when the recontracted or reoptimized basis sets are employed. The BLYP combustion enthalpies experience similar changes with respect to the choice of basis set. Considering the BLYP combustion enthalpies, from Table 5.6, of methane, ethane, propane, and butane, it is observed that there are changes of 3.4, 10.3, 15.2, and 20.1 kcal/mol at the double-ζ level, respectively, when the recontracted basis sets are employed. Those changes increase to 5.5, 19.3, 27.5, and 35.6 kcal/mol, respectively, when the reoptimized basis sets are employed. Significant changes at the triple- and quadruple-ζ level are not apparent in the BLYP combustion enthalpies when the recontracted basis sets are employed. However, significant changes relative to the cc-pV*n*Z basis sets at the triple-ζ and higher levels are observed with the reoptimized basis sets. Consider spiropentane and benzene: at the triple-ζ level, their combustion enthalpies change by 7.5 and 5.5 kcal/mol, respectively, while at the quadruple-ζ level, they change by 4.5 and 3.2 kcal/mol, respectively. In addition, the differences between the cc-pV*n*Z and cc-pV*n*Z-BLYP P, S3, and S4 KS limits, in Table 5.7, for the combustion enthalpies of spiropentane are 0.7, 2.3, and 3.4 kcal/mol, and for benzene are 0.5, 1.0, and 2.2 kcal/mol, respectively. Both recontraction and reoptimization move the BLYP combustion enthalpies closer to their experimental values. While these combustion enthalpies provide a small set for examination of the new basis sets, the MADs in Tables 5.4 through 5.7, they are far from experiment. The lowest MAD, 14.3 kcal/mol, was computed using from the cc-pV*n*Z-B3LYP P KS limit.

The total energies of 86 molecules, listed in Table 5.8 were computed with the cc-pV*n*Z basis sets and the cc-pV*n*Z[rc](*tr*) and reoptimized correlation consistent basis sets. The mean signed deviations (MSDs) and mean absolute deviations (MADs) are shown in Table 5.9 (tabulated energies of all molecules investigated here can be found in the supplemental material). These molecules were chosen from the G2/97 test set. Optimized geometries have been used (computed at the B3LYP/cc-pVTZ level; the recontracted and reoptimized basis set energetics use the zero-point and thermal correction energies calculated using B3LYP/cc-pVTZ) for the energetics in this comparison to demonstrate the difference in energies with respect to the change in basis set construction. It is noted first that the double-ζ energies are most affected by both recontraction and reoptimization, and that the triple- and quadruple-ζ energies tend to be only slightly affected by both basis set modifications.

Comparing the B3LYP energies computed with the cc-pV*n*Z[rc](*tr*) basis sets to those computed with cc-pV*n*Z-B3LYP, it is observed that recontraction tends to make the largest impact for the double-ζ levels. For example, the MAD of the cc-pVDZ[rc] basis set energies in Table 5.9 is 11.3 mE_h compared with the cc-pVDZ-B3LYP MAD of 9.2 mE_h, whereas the MADs of the triple-, quadruple-, and quintuple-ζ recontracted basis set energies are 2.2, 1.2, and 0.1 mE_h, respectively, but are 2.2, 1.1, and 0.1 mE_h using the cc-pV*n*Z-B3LYP basis sets. Likewise, in the BLYP energies, recontraction makes the largest impact for the double- ζ levels. For example, the MAD of the cc-pVDZ[rc] basis set energies in Table 5.9 is 16.6 mE_h compared with the cc-pVDZ-BLYP MAD of 14.1 mE_h, whereas the MADs of the triple-, quadruple-, and quintuple-ζ

recontracted basis set energies are 3.5, 2.0, and 0.3 mE_h, respectively, but are 3.8, 2.0, and 0.4 mE_h using the cc-pV*n*Z-BLYP basis sets.

5.3.3 Enthalpies of Formation and Computational Efficiencies

Table 5.10 lists the enthalpies of formation for the 86 molecules and the corresponding MADs and MSDs from experimental values of the test set computed for B3LYP with each basis set family. Also, Table 5.11 lists the corresponding extrapolated enthalpies of formation using the P, S3, and S4 extrapolation schemes with the MAD and MSDs from experimental values. Recontraction of the basis sets lowers the MAD of the B3LYP enthalpies of formation from 8.8 to 6.6 kcal/mol at the double-ζ level, but the reoptimized B3LYP basis sets raise the MAD to 9.1 kcal/mol. Despite the worsening of the MAD at the B3LYP/double-ζ level, the reoptimized basis sets afford a MAD of 3.7 kcal/mol from experiment at the KS limit (with the Peterson extrapolation scheme), compared with 4.0 kcal/mol from the cc-pV*n*Z basis sets and 3.7 kcal/mol from the cc-pV*n*Z[rc](*tr*) basis sets. Table 5.12 lists the enthalpies of formation for the 86 molecules and the corresponding MADs and MSDs from experimental values of the test set computed for BLYP with each basis set family. Also, Table 5.13 lists the extrapolated enthalpies of formation using the P, S3, and S4 extrapolation schemes with the corresponding MADs and MSDs from experimental values. Recontraction also lowers the MAD of the BLYP enthalpies of formation from 12.2 kcal/mol, computed with the cc-pV*n*Z basis sets, to 9.5 kcal/mol at the double-ζ level, while reoptimization only slightly lowers the MAD to 11.5 kcal/mol. Despite this, the reoptimized basis sets yield much lower MSDs overall, with the lowest absolute MAD at 1.1 kcal/mol for B3LYP at the

triple-ζ level. With regard to the extrapolations, the MSDs and MADs, for a given functional and basis set, are all within 0.5 kcal/mol of each other, and the lowest deviations from the extrapolations are calculated with the S4 extrapolation. Consequently, the S4 extrapolation best accounts for the extrapolated enthalpy of formation. Also, the B3LYP and BLYP reoptimized basis sets yield the lowest deviations to experimental enthalpies. This indicates that, on average, the reoptimized basis sets yield enthalpies of formation closer to experiment than the other basis set families. Overall, recontraction of the basis sets reduces the deviation of B3LYP and BLYP enthalpies.

As the basis sets increase in zeta quality, the respective energies should converge towards the same limit. This should be reflected in the small deviations of the calculated KS limits in Tables 5.11 and 5.13, provided that the extrapolation schemes adequately model the behavior of the energies with respect to increasing basis set size. An MSD that is closer to zero indicates that the extrapolation scheme more correctly models the convergent behavior of the energies with respect to the original cc-pV*n*Z basis sets. What is observed is that the MSD of the three extrapolation schemes is negative for both the B3LYP and BLYP energies using both the recontracted and reoptimized basis sets. The S4 limits tend to be more negative than the S3 limit determined using the extrapolation scheme, implying the S3 fit to be more indicative of the correct basis set behavior. Moreover, the magnitude of the S3 KS limits is larger than the Peterson KS limits, indicating that the Peterson extrapolation scheme better approximates the basis set behavior than the Schwartz schemes.

Recontraction and reoptimization impacts the efficiency of B3LYP and BLYP molecular total energy calculations. This is illustrated in Tables 5.14 and 5.15, in which the mean CPU savings for the cc-pV*n*Z[rc](*tr*) and reoptimized basis sets as a percent ratio of the cc-pV*n*Z basis sets. In addition, the tables list CPU savings for groups of *N* molecules containing *M* atoms, in which *M* = 2-14. As shown in the tables, the majority of CPU savings occurs at the quadruple- and quintuple-ζ levels for both B3LYP and BLYP. The CPU savings for the quadruple- and quintuple-ζ sets are in the ranges of 44-63% and 59-74%, respectively. The high efficiency of these sets are most likely due to the removal of the *g* and *h* functions. Also, for both cc-pV*n*Z[rc](*tr*) and the reoptimized sets, the double- and triple-ζ savings are nearly negligible.

As previously stated, due to the different convergence rates of molecular energies, enthalpies of formation and combustion enthalpies often do not necessarily display smooth, monotonic behavior, despite having used a series of cc-pV*n*Z basis sets to obtain them. However, the convergence behavior of enthalpies of formation for the cc-pV*n*Z[rc](*tr*) and reoptimized basis sets. Figures 5.1 and 5.2 illustrate the convergence rates of CHF_3 for B3LYP and BLYP, respectively, and Figures 5.3 and 5.4 illustrate the convergence rates of HCOCOH for B3LYP and BLYP, respectively. In addition, these figures illustrate convergence behavior for enthalpies computed with the cc-pV*n*Z, cc-pV*n*Z[rc](*tr*) and reoptimized basis sets having augmented functions, counterpoise correction, and a combination of both. In these examples, the reoptimized sets for both molecules in both functionals yields monotonic convergence of enthalpies. Looking at Figures 5.1 and 5.2, the reoptimized basis sets for both functionals seem to produce monotonic convergence. The addition of augmented sets do not appear to

repair convergence in the cc-pV*n*Z and cc-pV*n*Z[rc](*tr*) sets, and, in fact, convergence does not occur in the reoptimized sets. Interestingly, the counterpoise correction are, at the very least (that is, without augmented functions), necessary to produce convergence in all the examples in Figures 5.1 and 5.2. As well, in Figures 5.3 and 5.4, the reoptimized basis sets for both functionals seem to produce monotonic convergence. The addition of augmented sets for HCOCOH repairs convergence in the cc-pV*n*Z and cc-pV*n*Z[rc](*tr*) sets, and only breaks convergence in the reoptimized sets for B3LYP. As before, the counterpoise correction are, at the very least (that is, without augmented functions), necessary to produce convergence in all the examples in Figures 5.3 and 5.4. So, in these examples, the reoptimized sets do indeed produce monotonic convergence of the KS limit for enthalpies. Further, for any cases in which monotonic convergence is broken, the counterpoise correction alone seems to provide an adequate solution, whereas the addition of augmented functions may or may not yield the same expectation.[113,117]

5.3.4 Energetics and Computational Efficiency Comparisons in Fullerene Computations

To assess the utility of the recontracted and reoptimized cc-pV*n*Z basis sets for larger molecules, their efficiency in fullerene calculations has been examined. The molecules employed in the tests were C_{32}, C_{36}, C_{44}, C_{48}, C_{50}, and C_{60}. The atomization energies were computed using optimized geometries at the B3LYP/cc-pVTZ level. Table 5.16 lists the atomization energies for B3LYP and BLYP using the cc-pVnZ sets in E_h, and the corresponding differences with regard to the cc-pV*n*Z[rc](tr) and

reoptimized basis sets in mE_h. Also, Table 5.17 illustrates the CPU savings that can be obtained using the cc-pV*n*Z[rc](tr) and reoptimized basis sets.

The CPU savings of the correlation energy recovery is very prevalent in the fullerenes, given that these contain upwards of one hundred carbon atoms. In fact, Table 5.16 illustrates that the cc-pV*n*Z[rc](tr) and reoptimized basis sets compute lower atomization energies, by a magnitude of 500 kcal/mol. This is reflective of more stable fullerene being computed by the cc-pV*n*Z[rc](tr) and reoptimized basis sets. With increasing -ζ level, the atomization energies behave in a convergent manner. Also, we did not compute a basis set limit since the point was to address the behavior of the cc-pV*n*Z[rc](tr) and reoptimized basis sets for a set of large molecules. However, it should be noted that the convergence behavior between the regular cc-pVnZ and the cc-pV*n*Z[rc](tr) and reoptimized basis sets are notably different: the regular sets converge to an upper bound, whereas the cc-pV*n*Z[rc](tr) and reoptimized basis sets all converge to a lower-bounded atomization energy. This observation obviously stems directly from the reconstruction of the cc-pVnZ basis sets. The only experimental comparison that could be made was for C_{60}. The experimental values (9797.6, 9762.2, and 9787.4 kcal/mol) in Table 5.16 compare very well to the results for the B3LYP sets, mainly with the cc-pVQZ[rc](-1*g*) (-9806.8 kcal/mol), cc-pVTZ-B3LYP (-9774.94 kcal/mol), and cc-pVQZ-B3LYP (-9742.14 kcal/mol) basis sets.

In Table 5.17, the double-ζ recontracted and reoptimized basis sets perform in a similar manner to the standard basis sets. At the triple-ζ level, the recontracted basis sets show little difference in computational time relative to the cc-pV*n*Z basis sets. However, the reoptimized cc-pV*n*Z basis sets show CPU time reductions between 9-

16% in B3LYP calculations and 13-22% in BLYP calculations. This increase in efficiency of the reoptimized basis sets must then be due to their construction, indicating that explicit reoptimization of the primitive basis functions for a specific density functional leads to greater efficiency than recontraction of the original primitives. At the quadruple-ζ level, both the recontracted and reoptimized basis sets display significant reductions in CPU time relative to the standard cc-pV*n*Z sets, primarily due to the removal of the *g* function. Employing the recontracted sets, CPU time reductions between 58-66% are observed with B3LYP, while reductions between 56-71% are observed with BLYP. Even at the quadruple-ζ level, the reoptimized basis sets show a greater increase in computational efficiency having larger reductions in CPU time than the recontracted basis sets. For example, the CPU time reduction in computing the C_{48} BLYP/cc-pVQZ[rc](-1*g*) energy is 63%, while the BLYP/cc-pVQZ-BLYP reduction is 70%; the CPU time reduction in computing the C_{36} B3LYP/cc-pVQZ[rc](-1*g*) energy is 58%, while the B3LYP/cc-pVQZ-B3LYP reduction is 66%. The decrease in CPU efficiency required of these reoptimized sets can open the door for the ease of applications involving quadruple- and quintuple-ζ level computations of large molecules.

5.4 Conclusions

New reoptimized cc-pV*n*Z basis sets for B3LYP and BLYP calculations have been presented and discussed. In 20 combustion enthalpies and 86 molecules from first row atoms, these new basis sets have demonstrated lower total energies and a marked improvement in the computational cost of computing triple-ζ through quintuple-ζ thermochemical properties. In atomic energies, the reoptimization makes a larger

impact beyond the triple-ζ level than recontraction alone. Even with the *g* and *h* functions truncated from the reoptimized basis sets, the BLYP energies of the oxygen and fluorine atoms are lowered by more than 1 mE_h at the quintuple-ζ level. We have also found that in KS extrapolations of the total energies, the Peterson extrapolation scheme models the convergent behavior of the recontracted and reoptimized basis set energies more accurately than the Schwartz schemes relative to the original cc-pV*n*Z basis set energies.

In calculations of molecular enthalpies of formation and combustion enthalpies, the reoptimized cc-pV*n*Z basis sets produce energetic values that are closer to experiment at the triple-ζ through quintuple-ζ levels than both the original and recontracted cc-pV*n*Z basis sets. Differences greater than 1.0 kcal/mol at higher ζ-levels coupled to the observation that the reoptimized sets deviate less from experiment, on average, indicates that, in order to achieve near "chemical accuracy" with BLYP and B3LYP, 1) optimal basis sets need to be employed and 2) basis sets beyond triple-ζ are necessary.[114,117] To achieve monotonic convergence for enthalpies, the Counterpoise correction must be included in these computations, as the addition of augmented functions does not always guarantee monotonic convergence.

The computational efficiency of the recontracted and reoptimized cc-pV*n*Z basis sets has been demonstrated in energy calculations of the 86 molecule test set and fullerenes ranging from C_{32} to C_{60}. At the double- and triple-ζ levels, the recontracted and reoptimized sets do not yield much of a reduction in computational time, but at the quadruple- and quintuple-ζ level, a reduction in computational time of at least 40% and not more than 80% can be observed, relative to the original cc-pV*n*Z basis sets. Utilizing

the reoptimized sets in B3LYP and BLYP energy calculations yields slightly better reductions in computational time than the recontracted basis sets.

Given the widespread application of B3LYP and BLYP in computational research, these newly reoptimized cc-pV*n*Z basis sets are recommended for use in B3LYP and BLYP calculations, due to their performance in computing molecular properties (relative to experiment) and their significant reduction in computational cost over the original (non-optimal) cc-pV*n*Z basis sets at higher ζ-levels.

Table 5.1. A comparison of the number of primitive (parentheses) and contracted [brackets] functions of the cc-pV*n*Z, cc-pV*n*Z[rc](tr), reoptimized cc-pV*n*Z, and pc-*n* basis sets.

Atom	ζ	cc-pV*n*Z	cc-pV*n*Z[rc](tr) / reoptimized	pc-*n*
H	D	(4*s*1*p*)	(4*s*1*p*)	(4*s*1*p*)
		[2*s*1*p*]	[2*s*1*p*]	[2*s*1*p*]
	T	(5*s*2*p*1*d*)	(5*s*2*p*1*d*)	(6*s*2*p*1*d*)
		[3*s*2*p*1*d*]	[3*s*2*p*1*d*]	[3*s*2*p*1*d*]
	Q	(6*s*3*p*2*d*1*f*)	(6*s*3*p*2*d*)	(9*s*4*p*2*d*1*f*)
		[4*s*3*p*2*d*1*f*]	[4*s*3*p*2*d*]	[5*s*4*p*2*d*1*f*]
	5	(8*s*4*p*3*d*2*f*1*g*)	(8*s*4*p*3*d*)	(11*s*6*p*3*d*2*f*1*g*)
		[5*s*4*p*3*d*2*f*1*g*]	[5*s*4*p*3*d*]	[7*s*6*p*3*d*2*f*1*g*]
B-F	D	(9*s*4*p*1*d*)	(9*s*4*p*1*d*)	(7*s*4*p*1*d*)
		[3*s*2*p*1*d*]	[3*s*2*p*1*d*]	[3*s*2*p*1*d*]
	T	(10*s*5*p*2*d*1*f*)	(10*s*5*p*2*d*1*f*)	(10*s*6*p*2*d*1*f*)
		[4*s*3*p*2*d*1*f*]	[4*s*3*p*2*d*1*f*]	[4*s*3*p*2*d*1*f*]
	Q	(12*s*6*p*3*d*2*f*1*g*)	(11*s*6*p*3*d*2*f*)	(14*s*9*p*4*d*2*f*1*g*)
		[5*s*4*p*3*d*2*f*1*g*]	[5*s*4*p*3*d*2*f*]	[6*s*5*p*4*d*2*f*1*g*]
	5	(14*s*8*p*4*d*3*f*2*g*1*h*)	(12*s*8*p*4*d*3*f*)	(18*s*11*p*6*d*3*f*2*g*1*h*)
		[6*s*5*p*4*d*3*f*2*g*1*h*)	[6*s*5*p*4*d*3*f*]	[8*s*7*p*6*d*3*f*2*g*1*h*]

Table 5.2. The atomic energies (E_h) of the B3LYP/cc-pVnZ and their calculated complete basis set limits, followed by the differences (mE_h) of the cc-pV*n*Z[rc](tr) and reoptimized basis sets with respect to B3LYP/cc-pV*n*Z atomic energies (E_h) and their calculated complete basis set limits.

B3LYP	H	B	C	N	O	F
cc-pVDZ	-0.501258	-24.659561	-37.850417	-54.587815	-75.066315	-99.724849
cc-pVTZ	-0.502156	-24.662345	-37.856816	-54.600202	-75.089006	-99.760647
cc-pVQZ	-0.502346	-24.663417	-37.858855	-54.603684	-75.095212	-99.770234
cc-pV5Z	-0.502428	-24.664064	-37.859689	-54.605036	-75.097480	-99.773568
P	-0.502465	-24.664242	-37.860107	-54.605761	-75.098800	-99.775641
S3	-0.502380	-24.663541	-37.859009	-54.604007	-75.095772	-99.771081
S4	-0.502341	-24.663393	-37.858699	-54.603430	-75.094726	-99.769443
cc-pVDZ[rc]	-0.228	-1.587	-2.047	-2.712	-3.066	-3.558
cc-pVTZ[rc]	-0.001	-0.631	-0.639	-0.655	-0.663	-0.692
cc-pVQZ[rc](-1g)	0.000	-0.526	-0.526	-0.602	-0.584	-0.597
cc-pV5Z[rc](-2g1h)	0.000	-0.063	-0.146	-0.161	-0.123	-0.091
P	0.000	-0.129	-0.193	-0.240	-0.198	-0.171
S3	0.013	-0.324	-0.330	-0.329	-0.289	-0.262
S4	0.005	-0.371	-0.390	-0.410	-0.383	-0.373
cc-pVDZ-B3LYP	-0.346	-1.739	-2.427	-3.458	-4.318	-5.264
cc-pVTZ-B3LYP	-0.059	-0.714	-0.811	-1.013	-1.315	-1.566
cc-pVQZ-B3LYP	-0.030	-0.543	-0.599	-0.756	-0.890	-0.995
cc-pV5Z-B3LYP	-0.006	-0.058	-0.165	-0.200	-0.194	-0.177
P	-0.003	-0.108	-0.194	-0.243	-0.216	-0.183
S3	-0.012	-0.346	-0.397	-0.471	-0.563	-0.620
S4	-0.023	-0.398	-0.469	-0.575	-0.696	-0.784

Table 5.3. The atomic energies (E_h) of the BLYP/cc-pVnZ and their calculated complete basis set limits, followed by the differences (mE_h) of the cc-pV*n*Z[rc](tr) and reoptimized basis sets with respect to BLYP/cc-pV*n*Z atomic energies (E_h) and their calculated complete basis set limits.

BLYP	H	B	C	N	O	F
cc-pVDZ	-0.496403	-24.646606	-37.836472	-54.571454	-75.052588	-99.711636
cc-pVTZ	-0.497555	-24.650055	-37.843970	-54.585596	-75.077711	-99.750790
cc-pVQZ	-0.497781	-24.651312	-37.846304	-54.589501	-75.084550	-99.761261
cc-pV5Z	-0.497889	-24.652238	-37.847563	-54.591269	-75.087330	-99.765338
P	-0.497931	-24.652413	-37.847979	-54.592030	-75.088727	-99.767513
S3	-0.497830	-24.651530	-37.846604	-54.589972	-75.085278	-99.762351
S4	-0.497781	-24.651347	-37.846236	-54.589311	-75.084115	-99.760551
cc-pVDZ[rc]	-0.405	-2.476	-3.192	-4.226	-4.872	-5.744
cc-pVTZ[rc]	-0.002	-1.068	-1.074	-1.093	-1.107	-1.154
cc-pVQZ[rc](-1g)	0.000	-0.885	-0.871	-0.952	-0.928	-0.947
cc-pV5Z[rc](-2g1h)	-0.001	-0.183	-0.157	-0.262	-0.251	-0.110
P	-0.001	-0.275	-0.247	-0.367	-0.344	-0.228
S3	0.023	-0.587	-0.532	-0.545	-0.498	-0.415
S4	0.010	-0.657	-0.626	-0.671	-0.646	-0.596
cc-pVDZ-B3LYP	-0.622	-2.789	-3.941	-5.646	-7.131	-8.814
cc-pVTZ-B3LYP	-0.114	-1.227	-1.437	-1.806	-2.317	-2.782
cc-pVQZ-B3LYP	-0.060	-0.922	-1.029	-1.269	-1.520	-1.719
cc-pV5Z-B3LYP	-0.014	-0.175	-0.199	-0.345	-0.392	-0.291
P	-0.008	-0.240	-0.253	-0.383	-0.397	-0.281
S3	-0.027	-0.631	-0.678	-0.837	-1.023	-1.108
S4	-0.047	-0.711	-0.796	-1.007	-1.240	-1.382

Table 5.4. Combustion enthalpies at 298 K (kcal/mol) computed with B3LYP and the cc-pV*n*Z, cc-pV*n*Z[rc](tr), and reoptimized basis sets.

Molecule	cc-pV*n*Z				cc-pV*n*Z[rc](tr)				cc-pV*n*Z-B3LYP				
	D	T	Q	5	D	T	Q	5	D	T	Q	5	Expt.
CH_4	-167.6	-184.8	-189.1	-190.5	-170.4	-184.8	-189.1	-190.5	-171.8	-186.7	-190.2	-190.7	-191.8
C_2H_2	-283.8	-295.0	-297.2	-297.6	-288.6	-294.9	-297.2	-297.5	-292.1	-296.0	-298.2	-297.6	-300.2
C_2H_4	-284.2	-304.6	-308.8	-310.0	-290.7	-304.5	-308.9	-310.1	-295.4	-307.0	-310.7	-310.4	-316.3
C_2H_6	-297.0	-325.7	-331.9	-334.2	-305.2	-325.6	-332.1	-334.3	-311.3	-329.5	-334.8	-334.7	-341.5
CH_3CCH	-437.9	-463.6	-468.8	-469.3	-443.7	-463.7	-468.4	-469.2	-444.5	-464.9	-469.0	-469.2	-442.1
CH_2CCH_2 (allene)	-404.9	-428.8	-433.3	-434.3	-413.6	-428.7	-433.4	-434.3	-419.3	-431.2	-435.2	-434.5	-443.1
C_3H_4 (cyclopropene)	-429.9	-454.7	-459.2	-460.2	-439.0	-454.6	-459.3	-460.2	-444.7	-457.3	-461.2	-460.4	-464.1
CH_3CHCH_2	-412.2	-444.6	-451.0	-452.9	-422.5	-444.4	-451.2	-453.0	-429.6	-448.3	-453.9	-453.4	-460.5
C_3H_6 (cyclopropane)	-421.6	-454.2	-460.6	-462.5	-432.1	-453.9	-460.7	-462.6	-439.1	-458.1	-463.5	-463.0	-468.4
C_3H_8	-432.5	-473.2	-481.5	-484.4	-444.5	-472.9	-481.8	-484.6	-452.9	-478.3	-485.4	-485.2	-530.4
$CH_2CHCHCH_2$ (trans-2-butene)	-485.8	-562.2	-573.5	-576.2	-509.7	-562.4	-573.1	-575.7	-510.1	-565.9	-576.0	-576.0	-576.1
C_4H_6 (methyl-cyclopropane)	-587.6	-633.3	-641.8	-644.3	-602.9	-633.0	-642.0	-644.4	-611.5	-638.4	-645.6	-645.0	-639.4
C_4H_6 (bicyclo[1.1.0]butane)	-553.0	-591.2	-597.7	-599.4	-566.5	-590.9	-597.9	-599.5	-574.3	-595.2	-600.7	-599.9	-601.7
C_4H_6 (cyclobutene)	-534.8	-573.1	-579.6	-581.4	-549.0	-572.8	-580.0	-581.6	-558.0	-577.2	-583.1	-582.0	-587.2
C_4H_8 (cyclobutane)	-551.2	-597.7	-606.3	-609.0	-566.1	-597.4	-606.6	-609.1	-575.5	-602.8	-610.3	-609.7	-650.2
C_4H_8 (isobutylene)	-539.3	-583.6	-592.1	-594.7	-553.4	-583.4	-592.4	-594.9	-562.9	-588.7	-596.1	-595.4	-645.2
C_4H_{10} (butane)	-559.9	-612.5	-623.0	-626.6	-575.7	-612.2	-623.4	-626.8	-586.5	-618.9	-627.9	-627.6	-687.8
$(CH_3)_3CH$ (isobutane)	-598.0	-651.6	-662.0	-665.5	-614.3	-651.3	-662.4	-665.7	-624.7	-657.9	-666.8	-666.5	-685.7
C_5H_8 (spiropentane)	-679.3	-728.4	-737.2	-739.5	-696.1	-728.0	-737.5	-739.7	-706.4	-733.7	-741.2	-740.2	-746.0
C_6H_6 (benzene)	-695.3	-742.2	-749.5	-750.4	-713.1	-742.0	-749.7	-750.7	-723.0	-746.1	-752.6	-750.9	-746.0
MAD	58.4	23.1	17.2	15.7	46.5	23.3	17.1	15.6	39.7	19.4	15.0	15.3	
MSD	-58.4	-20.9	-14.0	-12.0	-46.3	-21.1	-13.8	-12.0	-39.5	-17.1	-11.1	-11.6	

Table 5.5. Combustion enthalpies at 298 K (kcal/mol) extrapolated from B3LYP and the cc-pV*n*Z, cc-pV*n*Z[rc](tr), and reoptimized basis sets.

Molecule	cc-pV*n*Z			cc-pV*n*Z[rc](tr)			cc-pV*n*Z-B3LYP			
	P	S3	S4	P	S3	S4	P	S3	S4	Expt.
CH_4	-191.5	-189.5	-188.7	-191.4	-189.3	-188.6	-191.6	-190.3	-189.7	-191.8
C_2H_2	-298.2	-297.4	-297.0	-298.1	-297.1	-296.8	-298.3	-297.6	-297.4	-300.2
C_2H_4	-311.0	-309.4	-308.5	-311.1	-309.0	-308.4	-311.5	-310.3	-309.8	-316.3
C_2H_6	-335.5	-332.8	-331.6	-335.7	-332.4	-331.4	-336.3	-334.5	-333.7	-341.5
CH_3CCH	-470.7	-469.1	-468.1	-470.4	-468.6	-467.8	-470.3	-469.2	-468.4	-442.1
CH_2CCH_2 (allene)	-435.4	-433.9	-432.9	-435.5	-433.4	-432.7	-435.8	-434.6	-434.1	-443.1
C_3H_4 (cyclopropene)	-461.3	-459.9	-458.8	-461.4	-459.3	-458.6	-461.7	-460.6	-460.1	-464.1
CH_3CHCH_2	-454.3	-451.9	-450.6	-454.6	-451.4	-450.4	-455.1	-453.4	-452.5	-460.5
C_3H_6 (cyclopropane)	-463.9	-461.5	-460.2	-464.2	-460.9	-459.9	-464.7	-463.0	-462.2	-468.4
C_3H_8	-486.2	-482.8	-481.1	-486.6	-482.2	-480.8	-487.3	-484.9	-483.8	-530.4
$CH_2CHCHCH_2$ (trans-2-butene)	-578.8	-576.1	-573.1	-578.2	-574.4	-572.1	-578.9	-576.7	-574.4	-576.1
C_4H_6 (methyl-cyclopropane)	-646.2	-643.2	-641.3	-646.5	-642.3	-640.9	-647.2	-645.1	-643.9	-639.4
C_4H_6 (bicyclo[1.1.0]butane)	-600.9	-598.9	-597.3	-601.2	-598.1	-597.0	-601.6	-600.2	-599.3	-601.7
C_4H_6 (cyclobutene)	-582.9	-580.8	-579.3	-583.3	-580.1	-579.0	-583.9	-582.3	-581.4	-587.2
C_4H_8 (cyclobutane)	-610.9	-607.8	-605.9	-611.3	-607.0	-605.5	-612.0	-609.7	-608.5	-650.2
C_4H_8 (isobutylene)	-596.6	-593.5	-591.6	-597.0	-592.7	-591.3	-597.7	-595.4	-594.3	-645.2
C_4H_{10} (butane)	-628.8	-624.7	-622.5	-629.3	-623.9	-622.2	-630.2	-627.4	-625.9	-687.8
$(CH_3)_3CH$ (isobutane)	-667.7	-663.7	-661.5	-668.2	-662.9	-661.2	-669.1	-666.3	-664.9	-685.7
C_5H_8 (spiropentane)	-741.5	-738.7	-736.6	-742.0	-737.7	-736.2	-742.6	-740.5	-739.3	-746.0
C_6H_6 (benzene)	-752.3	-750.7	-748.8	-752.7	-749.8	-748.5	-753.1	-751.7	-750.7	-746.0
MAD	14.9	16.4	17.5	14.7	16.9	17.7	14.3	15.4	16.0	
MSD	-10.5	-12.9	-14.4	-10.3	-13.6	-14.7	-9.7	-11.5	-12.5	

Table 5.6. Combustion enthalpies at 298 K (kcal/mol) computed with BLYP and the cc-pV*n*Z, cc-pV*n*Z[rc](tr), and reoptimized basis sets.

Molecule	cc-pV*n*Z				cc-pV*n*Z[rc](tr)				cc-pV*n*Z-BLYP				
	D	T	Q	5	D	T	Q	5	D	T	Q	5	Expt.
CH_4	-173.1	-190.5	-195.3	-196.8	-176.5	-190.6	-195.1	-196.7	-178.6	-193.2	-196.5	-197.1	-191.8
C_2H_2	-274.4	-286.7	-289.2	-289.5	-280.6	-286.7	-289.1	-289.4	-285.1	-288.3	-290.1	-289.5	-300.2
C_2H_4	-272.8	-295.4	-300.2	-301.6	-281.2	-295.4	-300.1	-301.6	-287.8	-299.0	-302.3	-302.0	-316.3
C_2H_6	-284.1	-315.8	-322.9	-325.6	-294.4	-315.7	-323.0	-325.7	-303.4	-321.5	-326.3	-326.3	-341.5
CH_3CCH	-453.5	-478.8	-484.0	-484.2	-460.9	-479.0	-483.5	-484.1	-461.2	-480.3	-483.9	-484.1	-442.1
CH_2CCH_2 (allene)	-390.2	-416.6	-421.6	-422.6	-401.3	-416.5	-421.5	-422.6	-409.1	-420.1	-423.6	-422.9	-443.1
C_3H_4 (cyclopropene)	-417.0	-444.3	-449.2	-450.3	-428.5	-444.2	-449.1	-450.3	-436.1	-448.0	-451.3	-450.5	-464.1
CH_3CHCH_2	-396.7	-432.6	-439.7	-442.0	-409.9	-432.5	-439.8	-442.0	-419.8	-438.1	-443.0	-442.6	-460.5
C_3H_6 (cyclopropane)	-407.9	-444.0	-451.1	-453.4	-421.3	-443.8	-451.1	-453.5	-431.1	-449.6	-454.4	-454.0	-468.4
C_3H_8	-415.5	-460.6	-470.0	-473.5	-430.7	-460.4	-470.1	-473.6	-443.0	-468.2	-474.6	-474.4	-530.4
$CH_2CHCHCH_2$ (trans-2-butene)	-453.3	-535.1	-547.0	-548.8	-484.0	-535.2	-546.0	-548.6	-483.6	-540.0	-548.9	-548.9	-576.1
C_4H_6 (methyl-cyclopropane)	-564.3	-615.0	-624.4	-627.4	-583.8	-614.8	-624.4	-627.5	-595.9	-622.4	-628.7	-628.2	-639.4
C_4H_6 (bicyclo[1.1.0]butane)	-537.9	-580.0	-587.2	-589.1	-554.9	-579.7	-587.2	-589.2	-565.6	-585.7	-590.5	-589.6	-601.7
C_4H_6 (cyclobutene)	-511.4	-554.4	-561.6	-563.7	-529.4	-554.1	-561.8	-563.9	-541.8	-560.4	-565.5	-564.4	-587.2
C_4H_8 (cyclobutane)	-533.5	-585.0	-594.5	-597.8	-552.5	-584.7	-594.7	-597.9	-565.6	-592.5	-599.1	-598.6	-650.2
C_4H_8 (isobutylene)	-519.9	-568.9	-578.5	-581.5	-537.9	-568.8	-578.6	-581.6	-551.1	-576.4	-583.0	-582.4	-645.2
C_4H_{10} (butane)	-538.9	-597.3	-609.0	-613.4	-559.0	-597.0	-609.3	-613.5	-574.5	-606.8	-614.8	-614.5	-687.8
$(CH_3)_3CH$ (isobutane)	-574.8	-634.1	-645.8	-650.0	-595.6	-633.9	-646.0	-650.2	-610.5	-643.5	-651.5	-651.2	-685.7
C_5H_8 (spiropentane)	-660.4	-714.6	-724.2	-726.9	-681.7	-714.3	-724.3	-727.0	-695.7	-722.1	-728.7	-727.7	-746.0
C_6H_6 (benzene)	-675.8	-727.5	-735.3	-736.2	-698.6	-727.4	-735.3	-736.4	-711.4	-733.0	-738.5	-736.7	-746.0
MAD	74.6	36.0	29.2	27.2	59.9	36.1	29.2	27.1	50.6	30.7	26.1	26.6	
MSD	-73.4	-32.3	-24.7	-22.5	-58.1	-32.5	-24.7	-22.4	-48.7	-26.7	-21.4	-21.9	

Table 5.7. Combustion enthalpies at 298 K (kcal/mol) extrapolated from BLYP and the cc-pV*n*Z, cc-pV*n*Z[rc](tr), and reoptimized basis sets.

Molecule	cc-pV*n*Z			cc-pV*n*Z[rc](tr)			cc-pV*n*Z-BLYP			
	P	S3	S4	P	S3	S4	P	S3	S4	Expt.
CH_4	-197.9	-195.6	-194.8	-197.7	-195.4	-194.7	-197.9	-196.7	-196.1	-191.8
C_2H_2	-290.1	-289.4	-288.9	-290.0	-288.9	-288.6	-290.1	-289.5	-289.4	-300.2
C_2H_4	-302.6	-300.8	-299.8	-302.7	-300.3	-299.6	-303.0	-302.0	-301.5	-316.3
C_2H_6	-327.1	-323.9	-322.5	-327.2	-323.3	-322.3	-327.7	-326.1	-325.3	-341.5
CH_3CCH	-485.7	-484.2	-483.1	-485.2	-483.6	-482.8	-485.1	-484.2	-483.4	-442.1
CH_2CCH_2 (allene)	-423.8	-422.2	-421.1	-423.8	-421.5	-420.8	-424.0	-423.1	-422.6	-443.1
C_3H_4 (cyclopropene)	-451.5	-449.9	-448.8	-451.5	-449.2	-448.4	-451.6	-450.8	-450.3	-464.1
CH_3CHCH_2	-443.5	-440.8	-439.3	-443.7	-440.0	-438.9	-444.1	-442.7	-441.9	-460.5
C_3H_6 (cyclopropane)	-455.0	-452.2	-450.7	-455.1	-451.4	-450.3	-455.5	-454.1	-453.3	-468.4
C_3H_8	-475.5	-471.5	-469.6	-475.7	-470.6	-469.2	-476.3	-474.3	-473.2	-530.4
$CH_2CHCHCH_2$ (trans-2-butene)	-551.8	-549.4	-546.2	-551.1	-547.2	-545.0	-551.4	-549.9	-547.7	-576.1
C_4H_6 (methyl-cyclopropane)	-629.5	-626.1	-624.0	-629.6	-624.9	-623.4	-630.1	-628.4	-627.3	-639.4
C_4H_6 (bicyclo[1.1.0]butane)	-590.7	-588.5	-586.8	-590.9	-587.4	-586.3	-591.2	-590.1	-589.3	-601.7
C_4H_6 (cyclobutene)	-565.4	-563.1	-561.3	-565.7	-562.0	-560.8	-566.1	-564.9	-564.1	-587.2
C_4H_8 (cyclobutane)	-599.8	-596.3	-594.1	-600.1	-595.2	-593.6	-600.6	-598.8	-597.7	-650.2
C_4H_8 (isobutylene)	-583.6	-580.0	-577.9	-583.8	-579.0	-577.5	-584.4	-582.5	-581.4	-645.2
C_4H_{10} (butane)	-615.8	-611.0	-608.5	-616.2	-609.9	-608.1	-616.9	-614.5	-613.1	-687.8
$(CH_3)_3CH$ (isobutane)	-652.5	-647.8	-645.3	-652.8	-646.6	-644.8	-653.5	-651.2	-649.8	-685.7
C_5H_8 (spiropentane)	-729.1	-725.9	-723.7	-729.4	-724.6	-723.1	-729.8	-728.2	-727.1	-746.0
C_6H_6 (benzene)	-738.2	-736.7	-734.6	-738.4	-735.3	-734.0	-738.7	-737.7	-736.8	-746.0
MAD	25.7	28.0	29.5	25.6	28.9	29.9	25.2	26.4	27.2	
MSD	-20.7	-23.4	-25.1	-20.7	-24.4	-25.6	-20.3	-21.7	-22.6	

Table 5.8. The 86 molecules for which enthalpies of formation at 298K were computed.

H_2	CH_3	HCOCOH (glyoxal)	CH_3CONH_2
CH	NH_3	CF_3CN	C_4H_4O (furan)
NH	C_2H_2	C_2F_4	$(CH_3)_2CH$
OH	H_2CO	CH_3NH_2	$(CH_3)_2NH$
FH	NCCN	CH_3CCH	$CH_3CH_2NH_2$
CN	BF_3	CH_2CCH_2 (allene)	$CH_2CHCHCH_2$ (trans-2-butene)
CO	NF_3	C_3H_4 (cyclopropene)	C_4H_6 (methyl-cyclopropane)
N_2	CH_4	CH_3CHO	C_4H_6 (bicyclo[1.1.0]butane)
NO	C_2H_3	C_2H_4O (oxirane)	C_4H_6 (cyclobutene)
O_2	H_2COH	CH_2CHCN	C_4H_6 (dimethylacetylene)
F_2	CH_3O	CH_3NO_2	CH_3COCH_3
CH_2 (triplet)	CH_2CO (ketene)	CH_3ONO	C_4H_5N (pyrrole)
CH_2 (singlet)	HCOOH	CH_3COF	C_3H_8
NH_2	CH_2F_2	C_2H_6	C_5H_5N (pyridine)
H_2O	CHF_3	C_2H_4NH (aziridine)	C_4H_8 (isobutylene)
CCH (linear)	CF_4	CH_3CH_2O	$C_2H_5OCH_3$
HCN	C_2H_4	$HCOOCH_3$	C_6H_6 (benzene)
HCO	H_3COH	CH_3COOH	$(CH_3)_3N$
CO_2	H_2NNH_2	CH_3CHCH_2	C_5H_8 (spiropentane)
N_2O	CH_3CN	C_3H_6 (cyclopropane)	C_4H_{10} (butane)
NO_2	CH_3CO	CH_3CH_2OH	
O_3	CH_2CHF	CH_3OCH_3	

Table 5.9. The differences for total energies (in mE_h) of the cc-pV*n*Z[rc](*tr*) and reoptimized basis sets with respect to B3LYP/cc-pVnZ and BLYP/cc-pV*n*Z. The energies were computed with fixed B3LYP/cc-pVTZ geometries.

B3LYP	MSD	MAD
cc-pVDZ[rc]	-11.250	11.250
cc-pVTZ[rc]	-2.213	2.213
cc-pVQZ[rc](-1*g*)	-1.164	1.164
cc-pV5Z[rc](-2*g*1*h*)	-0.075	0.083
P	-0.006	0.116
S3	-0.495	0.502
S4	-0.863	0.864
cc-pVDZ-B3LYP	-9.248	9.248
cc-pVTZ-B3LYP	-2.205	2.221
cc-pVQZ-B3LYP	-1.122	1.122
cc-pV5Z-B3LYP	-0.087	0.108
P	0.000	0.179
S3	-0.567	0.617
S4	-0.846	0.908
BLYP		
cc-pVDZ[rc]	-16.627	16.627
cc-pVTZ[rc]	-3.486	3.486
cc-pVQZ[rc](-1*g*)	-1.986	1.986
cc-pV5Z[rc](-2*g*1*h*)	-0.340	0.340
P	-0.273	0.274
S3	-0.999	1.005
S4	-1.544	1.546
cc-pVDZ-BLYP	-14.140	14.140
cc-pVTZ-BLYP	-3.790	3.790
cc-pVQZ-BLYP	-1.986	1.986
cc-pV5Z-BLYP	-0.391	0.391
P	-0.221	0.248
S3	-1.308	1.313
S4	-1.773	1.775

Table 5.10. B3LYP enthalpies of formation (kcal/mol) computed with the cc-pV*n*Z basis sets at geometries optimized with B3LYP/cc-pVTZ and experimental values. MADs and MSDs are also listed. Zero-point energies and thermal corrections were taken from the B3LYP/cc-pVTZ frequencies.

	cc-pV*n*Z				cc-pVnZ[rc](tr)				cc-pVnZ-B3LYP				Expt.
Molecule	D	T	Q	5	D	T	Q	5	D	T	Q	5	
H_2	1.83	-1.20	-1.30	-1.30	0.50	-1.23	-1.30	-1.29	0.90	-1.14	-1.25	-1.28	0.00
CH	143.38	140.75	140.42	140.29	142.74	140.75	140.42	140.31	143.10	140.79	140.48	140.34	142.40
NH	85.38	81.60	80.94	80.70	84.54	81.58	80.97	80.72	84.70	81.31	80.85	80.69	85.20
OH	12.94	7.87	6.81	6.42	12.09	7.85	6.83	6.41	12.02	7.25	6.55	6.34	8.90
FH	-56.05	-63.17	-64.71	-65.27	-56.85	-63.21	-64.69	-65.29	-57.45	-64.00	-65.04	-65.41	-65.10
CN	110.62	105.83	105.02	105.08	109.49	105.79	105.16	105.21	110.47	106.16	105.32	105.27	104.90
CO	-21.37	-25.73	-26.52	-26.26	-22.21	-25.80	-26.34	-26.16	-20.87	-25.29	-25.99	-26.07	-26.40
N_2	3.79	-2.97	-3.97	-4.02	2.79	-3.02	-3.79	-3.84	4.13	-2.68	-3.70	-3.87	0.00
NO	19.80	17.14	16.44	16.55	20.20	17.03	16.67	16.71	21.62	17.51	16.95	16.73	21.60
O_2	-3.96	-4.43	-4.79	-4.54	-2.37	-4.57	-4.57	-4.47	0.07	-3.83	-3.94	-4.39	0.00
F_2	-2.02	-3.01	-2.57	-2.10	-1.08	-3.10	-2.51	-2.14	1.06	-2.02	-2.03	-2.07	0.00
CH_2 (triplet)	96.25	91.75	91.38	91.30	94.90	91.73	91.41	91.33	95.81	91.78	91.45	91.35	93.50
CH_2 (singlet)	107.16	102.00	101.39	101.19	105.66	101.99	101.42	101.24	106.43	102.12	101.53	101.29	102.80
NH_2	47.15	40.08	38.87	38.40	45.37	40.05	38.94	38.46	46.18	39.68	38.76	38.41	44.50
H_2O	-46.33	-55.67	-57.69	-58.47	-48.06	-55.71	-57.62	-58.45	-47.42	-56.64	-58.11	-58.60	-57.80
CCH (linear)	144.38	136.41	135.67	135.63	142.54	136.39	135.73	135.70	143.89	136.73	135.85	135.73	135.10
HCN	36.18	28.69	27.73	27.81	34.41	28.61	27.88	27.91	35.93	28.85	28.06	27.96	31.50
HCO	11.55	6.37	5.45	5.52	10.75	6.28	5.64	5.64	12.06	6.69	5.95	5.71	10.00
CO_2	-91.32	-97.92	-98.91	-98.39	-92.08	-98.07	-98.62	-98.26	-90.18	-97.13	-98.00	-98.10	-94.10
N_2O	15.87	9.91	8.82	9.14	16.33	9.70	9.17	9.33	19.04	10.81	9.70	9.42	19.60
NO_2	2.22	-1.17	-2.41	-2.12	3.89	-1.41	-1.97	-1.85	6.53	-0.54	-1.36	-1.77	7.90
O_3	37.84	34.66	33.48	33.64	40.72	34.40	33.94	33.81	44.12	35.15	34.78	33.90	34.10
CH_3	38.98	32.29	31.87	31.79	36.64	32.26	31.92	31.85	38.06	32.29	31.97	31.87	35.10
NH_3	-3.44	-13.35	-15.01	-15.71	-6.19	-13.40	-14.88	-15.62	-4.60	-13.87	-15.10	-15.67	-11.00
C_2H_2	64.76	54.54	53.71	53.68	62.34	54.51	53.79	53.73	64.10	54.69	53.91	53.75	54.20
H_2CO	-21.55	-28.55	-29.57	-29.52	-22.80	-28.65	-29.35	-29.38	-21.34	-28.28	-29.05	-29.32	-26.00
	cc-pV*n*Z				cc-pVnZ[rc](tr)				cc-pVnZ-B3LYP				Expt.

Molecule	D	T	Q	5	D	T	Q	5	D	T	Q	5	
NCCN	78.74	68.07	66.56	66.81	76.86	67.87	66.84	66.99	79.69	68.84	67.27	67.11	73.30
BF_3	-264.28	-274.86	-274.42	-273.12	-262.76	-274.99	-274.01	-273.09	-259.95	-271.03	-272.62	-272.93	-271.40
NF_3	-37.02	-41.32	-41.77	-41.15	-33.58	-41.63	-41.36	-41.01	-30.33	-40.40	-40.55	-40.93	-31.60
CH_4	-12.38	-20.06	-20.35	-20.30	-15.44	-20.11	-20.25	-20.22	-13.28	-19.92	-20.09	-20.17	-17.90
C_2H_3	76.87	68.03	67.28	67.18	74.31	67.97	67.39	67.32	76.20	68.27	67.53	67.36	71.60
H_2COH	2.18	-6.67	-8.04	-8.32	0.53	-6.80	-7.83	-8.19	2.53	-6.65	-7.75	-8.20	-4.10
CH_3O	6.64	-0.75	-1.71	-1.77	5.17	-0.86	-1.51	-1.64	6.71	-0.62	-1.32	-1.62	5.00
CH_2CO (ketene)	-7.34	-16.83	-17.94	-17.71	-9.53	-16.97	-17.68	-17.55	-6.77	-16.13	-17.21	-17.44	-11.40
HCOOH	-84.03	-92.84	-94.25	-94.05	-85.13	-93.04	-93.88	-93.84	-82.92	-92.45	-93.43	-93.75	-90.50
CH_2F_2	-102.47	-110.47	-111.10	-110.79	-102.26	-110.60	-110.83	-110.65	-100.44	-109.19	-110.27	-110.58	-107.70
CHF_3	-163.03	-169.28	-169.19	-168.35	-161.39	-169.48	-168.80	-168.16	-158.40	-166.78	-167.80	-168.01	-166.60
CF_4	-222.06	-225.71	-224.64	-223.21	-218.94	-225.98	-224.14	-222.96	-213.96	-221.75	-222.62	-222.73	-223.00
C_2H_4	20.79	10.72	9.99	9.92	17.56	10.65	10.13	10.08	19.95	10.96	10.29	10.13	12.50
H_3COH	-37.96	-48.72	-50.30	-50.57	-40.22	-48.86	-50.06	-50.42	-38.10	-48.78	-49.97	-50.44	-48.20
H_2NNH_2	30.50	17.36	14.91	14.20	27.50	17.18	15.22	14.39	29.81	16.80	15.06	14.36	22.80
CH_3CN	25.92	14.63	13.28	13.37	22.71	14.48	13.54	13.56	25.40	14.97	13.82	13.64	17.70
CH_3CO	2.44	-6.77	-8.13	-8.04	0.28	-6.94	-7.81	-7.83	2.81	-6.29	-7.40	-7.75	-2.50
CH_2CHF	-27.35	-37.06	-37.83	-37.70	-29.03	-37.19	-37.59	-37.50	-26.25	-35.98	-37.11	-37.42	-33.20
HCOCOH (glyoxal)	-45.02	-54.17	-55.89	-55.58	-46.01	-54.43	-55.44	-55.29	-43.46	-53.38	-54.73	-55.13	-50.70
CF_3CN	-114.79	-122.72	-122.78	-121.52	-113.04	-123.06	-122.22	-121.22	-107.76	-119.34	-120.79	-120.96	-118.40
C_2F_4	-160.25	-167.21	-167.19	-166.15	-157.19	-167.56	-166.60	-165.80	-151.84	-162.98	-164.96	-165.58	-157.40
CH_3NH_2	3.68	-8.38	-10.08	-10.48	0.16	-8.52	-9.80	-10.29	2.86	-8.49	-9.76	-10.28	-5.50
CH_3CCH	57.34	43.67	42.54	42.55	53.64	43.58	42.73	42.68	56.71	44.04	42.98	42.74	44.20
CH_2CCH_2 (allene)	54.15	41.41	40.35	40.31	50.69	41.30	40.53	40.48	53.67	41.81	40.79	40.54	45.50
C_3H_4 (cyclopropene)	79.19	67.37	66.24	66.24	76.13	67.21	66.44	66.42	79.02	67.94	66.70	66.48	66.20
CH_3CHO	-31.40	-41.86	-43.20	-43.06	-33.94	-42.05	-42.86	-42.83	-31.15	-41.35	-42.41	-42.72	-39.70
C_2H_4O (oxirane)	-1.92	-13.08	-14.47	-14.55	-3.72	-13.29	-14.17	-14.31	-1.26	-12.52	-13.84	-14.26	-12.60
CH_2CHCN	55.25	41.62	40.04	40.10	51.86	41.44	40.34	40.37	55.05	42.22	40.71	40.47	43.20
	cc-pV*n*Z				cc-pVnZ[rc](tr)				cc-pVnZ-B3LYP				Expt.
Molecule	D	T	Q	5	D	T	Q	5	D	T	Q	5	

CH_3NO_2	15.55	5.76	3.65	3.82	15.58	5.43	4.30	4.21	18.60	6.20	4.93	4.34	-17.80
CH_3ONO	-14.33	-22.54	-23.90	-23.55	-14.36	-22.87	-23.30	-23.20	-10.18	-21.73	-22.56	-23.08	-15.90
CH_3COF	-98.45	-108.50	-109.58	-109.08	-99.96	-108.74	-109.15	-108.81	-96.51	-107.16	-108.38	-108.66	-105.70
C_2H_6	-10.72	-21.62	-22.23	-22.15	-14.88	-21.74	-22.01	-21.97	-11.55	-21.26	-21.74	-21.89	-20.10
C_2H_4NH (aziridine)	41.23	28.47	26.72	26.52	38.13	28.22	27.04	26.79	41.16	28.81	27.29	26.85	30.20
CH_3CH_2O	17.06	6.20	4.95	5.03	14.48	6.02	5.29	5.25	17.27	6.61	5.67	5.33	-3.30
$HCOOCH_3$	-76.92	-88.97	-90.49	-90.16	-78.92	-89.25	-89.94	-89.83	-75.55	-88.24	-89.27	-89.71	-85.00
CH_3COOH	-92.52	-104.81	-106.54	-106.25	-94.93	-105.09	-106.06	-105.94	-91.30	-104.16	-105.44	-105.82	-103.40
CH_3CHCH_2	17.10	3.79	2.74	2.71	12.77	3.65	3.00	2.97	16.44	4.26	3.30	3.06	4.80
C_3H_6 (cyclopropane)	26.44	13.36	12.31	12.34	22.32	13.15	12.56	12.59	25.96	13.98	12.88	12.68	12.70
CH_3CH_2OH	-41.60	-55.64	-57.44	-57.53	-44.98	-55.85	-57.07	-57.29	-41.63	-55.41	-56.76	-57.23	-56.20
CH_3OCH_3	-33.13	-45.74	-47.04	-46.98	-36.04	-45.96	-46.62	-46.72	-32.41	-45.22	-46.19	-46.64	-44.00
CH_3CONH_2	-46.29	-61.58	-63.95	-63.99	-49.83	-61.86	-63.44	-63.64	-46.35	-61.38	-63.08	-63.56	-57.00
C_4H_4O (furan)	4.99	-7.81	-9.49	-9.42	3.22	-8.12	-8.95	-8.97	7.43	-6.67	-8.35	-8.84	-8.30
$(CH_3)_2CH$	31.00	17.79	16.74	16.76	26.38	17.61	17.05	17.03	30.40	18.27	17.37	17.12	21.50
$(CH_3)_2NH$	7.37	-6.85	-8.62	-8.77	3.13	-7.09	-8.19	-8.47	7.01	-6.62	-7.93	-8.41	-4.40
$CH_3CH_2NH_2$	1.08	-13.83	-15.73	-15.91	-3.51	-14.05	-15.32	-15.62	0.57	-13.63	-15.08	-15.56	-11.30
$CH_2CHCHCH_2$ (trans-2-butene)	41.05	25.51	24.12	24.03	36.63	25.36	24.44	24.38	40.71	26.18	24.78	24.48	26.30
C_4H_6 (methyl-cyclopropane)	60.83	45.55	44.12	44.12	56.60	45.31	44.43	44.41	60.67	46.26	44.80	44.50	47.90
C_4H_6 (bicyclo[1.1.0]butane)	70.57	56.86	55.35	55.38	66.99	56.57	55.69	55.70	70.94	57.80	56.09	55.80	51.90
C_4H_6 (cyclobutene)	54.36	41.04	39.62	39.65	50.69	40.78	40.02	39.99	54.65	41.73	40.39	40.09	37.40
C_4H_6 (dimethylacetylene)	50.91	33.90	32.52	32.56	45.92	33.76	32.81	32.77	50.38	34.54	33.20	32.87	34.80
CH_3COCH_3	-40.74	-54.63	-56.29	-56.08	-44.59	-54.89	-55.82	-55.75	-40.38	-53.94	-55.24	-55.60	-51.90
C_4H_5N (pyrrole)	39.85	24.71	22.34	22.06	36.83	24.41	22.87	22.56	40.93	25.38	23.20	22.65	25.90
C_3H_8	-6.96	-21.10	-22.07	-21.96	-12.18	-21.29	-21.72	-21.68	-7.63	-20.54	-21.34	-21.58	-25.00
C_5H_5N (pyridine)	46.94	30.92	28.43	28.34	43.87	30.57	29.06	28.95	48.38	31.91	29.56	29.09	33.60
C_4H_8 (isobutylene)	12.53	-4.14	-5.55	-5.52	7.08	-4.35	-5.14	-5.15	12.09	-3.45	-4.72	-5.03	-4.00
$C_2H_5OCH_3$	-37.11	-53.11	-54.65	-54.46	-41.20	-53.39	-54.10	-54.10	-36.34	-52.32	-53.50	-53.97	-51.70
	cc-pV*n*Z				cc-pVnZ[rc](tr)				cc-pVnZ-B3LYP				Expt.
Molecule	D	T	Q	5	D	T	Q	5	D	T	Q	5	

C_6H_6 (benzene)	38.16	20.94	18.87	18.70	34.23	20.69	19.38	19.28	39.13	22.14	19.86	19.42	19.70
$(CH_3)_3N$	9.67	-7.01	-8.94	-8.91	4.63	-7.35	-8.34	-8.52	9.81	-6.56	-7.93	-8.41	-5.70
C_5H_8 (spiropentane)	65.16	47.18	45.39	45.47	60.07	46.83	45.85	45.89	65.29	48.26	46.37	46.01	44.30
C_4H_{10} (butane)	-11.27	-28.65	-29.98	-29.80	-17.55	-28.91	-29.49	-29.43	-11.82	-27.90	-29.01	-29.31	-30.00
MAD	8.82	3.16	3.82	3.75	6.57	3.25	3.60	3.60	9.11	2.81	3.34	3.56	
MSD	-8.23	1.73	2.87	2.79	-6.22	1.90	2.57	2.58	-9.05	1.12	2.19	2.51	

Table 5.11. B3LYP CBS-extrapolated enthalpies of formation (kcal/mol) computed with the cc-pV*n*Z, cc-pV*n*Z[rc](tr) , and cc-pV*n*Z-B3LYP basis sets at geometries optimized with B3LYP/cc-pVTZ. MADs and MSDs from experiment are also listed. Zero-point energies and thermal corrections were taken from the B3LYP/cc-pVTZ frequencies.

Molecule	cc-pV*n*Z			cc-pV*n*Z[rc](tr)			cc-pV*n*Z-B3LYP			
	P	S3	S4	P	S3	S4	P	S3	S4	Expt.
H_2	1.32	1.46	1.35	-1.31	-1.38	-1.32	-1.30	-1.35	-1.28	0.00
CH	140.22	140.30	140.40	140.24	140.34	140.43	140.29	140.37	140.46	142.40
NH	80.56	80.80	80.95	80.60	80.86	80.99	80.60	80.71	80.85	85.20
OH	6.20	6.64	6.86	6.21	6.69	6.88	6.18	6.37	6.56	8.90
FH	-65.59	-64.94	-64.63	-65.59	-64.90	-64.62	-65.63	-65.30	-65.03	-65.10
CN	104.84	104.97	105.16	105.02	105.12	105.27	105.04	105.27	105.45	104.90
CO	-26.54	-26.48	-26.30	-26.35	-26.34	-26.21	-26.25	-26.10	-25.92	-26.40
N_2	-4.29	-4.13	-3.86	-4.05	-3.95	-3.73	-4.12	-3.90	-3.63	0.00
NO	16.33	16.51	16.62	16.60	16.59	16.71	16.61	16.77	16.93	21.60
O_2	-4.70	-4.63	-4.61	-4.49	-4.66	-4.59	-4.32	-4.31	-4.17	0.00
F_2	-2.07	-2.57	-2.57	-2.04	-2.65	-2.61	-2.06	-2.22	-2.12	0.00
CH_2 (triplet)	91.22	91.18	91.35	91.26	91.28	91.40	91.29	91.26	91.41	93.50
CH_2 (singlet)	101.06	101.17	101.37	101.12	101.28	101.43	101.17	101.34	101.51	102.80
NH_2	38.16	38.59	38.89	38.24	38.73	38.96	38.22	38.48	38.74	44.50
H_2O	-58.89	-58.01	-57.60	-58.83	-57.89	-57.54	-58.91	-58.45	-58.08	-57.80
CCH (linear)	135.44	135.38	135.67	135.52	135.52	135.76	135.51	135.61	135.89	135.10
HCN	27.52	27.57	27.85	27.71	27.74	27.96	27.76	27.81	28.08	31.50
HCO	5.25	5.41	5.62	5.46	5.54	5.72	5.55	5.74	5.95	10.00
CO_2	-98.78	-98.85	-98.60	-98.49	-98.70	-98.48	-98.33	-98.22	-97.95	-94.10
N_2O	8.76	8.87	9.10	9.16	8.97	9.21	9.17	9.40	9.72	19.60
NO_2	-2.54	-2.18	-2.02	-2.02	-2.09	-1.90	-1.91	-1.72	-1.44	7.90
O_3	33.27	33.66	33.81	33.72	33.64	33.87	33.99	34.01	34.35	34.10
CH_3	31.69	31.55	31.79	31.77	31.72	31.88	31.81	31.67	31.88	35.10
NH_3	-16.03	-15.42	-15.01	-15.89	-15.20	-14.88	-15.90	-15.54	-15.17	-11.00
C_2H_2	53.46	53.31	53.68	53.54	53.49	53.78	53.57	53.49	53.84	54.20
H_2CO	-29.82	-29.70	-29.43	-29.57	-29.53	-29.31	-29.48	-29.36	-29.09	-26.00
NCCN	66.34	66.42	66.83	66.67	66.63	66.97	66.70	66.98	67.40	73.30

Molecule	cc-pV*n*Z			cc-pV*n*Z[rc](tr)			cc-pV*n*Z-B3LYP			
	P	S3	S4	P	S3	S4	P	S3	S4	Expt.
BF_3	-273.24	-274.69	-274.38	-272.97	-274.66	-274.30	-273.31	-272.98	-272.54	-271.40
NF_3	-41.40	-41.68	-41.53	-40.99	-41.78	-41.53	-40.88	-41.25	-40.90	-31.60
CH_4	-20.38	-20.72	-20.45	-20.25	-20.48	-20.32	-20.19	-20.47	-20.24	-17.90
C_2H_3	67.00	66.91	67.24	67.17	67.14	67.38	67.19	67.19	67.48	71.60
H_2COH	-8.65	-8.31	-7.95	-8.41	-8.13	-7.84	-8.41	-8.18	-7.82	-4.10
CH_3O	-2.03	-1.92	-1.64	-1.79	-1.75	-1.52	-1.76	-1.69	-1.41	5.00
CH_2CO (ketene)	-18.06	-18.13	-17.77	-17.77	-17.89	-17.62	-17.70	-17.57	-17.21	-11.40
HCOOH	-94.49	-94.33	-93.98	-94.08	-94.11	-93.82	-93.96	-93.86	-93.50	-90.50
CH_2F_2	-111.03	-111.30	-111.01	-110.74	-111.20	-110.92	-110.82	-110.62	-110.28	-107.70
CHF_3	-168.48	-169.27	-169.09	-168.07	-169.23	-168.99	-168.25	-168.11	-167.79	-166.60
CF_4	-223.18	-224.61	-224.56	-222.64	-224.61	-224.47	-222.95	-222.90	-222.60	-223.00
C_2H_4	9.74	9.56	9.92	9.95	9.84	10.09	9.98	9.87	10.20	12.50
H_3COH	-50.96	-50.63	-50.20	-50.69	-50.39	-50.05	-50.67	-50.47	-50.06	-48.20
H_2NNH_2	13.65	14.51	15.06	14.00	14.81	15.25	14.01	14.48	15.00	22.80
CH_3CN	12.98	13.00	13.42	13.29	13.30	13.61	13.36	13.43	13.83	17.70
CH_3CO	-8.44	-8.29	-7.93	-8.06	-8.02	-7.74	-7.99	-7.78	-7.43	-2.50
CH_2CHF	-37.93	-38.16	-37.81	-37.62	-37.94	-37.65	-37.67	-37.51	-37.13	-33.20
HCOCOH (glyoxal)	-56.13	-55.87	-55.50	-55.60	-55.62	-55.30	-55.43	-55.12	-54.72	-50.70
CF_3CN	-121.78	-122.77	-122.53	-121.16	-122.67	-122.39	-121.33	-121.16	-120.72	-118.40
C_2F_4	-166.34	-167.23	-167.01	-165.66	-167.18	-166.88	-166.01	-165.33	-164.87	-157.40
CH_3NH_2	-10.88	-10.50	-10.02	-10.55	-10.16	-9.81	-10.53	-10.30	-9.86	-5.50
CH_3CCH	42.24	42.03	42.53	42.46	42.34	42.71	42.50	42.41	42.88	44.20
CH_2CCH_2 (allene)	40.04	39.86	40.32	40.28	40.16	40.50	40.32	40.26	40.70	45.50
C_3H_4 (cyclopropene)	65.93	65.83	66.27	66.22	66.10	66.43	66.18	66.28	66.71	66.20
CH_3CHO	-43.47	-43.42	-43.02	-43.06	-43.12	-42.82	-42.95	-42.86	-42.47	-39.70
C_2H_4O (oxirane)	-14.93	-14.80	-14.37	-14.52	-14.56	-14.20	-14.54	-14.32	-13.88	-12.60
CH_2CHCN	39.65	39.67	40.18	40.06	40.02	40.41	40.10	40.25	40.75	43.20
CH_3NO_2	3.18	3.69	4.09	3.92	3.96	4.34	4.11	4.30	4.78	-17.80
	cc-pV*n*Z			cc-pV*n*Z[rc](tr)			cc-pV*n*Z-B3LYP			

Molecule	P	S3	S4	P	S3	S4	P	S3	S4	Expt.
CH_3ONO	-24.00	-23.90	-23.58	-23.33	-23.66	-23.36	-23.20	-23.22	-22.79	-15.90
CH_3COF	-109.48	-109.71	-109.34	-108.98	-109.44	-109.13	-108.94	-108.80	-108.39	-105.70
C_2H_6	-22.33	-22.69	-22.30	-22.04	-22.33	-22.09	-21.98	-22.25	-21.90	-20.10
C_2H_4NH (aziridine)	26.07	26.35	26.85	26.51	26.66	27.05	26.52	26.79	27.27	30.20
CH_3CH_2O	4.66	4.66	5.07	5.06	4.96	5.28	5.14	5.15	5.55	-3.30
$HCOOCH_3$	-90.66	-90.69	-90.23	-90.04	-90.34	-89.97	-89.90	-89.92	-89.45	-85.00
CH_3COOH	-106.80	-106.71	-106.24	-106.23	-106.37	-105.99	-106.09	-106.01	-105.52	-103.40
CH_3CHCH_2	2.43	2.21	2.70	2.81	2.62	2.95	2.85	2.73	3.18	4.80
C_3H_6 (cyclopropane)	12.05	11.81	12.29	12.43	12.18	12.51	12.42	12.38	12.83	12.70
CH_3CH_2OH	-58.02	-57.84	-57.30	-57.59	-57.48	-57.07	-57.51	-57.40	-56.88	-56.20
CH_3OCH_3	-47.35	-47.43	-46.96	-46.87	-47.07	-46.71	-46.81	-46.87	-46.39	-44.00
CH_3CONH_2	-64.65	-64.25	-63.65	-64.04	-63.82	-63.35	-63.93	-63.71	-63.13	-57.00
C_4H_4O (furan)	-9.90	-9.79	-9.30	-9.19	-9.41	-9.00	-9.20	-8.93	-8.38	-8.30
$(CH_3)_2CH$	16.47	16.24	16.72	16.89	16.67	16.98	16.93	16.79	17.24	21.50
$(CH_3)_2NH$	-9.23	-9.06	-8.51	-8.72	-8.61	-8.22	-8.67	-8.58	-8.06	-4.40
$CH_3CH_2NH_2$	-16.40	-16.19	-15.61	-15.91	-15.73	-15.32	-15.86	-15.72	-15.18	-11.30
$CH_2CHCHCH_2$ (trans-2-butene)	23.67	23.52	24.10	24.14	23.99	24.40	24.16	24.17	24.71	26.30
C_4H_6 (methyl-cyclopropane)	43.73	43.58	44.15	44.18	43.98	44.40	44.16	44.21	44.76	47.90
C_4H_6 (bicyclo[1.1.0]butane)	54.95	54.94	55.46	55.46	55.30	55.69	55.38	55.65	56.16	51.90
C_4H_6 (cyclobutene)	39.26	39.21	39.71	39.79	39.61	39.98	39.78	39.86	40.35	37.40
C_4H_6 (dimethylacetylene)	32.18	31.88	32.50	32.52	32.32	32.76	32.57	32.48	33.08	34.80
CH_3COCH_3	-56.58	-56.60	-56.08	-56.02	-56.17	-55.79	-55.89	-55.84	-55.33	-51.90
C_4H_5N (pyrrole)	21.45	21.95	22.56	22.19	22.42	22.90	22.15	22.64	23.26	25.90
C_3H_8	-22.24	-22.62	-22.11	-21.80	-22.13	-21.81	-21.74	-21.99	-21.52	-25.00
C_5H_5N (pyridine)	27.66	28.10	28.73	28.55	28.62	29.13	28.52	29.02	29.68	33.60
C_4H_8 (isobutylene)	-5.91	-6.16	-5.55	-5.36	-5.62	-5.20	-5.31	-5.43	-4.85	-4.00
$C_2H_5OCH_3$	-54.92	-55.13	-54.53	-54.28	-54.64	-54.21	-54.19	-54.32	-53.73	-51.70
C_6H_6 (benzene)	18.16	18.32	18.98	18.94	18.88	19.39	18.87	19.28	19.95	19.70
		cc-pV*n*Z			cc-pV*n*Z[rc](tr)			cc-pV*n*Z-B3LYP		
Molecule	P	S3	S4	P	S3	S4	P	S3	S4	Expt.

$(CH_3)_3N$	-9.45	-9.42	-8.78	-8.75	-8.86	-8.42	-8.68	-8.73	-8.11	-5.70
C_5H_8 (spiropentane)	44.97	44.82	45.49	45.62	45.33	45.81	45.56	45.72	46.37	44.30
C_4H_{10} (butane)	-30.19	-30.60	-29.97	-29.59	-29.99	-29.59	-29.54	-29.79	-29.20	-30.00
MAD	4.00	4.01	3.73	3.74	3.82	3.62	3.71	3.63	3.37	
MSD	3.10	3.10	2.73	2.76	2.88	2.58	2.74	2.64	2.25	

Table 5.12. BLYP enthalpies of formation (kcal/mol) computed with the cc-pV*n*Z basis sets at geometries optimized with B3LYP/cc-pVTZ and experimental values. MADs and MSDs are also listed. Zero-point energies and thermal corrections were taken from the B3LYP/cc-pVTZ frequencies.

	cc-pV*n*Z				cc-pV*n*Z[rc](tr)				cc-pV*n*Z-BLYP				
Molecule	D	T	Q	5	D	T	Q	5	D	T	Q	5	Expt.
H_2	3.00	-0.44	-0.51	-0.47	1.20	-0.47	-0.51	-0.47	1.88	-0.31	-0.42	-0.45	0.00
CH	143.56	140.73	140.40	140.33	142.72	140.74	140.42	140.31	143.32	140.80	140.50	140.35	142.40
NH	84.41	80.39	79.67	79.41	83.38	80.38	79.72	79.44	83.59	80.03	79.58	79.40	85.20
OH	12.11	6.71	5.52	5.05	11.02	6.67	5.54	5.05	10.83	5.88	5.19	4.95	8.90
FH	-57.13	-64.60	-66.35	-66.95	-58.18	-64.65	-66.32	-67.04	-59.04	-65.76	-66.80	-67.22	-65.10
CN	98.40	93.90	93.23	93.49	97.01	93.85	93.39	93.56	98.75	94.49	93.69	93.66	104.90
CO	-28.38	-32.22	-32.86	-32.36	-29.43	-32.31	-32.66	-32.30	-27.09	-31.44	-32.11	-32.17	-26.40
N_2	-6.85	-13.31	-14.19	-14.12	-8.08	-13.35	-14.00	-13.94	-5.68	-12.73	-13.79	-13.96	0.00
NO	7.61	5.77	5.19	5.44	8.12	5.63	5.43	5.60	10.49	6.45	5.86	5.63	21.60
O_2	-18.28	-17.24	-17.39	-16.97	-16.19	-17.42	-17.19	-16.90	-12.55	-16.16	-16.33	-16.77	0.00
F_2	-15.48	-14.95	-14.22	-13.43	-14.11	-15.07	-14.17	-13.60	-10.66	-13.52	-13.41	-13.47	0.00
CH_2 (triplet)	98.92	94.05	93.69	93.71	97.12	94.05	93.76	93.70	98.44	94.14	93.84	93.72	93.50
CH_2 (singlet)	108.66	103.00	102.37	102.25	106.68	103.00	102.44	102.25	107.79	103.15	102.59	102.31	102.80
NH_2	46.27	38.75	37.44	36.95	44.04	38.72	37.54	37.00	44.99	38.20	37.35	36.93	44.50
H_2O	-47.05	-56.88	-59.11	-60.01	-49.30	-56.95	-59.03	-59.98	-48.72	-58.21	-59.63	-60.16	-57.80
CCH (linear)	140.95	132.88	132.22	132.43	138.63	132.88	132.35	132.40	140.76	133.39	132.57	132.45	135.10
HCN	29.38	21.95	21.06	21.38	27.19	21.86	21.28	21.44	29.64	22.37	21.61	21.53	31.50
HCO	4.20	-0.49	-1.28	-0.95	3.18	-0.60	-1.04	-0.87	5.46	0.16	-0.52	-0.76	10.00
CO_2	-104.88	-110.05	-110.74	-109.77	-105.79	-110.26	-110.38	-109.68	-102.36	-108.63	-109.39	-109.45	-94.10
N_2O	-6.51	-10.69	-11.51	-10.85	-5.90	-10.96	-11.12	-10.66	-1.39	-9.15	-10.23	-10.49	19.60
NO_2	-21.79	-23.11	-24.14	-23.55	-19.69	-23.44	-23.69	-23.27	-15.40	-21.90	-22.74	-23.15	7.90
O_3	6.05	5.93	5.05	5.47	9.89	5.58	5.48	5.63	15.09	7.08	6.63	5.78	34.10
CH_3	42.57	35.24	34.86	34.92	39.47	35.23	34.96	34.94	41.53	35.37	35.09	34.98	35.10
NH_3	-3.22	-13.74	-15.53	-16.30	-6.70	-13.80	-15.36	-16.20	-4.85	-14.44	-15.60	-16.25	-11.00
C_2H_2	63.30	52.83	52.08	52.33	60.22	52.84	52.25	52.27	63.01	53.20	52.49	52.33	54.20
H_2CO	-26.11	-32.78	-33.67	-33.34	-27.73	-32.91	-33.39	-33.23	-25.22	-32.14	-32.85	-33.12	-26.00
NCCN	61.23	51.17	49.87	50.63	58.89	50.98	50.28	50.70	63.55	52.57	51.03	50.90	73.30

Molecule	cc-pV*n*Z				cc-pV*n*Z[rc](tr)				cc-pV*n*Z-BLYP				
	D	T	Q	5	D	T	Q	5	D	T	Q	5	Expt.
BF_3	-273.53	-279.98	-278.81	-276.59	-271.29	-280.19	-278.27	-276.72	-265.20	-275.76	-276.14	-276.40	-271.40
NF_3	-62.86	-63.06	-62.95	-61.62	-58.34	-63.47	-62.53	-61.70	-52.70	-61.15	-61.12	-61.51	-31.60
CH_4	-7.59	-16.10	-16.30	-16.04	-11.68	-16.13	-16.13	-15.99	-8.65	-15.72	-15.83	-15.93	-17.90
C_2H_3	77.80	68.58	67.90	68.08	74.46	68.55	68.10	68.12	77.35	69.03	68.37	68.19	71.60
H_2COH	0.68	-7.94	-9.24	-9.32	-1.46	-8.08	-8.98	-9.22	1.50	-7.74	-8.74	-9.20	-4.10
CH_3O	5.66	-1.85	-2.80	-2.64	3.69	-1.97	-2.53	-2.54	6.02	-1.48	-2.17	-2.50	5.00
CH_2CO (ketene)	-14.28	-23.22	-24.10	-23.42	-17.08	-23.37	-23.75	-23.34	-12.68	-22.01	-22.97	-23.18	-11.40
HCOOH	-92.81	-100.47	-101.69	-101.09	-94.16	-100.73	-101.24	-100.91	-90.50	-99.57	-100.44	-100.75	-90.50
CH_2F_2	-107.74	-114.07	-114.40	-113.51	-107.41	-114.26	-114.06	-113.54	-103.99	-112.13	-113.06	-113.39	-107.70
CHF_3	-173.13	-176.21	-175.55	-173.86	-170.90	-176.50	-175.10	-173.91	-165.48	-172.61	-173.40	-173.61	-166.60
CF_4	-236.53	-235.39	-233.43	-230.82	-232.37	-235.80	-232.86	-230.89	-223.83	-229.81	-230.35	-230.44	-223.00
C_2H_4	23.82	13.28	12.67	12.91	19.62	13.24	12.90	12.99	23.25	13.80	13.23	13.07	12.50
H_3COH	-36.92	-47.82	-49.39	-49.43	-39.89	-47.97	-49.07	-49.31	-36.80	-47.69	-48.81	-49.30	-48.20
H_2NNH_2	27.94	14.49	11.89	11.23	24.17	14.29	12.28	11.43	27.17	13.85	12.20	11.41	22.80
CH_3CN	22.42	10.98	9.76	10.26	18.27	10.84	10.13	10.36	22.45	11.75	10.67	10.50	17.70
CH_3CO	-1.83	-10.69	-11.90	-11.39	-4.71	-10.89	-11.48	-11.26	-0.71	-9.76	-10.78	-11.13	-2.50
CH_2CHF	-30.08	-38.87	-39.35	-38.68	-32.21	-39.01	-39.02	-38.63	-27.63	-37.24	-38.17	-38.48	-33.20
HCOCOH (glyoxal)	-56.41	-64.13	-65.59	-64.71	-57.68	-64.45	-65.03	-64.49	-53.24	-62.63	-63.85	-64.23	-50.70
CF_3CN	-134.95	-138.61	-137.92	-135.44	-132.54	-139.06	-137.23	-135.45	-123.56	-133.62	-134.82	-134.98	-118.40
C_2F_4	-179.84	-181.49	-180.59	-178.25	-175.77	-181.98	-179.91	-178.28	-166.46	-175.64	-177.22	-177.84	-157.40
CH_3NH_2	6.48	-6.09	-7.81	-8.00	1.93	-6.24	-7.43	-7.83	5.69	-6.05	-7.22	-7.80	-5.50
CH_3CCH	58.97	44.93	43.94	44.41	54.18	44.89	44.28	44.40	58.86	45.71	44.75	44.51	44.20
CH_2CCH_2 (allene)	54.58	41.62	40.71	41.14	50.14	41.56	41.03	41.17	54.76	42.42	41.53	41.28	45.50
C_3H_4 (cyclopropene)	81.35	69.34	68.33	68.81	77.31	69.20	68.68	68.86	81.81	70.30	69.19	68.96	66.20
CH_3CHO	-32.96	-43.16	-44.32	-43.71	-36.33	-43.36	-43.86	-43.55	-31.92	-42.12	-43.06	-43.37	-39.70
C_2H_4O (oxirane)	-2.82	-13.49	-14.74	-14.40	-5.25	-13.72	-14.33	-14.23	-1.30	-12.50	-13.71	-14.13	-12.60
CH_2CHCN	49.31	35.84	34.44	35.04	45.01	35.69	34.89	35.17	50.12	36.97	35.57	35.35	43.20
CH_3NO_2	-1.71	-9.54	-11.41	-10.73	-1.79	-9.95	-10.67	-10.37	3.22	-8.39	-9.59	-10.14	-17.80
	cc-pV*n*Z				cc-pV*n*Z[rc](tr)				cc-pV*n*Z-BLYP				

Molecule	D	T	Q	5	D	T	Q	5	D	T	Q	5	Expt.
CH_3ONO	-32.82	-38.96	-40.00	-39.13	-32.86	-39.37	-39.31	-38.82	-26.34	-37.32	-38.09	-38.59	-15.90
CH_3COF	-105.29	-113.79	-114.51	-113.30	-107.28	-114.09	-113.96	-113.18	-101.56	-111.62	-112.65	-112.92	-105.70
C_2H_6	-2.80	-14.57	-15.06	-14.59	-8.38	-14.65	-14.70	-14.48	-3.57	-13.80	-14.20	-14.36	-20.10
C_2H_4NH (aziridine)	43.11	30.25	28.56	28.75	39.04	30.00	29.01	28.94	43.58	30.93	29.53	29.05	30.20
CH_3CH_2O	19.23	8.22	7.01	7.52	15.76	8.03	7.49	7.68	19.96	9.07	8.18	7.82	-3.30
$HCOOCH_3$	-83.44	-94.15	-95.38	-94.43	-85.96	-94.49	-94.69	-94.17	-80.40	-92.64	-93.53	-93.94	-85.00
CH_3COOH	-97.65	-108.92	-110.44	-109.55	-100.80	-109.27	-109.82	-109.31	-95.12	-107.59	-108.72	-109.09	-103.40
CH_3CHCH_2	23.19	9.37	8.48	8.94	17.52	9.28	8.90	9.09	23.01	10.30	9.47	9.23	4.80
C_3H_6 (cyclopropane)	34.41	20.76	19.86	20.39	28.89	20.59	20.26	20.52	34.35	21.83	20.87	20.66	12.70
CH_3CH_2OH	-37.46	-51.66	-53.41	-53.05	-41.93	-51.88	-52.89	-52.88	-36.99	-51.01	-52.26	-52.76	-56.20
CH_3OCH_3	-30.18	-42.51	-43.61	-43.06	-33.99	-42.74	-43.06	-42.86	-28.50	-41.40	-42.26	-42.72	-44.00
CH_3CONH_2	-49.52	-64.19	-66.41	-65.91	-54.04	-64.51	-65.75	-65.62	-48.58	-63.46	-64.98	-65.46	-57.00
C_4H_4O (furan)	1.76	-9.56	-10.95	-10.15	-0.46	-9.88	-10.24	-9.87	6.26	-7.68	-9.15	-9.62	-8.30
$(CH_3)_2CH$	39.99	26.02	25.09	25.62	33.84	25.88	25.58	25.77	39.68	26.97	26.19	25.92	21.50
$(CH_3)_2NH$	12.74	-1.79	-3.47	-3.16	7.24	-2.03	-2.86	-2.92	12.94	-1.10	-2.29	-2.81	-4.40
$CH_3CH_2NH_2$	6.86	-8.53	-10.38	-10.11	0.88	-8.74	-9.80	-9.89	6.69	-7.94	-9.25	-9.77	-11.30
$CH_2CHCHCH_2$ (trans-2-butene)	44.78	29.16	27.99	28.51	39.14	29.08	28.48	28.69	45.45	30.37	29.16	28.86	26.30
C_4H_6 (methyl-cyclopropane)	66.23	50.70	49.44	50.07	60.67	50.51	49.95	50.20	66.88	51.97	50.67	50.35	47.90
C_4H_6 (bicyclo[1.1.0]butane)	77.72	63.95	62.60	63.27	72.95	63.69	63.14	63.43	78.99	65.44	63.89	63.59	51.90
C_4H_6 (cyclobutene)	60.37	47.00	45.73	46.41	55.49	46.77	46.33	46.58	61.55	48.25	47.05	46.76	37.40
C_4H_6 (dimethylacetylene)	55.67	38.15	36.99	37.68	49.15	38.08	37.48	37.71	55.83	39.43	38.21	37.88	34.80
CH_3COCH_3	-38.99	-52.65	-54.10	-53.23	-44.10	-52.94	-53.45	-53.02	-37.66	-51.27	-52.42	-52.78	-51.90
C_4H_5N (pyrrole)	39.65	25.40	23.23	23.63	35.87	25.12	23.97	23.96	42.35	26.64	24.70	24.14	25.90
C_3H_8	4.09	-10.89	-11.71	-11.03	-2.87	-11.03	-11.16	-10.87	3.76	-9.75	-10.45	-10.70	-25.00
C_5H_5N (pyridine)	45.27	30.29	28.01	28.75	41.44	29.98	28.88	29.14	48.74	32.05	29.89	29.40	33.60
C_4H_8 (isobutylene)	21.83	4.66	3.45	4.15	14.70	4.50	4.07	4.36	22.14	6.00	4.89	4.56	-4.00
$C_2H_5OCH_3$	-30.99	-46.76	-48.06	-47.18	-36.36	-47.04	-47.31	-46.92	-29.04	-45.18	-46.21	-46.70	-51.70
C_6H_6 (benzene)	42.43	25.87	24.06	24.75	37.44	25.70	24.82	25.08	45.20	27.82	25.79	25.33	19.70
		cc-pV*n*Z				cc-pV*n*Z[rc](tr)				cc-pV*n*Z-BLYP			
Molecule	D	T	Q	5	D	T	Q	5	D	T	Q	5	Expt.

$(CH_3)_3N$	17.76	1.02	-0.74	-0.06	11.26	0.69	0.09	0.23	18.94	2.17	0.94	0.41	-5.70
C_5H_8 (spiropentane)	75.78	57.51	55.90	56.79	68.96	57.19	56.62	57.00	76.88	59.28	57.57	57.20	44.30
C_4H_{10} (butane)	2.94	-15.26	-16.39	-15.48	-5.38	-15.46	-15.65	-15.26	3.01	-13.76	-14.73	-15.05	-30.00
MAD	12.23	7.92	8.11	7.93	9.51	7.99	8.03	7.92	11.45	7.55	7.77	7.88	
MSD	-5.28	4.15	5.12	4.61	-2.68	4.33	4.72	4.49	-7.11	3.08	4.03	4.35	

Table 5.13. BLYP CBS-extrapolated enthalpies of formation (kcal/mol) computed with the cc-pV*n*Z, cc-pV*n*Z[rc](tr) , and cc-pV*n*Z-B3LYP basis sets at geometries optimized with B3LYP/cc-pVTZ. MADs and MSDs from experiment are also listed. Zero-point energies and thermal corrections were taken from the B3LYP/cc-pVTZ frequencies.

Molecule	cc-pV*n*Z			cc-pV*n*Z[rc](tr)			cc-pV*n*Z-BLYP			
	P	S3	S4	P	S3	S4	P	S3	S4	Expt.
H_2	-0.50	-0.68	-0.57	-0.49	-0.58	-0.53	-0.47	-0.53	-0.45	0.00
CH	140.25	140.29	140.40	140.24	140.35	140.43	140.30	140.37	140.47	142.40
NH	79.26	79.53	79.69	79.31	79.61	79.74	79.31	79.42	79.56	85.20
OH	4.80	5.34	5.57	4.83	5.40	5.60	4.81	4.99	5.19	8.90
FH	-67.33	-66.56	-66.23	-67.37	-66.53	-66.24	-67.43	-67.09	-66.81	-65.10
CN	93.24	93.23	93.40	93.40	93.39	93.51	93.44	93.63	93.81	104.90
CO	-32.64	-32.74	-32.59	-32.47	-32.61	-32.50	-32.35	-32.22	-32.04	-26.40
N_2	-14.38	-14.31	-14.07	-14.13	-14.12	-13.92	-14.22	-14.00	-13.71	0.00
NO	5.22	5.33	5.41	5.51	5.39	5.48	5.52	5.69	5.85	21.60
O_2	-17.10	-17.13	-17.17	-16.89	-17.22	-17.19	-16.73	-16.67	-16.53	0.00
F_2	-13.38	-14.09	-14.15	-13.45	-14.26	-14.27	-13.42	-13.63	-13.54	0.00
CH_2 (triplet)	93.61	93.50	93.68	93.63	93.63	93.75	93.67	93.62	93.78	93.50
CH_2 (singlet)	102.10	102.15	102.37	102.13	102.30	102.45	102.21	102.36	102.54	102.80
NH_2	36.68	37.15	37.47	36.78	37.33	37.57	36.78	37.01	37.28	44.50
H_2O	-60.47	-59.44	-59.01	-60.38	-59.29	-58.93	-60.45	-60.02	-59.64	-57.80
CCH (linear)	132.22	131.99	132.28	132.24	132.16	132.38	132.25	132.31	132.59	135.10
HCN	21.07	20.97	21.25	21.25	21.17	21.37	21.34	21.35	21.62	31.50
HCO	-1.24	-1.23	-1.05	-1.03	-1.09	-0.95	-0.90	-0.75	-0.54	10.00
CO_2	-110.16	-110.50	-110.33	-109.85	-110.36	-110.22	-109.65	-109.59	-109.35	-94.10
N_2O	-11.21	-11.30	-11.14	-10.79	-11.21	-11.04	-10.75	-10.51	-10.20	19.60
NO_2	-23.97	-23.73	-23.66	-23.43	-23.69	-23.57	-23.30	-23.06	-22.80	7.90
O_3	5.13	5.43	5.46	5.58	5.31	5.45	5.84	5.95	6.26	34.10
CH_3	34.81	34.55	34.80	34.87	34.77	34.92	34.93	34.75	34.97	35.10
NH_3	-16.65	-15.97	-15.54	-16.47	-15.68	-15.37	-16.44	-16.11	-15.73	-11.00
C_2H_2	52.08	51.75	52.12	52.11	51.97	52.24	52.17	52.03	52.39	54.20
H_2CO	-33.65	-33.71	-33.46	-33.40	-33.51	-33.33	-33.26	-33.17	-32.91	-26.00
NCCN	50.11	49.90	50.27	50.43	50.15	50.43	50.49	50.73	51.16	73.30

Molecule	cc-pV*n*Z			cc-pV*n*Z[rc](tr)			cc-pV*n*Z-BLYP			
	P	S3	S4	P	S3	S4	P	S3	S4	Expt.
BF_3	-276.68	-278.68	-278.55	-276.45	-278.74	-278.54	-276.43	-276.77	-276.39	-271.40
NF_3	-61.86	-62.50	-62.53	-61.59	-62.78	-62.66	-61.41	-61.78	-61.49	-31.60
CH_4	-16.14	-16.66	-16.37	-16.01	-16.34	-16.20	-15.93	-16.26	-16.02	-17.90
C_2H_3	67.86	67.59	67.93	68.00	67.87	68.09	68.05	67.98	68.29	71.60
H_2COH	-9.67	-9.44	-9.10	-9.42	-9.22	-8.96	-9.38	-9.20	-8.84	-4.10
CH_3O	-2.94	-2.94	-2.66	-2.69	-2.73	-2.51	-2.62	-2.56	-2.27	5.00
CH_2CO (ketene)	-23.80	-24.14	-23.83	-23.53	-23.87	-23.66	-23.40	-23.35	-23.00	-11.40
HCOOH	-101.55	-101.60	-101.31	-101.11	-101.37	-101.14	-100.93	-100.87	-100.53	-90.50
CH_2F_2	-113.78	-114.36	-114.16	-113.58	-114.33	-114.12	-113.58	-113.42	-113.11	-107.70
CHF_3	-174.00	-175.28	-175.24	-173.73	-175.36	-175.25	-173.79	-173.70	-173.42	-166.60
CF_4	-230.77	-232.91	-233.08	-230.42	-233.11	-233.15	-230.57	-230.60	-230.37	-223.00
C_2H_4	12.70	12.29	12.66	12.88	12.64	12.86	12.96	12.76	13.10	12.50
H_3COH	-49.86	-49.64	-49.21	-49.57	-49.35	-49.03	-49.50	-49.34	-48.92	-48.20
H_2NNH_2	10.62	11.53	12.09	11.04	11.91	12.33	11.11	11.55	12.07	22.80
CH_3CN	9.82	9.58	10.00	10.12	9.96	10.23	10.24	10.25	10.66	17.70
CH_3CO	-11.84	-11.92	-11.59	-11.47	-11.61	-11.39	-11.34	-11.18	-10.83	-2.50
CH_2CHF	-38.94	-39.50	-39.20	-38.70	-39.28	-39.06	-38.68	-38.61	-38.25	-33.20
HCOCOH (glyoxal)	-65.30	-65.34	-65.04	-64.76	-65.08	-64.84	-64.49	-64.23	-63.86	-50.70
CF_3CN	-135.74	-137.40	-137.35	-135.26	-137.44	-137.33	-135.28	-135.17	-134.78	-118.40
C_2F_4	-178.46	-180.06	-180.09	-177.99	-180.22	-180.13	-178.16	-177.58	-177.20	-157.40
CH_3NH_2	-8.44	-8.18	-7.69	-8.09	-7.75	-7.42	-8.01	-7.83	-7.38	-5.50
CH_3CCH	44.05	43.54	44.04	44.21	43.93	44.26	44.30	44.13	44.61	44.20
CH_2CCH_2 (allene)	40.81	40.34	40.80	41.00	40.71	41.01	41.09	40.94	41.39	45.50
C_3H_4 (cyclopropene)	68.44	68.06	68.49	68.68	68.40	68.69	68.70	68.71	69.14	66.20
CH_3CHO	-44.15	-44.40	-44.02	-43.74	-44.03	-43.78	-43.56	-43.53	-43.15	-39.70
C_2H_4O (oxirane)	-14.82	-14.92	-14.52	-14.42	-14.64	-14.33	-14.38	-14.22	-13.78	-12.60
CH_2CHCN	34.53	34.23	34.72	34.90	34.65	34.98	35.01	35.07	35.57	43.20
CH_3NO_2	-11.41	-11.13	-10.81	-10.63	-10.86	-10.56	-10.36	-10.17	-9.72	-17.80
	cc-pV*n*Z			cc-pV*n*Z[rc](tr)			cc-pV*n*Z-BLYP			

Molecule	P	S3	S4	P	S3	S4	P	S3	S4	Expt.
CH_3ONO	-39.60	-39.77	-39.54	-38.89	-39.53	-39.33	-38.70	-38.73	-38.32	-15.90
CH_3COF	-113.75	-114.38	-114.09	-113.29	-114.11	-113.91	-113.15	-113.08	-112.69	-105.70
C_2H_6	-14.81	-15.46	-15.05	-14.53	-14.98	-14.78	-14.43	-14.77	-14.40	-20.10
C_2H_4NH (aziridine)	28.24	28.31	28.80	28.68	28.70	29.05	28.76	28.96	29.45	30.20
CH_3CH_2O	7.09	6.86	7.27	7.50	7.24	7.52	7.66	7.63	8.04	-3.30
$HCOOCH_3$	-94.96	-95.34	-94.96	-94.32	-94.95	-94.67	-94.09	-94.18	-93.72	-85.00
CH_3COOH	-110.16	-110.38	-109.96	-109.56	-109.99	-109.70	-109.32	-109.31	-108.84	-103.40
CH_3CHCH_2	8.61	8.06	8.55	8.95	8.57	8.86	9.06	8.84	9.31	4.80
C_3H_6 (cyclopropane)	20.04	19.48	19.96	20.39	19.95	20.23	20.44	20.30	20.76	12.70
CH_3CH_2OH	-53.61	-53.67	-53.13	-53.16	-53.21	-52.84	-52.99	-52.95	-52.42	-56.20
CH_3OCH_3	-43.47	-43.85	-43.41	-42.98	-43.42	-43.12	-42.85	-42.97	-42.50	-44.00
CH_3CONH_2	-66.64	-66.52	-65.95	-65.99	-66.00	-65.60	-65.78	-65.65	-65.08	-57.00
C_4H_4O (furan)	-10.70	-10.96	-10.55	-10.03	-10.57	-10.24	-9.93	-9.77	-9.24	-8.30
$(CH_3)_2CH$	25.27	24.70	25.19	25.66	25.25	25.53	25.77	25.54	26.00	21.50
$(CH_3)_2NH$	-3.68	-3.78	-3.23	-3.14	-3.22	-2.87	-3.03	-3.01	-2.48	-4.40
$CH_3CH_2NH_2$	-10.68	-10.71	-10.13	-10.17	-10.13	-9.76	-10.02	-9.97	-9.42	-11.30
$CH_2CHCHCH_2$ (trans-2-butene)	28.09	27.56	28.12	28.49	28.11	28.47	28.60	28.47	29.03	26.30
C_4H_6 (methyl-cyclopropane)	49.60	49.08	49.64	50.01	49.59	49.94	50.06	50.00	50.56	47.90
C_4H_6 (bicyclo[1.1.0]butane)	62.76	62.38	62.88	63.23	62.84	63.17	63.22	63.38	63.90	51.90
C_4H_6 (cyclobutene)	45.92	45.52	46.00	46.41	46.02	46.32	46.49	46.46	46.96	37.40
C_4H_6 (dimethylacetylene)	37.23	36.51	37.12	37.51	37.06	37.45	37.62	37.43	38.03	34.80
CH_3COCH_3	-53.81	-54.21	-53.72	-53.24	-53.68	-53.38	-53.02	-53.06	-52.56	-51.90
C_4H_5N (pyrrole)	22.94	23.10	23.65	23.64	23.63	24.03	23.71	24.07	24.68	25.90
C_3H_8	-11.38	-12.13	-11.61	-10.95	-11.50	-11.23	-10.83	-11.17	-10.68	-25.00
C_5H_5N (pyridine)	27.96	27.99	28.57	28.78	28.58	29.00	28.90	29.28	29.93	33.60
C_4H_8 (isobutylene)	3.69	3.00	3.61	4.19	3.68	4.04	4.33	4.09	4.69	-4.00
$C_2H_5OCH_3$	-47.71	-48.33	-47.77	-47.06	-47.73	-47.37	-46.87	-47.09	-46.50	-51.70
C_6H_6 (benzene)	24.11	23.80	24.41	24.79	24.45	24.87	24.86	25.12	25.79	19.70
		cc-pV*n*Z			cc-pV*n*Z[rc](tr)			cc-pV*n*Z-BLYP		
Molecule	P	S3	S4	P	S3	S4	P	S3	S4	Expt.

$(CH_3)_3N$	-0.68	-1.02	-0.41	0.04	-0.33	0.04	0.19	0.06	0.69	-5.70
C_5H_8 (spiropentane)	56.17	55.56	56.22	56.78	56.21	56.62	56.81	56.83	57.50	44.30
C_4H_{10} (trans-butane)	-15.96	-16.84	-16.21	-15.37	-16.05	-15.72	-15.24	-15.60	-14.99	-30.00
MAD	8.04	8.05	8.00	7.96	8.06	8.00	7.94	7.84	7.76	
MSD	4.98	5.24	4.89	4.63	4.95	4.70	4.55	4.51	4.12	

Table 5.14. The mean CPU savings of single point B3LYP calculations on the 86 molecule set for the cc-pVnZ(rc)(tr) and reoptimized basis sets as a percentage of the B3LYP/cc-pVnZ calculation CPU requirements at each basis set level. All calculations were based upon B3LYP/cc-pVTZ optimized structures. *M* represents the number of atoms in the molecule, and *N* represents the number of molecules containing M atoms.

N molecules with M atoms		cc-pV*n*Z[rc](tr)			
N	*M*	D	T	Q	5
11	2	---	---	44.07%	59.34%
10	3	---	---	50.22%	65.74%
7	4	---	2.79%	55.34%	67.67%
9	5	---	---	55.10%	67.96%
9	6	---	---	57.43%	68.67%
10	7	---	---	58.30%	70.27%
5	8	---	---	59.94%	71.78%
6	9	---	---	60.55%	72.53%
10	10	1.21%	---	65.44%	72.87%
2	11	---	---	60.97%	72.28%
3	12	---	---	61.91%	71.57%
2	13	---	---	63.09%	73.68%
1	14	---	---	62.62%	73.71%
N molecules with M atoms		cc-pV*n*Z-B3LYP			
N	*M*	D	T	Q	5
11	2	---	---	43.82%	59.43%
10	3	1.60%	1.62%	51.26%	66.43%
7	4	---	1.82%	54.95%	67.49%
9	5	---	---	54.93%	68.03%
9	6	---	---	56.83%	68.64%
10	7	---	---	58.73%	70.43%
5	8	---	1.36%	60.28%	71.90%
6	9	2.50%	---	60.53%	72.73%
10	10	1.92%	5.37%	63.44%	73.15%
2	11	1.16%	---	61.19%	72.47%
3	12	1.15%	2.48%	62.13%	72.58%
2	13	1.18%	---	63.26%	73.97%
1	14	---	2.13%	63.02%	74.11%

Table 5.15. The mean CPU savings of single point BLYP calculations on the 86 molecule set for the cc-pVnZ(rc)(tr) and reoptimized basis sets as a percentage of the BLYP/cc-pVnZ calculation CPU requirements at each basis set level. All calculations were based upon B3LYP/cc-pVTZ optimized structures. *M* represents the number of atoms in the molecule, and *N* represents the number of molecules containing M atoms.

N molecules with M atoms		BLYP [rc](tr)			
N	*M*	D	T	Q	5
11	2	---	---	44.18%	59.62%
10	3	---	---	49.81%	65.96%
7	4	---	---	54.94%	67.66%
9	5	---	---	54.75%	67.66%
9	6	---	---	57.15%	68.82%
10	7	---	---	58.52%	70.50%
5	8	---	---	60.55%	71.46%
6	9	---	---	61.28%	71.90%
10	10	---	---	61.31%	72.14%
2	11	---	2.60%	61.53%	72.69%
3	12	---	---	62.67%	72.36%
2	13	---	---	63.05%	73.57%
1	14	---	---	62.47%	73.36%
N molecules with M atoms		cc-pV*n*Z-BLYP			
N	*M*	D	T	Q	v5z
11	2	---	---	43.75%	59.22%
10	3	---	---	50.51%	65.94%
7	4	---	---	58.54%	69.95%
9	5	---	---	55.22%	69.32%
9	6	---	---	56.83%	69.38%
10	7	---	---	58.57%	69.97%
5	8	1.05%	---	59.97%	71.32%
6	9	---	---	60.89%	71.83%
10	10	1.52%	1.51%	61.47%	72.36%
2	11	---	1.02%	61.75%	72.54%
3	12	2.25%	1.10%	62.29%	72.75%
2	13	---	2.50%	62.81%	73.31%
1	14	2.27%	---	63.58%	73.79%

Table 5.16. The atomization energies for fullerenes using B3LYP and BLYP/cc-pVnZ (in kcal/mol), and the differences of the cc-pV*n*Z[rc](tr) and reoptimized basis sets with respect to the corresponding method, and experimental values.

B3LYP	C_{32}	C_{36}	C_{44}	C_{48}	C_{50}	C_{60}
cc-pVDZ	4415.82	5484.09	6832.51	7298.81	7863.64	9599.85
cc-pVTZ	4794.47	5525.45	6884.09	7355.47	7923.81	9672.87
cc-pVQZ	4806.81	5539.24	6900.46	7373.24	7942.25	9694.40
cc-pVDZ[rc]	4756.55	5868.99	7302.87	7809.52	8400.78	10241.78
cc-pVTZ[rc]	4930.58	5677.47	7068.97	7558.08	8132.90	9922.69
cc-pVQZ[rc](-1*g*)	4863.28	5603.58	6980.73	7460.33	8034.54	9806.88
cc-pVDZ-B3LYP	4678.93	5779.37	7188.01	7686.01	8268.47	10075.42
cc-pVTZ-B3LYP	4855.64	5589.97	6960.36	7445.34	8009.41	9774.94
cc-pVQZ-B3LYP	4814.22	5550.60	6924.42	7406.36	7975.27	9742.14
BLYP						
cc-pVDZ	4801.92	5531.85	6879.75	7351.45	7912.16	9642.03
cc-pVTZ	4824.73	5557.63	6912.25	7387.12	7950.58	9688.74
cc-pVQZ	4836.76	5570.98	6928.02	7404.29	7968.29	9709.31
cc-pVDZ[rc]	5337.52	6135.58	7616.97	8151.14	8752.37	10646.36
cc-pVTZ[rc]	5041.18	5799.74	7206.58	7709.03	8283.52	10086.39
cc-pVQZ[rc](-1*g*)	4942.54	5691.08	7076.60	7565.43	8138.44	9915.58
cc-pVDZ-BLYP	5231.48	6012.70	7460.82	7983.82	8572.91	10421.90
cc-pVTZ-BLYP	4966.67	5712.44	7098.38	7598.16	8161.06	9940.33
cc-pVQZ-BLYP	4925.94	5670.28	7048.15	7536.91	8104.32	9871.86
Experiment						
Reference [144]	-	-	-	-	-	9797.6
Reference [145]	-	-	-	-	-	9762.2
Reference [146]	-	-	-	-	-	9787.4

Table 5.17. CPU time savings relative to the standard cc-pV*n*Z basis sets in computing total energies using the recontracted and reoptimized cc-pV*n*Z basis sets.

B3LYP	C_{32}	C_{36}	C_{44}	C_{48}	C_{50}	C_{60}
cc-pVDZ[rc]	1%	---	---	---	---	---
cc-pVTZ[rc]	1%	---	---	---	1%	2%
cc-pVQZ[rc](-1*g*)	66%	58%	63%	63%	62%	66%
cc-pVDZ-B3LYP	---	---	---	4%	---	---
cc-pVTZ-B3LYP	11%	9%	17%	15%	15%	16%
cc-pVQZ-B3LYP	67%	66%	70%	65%	64%	65%
BLYP						
cc-pVDZ[rc]	---	---	---	---	---	---
cc-pVTZ[rc]	2%	1%	2%	2%	2%	3%
cc-pVQZ[rc](-1*g*)	69%	71%	65%	63%	59%	56%
cc-pVDZ-BLYP	---	6%	---	---	---	---
cc-pVTZ-BLYP	16%	16%	22%	16%	15%	13%
cc-pVQZ-BLYP	72%	75%	70%	70%	68%	56%

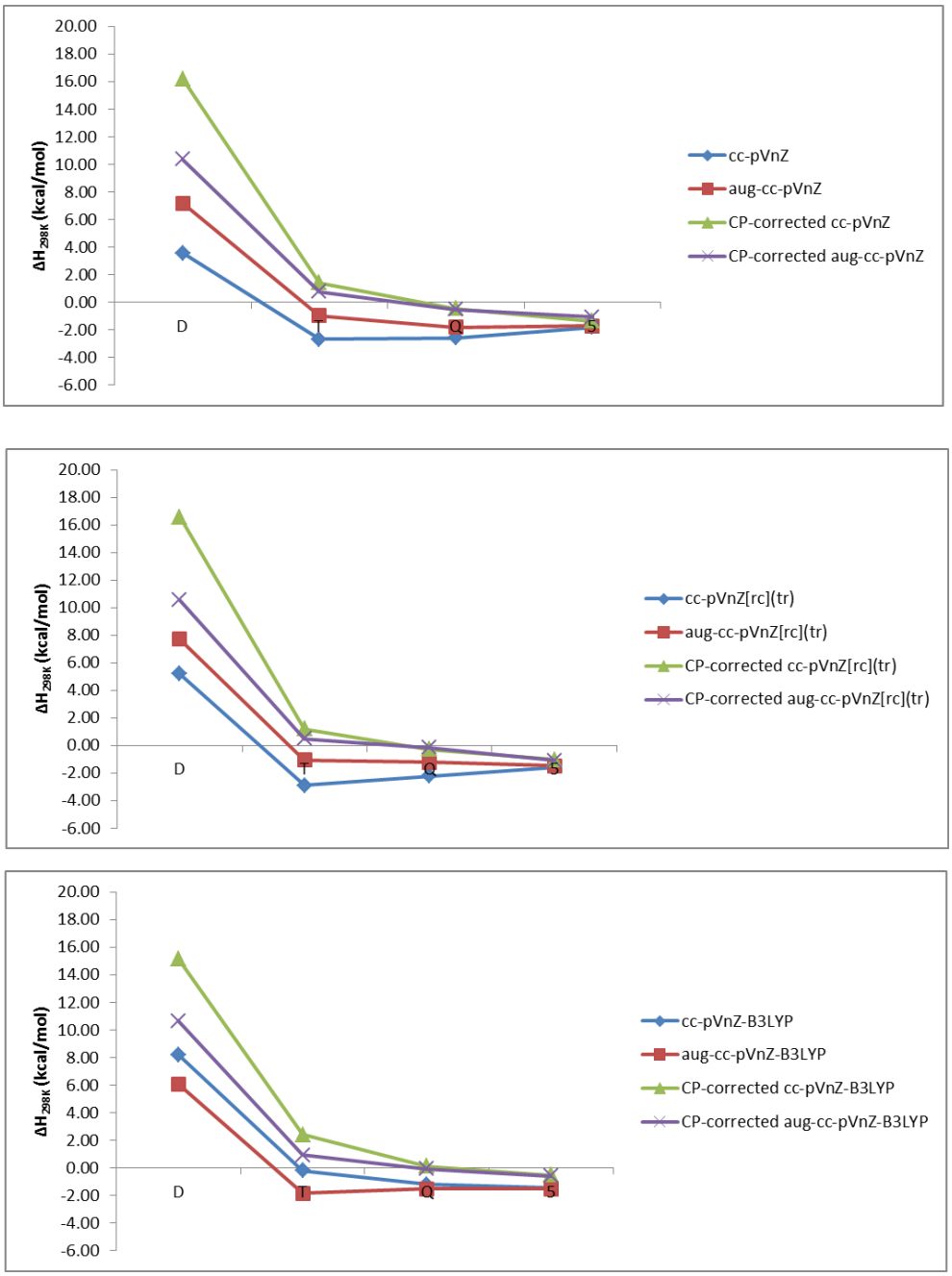

Figure 5.1. Basis set convergence graphs of CHF_3 computed with B3LYP with the cc-pV*n*Z (top), cc-pV*n*Z[rc](tr) (middle) , and cc-pV*n*Z-B3LYP (bottom). Each graph illustrates convergence behavior for the given basis set itself, the basis set with augmented functions, the basis set with Counterpoise correction, and the basis set with augmented functions and Counterpoise correction. The y-axis illustrates deviation from experiment.

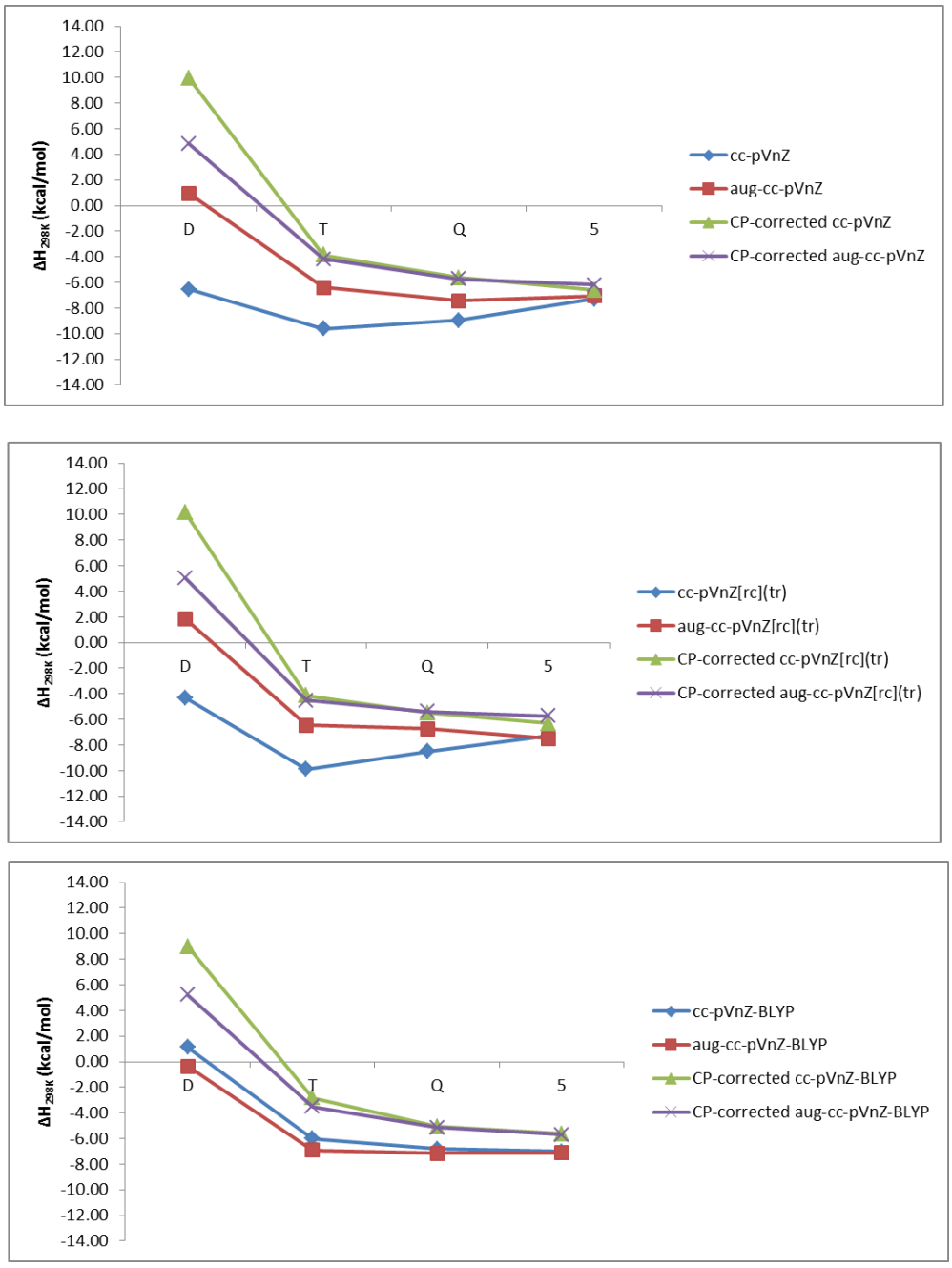

Figure 5.2. Basis set convergence graphs of C_2F_4 computed with BLYP with the cc-pV*n*Z (top), cc-pV*n*Z[rc](tr) (middle) , and cc-pV*n*Z-BLYP (bottom). Each graph illustrates convergence behavior for the given basis set itself, the basis set with augmented functions, the basis set with Counterpoise correction, and the basis set with augmented functions and Counterpoise correction. The y-axis illustrates deviation from experiment.

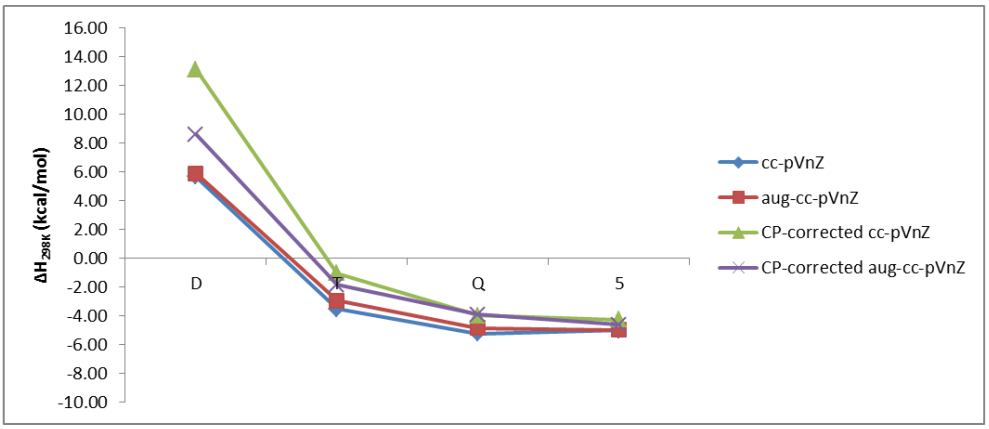

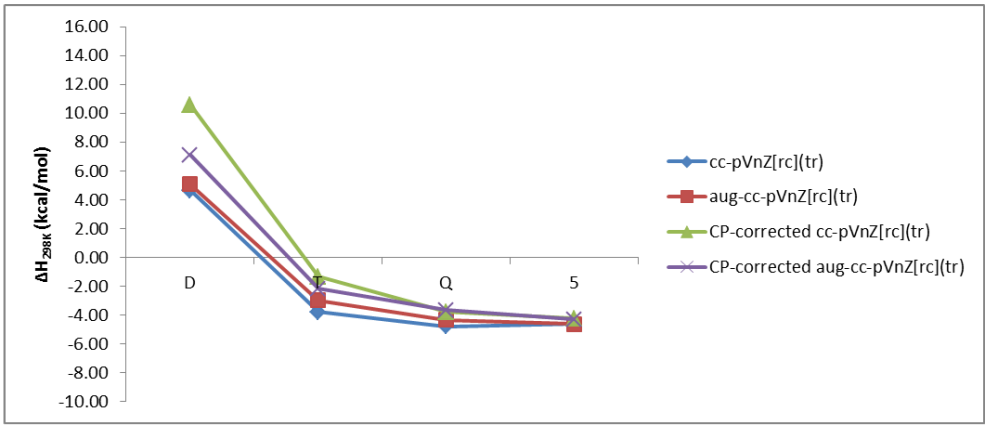

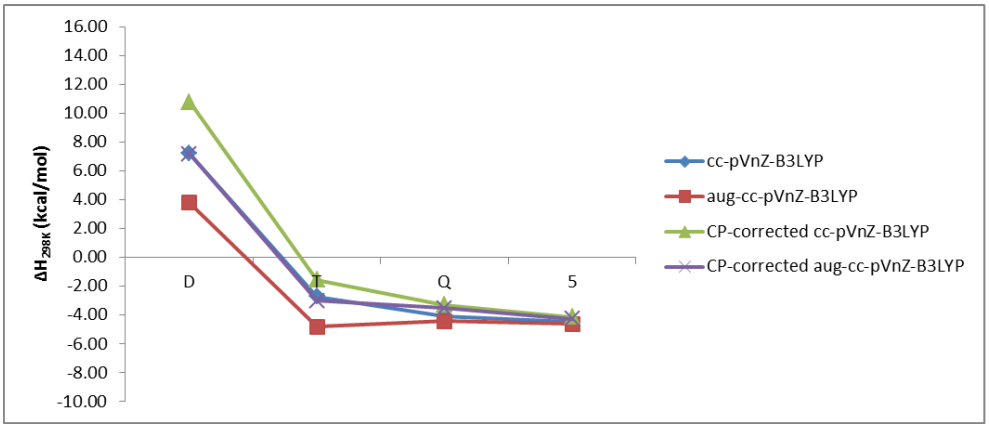

Figure 5.3. Basis set convergence graphs of HCOCOH computed with B3LYP with the cc-pV*n*Z (top), cc-pV*n*Z[rc](tr) (middle) , and cc-pV*n*Z-B3LYP (bottom). Each graph illustrates convergence behavior for the given basis set itself, the basis set with augmented functions, the basis set with Counterpoise correction, and the basis set with augmented functions and Counterpoise correction. The y-axis illustrates deviation from experiment.

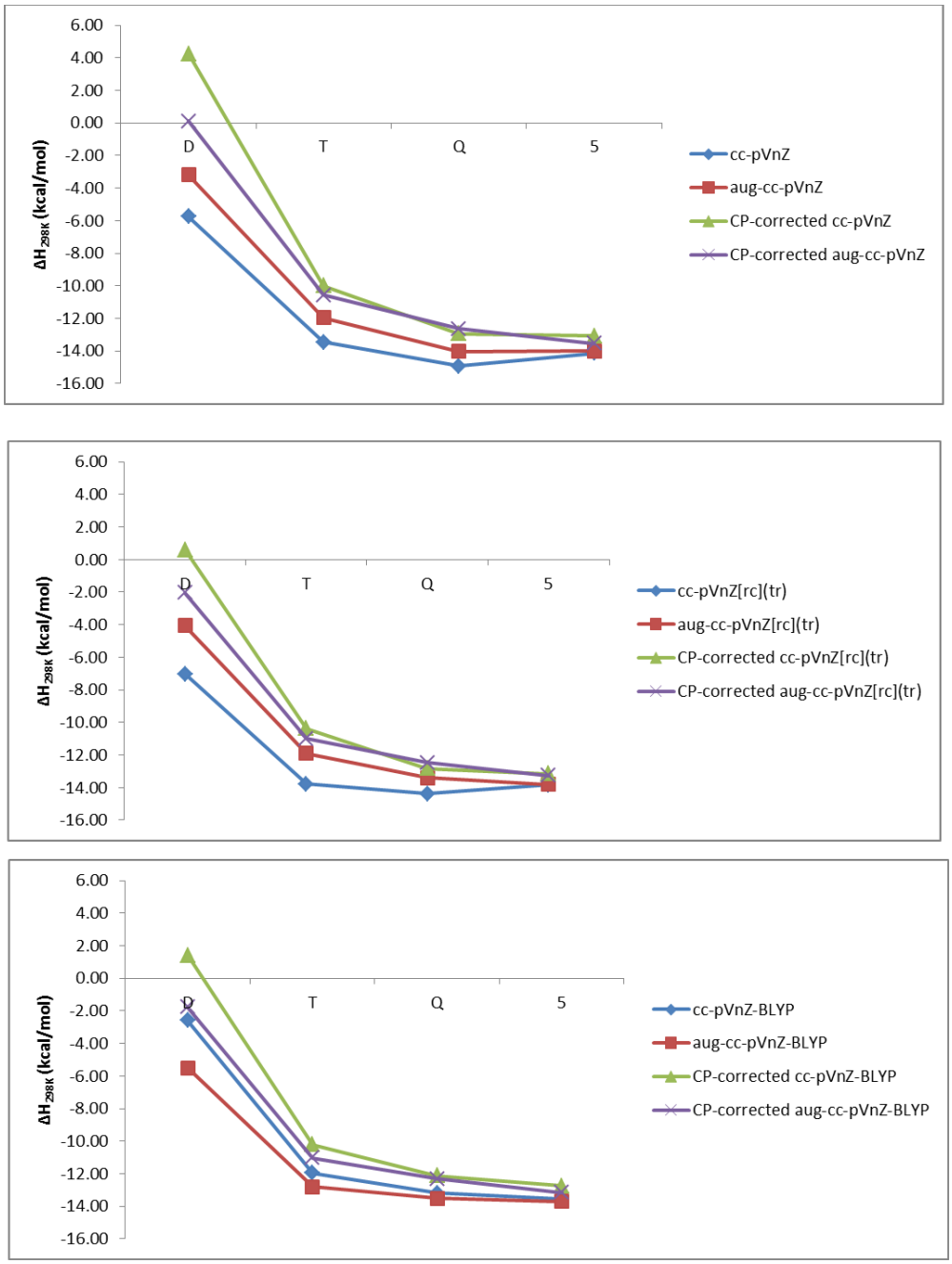

Figure 5.4. Basis set convergence graphs of HCOCOH computed with BLYP with the cc-pV*n*Z (top), cc-pV*n*Z[rc](tr) (middle) , and cc-pV*n*Z-BLYP (bottom). Each graph illustrates convergence behavior for the given basis set itself, the basis set with augmented functions, the basis set with Counterpoise correction, and the basis set with augmented functions and Counterpoise correction. The y-axis illustrates deviation from experiment

CHAPTER 6

THE FRAGMENT HAMILTONIAN METHOD

6.1 Introduction

Atomistic potentials have long been employed successfully to describe material behavior in varying solid-state phases[147-150] as well as in applications such as defects,[151] liquids,[152] surfaces,[151-153] and alloys,[151] in which the electron density of at least two unlike elements interact. These atomistic potentials, including the embedded atom method (EAM),[153] the modified embedded atom method (MEAM),[147] the Finnis-Sinclair potential (FS),[150] and the angular embedded atom method (A-EAM),[149] describe the atomic interactions directly but the electronic interactions are treated indirectly. The indirect treatment of the electronic interactions is facilitated by implementing the potential energy curve of a solid-state structure, computed from a first principles method, usually density functional theory (DFT), as a reference on which the atomistic potential is constructed. The face cubic centered (fcc) phase is commonly used as a reference solid-state phase because it has the highest number of nearest neighbors and this atomic arrangement is the most symmetric of any phase. Thus, the fcc potential energy curve would be computed, and the dissociation energy would be subtracted from all energy points to produce a binding curve, which isolates information concerning the binding energy between atoms through the pertinent electronic interactions. From here, the reference binding curve, as well as other DFT computations demanded by the atomistic potential, are implemented in the derivation of method-specific parameters and densities. On a side note, the multi-state modified embedded atom method (MS-MEAM) is the only current example of an atomistic potential that requires multiple reference structures of different symmetries and nearest-neighbors.[148] These, in turn,

approximate the electronic information for an atomic system involving anywhere from two atoms to thousands of atoms.

In EAM, MEAM, FS, and other atomistic potentials, the total energy of the system is approximated with the following expression:

$$E_{total} = \sum_{i=1}^{n} \left[F(\bar{\rho}_i) + \frac{1}{2} \sum_{j \neq i} \phi(r_{ij}) \right] \quad [6.1]$$

In Equation [6.1], for all atoms *i*, *F* is the embedding energy functional, which is the energy cost to embed a nearest neighbor atom *j* into the background density, $\bar{\rho}_i$ of atom *i,* and the pair potential, ϕ_{ij}, is the atom interaction between atoms *i* and *j*. The latter is defined numerically with the reference structure and Equation [6.1]; given the symmetry of the reference structure around atoms *i*, the summation can be removed, and the pair potential can be expressed as:

$$\phi(r_{ij}) = 2\left[E_{reference} - F(\bar{\rho}_i)\right] \quad [6.2]$$

Equation [6.2] demonstrates that the embedding energy is functionally important for construction of an atomistic potential. The embedding energy is an analytic functional that is specific to the type of atomistic potential, and thus various forms have been derived. The embedding energy functional for the FS potential has the form:

$$F^{FS} = A\sqrt{\bar{\rho}_i} \quad [6.3]$$

In Equation [6.3], the background density is related to the hopping integral, *I*, corresponding to the nearest-neighbor exchange between electrons in nearby atoms *i and j*:

$$I = \langle \psi_i | H | \psi_j \rangle \quad [6.4]$$

The hopping integral, in turn, is related to the bandwidth of the electronic states obtained from the second moment of the density of states. Another example of an embedding energy functional comes from the MEAM formulation:

$$F^{MEAM} = A\bar{\rho}\ln(\bar{\rho}) \quad [6.5]$$

In Equation [6.5], the MEAM embedding energy is a functional of the background density, as well. The presence of the logarithm originates from fitted relationship, determined by Baskes, between the electron density and the number of nearest neighbors in a set of crystalline systems. Thus, the background density is dependent of the atomic configuration. Development of the background density has been executed to account for multiple symmetries.[147,148] Unlike the previous expressions for the embedding energy, the Mishin embedding energy[154] is a rational function:

$$F^{Mishin} = \frac{\sum_i X_i(\bar{\rho}_i - 1)^i}{\sum_j X_j\left(\bar{\rho}_j - 1\right)^j} \quad [6.6]$$

The only constraints on the expansion of the Mishin embedding energy is that X_0 and X_2 are fitted using the cohesive energy and the bulk modulus of the reference structure. All other *i* and *j* parameters can be freely optimized for other first principles values. Finally, the last example is the A-EAM embedding function:[149]

$$F^{FS} = A\bar{\rho}_i^2 \quad [6.7]$$

In Equation [6.7], the background density for A-EAM accounts for the nearest-neighbor interactions of atoms *j* around atom *i,* and also for interactions of atoms *k* and *j* that interact with atoms *i*. Both sets of interactions are approximated as functions of parameterized exponentials.

Of the above examples, the FS embedding energy functional alone requires information directly from the electronic structure of the reference data. The remaining

embedding energy functionals require structural reference data and are fitted by means of parameterization or density functionalization. These examples illustrate the fact that atomistic potentials are limited to information obtained from either the many-electron wavefunction or structural data of a reference atom. The following section presents the formulation and application of an atomistic potential called the fragment Hamiltonian (FH) method,[155] the foundation of which is a new embedding energy functional that accounts for both electronic and structural aspect of solid-state structures. The development of the FH method, as described within the first and second sections, was developed to Dr. Steve Valone,[155] and the derivation in the third section was formulated by the author. The fourth section describes application of the FH method to Ni, and the conclusions are given in the final section.

6.2 The Fragment Hamiltonian Method

6.2.1 Foundation

The basis of the FH method depends upon the solid-state structure as the composition of numerous atomic fragments. This includes characterization of the constituent atoms or solid-state unit cells, as fragments, and of the electronic behavior as a result of any interatomic interactions. Therefore, it is necessary for the method to account for traits of the many-electron wavefunction, the Hamiltonian decomposition, and charge state variables for these fragments.

To understand conceptually what a fragment is in view of the FH method, a conceptual understanding of the many-electron wavefunction features in the FH method is explored:

$$\psi = \sum_i c_i |i\rangle \qquad [6.8]$$

In the above wavefunction, | *i* > are many-electron nonadiabatic states and c_i are the expansion coefficients. The nonadiabatic states are antisymmetric and normalized, and the number of electrons is an integer value for each fragment. For a fragment, A, Equation [6.8] is an implicit functional of the correspondingly defined wavefunction:

$$|A\rangle = \sum_j c_j |A_j\rangle \qquad [6.9]$$

$$|A_j\rangle = \sum_i \delta_{ij}\, c_j |i\rangle \Big/ \sqrt{n_j^A} \qquad [6.10]$$

$$n_j^A = \sum_i \delta_{ij}\, c_{i*} c_i = C_{j*} C_j \qquad [6.11]$$

The above equations demonstrate that for a fragment A, the wavefunction |A> is expanded as a sum of charge states *j* of | A_j>, all of which are composed of many-electron wavefunctions of the form in Equation [6.8]. Also, the Kronecker delta function, δ_{ij}, captures the non-adiatbatic state that contributes to the charge state |A_j>. Further, the above illustrates that the only normalized occupation numbers, n_A, are defined, but the coefficients C_j are not defined because the information regarding the phase of the wavefunction is not concerned.

Ionic and covalent behavior is also considered in the FH method in a manner consistent with the Heitler-London model. As an example, the H_2 covalent wavefunction; with both atoms labeled as A and B, the covalent wavefunction is:

$$|cov\rangle = \frac{1}{\sqrt{2}}[\phi_A(1)\phi_B(2) + \phi_A(2)\phi_B(1)] \qquad [6.12]$$

Also, the ionic wavefunction is:

$$|ion\rangle = \phi_A(1)\phi_B(2) = \phi_A(2)\phi_B(1) \quad [6.13]$$

Spin has been neglected, and any covalent and ionic wavefunctions are further referred as $|A^0\rangle$ and $|A^-\rangle$, respectively.

Next, a conceptual understanding of Hamiltonian decompositions in the FH method is investigated. To begin, the electronic Hamiltonian operator corresponding, which is used to solve Schrödinger Equation, is considered:

$$\hat{H} = \hat{T}_e + \hat{V}_{ee} + \hat{V}_{ne} \quad [6.14]$$

The above equation considers the kinetic energy of the electrons, and the potential energy between electrons and also between nuclei and electrons, respectively. For an arrangement of atoms, denoted as fragment A, the corresponding electronic "fragment Hamiltonian", may be written:

$$\hat{H}^{(f)} = \sum_A \hat{H}^A + \frac{1}{2}\sum_A \sum_B \hat{V}^{AB} \quad [6.15]$$

Equation [6.14] accounts for not only for the Hamiltonian for fragment A, but also the potential energy interactions between fragments A and B. The latter may be like or unlike fragments A, therefore allowing impurities to be considered. Consistent with the many-electron nature of each fragment, an integer number of electrons must be assigned to the fragments.

With this Hamiltonian construction, the electron fluctuation between atoms must be considered. Looking at the example with H_2, the electrons are allowed to move in an integer-like fashion between atoms. Thus, the three possible cases are that 1) both atoms have a neutral charge; 2) H atom A has a negative charge and H atom B has a positive charge; or 3) H atom B has a negative charge and H atom A has a positive

charge. This can be extended further for a unit cell having a center atom A surrounded by first nearest-neighbor (1NN) atoms B in a two-dimensional square formation (2D-sq):

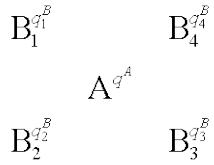

In the 2D-sq unit cell, q_A and q_B are the charges on atoms A and B, respectively, determined by the difference in the nuclear and electronic charges:

$$q^{\alpha} = Z^{\alpha} - N^{\alpha} \qquad [6.16]$$

The *α* designates the identity of the given atom or fragment, *N* designates the number of electrons, and *Z* designates the nuclear charge. The allowed electronic fluctuations for the 2D-sq cell include the following possibilities:

$$1)\ |00000\rangle\ q^A = q_1^{B_1} = q_1^{B_2} = q_1^{B_3} = q_1^{B_4} = 0$$

$$2)\ |+-000\rangle\ q^A = +1;\ q_1^{B_1} = -1;\ q_1^{B_2} = q_1^{B_3} = q_1^{B_4} = 0$$

$$3)\ |+0-00\rangle\ q^A = +1;\ q_1^{B_2} = -1;\ q_1^{B_1} = q_1^{B_3} = q_1^{B_4} = 0$$

$$4)\ |+00-0\rangle\ q^A = +1;\ q_1^{B_3} = -1;\ q_1^{B_1} = q_1^{B_2} = q_1^{B_4} = 0 \qquad [6.17a]$$

$$5)\ |+000-\rangle\ q^A = +1;\ q_1^{B_4} = -1;\ q_1^{B_1} = q_1^{B_2} = q_1^{B_3} = 0$$

$$6)\ |-+000\rangle\ q^A = -1;\ q_1^{B_1} = +1;\ q_1^{B_2} = q_1^{B_3} = q_1^{B_4} =$$

$$7)\ |-0+00\rangle\ q^A = -1;\ q_1^{B_2} = +1;\ q_1^{B_1} = q_1^{B_3} = q_1^{B_4} = 0$$

$$8)\ |-00+0\rangle\ \ q^A=-1;\ q_1^{B_3}=+1;\ q_1^{B_1}=q_1^{B_2}=q_1^{B_4}=0$$
$$9)\ |-000+\rangle\ \ q^A=-1;\ q_1^{B_4}=+1;\ q_1^{B_1}=q_1^{B_2}=q_1^{B_3}=0 \qquad [6.17b]$$

The charge sets in Equation [6.17] illustrate the wavefunction as a function of the charge distribution and the individual charges on atoms A and B. They charge sets obey neutrality of the 2D-sq cell, and consider only 1NN electron transitions. This leads to the question of how the charge fluctuates from [6.17.2] to [6.17.3] so that the extra electron on B_1 migrates to B_2; indeed, this transition occurs between the cationic state in A and the anionic state between both B_1 and B_2. For the many-electron wavefunction to describe the difference in electronic states for these three atoms before and after the migration, the | *i* > states in Equation [6.10] must have their own electronic distribution on the Hamiltonian in Equation [6.15], such that:

$$\widehat{H}^A=\sum_i \widehat{H}_i^A \qquad [6.18]$$

From here, the total FH energy is a sum of the energy for fragment A and the pair interactions with fragment B:

$$E=\sum_A E^A+\sum_A\sum_B V^{AB} \qquad [6.19]$$

The energy for fragment A is first considered and determined using the wavefunctions in Equations [6.9] through [6.11]:

$$E^A=\left\langle A\middle|\widehat{H}_i^A\middle|A\right\rangle=\sum_j\sum_{j^*}\sqrt{n_{Aj}n_{Aj^*}}H_{jj^*}^A \qquad [6.20]$$

in which *i* is an element of the charge states *j*, according to Equation [6.10]:

$$H_{jj^*}^{A} = \langle A_j | H_{j'j}^{A} | A_j \rangle \quad [6.21]$$

The fragment Hamiltonians from Equation [6.20] are averaged to yield a fragment Hamiltonian that is Hermitian in the energy matrix on the right-hand side of Equation [6.21]:

$$H_{j'j}^{A} = \frac{H_{j'}^{A} + H_{j}^{A}}{2} \quad [6.22]$$

The right-hand side of Equation [6.21] can be transformed into a matrix:

$$E^{A} = \sum_{j} \sum_{j^*} \sqrt{n_{Aj} n_{Aj^*}} H_{jj^*}^{A} = \sum_{j} \sum_{j^*} C_j C_{j^*} H_{jj^*}^{A} = tr(\boldsymbol{H}_A \Gamma_A) \quad [6.23]$$

In the above expression, Γ_A is the occupancy density matrix, and $tr(\Gamma_A) = 1$ is required since the wavefunction is normalized. Also illustrated is that the occupancy density matrix contains the C_j coefficients that represent the charge balance that is related to the ionic charge of fragment A. This leads to the elucidation of the charge state variables that govern the FH method. As stated earlier in this section, the C_j coefficients are not defined, but they are used to define the occupational numbers given in Equation [6.11]. However, the FH method is an embedded atom method, and therefore not *directly* dependent on occupational numbers. As a result, different variables must be used to describe the behavior of the electron density, which has traditionally been the foundation of any embedded atom method. Equation [6.23] is a good place to begin for this, as it can be rewritten in matrix form as a function of the C_j coefficients. For simplicity, a simple diatomic, A-B, is considered; the possible states include |0> = $|A^0B^0>$, |+> = $|A^+B^->$, and |-> = $|A^-B^+>$. The coefficients are labeled such that *j* denotes the net charge:

$$\Gamma_A(C_j) = \begin{bmatrix} C_0^2 & C_0C_+ & C_0C_- \\ C_+C_0 & C_+^2 & C_+C_- \\ C_-C_0 & C_+C_0 & C_-^2 \end{bmatrix} \quad [6.24]$$

In a previous work by Valone,[156] the net charge and the ionic character are defined in the following manner:

$$q = C_+^2 - C_-^2 \quad [6.25]$$

$$\tau = C_+^2 + C_-^2 \quad [6.26]$$

Also, C_o is normalized with respect to the ionic character:

$$1 = C_0^2 + \tau \quad [6.27]$$

Using Equations [6.25] through [6.27], the occupancy density matrix can be rewritten as a function of ionic character and net charge:

$$\Gamma_A(\tau, q) = \begin{bmatrix} 1-\tau & \sqrt{(1-\tau)(\tau+q)/2} & \sqrt{(1-\tau)(\tau-q)/2} \\ \sqrt{(1-\tau)(\tau+q)/2} & (\tau+q)/2 & \sqrt{(\tau^2-q^2)/2} \\ \sqrt{(1-\tau)(\tau-q)/2} & \sqrt{(\tau^2-q^2)/2} & (\tau-q)/2 \end{bmatrix} \quad [6.28]$$

The associated fragment Hamiltonian matrix in Equation [6.23] is:

$$\boldsymbol{H}_A = H_{00} + \begin{bmatrix} 0 & H_{0+} & H_{0-} \\ H_{+0} & H_{++} - H_{00} & H_{+-} \\ H_{-0} & H_{-+} & H_{++} - H_{00} \end{bmatrix} \quad [6.29]$$

Finally, the energy for fragment A, E_A, can be solved using the above matrices:

$$E_A = E_A^{gap}(q_A, \tau_A) - 2[W^{1e+} f^{hop+}(q_A, \tau_A) + W^{1e-} f^{hop-}(q_A, \tau_A)] \quad [6.30]$$

The interior variables are defined as follows: the electron hopping depends on the charge and ionicity:

$$f^{hop\pm}(q_A, \tau_A) = \sqrt{(1-\tau_A)(\tau_A \pm q_A)/2} \quad [6.31]$$

The one-electron hopping energy is $W^{1e\pm}$. The effective gap energy is written

$$E_A^{gap}(q_A, \tau_A) = E_{A^0}^* + U_A^{eff}\tau_A - \mu_A^* q_A - W_A^{2e}\Delta f_A^{gap}(q_A, \tau_A) \quad [6.32]$$

as a function of the energy of the neutral atom:

$$E_{A^0}^{*} = H_{00}^{A} \quad [6.33]$$

The effective gap energy is a function of the effective fragment gap:

$$U_A^{eff} = \eta_A^{*} - W_A^{2e} \quad [6.34]$$

Equation [6.34] is a function of the effective fundamental gap:

$$\eta_A^{*} = \left[\left(\frac{H_{++} - H_{00}}{2}\right) - \left(\frac{H_{00} - H_{--}}{2}\right)\right] \quad [6.35]$$

The effective gap energy is also a function of the chemical potential:

$$\mu_A^{*} = -\left(\frac{H_{++} - H_{--}}{2}\right) \quad [6.36]$$

and the two-electron hopping energy, which modulates the effective fundamental gap:

$$W_A^{2e} = -H_{+-}^{A} \quad [6.37]$$

Finally, the effective gap function associated with the two-electron hopping energy:

$$\Delta f_A^{gap}(q_A, \tau_A) = \sqrt{\tau_A^2 - q_A^2} - \tau_A \quad [6.38]$$

Equations [6.30] through [6.38] can be used to model the diatomic molecule A-B because they can account for all one- and two-electron hopping and effective energy gap that results from atomic cohesion as a function of ionic character and net charge. When the diatomic molecule is stretched to infinity, electron hopping is mitigated towards the limit of chemical hardness.

With the diatomic molecule, the FH method allows for A and B to be either of the atoms for fragments. In this possibility, both have atomic substructures that contain interatomic interactions. Therefore, the FH method must be able to account for the implicit many-body interactions. Another example to use for this is a linear molecule E-D-E', which is allowed to be a substructure for either A or B in the previous example.

Also, D, E, and E' may be either atoms or fragments, and E may or may not be identical to E'. Keeping with the three-charge-state restriction, Equations [6.25] through [6.39] still apply, and the possible wavefunctions are |000>, |+-0>, |-+0>, |0+->, and |0-+>. With this example, E-D-E' is neutral, and charge transfer between both E and E' is neglected (basically, charge transfer is only allowed between 1NN atoms).

Many-body effects through the linear molecule can be noted by analyzing the charge states of D, which are: $|D^0\rangle = |000\rangle$, $|D^+\rangle = |-+0\rangle = |0+-\rangle$, and $|D^-\rangle = |+-0\rangle = |0-+\rangle$. It should be noted that $|D^+\rangle = |-0+\rangle = |+0-\rangle$ is not allowed because this represents a second nearest-neighbor charge transfer. The resulting charge transfer expectation values of $H_{0+}^{D} = \langle D^0|H|D^+\rangle$ and $H_{0-}^{D} = \langle D^0|H|D^-\rangle$. The former and the latter values are dependent on charge-state coefficients of the end fragments. These coefficients quantify the ratio of occupation numbers for the left and right end-fragments, n_{L+}/n_{L-}. This ratio can be rewritten in terms of ionicity, because the occupation number is the square of the charge coefficients (Equation [6.11]) and the sum of the squares of the charge coefficients yields the ionicity (Equation [6.26]). Therefore, the ratio can be expressed as:

$$\tau_L/\tau_R = n_L/n_R \qquad [6.39]$$

Neutral atoms on the end fragments also have their own characteristics. For example, having the charge states $|E^0\rangle = |000\rangle$, $|0+-\rangle$, and $|0-+\rangle$, fragment E always experiences a neutral charge, and the central fragment D carries the non-neutral charge most of the time. Therefore, it is expected that the FH method can distinguish between surface and bulk atoms.

Finally, the pair interactions between fragments are considered. The previous examples, being diatomic and linear molecules, or even an atom, can indeed be a fragment. Whatever is defined as the fragment must be considered for the pair interactions between these embedded fragments to compute the total energy (Equation [6.19]). In Equation [6.19] two fragments, C and D, are considered. As written above, only one occupational density matrix needs to be considered, with $\Gamma_C(q_C,\tau_C) = \Gamma_D(q_D,\tau_D) = \Gamma_{CD}(q_{CD},\tau_{CD})$. Thus, solving for Equation [6.19] yields:

$$\begin{aligned} E = E_{CD}(q_C,\tau_C) = V_{C^oD^o} - \left(\mu_C - \mu_D - \frac{V_{C^+D^-} + V_{C^-D^+}}{2}\right) q_C \\ + \left(U_C^{eff} + U_D^{eff} + \frac{V_{C^+D^-} + V_{C^-D^+} + 2V_{C^0D^0}}{2} + V_{C_+^\pm D_+^-}\right)\tau_C \\ -2\left(W_C^{1e+} + W_D^{1e-} + V_{C_0^+D_0^-}\right) f^{hop+}(q,\tau) \\ -2\left(W_C^{1e-} + W_D^{1e+} + V_{C_0^-D_0^+}\right) f^{hop-}(q,\tau) \\ - 2\left(W_C^{2e} + W_D^{2e} + V_{C_+^\pm D_+^-}\right) f^{hop+}(q,\tau) \end{aligned} \quad [6.40]$$

In the first line are two pair interactions (*V*) due to non-zero charge interactions. In the second line, the first three pair interactions (*V*) also account for non-zero charge interactions, and the fourth pair interaction accounts for transitions between states (for C, + → -, and for D, - → +) that affect the effective gap. In the last three lines, pair interactions exist that vary the one- and two-electron hopping energies.

6.2.2 The Embedding Functional

With the foundation of the FH method having been studied, an embedding functional can now be derived that depends on the background density, as typified in EAMs. The FH method has been applied to Ni. For Ni, it is expected that the net charge,

q = 0. Therefore, this is applied to Equation [6.30], which is the embedding energy of fragment A, F_A, to give the following:

$$F_A = F_A^{gap}(\tau_A) - 2W_A^{1e} f^{hop}(\tau_A) \quad [6.41]$$

The "*E*"s in Equation [6.30] were changed to "*F*"s, as it is conventional to label the embedding energy with "*F*". With q = 0, the embedding energy gap is written as:

$$F_A^{gap}(\tau_A) = F_{A^o}^{*} + U_A^{eff}\tau_A \quad [6.42]$$

The charge neutrality removes the functional dependence on the chemical potential and the effective gap associated with the two-electron hopping energy. The one-electron contribution is written as a sum of cationic and anionic one-electron hopping energies:

$$W_A^{1e} = (W_A^{1e+} + W_A^{1e-}/2) \quad [6.43]$$

Further, the associated one-electron hopping function is a function of only the ionicity:

$$f^{hop\pm}(\tau_A) = \sqrt{(1-\tau_A)(\tau_A)} \quad [6.44]$$

The embedding energy has been simplified as a functional of only ionicity and is independent of the background density. Therefore, the embedding energy needs to be reformulated to be functionally dependent on the background density. It should be noted that such a reformulation allows for more variability of the embedding energy since the background density has no restrictions concerning the functional behavior. In contrast, the ionicity depends on the sum of occupation numbers, and consequently the ionicity is restricted to be less than 1.

The wavefunction defined in Equation [6.9] may be used as a guide to reformulating the embedding energy:

$$|A\rangle = \frac{|A^0\rangle + \lambda_A(|A^-\rangle + |A^+\rangle)/\sqrt{2}}{\sqrt{1+\lambda_A^2}} \quad [6.45]$$

The above expression is normalized with respect to the mixing parameter, λ_A. Also, is it implied that the mixing parameter is a function of the background density. Using Equation [6.26], the ionicity is found to be:

$$\tau_A(\bar{\rho}_A) = \frac{\lambda_A^2(\bar{\rho}_A)}{1 + \lambda_A^2(\bar{\rho}_A)} \quad [6.46]$$

Substituting the ionicity into the embedding energy gap and the one-electron hopping function gives:

$$F_A^{gap}(\bar{\rho}_A) = F_{A^o}^* + \frac{U_A^{eff}\lambda_A^2(\bar{\rho}_A)}{1 + \lambda_A^2(\bar{\rho}_A)} \quad [6.47]$$

So that:

$$f^{hop}(\tau_A) = \frac{\lambda_A^2(\bar{\rho}_A)}{1 + \lambda_A^2(\bar{\rho}_A)} \quad [6.48]$$

An approximation is made that assumes that the mixing parameter *is* the background density. Also, the embedding energy of the neutral atom in Equation [6.47] is zero as a result of the pair interaction that is introduced shortly. Combining Equations [6.47] and [6.48] into the embedding energy in Equation [6.42], the final form of the embedding energy becomes:

$$F_A(\bar{\rho}_A) = \frac{U_A^{eff}\bar{\rho}_A^2 + 2W_A^{1e}\bar{\rho}_A}{1 + \bar{\rho}_A^2} \quad [6.49]$$

The total cohesive energy is constructed using the FH embedding energy and the pair interaction between fragments A and 1NN fragments B is:

$$E_A^{FH} = F_A^{FH}(\bar{\rho}_A) + \frac{L_A}{2}\phi_{AB} \quad [6.50]$$

Equation [6.50] is synonymous with the EAM total energy in Equation [6.1], except that symmetry of 1NNs allows for replacement a summation of 1NNs by a constant L_A, the number of 1NNs.

The one-electron hopping energy must be identified for efficient implementation of the FH embedding energy. The FH method at this point is constructed to account for charge fluctuations between fragments A and 1NNs B. However, since the FH method is applied to the elemental material, Ni, then the 1NNs B are the same element as A. With that, charge transfer matrices must be constructed: $H_{0+}{}^{A} = \langle A^0|H|A^+\rangle$ and $H_{0-}{}^{A} = \langle A^0|H|A^-\rangle$. Noting the coordination of the 1NNs A around the central fragment A, whatever the symmetry may be, the wavefunctions involved in the charge transfer matrix are normalized by the square root of the coordination number. Therefore, the one-electron hopping energy is determined to be:

$$W_A^{1e+} = -\langle A^0|H_{0+}^A|A^{\pm}\rangle \approx \frac{L_{A^{\pm}}}{\sqrt{L_{A^{\pm}}}} w_A^{1e\pm} = \sqrt{L_{A^{\pm}}} w_A^{1e\pm} \qquad [6.51]$$

In the above expression, $w_A{}^{1e}$ is the one-electron hopping energy between A and any of the 1NNs. With the FH embedding energy as a function of the background density, then $w_A{}^{1e}$ is also expected to have this functional dependence between the energy and background density. Also, with the FH method as an EAM, first principles data is used to construct the EAM around the embedding energy functional. In this process, $w_A{}^{1e}$ is be numerically fitted.

As for the effective fragment gap in the FH embedding energy, it is known to be a function of the two-electron hopping energy and the effective fundamental gap, given in Equation [6.35]. The former involves two electrons hopping from the central fragment to

two of the 1NNs. Therefore, the two-electron hopping energy has coordination dependence:

$$W_A^{2e+} = L_{A^{\pm}} w_A^{2e\pm} \quad [6.52]$$

In the above expression, w_A^{2e} is the two-electron hopping energy between A and any of the 1NNs. This parameter, along with the effective fundamental gap, is also fitted to first principles data.

6.2.3 Derivation of the Two-Electron Hopping Energy

This section illustrates the derivation of an expression for the two-electron hopping energy for the FH method. The two-electron hopping energy is necessary for the method to distinguish between the fcc and hexagonal closed packed (hcp) structures for Ni. To begin, the total cohesive energy for the fcc and hcp structures are introduced:

$$E_{fcc}^{FH} = F_{fcc}^{FH}(\bar{\rho}) + \frac{L_{fcc}}{2}\phi(R) \quad [6.53]$$

$$E_{hcp}^{FH} = F_{hcp}^{FH}(\bar{\rho}) + \frac{L_{hcp}}{2}\phi(R) \quad [6.54]$$

It should be noted that both structures have the same number of 1NNs ($L_{fcc} = L_{hcp} = 12$). Also, the pair potential is derived from the one-dimensional linear chain structure. Since the background density, like the pair potential, is a function of R, and the 1NNs are the same for both structures, then Equation [6.53] can be subtracted from Equation [6.54] to remove the pair potential:

$$E_{hcp}^{FH}(\bar{\rho}) - E_{fcc}^{FH}(\bar{\rho}) = F_{hcp}^{FH}(\bar{\rho}) - F_{fcc}^{FH}(\bar{\rho}) \quad [6.55]$$

Substituting the expression for the embedding energy into Equation [6.55] for hcp and fcc:

$$E_{hcp}^{FH}(\bar{\rho}) - E_{fcc}^{FH}(\bar{\rho}) = \left(\frac{U^{eff}\bar{\rho}_{hcp}^2 + 2W^{1e}\bar{\rho}_{hcp}}{1+\bar{\rho}_{hcp}^2}\right) - \left(\frac{U^{eff}\bar{\rho}_{fcc}^2 + 2W^{1e}\bar{\rho}_{fcc}}{1+\bar{\rho}_{fcc}^2}\right) \quad [6.56]$$

Further work depends on the identities of the interior functions on the right-hand side of Equation [6.56]. The background density is not yet of concern. The one-electron hopping function, however, is the same for both hcp and fcc; it is governed by coordination, and both structures have the same coordination ($L_{fcc} = L_{hcp} = 12$). Therefore:

$$W^{1e} = W_{fcc}^{1e} = W_{hcp}^{1e} \quad [6.57]$$

The effective fragment gap is written as the difference from the effective fundamental gap and the two-electron hopping function:

$$U^{eff} = \eta^* - W^{2e} \quad [6.58]$$

The effective fundamental gap is singular for the specified element, and therefore the same for both fcc and hcp structures:

$$\eta^* = \eta_{fcc}^* = \eta_{hcp}^* \quad [6.59]$$

The background density for fcc and hcp are similar in this case because they involve the same number of nearest neighbors and it is dependent on the specified element. Therefore,

$$\bar{\rho}^2 = \bar{\rho}_{fcc}^2 = \bar{\rho}_{hcp}^2 \quad [6.60]$$

However, the two-electron hopping function is designated by the method to be zero for the fcc structure and an unknown non-zero value for the hcp structure:

$$W_{fcc}^{2e+} = 0 \quad [6.61]$$

$$W_{hcp}^{2e+} \neq 0 \qquad [6.62]$$

This unknown non-zero value for Equation [6.62] must be solved. With the information in Equation [6.57], and the fact that the effective fragment gap for fcc is different than that of hcp, Equation [6.56] can be further rewritten:

$$E_{hcp}^{FH}(\bar{\rho}) - E_{fcc}^{FH}(\bar{\rho}) = \left[\frac{\left(U_{hcp}^{eff}\bar{\rho}^2 + 2W_{hcp}^{1e}\bar{\rho}\right) - \left(U_{fcc}^{eff}\bar{\rho}^2 + 2W_{fcc}^{1e}\bar{\rho}\right)}{1+\bar{\rho}^2}\right] \qquad [6.63]$$

The terms containing the one-electron hopping energy cancel and the background density can be undistributed in the numerator on the right-hand side:

$$E_{hcp}^{FH}(\bar{\rho}) - E_{fcc}^{FH}(\bar{\rho}) = \left[\frac{\left(U_{hcp}^{eff} - U_{fcc}^{eff}\right)\bar{\rho}^2}{1+\bar{\rho}^2}\right] \qquad [6.64]$$

Substituting in Equation [6.58] for hcp and fcc:

$$E_{hcp}^{FH}(\bar{\rho}) - E_{fcc}^{FH}(\bar{\rho}) = \left[\frac{\left[\left(\eta_{hcp}^{*} - W_{hcp}^{2e}\right) - \left(\eta_{fcc}^{*} - W_{fcc}^{2e}\right)\right]\bar{\rho}^2}{1+\bar{\rho}^2}\right] \qquad [6.65]$$

Then, substituting Equations [6.61] and [6.62] yields cancellation of the effective fundamental gaps for fcc and hcp as well as the removal of the two-electron hopping energy for fcc:

$$E_{hcp}^{FH}(\bar{\rho}) - E_{fcc}^{FH}(\bar{\rho}) = \left[\frac{W_{hcp}^{2e}\bar{\rho}^2}{1+\bar{\rho}^2}\right] \qquad [6.66]$$

To proceed further, the background density must be further investigated:

$$\bar{\rho}(L,R) = \left(\frac{L}{L_{fcc}}\right)\exp\left[-\beta\left(\frac{R}{R_{eq}} - 1\right)\right] \qquad [6.67]$$

In Equation [6.15], the independent variables are *L*, the number of 1NNs, and *R*, the interatomic distance. The constants include the number of 1NNs, L_{fcc} = 12, and the

equilibrium interatomic distance, R_{fcc}^{eq} = 2.49 Å, and a fitted parameter, β, all of which were derived from fcc. It was previously noted that for the hcp structure, the number of 1NNs is L_{hcp} = 12. In addition, it should be noted that the hcp equilibrium interatomic distance is also R_{hcp}^{eq} = 2.49 Å. Thus, $R_{hcp}^{eq} = R_{fcc}^{eq}$. As a result, the background densities for hcp and fcc are equal, not only at the equilibrium interatomic distance, but at all interatomic distances:

$$\bar{\rho}_{hcp}(L_{hcp}, R) = \bar{\rho}_{fcc}(L_{fcc}, R) \quad [6.68]$$

For the hcp-fcc energy difference, the associated interatomic distance is at equilibrium. Applying $R_{hcp}^{eq} = R_{fcc}^{eq}$ to Equation [6.68] with Equation [6.67], it is determined that:

$$\bar{\rho}_{hcp}(L_{hcp}, R) = \bar{\rho}_{fcc}(L_{fcc}, R) = 1 \quad [6.69]$$

Substitution of Equation [6.69], followed by rearrangement to isolate the two-electron hopping energy gives:

$$W_{hcp}^{2e} = 2\left(E_{hcp}^{FH}(\bar{\rho}) - E_{fcc}^{FH}(\bar{\rho})\right) \quad [6.70]$$

The hcp-fcc energy difference, although inherently a function of the background density, must be solved by other means. Both the hcp and fcc structures differ by the planar stacking pattern; hcp has an ABABAB stacking pattern, whereas fcc has an ABCABC stacking pattern. The background density is unable to distinguish between both structures, given that $L_{fcc} = L_{hcp}$ and $R_{hcp}^{eq} = R_{fcc}^{eq}$. Consequently, a generalized stacking fault (GSF) curve is obtained using a first principles method, specifically density functional theory (DFT) with the PW91 GGA exchange-correlation functional. This involved shifting some of the atomic planes of an fcc supercell along the (111) plane in the [112] direction such that an hcp ABAB stacking pattern existed within the fcc ABCABC stacking pattern. The planes were displaced as far as $a_o/\sqrt{6}$ = 1.44 Å and

ten total energy points were obtained between 0.00 Å and 1.44 Å. The hcp stacking pattern was found to be at 0.72 Å along the displacement vector, and the fcc stacking pattern was existed at 0.00 Å and 1.44 Å along the displacement vector. All total energy points were subtracted from the total energy associated with the fcc stacking pattern. The total energy difference is divided by the area of the supercell that was parallel to the (111) plane. The resulting GSF curve had units of eV/Å^2, and was converted to units of mJ/m^2, for comparison to GSF energies in the literature. The final form of the GSF curve was fitted in the following function:

$$\Delta E_{GSF}^{VASP} = d^2[a_1 exp(-b_1(d-c_1)^2) + a_2 exp(-b_2(d-c_2)^2)]\frac{mJ}{m^2} \qquad [6.71]$$

The dependent variable is the displacement vector, *d*, and the fitted variables are a_i, b_i, *and* c_i, for which *i*=1,2. The above fitted expression fits the stable GSF energy as well as the unstable GSF energy, which has the ABCCAB stacking pattern and is an intermediate pathway in the GSF curve.

Equation [6.71] is related to the VASP hcp-fcc difference, but it does not yet equate to the difference for the FH method. Equation [6.71] can be equated to the hcp-fcc difference through the following: 1) changing the energy units from mJ/m^2 to eV, by multiplying by the area of the supercell in VASP, which the atomic planes were shifted (10.75 Å^2), then 2) multiplying by 2 to account for the interaction of two fixed atomic planes that are above and below the stacking fault, and finally by 3) dividing by 16021.7646 mJ/m^2. Therefore, Equation [6.18] is rewritten and the VASP hcp-fcc energy difference in terms of eV becomes:

$$\Delta E_{GSF}^{VASP} = 0.001342 d^2[a_1 exp(-b_1(d-c_1)^2) + a_2 exp(-b_2(d-c_2)^2)]eV \qquad [6.72]$$

Equation [6.72] is illustrated in Figure 6.1, along with the corresponding VASP computations. The above expression is equitable to the hcp-fcc difference in Equation [6.55]:

$$E_{hcp}^{FH}(\bar{\rho}) - E_{fcc}^{FH}(\bar{\rho}) = F_{hcp}^{FH}(\bar{\rho}) - F_{fcc}^{FH}(\bar{\rho}) \qquad [6.73]$$

Consequently, Equation [6.72] is rewritten using Equation [6.70]:

$$W^{2e} = 0.002683d^2[a_1 exp(-b_1(d-c_1)^2) + a_2 exp(-b_2(d-c_2)^2)]eV \qquad [6.74]$$

Equation [6.74] expresses the two-electron hopping energy directly as a function of the displacement, *d*, of atomic planes along the (111) plane in the [112] direction. Consequently, the two-electron hopping energy becomes directly related to the hcp-fcc difference.

6.3 The Fragment Hamiltonian Method applied to Ni

Having developed the FH method, this section demonstrates the application of the method with Ni. All first principles computations for the model were done with the VASP 4.6 code[81] using the PW91 exchange-correlation functional.[157,158] Since the FH method accounts for only 1NNs, binding curves of the fcc, simple-cubic (sc), 2d square, and 1d linear chain structures were computed. They structures were fitted to the third-order Rose equation of state (EOS):

$$E_{Rose}(R) = -E_0\left(1 + a^* + \delta\frac{(a^*)^3}{\alpha + a^*}\right)\exp(-a^*) + E_{\text{off}} \qquad [6.75]$$

In Equation [6.75], E_o is the cohesive energy, R is the 1NN distance, δ is the third-order fitted parameter, E_{off} is the total offset energy of the binding curve at large R, and a^* has the following form:

$$a^* = \alpha\left(\frac{R}{R_0} - 1\right) \qquad [6.76]$$

In Equations [6.75] and [6.76], α is a fitted parameter related to the radial strain, R is the 1NN distance, and R_0 is the equilibrium 1NN distance. In the fits, the E_{off} were fitted for each structure because of the total energies of each structure at long range are not expected to be similar due to the differences in coordination. Table 6.3 lists the values of the parameters for each Rose EOS fit. As mentioned in the Introduction, specific for any EAM is the computation of the pair potential. A form like Equation [6.2] is used for the FH method with the fcc structure as the reference

$$\phi(R) = \frac{2}{L_{fcc}}\left(E_{fcc}^{VASP}(R) - F_{fcc}^{FH}\left(\bar{\rho}_{fcc}(R)\right)\right) \qquad [6.77]$$

In the above derivation of the pair potential, $E_{fcc}^{VASP}(R)$ is the VASP binding curve as a function of the 1NN distance, R, $F_{fcc}^{FH}\left(\bar{\rho}_{fcc}(R)\right)$ is the embedding functional as a function of the fcc background density, and L_{fcc} is the number of 1NNs for the fcc structure, which is 12.

The next factor that needs to be examined is the behavior of the VASP total energy difference between fcc and the other three structures. Elucidation of these energy differences is illustrated here as a preview of the behavior of any function that depends on the total energy difference between fcc and the other structures. This is done simply with Equation [6.50], the FH cohesive energy expression:

$$\Delta E_v(R, L_v) = E_v(R, L_v) - \frac{L_v}{L_{fcc}} E_{fcc}\left(R, L_{fcc}\right) \qquad [6.78]$$

In the above expression, v specifies the sc, 2D square, or 1D linear chain. Also, Equation [6.78] removes the pair potential from each total energy, thereby giving the

difference of the embedding energy between the *v* and fcc structures. Figure 6.2 illustrates the total energy difference. The illustration demonstrates that only ΔE_{sc} has the necessary functional behavior with the increase in ΔE with decreasing R. The other ΔE functions continue to decrease with increasing R. Therefore, the sc binding curve is the only other suitable function for fitting other parameters.

The background density for the FH method is taken to be a simple exponential decay function:

$$\bar{\rho}(R,L) = \sqrt{\frac{L}{L_{fcc}}}\rho^{(0)}\exp\left(-\beta^{(0)}\left(\frac{R}{R_0}-1\right)\right) \equiv \sqrt{L}\rho^{(a)}(R) \qquad [6.79]$$

In Equation [6.79], the background density is a function of the 1NN distance, R, and the 1NN atomic coordination, L. The constants include the $\beta^{(0)}$ parameter, which is fitted from the sc binding curve, R_0, which is taken to be the fcc 1NN equilibrium distance in Table 6.3, and the $\rho^{(0)}$ coefficient, which is also fitted from the sc binding curve. Both $\beta^{(0)}$ and $\rho^{(0)}$ are listed in Table 4.

Finally, the one-electron hopping function, w^{1e}, is also taken to be a simple exponential decay function:

$$w^{1e}(R) = w^{1e}\exp\left(-\gamma^{1e}\left(\frac{R}{R_0}-1\right)\right) \qquad [6.80]$$

The w^{1e} coefficient and the γ^{1e} are fitted from the sc binding curve and are listed in Table 6.4. Also, the effective gap energy, U^{eff}, is set to twice the value of the Parr-Pearson chemical hardness for Ni, listed in Table 6.4.[155] No functional relation was made between the reference structures and the two electron hopping energy, w^{2e}, and the associated decay constant, γ^{2e}, so they were set to zero.

Figure 6.3 illustrates a plot of $w^{1e}(R)$, $\bar{\rho}(R, L_{fcc})$, $\phi(R)$, and $F(\bar{\rho}_{fcc}(R), L_{fcc})$. The $w^{1e}(R)$ function increases slowly with the decreasing *R,* mainly due to the fitted one-electron parameter, γ^{1e}. In contrast, the $\bar{\rho}(R, L_{fcc})$ function increases much faster than the $w^{1e}(R)$ function with decreasing R. The $F(\bar{\rho}_{fcc}(R), L_{fcc})$ functional behaves as a negative exponential decay function, thus demonstrating an attractive energetic contribution to the FH method. In contrast, the $\phi(R)$ function behaves almost like a positive exponential decay function, providing the repulsive energetic balance to the $F(\bar{\rho}_{fcc}(R), L_{fcc})$, the sum of which produces the FH total energy.

Figure 6.4 illustrates the fcc, SC, 2d square, and 1d chain binding curves computed with the FH method and VASP. The fcc FH curve fits the VASP fcc curves perfectly and the sc FH curve fits the VASP curve almost perfectly, by design of course. The pair potential was derived using the fcc fitted binding curve, and the parameters in Table 6.4 were fitted to the sc VASP binding curve. As for the 2d square curve, the FH method deviates from the VASP data at equilibrium by approximately 0.1 eV. Also, for the 1d chain, the FH method deviates from VASP data at equilibrium by approximately 0.3 eV. The latter two structures were not applied as references from which parameters were derived, so perfect fits were not expected. Nevertheless, the FH method provides an approximation in fitting the 2d square and 1d chain.

Some energetic properties were computed with the FH method for Ni. This include the three principal elastic constants for fcc, C_{11}, C_{12}, and C_{44}, the vacancy formation energy, the (100) and (111) surface energies and the generalized stacking fault (GSF) pathway. The bulk modulus, 180.4 GPa, is implicitly entered into the FH method since the α variable of the Rose EOS is a function of the bulk modulus. The

computed elastic constants as well as experimental[159] and VASP values are given in Table 6.5. The values computed using the FH method agree within 10% of experimental values and are thus acceptable. However, the anisotropy ratio, computed with $A=(C_{11}-C_{12})/(2C_{44})$, is 0.5 using elastic constants from the FH method. This differs from the anisotropy ratio computed from VASP and experimental elastic constants, 0.48 and 0.4, respectively. The deficiency of the anisotropy ratio from the FH method is due to the lack of angular contributions to the background density, as found in MEAM.

The vacancy formation energy as computed with the FH method is 1.59 eV, compared to 1.62 eV from VASP computations, and 1.4-1.6 eV for MEAM.[160] The vacancy formation energy from the FH method agrees very well with these other values.

The (100) and (111) surface energies were computed with the FH method. Since the method only accounts for 1NN interactions, only the surface and near-surface atoms were considered in the computations. An description of the unit cells for each computation is given in Ref. [155]. The surface energies as a function of the surface radial strain is given in Figure 6.5. The FH method highly underestimates the surface energies, in comparison to VASP computations. This is likely due to the lack of angular contributions to the background density in the FH embedding function. Only radial contributions are accounted in the FH background density. Also, surface energetics depend highly on second nearest-neighbor interactions and the FH method implements the 1NN approximation.

Finally, the GSF pathway is considered. In this pathway, a displacement of the fcc bulk structure is executed along the (111) atomic plane in the <112> direction. This process is described as well in the previous section. Figure 6.6 illustrates the GSF

pathway as computed with the FH method and VASP. The FH method covers only approximately half-way through the GSF pathway, whereas the VASP computations were taken to the hcp coordination, which occurs at a displacement magnitude of $a_{lat}/\sqrt{(6)}$. The value a_{lat} is the fcc Ni lattice constant, which is a_{lat} = 2.4953 Å * $\sqrt{(2)}$ = 3.5289 Å. If computations with the FH method were done beyond the GSF energy maximum, which is the unstable stacking fault, the FH method would have progressed towards a γ_{GSF} = 0.0 eV. The FH method lacks the angular contributions to the background density to differentiate between the fcc and hcp atomic coordination, since they have the same number of nearest neighbors, $L_{fcc} = L_{hcp}$ = 12. . Therefore, the FH method currently cannot tell between the fcc and hcp structures. Future work will concentrate on amending this deficiency. The FH method predicts an unstable stacking fault energy of γ_{USF} = 275 mJ/m^2, which is in agreement with VASP computations that predict γ_{USF} = 265 mJ/m^2.

6.4 Conclusions

In this chapter, the FH method is developed. It takes into account the many-electron wavefunction, the Hamiltonian decomposition, and charge state variables for the atoms to describe the total energy of a many-electron system. The FH method is also able to account for the electronic behavior when two atoms, or fragments, bond as it depends on the effective energy gap, the one-hopping energy, the two-electron hopping energy, and hopping functions that are modulated with regard to charge and ionicity. Finally, the method can be extended to incorporate pair interactions between fragments.

The FH method was applied to Ni[155] through parameterization of the embedding function and the one-electron hopping energy. Parameterization was accomplished using VASP binding curve computations with the PW91 exchange-correlation functional of the fcc, sc, 2d square, and 1d chain structures. The FH method was found to fit the fcc and sc structures very well and the 2d square and 1d chain structures approximately. The three principal elastic constants for fcc, C_{11}, C_{12}, and C_{44}, the vacancy formation energy, the (100) and (111) surface energies and the generalized stacking fault (GSF) pathway were computed with the FH method. The computed elastic constants were found to agree very well with VASP computations and experimental findings. As well, the vacancy formation energy computed with the FH method also agreed with experiment within a few eVs. The (100) and (111) surface energies were highly underestimated by the FH method in comparison to VASP computation. The deficiency in the FH method was that the background density only accounted for radial contributions but not angular contributions, and the 1NN approximation limits the range of energetics for surface atom reconstruction.[153] Finally, the GSF pathway was computed with the FH method. While an unstable stacking fault energy was computed that nearly matched VASP computations, the stable GSF energy was not computed. The FH method is not able to differentiate between the fcc and hcp coordination, both of which include 12 1NN atoms.

Despite the performance of the FH method to recreate VASP binding curves of various structures, it is limited in the capability to accurately compute other important energetic properties. The FH method was found lacking in the computation of surface energies and the GSF pathway. More development of the background density is needed,

including angular functions that differentiate between atomic coordinations. Also, the 1NN approximation may not be sufficient. At least 2NN interactions need to be accounted, as in MEAM. With these modifications, the FH method will be applicable to a larger database of reference structures and should compute surface energetics and the GSF pathway more accurately.

Table 6.1: Fitted variables for the GSF curve obtained from VASP

Fitted Variable
a_1=700.000
b_1=3.000
c_1=0.376
a_2=100.000
b_2=0.473
c_2=2.800

Table 6.2: Fitted and VASP GSF energies in mJ/m^2

	Stable GSF	Unstable GSF
VASP (PBE)	135.39	268.49
Fit	135.20	268.77

Table 6.3: Fitted Rose EOS parameters for the reference crystal structures; table is taken from Ref. [155].

	fcc	sc	2d square	1d chain
E_0 (eV)	4.9165	4.2942	3.4962	2.0865
α	4.8858	4.8365	4.5289	4.2220
δ	0.22119	0.4041	0.3150	0.0874
R_0 (Å)	2.4953	2.3292	2.2591	2.1793
E_{off} (eV)	-0.53803	-0.49792	-0.46425	-0.59421

Table 6.4: Fitted parameters for the FH method; table is taken from Ref. [155].

$\rho^{(0)}$	$\beta^{(0)}$	w^{1e} (eV)	γ^{1e}	U^{eff}
2.50	1.55	2.625	2.6	6.46

Table 6.5: Elastic constants (in GPa) determined with VASP, FH, and Expt.; Table is taken from Ref. [155].

	C_{11}	C_{12}	C_{44}
VASP (PW91)	274.1	154.3	125.1
FH	262.6	139.3	123.8
Expt.	246.5	147.3	124.7

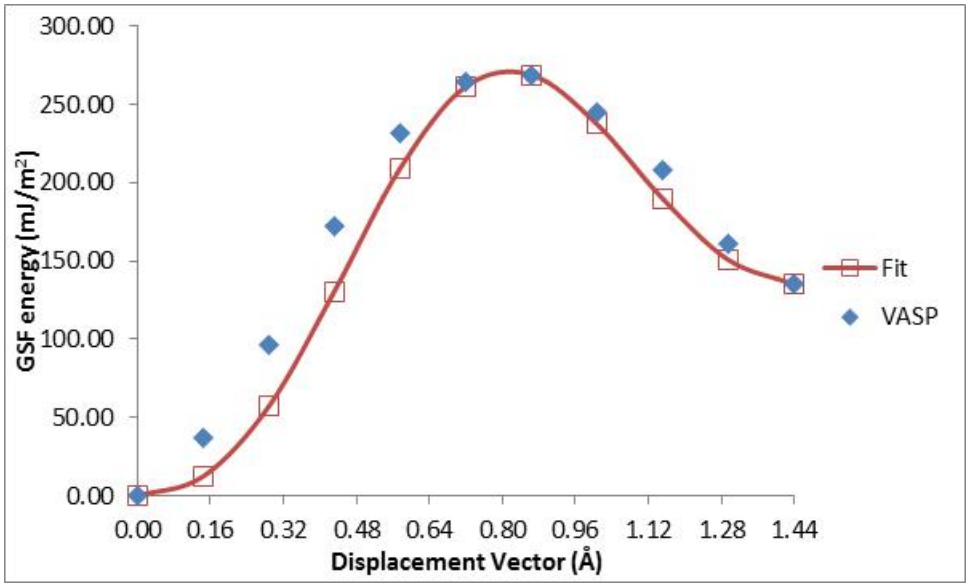

Figure 6.1: Fitted (red) and VASP (blue) GSF pathways

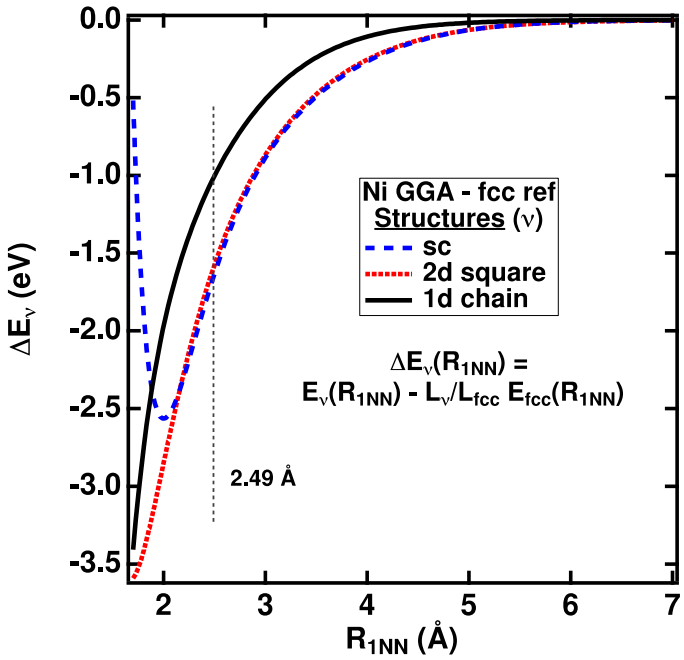

Figure 6.2: VASP total energy differences between fcc and the sc, 2d square, and 1d linear chain structures. The ΔE_{sc} function has the correct behavior as it only demonstrates an increase in the energy difference; figure is taken from Ref. [155].

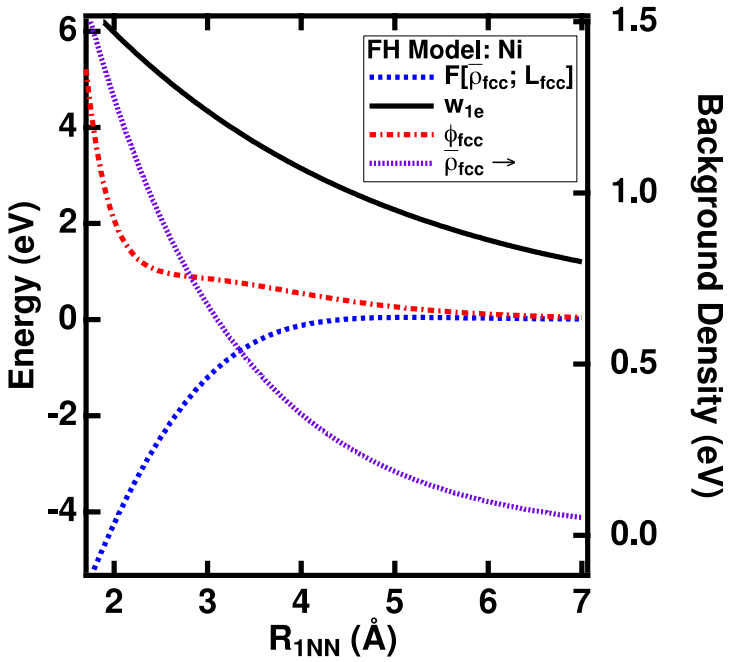

Figure 6.3: The FH embedding functional, the one-electron hopping energy, the pair potential, and the fcc background density (listed on top-right from top-to-bottom respectively); figure is taken from Ref. [155].

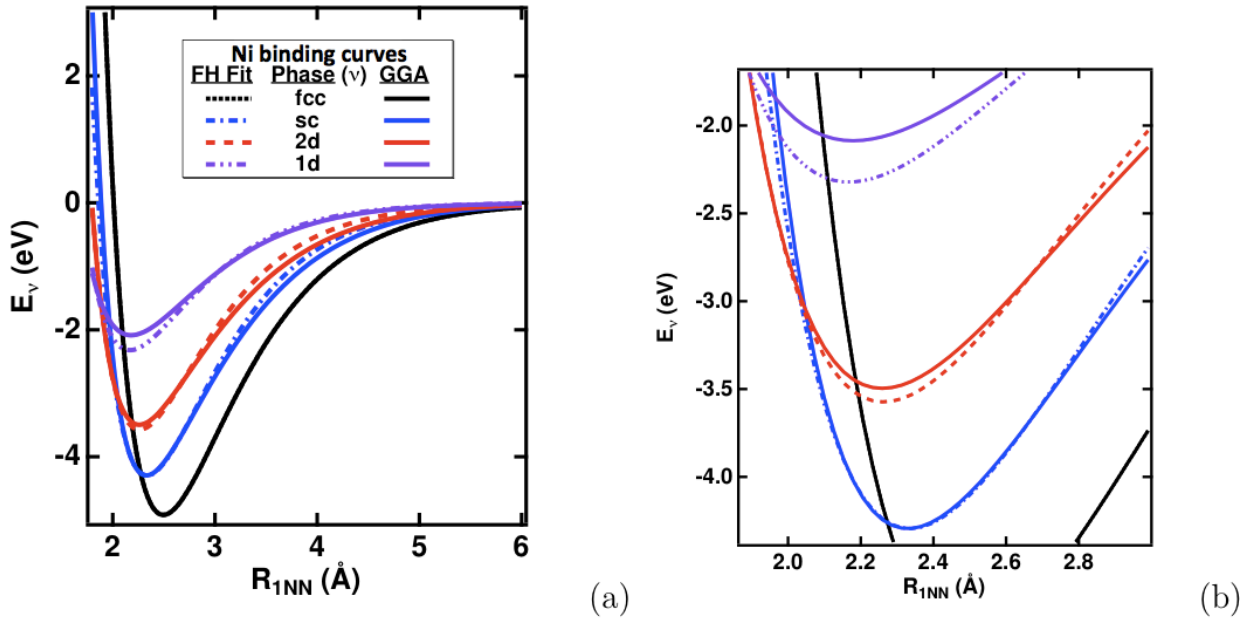

Figure 6.4: Ni binding curves for the fcc, sc, 2d square, and 1d chain structures; figure is taken from Ref. [155].

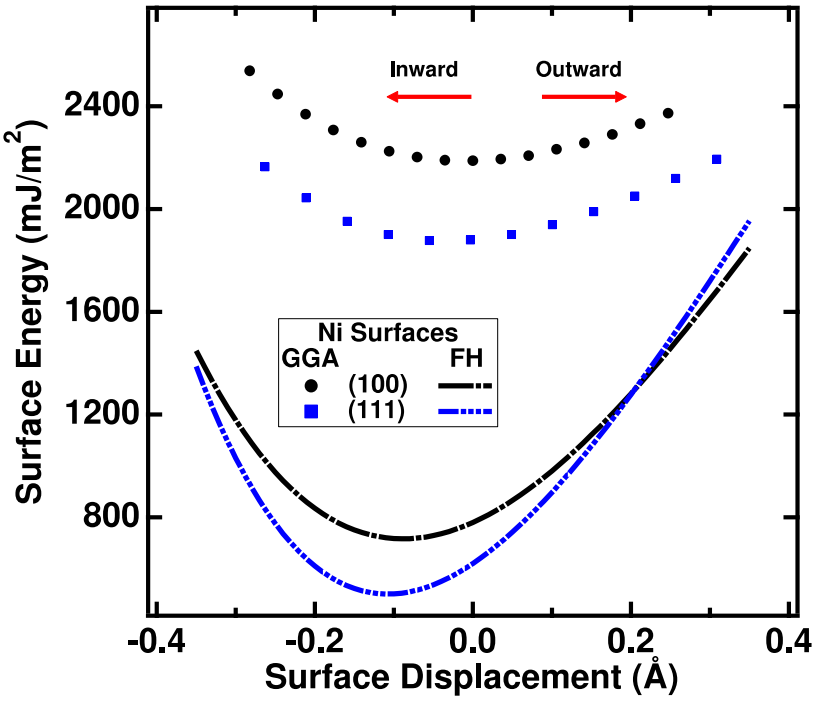

Figure 6.5: The (100) and (111) surface energies as a function of surface displacement; figure is taken from Ref. [155].

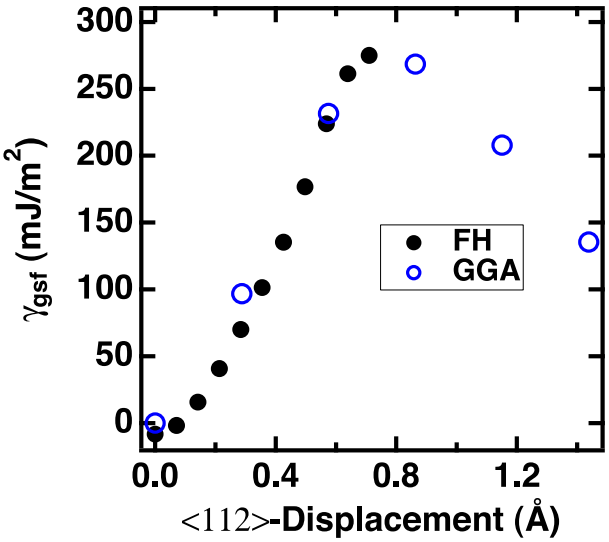

Figure 6.6: The GSF pathway as a function of the (111) planar displacement along the <112> direction; figure is taken from Ref. [155].

CHAPTER 7

THE MULTI-STATE MODIFIED EMBEDDED ATOM METHOD

7.1 Background – Potential Development

The development of atomistic potentials centers upon the refinement of mathematical models that capture the correct interatomic interactions. Central to this process is how the total energy, E_{total}, is described as a function of the atoms that comprise the system, and the computational cost. The simplest process by which to describe atomic interactions is a pair-potential (ϕ). The potential energy is described simply as a sum of all the atomic interactions:

$$E_{total} = \frac{1}{2}\sum_{i=1}^{n}\sum_{j=1}^{n}\phi(r_{ij}) \qquad [7.1]$$

In the above, $\phi(r_{ij})$ is fitted to the attractive and repulsive behavior of the observed atoms, *i* and *j*. Such pair potentials include the Lennard-Jones (LJ) and the Morse potentials. Both are simple and require fitting three and two parameters, respectively.

Pair potentials, however, are limited to single bonds, as illustrated in Equation [7.1], since they require a summation over pair of bonded atoms. Therefore, local coordination must be described. N-body potentials incorporate the local environment for each atom. Daw and Baskes[153] developed an N-body potential, the embedded atom method (EAM), which incorporates a pair potential, which describes the interaction between atom pairs, and the embedding energy functional (*F*), which accounts for the local environment by neighboring atoms in the background density (ρ_i):

$$E_{total} = \sum_{i}\left[F(\bar{\rho}_i) + \frac{1}{2}\sum_{j\neq i}^{n}\phi(r_{ij})\right] \qquad [7.2]$$

Many forms of both the pair potential $\phi(r_{ij})$ and the embedding energy functional F within EAM exist.[48,149,150,153,154,161] For example, Oh and Johnson incorporated simple parameterized exponentials in the pair potential and embedding energy functional and that yielded reasonable results in earlier EAM models for face cubic centered (fcc) metals.[162] As a test of fcc metals (Al, Cu, Ag, Au, Ni, Pd, and Pt), they computed vacancy formation energies within 0.1 eV of experiment, but they also computed anisotropy ratios that had a wide deviation range from 0.02 for Cu to 1.67 for Al. Baskes also derived a parameterized logarithmic form of the embedding function and, with a cohesive energy curve (as a reference structure), solved for the corresponding pair potential using an equation similar to Equation [7.2].[163] The only difference is that the summation in Equation [7.2] was replaced with *Z,* which counts the nearest neighbor atoms *j* since the bond distance within the local coordinate is the same for bulk materials and surfaces:

$$E_{total} = \sum_i \left[F(\bar{\rho}_i) + \frac{Z_i}{2} \phi(r_{ij}) \right] \qquad [7.3]$$

Implementation of the EAM has been shown to accurately describe numerous properties in metals, including defects,[151] liquids,[152] surfaces,[151-153] and alloys.[151] It was found that only first nearest-neighbor (1NN) interactions were necessary to reproduce material properties, including vacancy formation energies, bulk and elastic moduli, and lattice constants. However, the EAM was limited in its ability to describe bond bending and shearing, which introduces changes in the symmetrical orientation of atoms. Since the background density is composed of a sum of symmetric atomic densities, the EAM is unable to reproduce changes to the symmetry. To account for this deficiency, Baskes introduced corrective densities that would mimic the angular dependency of electron

density and therefore incorporate symmetry within the local coordination. As a result of this correction, the modified embedded atom method (MEAM) was developed and applied to forty-six elements, including ten fcc, twenty hexagonal closed-packed (hcp) ten body-cubic centered (bcc), three diamond cubic (DC), and three trimer molecules. MEAM was shown to reproduce cohesive energies, lattice constants, bulk and shear elastic moduli, and surface properties very well.[147,164] In this same study, Baskes also revisited the 1NN approximation by considering the atomic screening that occurs between the second nearest neighbors (2NN) and 1NNs, With respect to distance, 2NN interactions were expected to be negligible when the ratio of the 2NN distance and the 1NN distance was greater than 1.4 due to the exponential decay of the electron density. Therefore, the 1NN approximation should suffice for most solid-state structures.

However, for the bcc structure, the 2NN to 1NN ratio is approximately 1.15, and therefore the 2NN interactions were considered to be non-negligible. A modification to the total energy expression was consequently proposed by Baskes,[147,160] which incorporated a "screening function" (*S*):

$$E_{total} = \sum_i \left[F(\bar{\rho}_i) + \frac{Z_i}{2} \phi(r_{ij}) S_{ij}^{\phi}(C) \right] \qquad [7.4]$$

In the above, screening is a function of the screening parameter, *C*, between 2NN atoms *i* and *j*, and an intervening 1NN atom. If atoms *i* and *j* are both 1NNs, then *S* =1, and the pair potential remains unscreened. However, if atoms *i* and *j* are both 2NNs, then *S* may not be unity. To determine the magnitude of screening, a geometric perspective is utilized. Consider an ellipse on the [x,y] plane, and at the endpoints of the ellipse, on the *x* axis, 2NN atoms *i* and *k* exist. Also, along the ellipse between both

atoms, 1NN atom *j* is allowed to move. In this illustration, the screening parameter, *C*, can be found in the corresponding equation of this ellipse:

$$x^2 + y^2 \frac{1}{C} = \left(\frac{1}{2} r_{ik}\right)^2 \quad [7.5]$$

The screening parameter can be evaluated by the following equation:[160]

$$C = \frac{2\left(X_i + X_j\right) - 1 - \left(X_i - X_j\right)^2}{1 - \left(X_i - X_j\right)^2} \quad [7.6]$$

In which:

$$X_i = \left(\frac{r_{ik}}{r_{ij}}\right)^2, l = i, j \quad [7.7]$$

The screening of the pair potential between atoms *i* and *j* by an atom *k* is approximated by:

$$S_{ij}^{\phi} = \prod_{k \neq i,j} S_{ikj}^{\phi} \quad [7.8]$$

Modification of the 1NN approximation through the implementation of the screening function allowed for an improved description of the bcc structure in MEAM.

Central to MEAM is a reference structure that is used to build the potential energy expression. This can be fit simply with the Rose equation of state,[165] and then applied to solve for the embedding energy, pair potential, and the MEAM densities. The Rose equation of state is given in the following:

$$E_{Rose}(r) = -E_o \left(1 + \alpha \left(\frac{r}{a} - 1\right) + \delta \left(\frac{r}{a} - 1\right)^3\right) exp\left(-\alpha \left(\frac{r}{a} - 1\right)\right) \quad [7.9]$$

In Equation [7.9], E_o is the cohesive energy, *r* is a distance variable, *a* is the distance at which the energy minimum occurs, and E_o, α, and δ are fitting parameters to be optimized. The MEAM potential performs remarkably well for materials similar to the

reference structure. For non-equilibrium structures *that are not reference structures or not fitted by the MEAM potential*, however, it fails to give accurate energetics. At the same time, recent advances in the computational efficiency of first principles calculations have led to accurate energetics of non-equilibrium structures for materials that also exist in nature. This revealed a new opportunity to revise the MEAM formalism with a “multi-state” approach.

Baskes et al.[166] have developed a multi-state modified embedded atom method (MS-MEAM), which encompasses a vastly different approach to constructing a potential. It uses multiple reference structures from first principles data to solve for the embedding function, pair potential, and densities. The largest difference is the way in which these functions were fitted; in MEAM, the reference structure is used to solve for variables for the MEAM densities, which are parameterized exponentials. By contrast, MS-MEAM uses reference structures to map empirical functions for the MS-MEAM densities and the pair potential; only the embedding function has an analytical form as an initial guess, which is optimized to fit the fcc reference structure with the pair potential. To better model local defects and large strains, transformation pathways between reference structures are also fitted. MS-MEAM has superior transferability in metals as it not only reproduces fitted reference structures, but it also predicts other pathways between other reference structures. Screening is an important process for transformation pathways because the 1NN approximation fails during the transformation process. It was established for MS-MEAM that screening behaves as a sigmoidal function with respect to relative distance between atoms. MS-MEAM was first implemented for Cu[166] and demonstrated a much better fit of binding curves and energetic and thermodynamic

properties, compared to other Cu EAMs. It also correctly predicted the stacking fault energy for Pu.[167]

A Ti potential has been constructed using MS-MEAM in this study. Ti was chosen because it plays a large role in aerospace, marine, industrial, and medical applications. The first implementation of MS-MEAM used Cu, which is a fcc stable material at 0 K; however, a hexagonally closed-packed (hcp) material, such as Ti, has not yet been modeled with MS-MEAM. In addition, the fcc and bcc forms of Ti are less stable than the hcp form, but all three have nearly degenerate binding energies, as to be illustrated in the DFT computations. Further, the fact that Ti hcp is more stable than fcc is implicit within the derived densities, and regulates the predictive capabilities of Ti MS-MEAM.

The layout of this report continues with the development of the MS-MEAM formalism, followed by a summary of properties that was used to derive the MS-MEAM functions. The results section compares and contrast binding curves, transformation pathways, optimized energies and volumes, and measurements of energetic and thermodynamic properties calculated from MS-MEAM and compared to those obtained using two Ti EAMs, each having been constructed by Zhou[168] and Ackland.[169] These EAM potentials were selected for comparison because they were simple to implement and they represent a sample of the diversity of EAMs from the literature. Finally, this report concludes with a brief summary.

7.2 Methodology

The total energy expression for MS-MEAM is given above in Equation [7.2]. As explained in the Introduction, Equations [7.2] and [7.3] are both applicable when symmetry must be described within the local coordination, particularly for the 1NN

approximation. To account for 2NNs, the screening function is incorporated into the total energy expression, as shown in Equation [7.4].

The embedding function has the following analytical form as an initial guess that was derived in Baskes[163] and is used to solve for the embedding energy for multiple atomic symmetries:

$$F(\bar{\rho}_i) = A\bar{\rho}_i ln(\bar{\rho}_i) + B\bar{\rho}_i \quad [7.10]$$

The *A* and *B* are the only parameters in Equation [7.9]. In this study, *A* and *B* have been set to 0.1 and -10, respectively. The background density, $\bar{\rho}_i$, can be expanded as a sum of the symmetric and angular densities:

$$(\bar{\rho}_i)^2 = (Z_i\rho_i^0) + \sum_{l=1}^{3} s^l \Upsilon^l(r_{ij}) \quad [7.11]$$

The first function on the right-hand side of Equation [7.11] is the product of the number of first nearest neighbors, Z_1, and the total symmetric density, which contains symmetric density calculated from first principles and a corresponding screening function for 2NN interactions:

$$\rho_i^0 = \sum_{j \neq i} \rho_i^{a0}(r_{ij}) S_{ij}^{\rho^0} \quad [7.12]$$

The second function on the right-hand side of Equation [7.11] contains the angular contribution to the background density, which a sum of the symmetry factors (*s*) and the total angular density (*Y*) for the angular components *l*. The MS-MEAM formalism strives to define Y^l directly from first principles data. In the original MEAM formalism, the angular densities were parameterized exponentials. However, a first principles

derivation of Y^l may or may not produce angular densities that behave as exponentials (this is explored in the next section), and therefore, rewritten as a difference of the squares of net partial positive and negative densities. This makes Equation [7.11]:

$$(\bar{\rho}_i)^2 = (Z_i\rho_i^0) + \sum_{l=1}^{3} s^l \left[\left(\rho_i^{l+}\right)^2 - \left(\rho_i^{l-}\right)^2\right] \quad [7.13]$$

The symmetry factors have been absorbed into the second part of right-hand side so that the net partial positive and negative densities include information about the symmetry. This can be illustrated by expanding the net partial densities as a function of the *x, y*, and *z* coordinates for a corresponding crystal structure:

$$\left(\rho_i^{1\pm}\right)^2 = \sum_{\alpha}\left[\sum_{j\neq i}\frac{r_{ij}^{\alpha}}{r_{ij}}\rho_i^{a1\pm}(r_{ij})S_{ij}^{\rho^1}\right]^2 \quad [7.14]$$

$$\left(\rho_i^{2\pm}\right)^2 = \sum_{\alpha,\beta}\left[\sum_{j\neq i}\frac{r_{ij}^{\alpha}r_{ij}^{\beta}}{r_{ij}^2}\rho_i^{a2\pm}(r_{ij})S_{ij}^{\rho^2}\right]^2 - \frac{1}{3}\left[\sum_{j\neq i}\rho_i^{a2\pm}(r_{ij})S_{ij}^{\rho^2}\right] \quad [7.15]$$

$$\left(\rho_i^{3\pm}\right)^2 = \sum_{\alpha,\beta,\gamma}\left[\sum_{j\neq i}\frac{r_{ij}^{\alpha}r_{ij}^{\beta}r_{ij}^{\gamma}}{r_{ij}^3}\rho_i^{a3\pm}(r_{ij})S_{ij}^{\rho^3}\right]^2 - \frac{3}{5}\sum_{\alpha}\left[\sum_{j\neq i}\frac{r_{ij}^{\alpha}}{r_{ij}}\rho_i^{a3\pm}(r_{ij})S_{ij}^{\rho^3}\right]^2 \quad [7.16]$$

In the above equations, the α, β and γ terms interchangeably signify the *x, y, and z Cartesian axes.* To maintain orthogonality between the angular electron densities, the product of 3/5 and Equation [7.14] is subtracted from the first term on the right-hand side of Equation [7.16].[170] The screening between atoms in the net partial densities is also approximated as a product:

$$S_{ij}^{\rho^l} = \prod_{k \neq i,j} S_{ikj}^{\rho^l} \quad [7.17]$$

The $\rho^{al\pm}$ terms are the net atomic partial densities that come directly from Y^l and contain information on the reference data used to derive Y^l. Illustrated below, ρ^{al+} is set to be a parameterized exponential, and ρ^{al-} in the following equations result in exponential behavior:

$$\rho_i^{a1+}(r_{ij}) = \Upsilon^l(r_{ij}^{low}) exp\left[-\kappa(r - r_{ij}^{low})\right] \quad [7.18]$$

$$\rho_i^{a1-}(r_{ij}) = \sqrt{\Upsilon^l(r_{ij}^{low}) + \left[\rho_i^{a1+}(r_{ij})\right]^2} \quad [7.19]$$

In Equation [7.18], a Y^l and low r_{ij} is used to initialize ρ^{al+} and a positive integer κ is selected to ensure the exponential behavior of Equation [7.19].

The symmetry factors are quantified contributions to the net partial densities that correspond to the symmetry of an atomic configuration. They can be determined for a structure using the atomic coordinates for a selected central atom *i* and its 1NN atoms *j*. The coordinates must be transformed such that the central atom exists at (0, 0, 0) on the (*x*, *y, z*) coordinate. Expressions for the symmetry factors can be made by setting all $\rho^{al\pm}$ = 1.0, thereby removing the information derived from first principles data, and isolating the symmetry information of the crystal structure:

$$s^1 = \sum_{\alpha} \left[\sum_{j \neq i} \frac{r_{ij}^{\alpha}}{r_{ij}} \right]^2 \quad [7.20]$$

$$s^2 = \sum_{\alpha,\beta}\left[\sum_{j\neq i}\frac{r_{ij}^{\alpha}r_{ij}^{\beta}}{r_{ij}^2}\right]^2 - \frac{1}{3} \quad [7.21]$$

$$s^3 = \sum_{\alpha,\beta,\gamma}\left[\sum_{j\neq i}\frac{r_{ij}^{\alpha}r_{ij}^{\beta}r_{ij}^{\gamma}}{r_{ij}^3}\right]^2 - \frac{3}{5}\sum_{\alpha}\left[\sum_{j\neq i}\frac{r_{ij}^{\alpha}}{r_{ij}}\right]^2 \quad [7.22]$$

Table 7.1 lists the symmetry factors for structures that are analyzed in this study. Thus far, the fcc, hcp, bcc, and DC structures have been introduced. The rest of this section introduces the other nine structures. It should be noted that “dimer” in Table 7.1 specifies the dimer molecule, which is the only listed structure that is non-crystalline. Also, the graphene structure is a three-coordinate planar structure; the sum of graphene stacking is known to produce a graphite structure.

To construct a Ti MS-MEAM potential, eight MS-MEAM functions must be determined:

$$\rho_i^{a0}(r_{ij}), \phi(r_{ij}), \Upsilon^l(r_{ij}), l = 1-3, S_{ikj}^{\phi}, S_{ikj}^{\rho^0}, S_{ikj}^{\rho^2} \quad [7.23]$$

This is completed with first principles data using the *Vienna Ab initio Software Package* (VASP) 4.6.[171] This software package uses density functional theory (DFT) in combination with either the Projector Augmented Wave (PAW) method[172] or pseudopotentials in the Kohn Sham one-electron basis set for atomic configurations within periodic boundary conditions. For this study, the PAW method with the Perdew-Burke-Ernzerhof (PBE) generalized gradient approximation (GGA) exchange-correlation functional[35,36] was used to obtain first principles data for the reference structures. The

PAW pseudopotential that incorporates the $(3d)^2(4s)^2$ valence states was used. Plane wave convergence tests were executed and it was found that an energy cutoff of 500 eV and a kpoint mesh of 9x9x9 yielded a total energy convergence of 1.0 meV/atom. Since Ti is a paramagnetic metal, then spin polarization calculations were attempted, but they yielded a negligible change in the total energy in comparison to non-spin polarization. Therefore, all calculations were done using non-spin polarization. All total energy computations of reference structures and transformation pathways that are necessary to solve for the MS-MEAM functions are listed in Equation [7.23]. Total energy computations of references structures were computed as a function of the nearest neighbor distance, r_{NN}, which defined in reference to the fcc equilibrium distance, a_{fcc}, computed from VASP:

$$r_{NN} = \frac{x}{a_{fcc}} \qquad [7.24]$$

In Equation [7.24], x is the nearest neighbor distance in the considered structure. So, for fcc at equilibrium, $r_{NN} = 1.0$. All total energy computations for reference structures were computed at ranges of $r_{NN} = 0.7\text{-}2.0$ at increments of 0.1 and of $r_{NN} = 2.0\text{-}4.0$ at increments of 0.2. The first range was extended to smaller values if necessary to obtain equilibrium distances for a reference structure. Having computed total energies for the reference structures, total energies per atom (*E/atom*) were determined by dividing each total energy by the number of atoms in the VASP computations. Next, the dissociated fcc *E/atom*, taken at $r_{NN} = 4.0$, was subtracted from all *E/atom* values for each reference

structure, such that they all approached 0 eV with increasing r_{NN}. This produced cohesive energy values for each reference structure. They were then divided by the equilibrium fcc cohesive energy. In this scheme, the fcc cohesive energy to be -1.0 eV. The Rose equation of state[165], given in Equation [7.9], was used to fit the cohesive energy curves as a function of r_{NN}.

7.3 Determination of MS-MEAM Functions

The foundation of previous MEAM potentials were rooted upon a single reference structure and parameterization within exponential densities; the parameters were determined through error minimization between the MEAM total energy and experimental or first principles vacancy formation energy, stacking fault energy, and the energy associated with the shear elastic constant. In contrast, the foundation of a MS-MEAM potential is rooted upon the binding curves of multiple structures to capture the various symmetries for a given atom type. To do so, a set of MEAM functions, illustrated in Equation [7.23], must be determined from the first principles data that is obtained in the manner that was described in the previous section. Table 7.2 lists the reference structures that are necessary for determination of the MS-MEAM functions.

The MEAM total energy expression from Equation [7.6] is a natural starting point for this endeavor. In addition, the first five MS-MEAM functions in Equation [7.23] are derived using reference structures with negligible 2NN interactions. As a result, the

summation of *i* can be removed, which yields a total energy expression dependent on 1NNs solely:

$$E_i = F(\bar{\rho}_i) + \frac{Z_i}{2}\phi(r_{ij}) \quad [7.25]$$

At this point, the symmetric density, ρ^{a0}, can be determined using the fcc and SC binding curves. Using Equation [7.25] and the embedding energy functional, Equation [7.8], the fcc and SC fitted functions are divided by the number of 1NNs and the SC function is subtracted from the fcc function; this removes the $\phi(r_{ij})$ dependence. Then the symmetric density can be written as a function of the fcc-SC cohesive energy difference:

$$\rho^{a0}(r_{ij}) = \frac{\Delta E^{ref}_{fcc-SC}(r_{ij})}{2A\ln 2} \quad [7.26]$$

Next, the most symmetric structure listed in Table 7.1, fcc, is used with the embedding energy function, Equations [7.11], [7.12], and [7.26] to solve for $\phi(r_{ij})$. Again, 2NNs are negligible in fcc, so all screening functions in Equation [7.12] are equal to 1, and the summation is removed; Equation [7.25] may consequently be applied in place of Equation [7.11]. Since fcc lacks angular density contributions to its structure, then all s^l equals 0 in Equation [7.10]. With that, Equation [7.26] applied into the embedding energy function, and setting A = 1 and B = -10, the following expression can be used to solve for the pair potential:

$$\phi(r_{ij}) = \frac{2}{Z_{fcc}}\left(E_{fcc} - F\left[Z_{fcc}\rho^{a0}(r_{ij})\right]\right) \quad [7.27]$$

The next set of MEAM functions to be determined is the Y^l total angular densities. To do so, Equations [7.10] and [7.25] are required. Unlike the two previous MEAM functions, Y^l are solved numerically since no analytical form can be derived. For this Ti MS-MEAM potential, Y^3 is determined first. Table 7.2 shows that either the DC or hcp structures should be used to solve for Y^3 because both structures exhibit angular dependency for only l = 3. Further, because hcp is the most stable form of Ti at 0 K, the temperature at which the first principles data was computed and Ti hcp is important for energetic properties including the stacking fault energy, it is preferable to determine Y^3 using hcp. At each r_{ij}, Y^3 is solved such that the error in following equation is minimized:

$$\Delta_{min}^{l=3} = E_{hcp}^{fit} - \left(F\left[\left(Z_{fcc}\rho^{a0}(r_{ij})\right)^2 + s_3^{hcp}\Upsilon^3(r_{ij})\right] + \frac{Z_{hcp}}{2}\phi(r_{ij})\right) \quad [7.28]$$

Next, Y^2 is determined. Table 7.2 shows that either the line or 2D-hex structures may be used as reference structures for determination of Y^2. Since Ti is a transition metal, high coordination would be indicative of metallic bonding. Therefore, 2D-hex is a better choice because of its atomic coordination, which is higher than the line structure. Again, at each r_{ij}, Y^2 is solved such that the error in following equation is minimized:

$$\Delta_{min}^{l=2} = E_{2D-hex}^{fit} - \left(F\left[\left(Z_{2D-hex}\rho^{a0}(r_{ij}) \right)^2 + s_2^{2D-hex}\Upsilon^3(r_{ij}) \right] + \frac{Z_{2D-hex}}{2}\phi(r_{ij}) \right) \quad [7.29]$$

Finally, Y^1 is determined. Table 7.1 illustrates that the dimer, beam, and zigzag-2 structures have Y^1 dependence:. None of these structures have angular dependence solely on Y^1, but with Y^2 and Y^3 already known the remaining total angular density is easily computed. The dimer structure is used to compute Y^1, despite its fewer 1NNs than zigzag-2, in order to incorporate a low coordinative density reminiscent of a molecule, which is unlike the other structures in Table 7.1. At each r_{ij}, Y^1 is solved such that the error in following equation is minimized to 0:

$$\Delta_{min}^{l=1} = E_{dimer}^{fit} - \left(F\left[\left(Z_{dimer}\rho^{a0}(r_{ij}) \right)^2 + \sum_l s_{dimer}^l \Upsilon^l(r_{ij}) \right] + \frac{Z_{dimer}}{2}\phi(r_{ij}) \right) \quad [7.30]$$

It was determined through the fitting process that for the binding curves of the zigzag and beam structure to rise in energy with decreasing nearest neighbor distance, a dampening function was necessary for the 3rd angular density of the form:

$$\Upsilon^3(r) = \Upsilon^3(r_{NN}) exp[3.0(r - r_{NN})], r < 0.98 \quad [7.31]$$

The range was chosen so that the energy minimum of hcp around r_{ij} = 1.00 would not be affected. This modification affects all structures that have a dependence on the 3rd angular density below a scaled distance of 0.98.

The final three MEAM functions are screening functions, S^{ϕ}, $S^{\rho 0}$, and $S^{\rho 2}$, listed in Table 7.2 as being fitted using the Bain, Trigonal, and 2D transformation pathways, respectively. For the angular densities, it was noted in Baskes[147] that the total energy of the symmetric densities with respect to the shear elastic constants is a function of ρ^{a0} and Y^2; therefore, the approximation is made for the angular screening functions that:

$$S_{ikj}^{\rho^1} = S_{ikj}^{\rho^2} = S_{ikj}^{\rho^3} \quad [7.32]$$

The transformation pathways require non-uniform strains, so this approximation based on the shear elastic constants was found to be adequate for Cu MS-MEAM calculations, and are used in this paper as well. Consequently, screening functions for ϕ, ρ^{a0} and Y^2 are only required. The reality of this numerical fitting procedure is somewhat more complex however and requires some in-depth analysis. The concept of screening invites the energetic contributions of 2NNs from reference structures that have negligible 2NN interactions. The transformation pathways between reference structures occur due to deformations that break the symmetry of the reference structures. As a result, atomic rearrangements can reduce the screening of 2NN atoms by 1NN atoms, thus allowing for the increase in energetic contributions by 2NN atoms. The orientation of an atom *i* with respect to the 1NN and 2NN atom, which functionally relates to the screening parameter, can be computed with Equations [7.6] and [7.7] within a screening ellipse that essentially varies the possible energetic interaction between atom *i* and its 1NN and 2NN. For the reference pathways, the fcc, bcc, SC, 2D-sq, and 2D-hex

structures are involved. Of these, significant 2NN interactions are present only in bcc. Consequently, to obtain accurate energetics of the bcc structure, the screening functions must be computed.

The screening functions for the Bain, Trigonal, and 2D transformation pathways were found in Baskes et al.[166] to be like a sigmoid function:

$$y(x) = [1 - (1 - x)^m]^2 \qquad [7.33]$$

In Equation [7.33], *m* is the only fitted parameter. This function can be used to develop trial solutions for the screening functions, which are then optimized to fit the transformation pathways. For convenience, in Equation [7.33], the independent variable is renamed from *x* to *C*, the screening parameter, and *y(x)* is renamed to *S(C)*, denoting the screening function. For ϕ, ρ^{a0} and Y^2, screening values are determined at $C = 2.0$ and $C = 1.5$; the former allows for exact fitting of the bcc cohesive energy at $r_{ij} = 1.0$ and the latter was chosen to obtain screening data in the middle of the Trigonal and 2D pathways. Shown in Figure 7.1, for the fitting procedure, the Bain, C_3, and C_4 screening parameters are used. This permits exact fitting of the Bain pathway, and flexibility for fitting the Trigonal and 2D pathways, since C_3 and C_4 can be applied for both, as previously noted by Equations [B.14] and [B.15] in Appendix B. Specifically, to solve *S(C)* at $C = 2$ for ϕ, ρ^{a0} and Y^2, the Bain and C_4 screening parameters are applied. The Bain path at $C = 2$ corresponds to the bcc structure, which does not contribute angular

density to the energetics. Therefore, the following equation is minimized on the Bain screening parameter:

$$\Delta_{C=2}^{bcc} = E_{C=2}^{bain} - \left[F[\bar{\rho}_i] + \frac{Z_{bcc}^{1NN}}{2}\phi(r_{ij}) + \frac{Z_{bcc}^{2NN}}{2}\phi(r_{ij})S_{ij}^{\phi}(C) \right] \quad [7.34]$$

in which the background density contains 1NN and 2NN atoms:

$$\bar{\rho}_i = \rho_0 = Z_{bcc}^{1NN}\rho^{a0}(r_{ij}) + Z_{bcc}^{2NN}\rho^{a0}(r_{ij})S_{ij}^{\rho^0}(C) \quad [7.35]$$

The screening between atoms *i* and *j* is given by Equation [7.16]. Following that, on the Trigonal pathway with C_4 screening parameter, C = 2.0 has $\theta = 70.59^o$. This is midway between the fcc and SC structures, so the symmetry is broken on the pathway and 2NN atoms do contribute to the energetics. Therefore, the following equation is minimized on the C_4 screening parameter, using the *S(C)* already determined for ϕ and ρ^{a0}:

$$\Delta_{C=2}^{trig} = E_{C=2}^{trig} - \left[F[\bar{\rho}_i] + \frac{1}{2}\sum_{i\neq j}^{1NN}\phi(r_{ij}) + \frac{1}{2}\sum_{i\neq j}^{2NN}\phi(r_{ij})S_{ij}^{\phi}(C) \right] \quad [7.36]$$

in which the background density contains 1NN and 2NN atoms:

$$(\bar{\rho}_i)^2 = \left(\sum_{i\neq j}^{1NN}\rho^{a0}(r_{ij}) + \sum_{i\neq j}^{2NN}\rho^{a0}(r_{ij})S_{ij}^{\rho^0}(C) \right) + \left(\sum_{i\neq j}^{1NN}\Upsilon^2(r_{ij}) + \sum_{i\neq j}^{2NN}\Upsilon^2(r_{ij})S_{ij}^{\rho^2}(C) \right) \quad [7.37]$$

Next, *S(C)* is determined at C = 1.5 for ϕ, ρ^{a0} and Υ^2. At this screening parameter, no reference structures exist along the Bain, Trigonal, or 2D pathways for the Bain, C_3, and C_4 screening parameters. Therefore, three guess *S(C)* values must be selected for ϕ,

ρ^{a0} and Y^2 at C = 1.5, and resulting energies on the three pathways must be minimized with the VASP reference pathways at C = 1.5. The resultant *S(C)* must each be greater than 0.0. A multi-dimensional optimizer, such as the Amoeba algorithm,[173] can be used to execute this process in the following equation:

$$\Delta_{C=1.5}^{pathway} = E_{C=1.5}^{pathway} - \left[F[\bar{\rho}_i] + \frac{1}{2}\sum_{i\neq j}^{1NN} \phi(r_{ij}) + \frac{1}{2}\sum_{i\neq j}^{2NN} \phi(r_{ij}) S_{ij}^{\phi}(C) \right] \qquad [7.38]$$

The background density, $\bar{\rho}_i$, in Equation [7.30] is given in [7.29]. In Equation [7.30], the superscript "*pathway*" specifies all three pathways. The optimization process is subject to minimizing the sum of the squares of the error from Equation [7.29]:

$$\left(\Delta_{C=1.5}^{pathway}\right)^2 = \left(\Delta_{C=1.5}^{Bain}\right)^2 + \left(\Delta_{C=1.5}^{trig}\right)^2 + \left(\Delta_{C=1.5}^{trig2D}\right)^2 \qquad [7.39]$$

7.4 Results

7.4.1 MS-MEAM Functions

The MS-MEAM functions in Table 7.2 must first be determined. The total symmetric and angular densities are given in Figure 7.2. The symmetric density exhibits exponential behavior, which stems from Equation [7.49], since the $\Delta E_{fcc-SC}^{ref}(r_{ij})$ behaves this way. Equations [7.28]-[7.30] are used to derive the angular densities. As illustrated in Figure 7.2, the functionals behave differently. They are dependent on the symmetric density and the reference fits in their derivation. Despite the symmetric density being an exponential function, the angular densities resemble the reference fits. Specifically, the 1st angular density, derived from the $\Delta E_{fcc-dimer}^{ref}(r_{ij})$ fit, behaves like a positive Rose equation of state, Equation [7.9]; the 2nd angular density, derived from the $\Delta E_{fcc-2Dhex}^{ref}(r_{ij})$, behaves like an negative Rose equation of state; and the 3rd

angular density, derived from the $\Delta E_{fcc-hcp}^{ref}(r_{ij})$ fit, behaves like a positive Rose equation of state. The partial angular densities, derived from Equations [7.18] and [7.19], are given in Figures 7.3a and 7.3b. With one of the angular density types, taking the difference of the squares of the positive and negative partial densities yields the corresponding total angular density.

The screening functions for the pair potential, the symmetric, and angular densities, are given in Figure 7.4. They all have sigmoid behavior. The screening functions for the pair potential and the symmetric density were set equal in the range of $0 < C < 2$. This range partially relates to the Trigonal transformation pathway, as it applies to the range of $0.5 < C < 2$. Fitting the screening functions in this range with the Trigonal pathway produced screening values for the symmetric density that were larger in magnitude than screening values for the pair potential at each C. Preliminary computations of hcp containing self-interstitials yielded disordered structures that were more stable than hcp. It was found that the resulting disordered structures involved relaxed interstitial atoms having C values within the range of $0.5 < C < 1.5$. The corresponding screening values for the symmetric density, being larger than those for the pair potential, were lowering the embedding energy too much during relaxation of the interstitial atom. The screening function for the angular densities was found to have very little effect in destabilizing the interstitial atom in hcp. Therefore, the screening functions for the pair potential and the symmetric density were set equal in the range of $0 < C < 2$, and varied in tandem along with the screening function of the angular densities. This was found to destabilize the hcp structures containing the interstitial atoms, on the range of approximately between 9 eV and 20 eV. To increase the stability

of these interstitial atoms between 1 and 5 eV, the screening function for the symmetric density was optimized in the range of $2 \leq C < 3$ for fitting with the Bain transformation pathway. The resulting difference between the screening functions for the symmetric density and the pair potential at each C exists at the sixth decimal. Therefore, the Bain pathway requires *nearly* equal 2NN interactions with the pair potential and the symmetric density and both giving a higher screening contribution than screening from angular density. Also, fitting to the Bain pathway using equal screening functions as an initial guess was found to stabilize the preliminary hcp interstitial atoms within the range of 1 to 5 eV. The self-interstitials are further explored in a later section.

7.4.2 Comparison of EAM Potentials with DFT

7.4.2.1 Binding Curves

An analysis of computed binding curves is observed here for MS-MEAM, the Zhou EAM, and the Ackland EAM and compared to VASP computations. Figures 7.5 through 7.17 illustrate these computations for a corresponding crystal structure. Each figure shows sets of binding energy curves, which have been scaled with regard to the fcc equilibrium cohesive energy, as a function of r_{NN} defined in Equation [7.24]. For the Figures 7.5 through 7.10, it is seen that all three EAMs fit well with the VASP binding curves for the fcc, hcp, bcc, oDC10, SC, and 2D-hex structures, particularly at the energy well of each binding curve. For all six structures except 2D-hex, MS-MEAM replicates the binding energies within the expansion regions of the curves very well, but the MS-MEAM binding energies deviate for the expansion of SC by a scaled energy of approximately 0.1. The binding energies computed with the Zhou EAM also seem to

deviate within the expansion regions of the curves, not only for SC, but also for hcp, fcc, bcc, oDC10, and 2D-hex. It should be noted that the hcp and 2D-hex were reference structures, and thus it is no surprise that MS-MEAM fits the hcp and 2D-hex VASP computations very well. Despite the low cut-off around r_{NN} ~ 1.7, the Ackland EAM is able to replicate the expansion regions of all six structures. All three EAMs do not replicate the energetics of the compression regions very well.

A formidable test of these EAMs is the computation of binding curves for low coordinative structures. Figures 7.10 through 7.17 show computed binding curves for the 2D-sq, DC, zigzag, beam, graphene, line, and dimer, respectively, for all three EAMs in comparison to VASP computations. For the 2D-sq binding curve, MS-MEAM seems to deviate within the energy well by about 0.5 eV, while the Zhou and Ackland EAMs overlap more closely with VASP energy well. For all three EAMs, the binding curves follow closely the VASP binding energies within the expansion regions, but they deviate very largely in the compression regions. Figure 7.12 illustrates binding energy curves for the DC structure. The Zhou and Ackland EAMs seem to overlap with VASP computations approximately well within the energy well and the compression regions, whereas MS-MEAM suffers a large deviation from the energy well computed by VASP. The source of this large deviation stems from application of the 3rd angular density, which was derived with hcp. The DC structure has density contribution from the symmetry and 3rd angular density only (see Table 7.1 for corresponding symmetry factors). As noted in Table 7.2, either the hcp or DC structures may be used to derive the 3rd angular density. Preliminary computations had shown that if DC was used to derive the 3rd angular density, hcp would be less stable than fcc by a scaled energy of

0.003 eV, but the DC fit would be exact. However, the DC structure could not be applied because Ti is a hcp-stable material; that is, hcp Ti is more stable than Ti fcc. Attempts were made to rectify the DC binding curve using a dampening function on the symmetric density of the form like in Equation [7.31], except with $\Upsilon^3(r)$ replaced with $\rho^{a0}(r)$, but this could not raise the energy without compromising the behavior of all other binding curves. It was found that Equation [7.33], as shown applied to the 3rd angular density, raised the energy well to its current energy around a scaled energy of -0.9. Figure 7.13 illustrates the graphene binding curves computed by all three EAMs and VASP. Unfortunately, MS-MEAM deviates from the corresponding VASP binding curve, but not as much as the Zhou EAM deviates. Figure 7.14 illustrates the zigzag binding curves. The binding curve computed by MS-MEAM overlaps the energy well of the VASP binding curve very well, whereas the other EAMs deviate. It was found that the dampening function, Equation [7.33], was essential for MS-MEAM to fit the zigzag structure. Without the dampening function, the zigzag binding curve was observed to lower infinitely in energy as r_{NN} decreased. Figure 7.15 illustrates the beam binding curves. The energy wells of all three EAMs seem to surround the energy well computed by VASP; however, the computed compression and expansion energetics do not agree with VASP computations. Finally, Figures 7.16 and 7.17 illustrate the binding curves for the line and dimer structures, respectively. All three EAMs do not agree very well with the VASP binding curve for the line structure. The same lack of overlap with VASP is observed with the dimer structure for all three EAMs. It is, at first, surprising to see that MS-MEAM does not replicate the VASP binding curve for dimer because it was used as a reference structure to derive the 1st angular density. However, the dimer structure also

has density contributions from the 3rd angular density, which contains the dampening function, Equation [7.33]. The absence of a perfect fit by MS-MEAM for the dimer binding curve may stem from the presence of this dampening function.

7.4.2.2 Equilibrium Curves

Table 7.3 shows the equilibrium energies and the associated nearest-neighbor distance in different crystals considered in this work. All structures are scaled by the fcc cohesive energies, E_{eq}, and nearest-neighbor distance, r_{NN}. The fcc cohesive energies of fcc for all EAMs are in agreement, but differ very much from that obtained with VASP. This is likely due to the PBE functional used in the VASP computation, as GGA functionals in general are known to overcorrect for cohesive energies, in comparison to Local Density Approximation (LDA) functionals, which are known to generally overestimate cohesive energies.[174] The difference between both hcp structures in Table 7.3 is that the ideal c/a = $\sqrt{(8/3)}$ = 1.633, whereas the other hcp has a non-ideal c/a, which are measured later in this section. The hcp equilibrium energies are quite comparable to each other, with the MS-MEAM hcp non-ideal equilibrium energy being closest to the VASP value. The ideal c/a hcp structures are also nearly exact, with the MS-MEAM value being closest to the VASP value as well. Both ideal and non-ideal c/a hcp values are more stable than fcc. Especially important is the stabilities of hcp, fcc, and bcc with respect to each other. The non-ideal hcp structure is most stable, followed by the ideal hcp, then fcc, and then bcc in VASP. This trend is followed the Ackland EAM and the Zhou EAM, but not with MS-MEAM. For MS-MEAM, oDC10 is more stable than bcc. This is due to the construction of the screening functions. The oDC10 and the

bcc structures have screening values that are a function of C=5/3 and C=2, respectively. As a result, the screening for bcc with all screening functions is higher than the screening for oDC10. However, the screening in the symmetric and angular densities are too high at C=5/3. These screening functions can be altered but it is not desirable because lowering the screening functions of the symmetric and angular densities would compromise MS-MEAM fits for the Trigonal and 2D transformation pathways. The r_{NN} for bcc and oDC10 are very close between VASP computations and all three EAMs, with differences occurring at the third decimal place.

The absolute deviations in E and r increase with the remaining structures. For example, for the beam structure, the deviations in E_{eq} with respect to VASP are approximately 0.0265, 0.0560, and 0.0301 for the MS-MEAM, Zhou, and Ackland EAMs, respectively. Also, for the beam structure, the absolute deviations in r_{NN} with respect to VASP are approximately 0.0016, 0.0555, and 0.0886, for MS-MEAM, the Zhou, and Ackland EAMs, respectively. Another example is the graphene structure, the absolute deviations in E_{eq} with respect to VASP are approximately 0.1463, 0.2944, and 0.6219 for MS-MEAM, Zhou, and Ackland EAMs, respectively. Also, the absolute deviations in r with respect to VASP are approximately 0.1743, 0.0051, and 0.0808, respectively, for the MS-MEAM, Zhou, and Ackland EAMs. The large deviation in the E_{eq} scaled energy for graphene occurs because of the dampening function, Equation [7.33], that was used to correct for the compression behavior of the zigzag binding curve in MS-MEAM. As a final example, the absolute deviations in E_{eq} for zigzag with respect to VASP are approximately 0.0170, 0.1277, and 0.0262 for MS-MEAM, Zhou, and Ackland EAMs,

respectively. Also, the absolute deviations in *r* with respect to VASP are approximately 0.1743, 0.0335, and 0.0387, respectively, for the MS-MEAM, Zhou, and Ackland EAMs.

7.4.2.3 Transformation Pathways

Figures 7.18 through 7.22 show the transformation pathways computed with MS-MEAM, Zhou and Ackland EAM potentials. Figures 7.18 illustrates that the MS-MEAM-computed Bain pathway nearly matches the VASP-computed Bain pathway by virtue of the fitting procedure for the screening table. The Bain pathway computed with the Zhou and Ackland EAMs yield large deviations around the bcc scaled energy at $f = 0$, but they all converge to the same scaled energy for fcc at $f = 1$. Figure 7.19 illustrates the Trigonal pathways computed with VASP and all three EAMs. MS-MEAM computations yield the best fitting pathway with regard to VASP, with the SC point ($f = 0.4$) having an absolute deviation in the scaled energy of approximately 0.03. The Zhou and Ackland EAMs deviate very largely at the SC point in the Trigonal pathways with regard to VASP computations, but they do yield the same shape with the characteristic energy hill between bcc ($f = 0$) and fcc ($f = 1$). The 2D pathway computations are shown in Figure 7.20. Although the Zhou and Ackland EAM computations deviate less than the MS-MEAM computations, the latter illustrate a lowering in scaled energy with increasing *f* in line with the VASP computations. Unlike the VASP and MS-MEAM 2D pathways, the Ackland and Zhou EAMs compute 2D pathways in which the scaled energies change very little with increasing *f*.

The next two pathways were not used in fitting the screening functions. Figure 7.21 illustrates computations of the Zigzag transformation. Although MS-MEAM

computed a Zigzag pathway that deviates less than those computed by the Zhou and Ackland EAMs, the shape of the MS-MEAM Zigzag pathway varies through the VASP Zigzag pathway. This is probably due to the change in the density contributions with the change in the angle; as *f* goes from 0 to 1, the angle in the zigzag structure changes from 60.0^{o} to 180.0^{o}. Table 7.2 shows that the beam structure, having an angle of 60.0^{o}, has contributions from all three angular densities by virtue of non-zero symmetry factors. As the angle increases, the pathway passes through the zigzag structure, having an angle of 70.5^{o}, which also has contributions from all three angular densities, but the values of the symmetry factors change. The density contributions would be expected to change as the Zigzag pathway reaches the line structure, which has contributions only from the 2^{nd} angular density. In contrast to MS-MEAM, the Zhou and Ackland EAMs deviate more from the VASP Zigzag pathway, but they yield the same shape. Figure 7.22 illustrates the oDC pathways computed from VASP and all three EAMs. The MS-MEAM oDC pathway matches the VASP oDC pathway most precisely. In contrast, the Zhou and Ackland EAMs compute pathways that change very little and do not match the behavior of the VASP oDC pathway. It is expected that the screening functions play a dominant role in the MS-MEAM oDC pathway since, as the pathway goes from DC to oDC10, the corresponding C changes from 1 to 5/3, respectively.

7.4.2.4 Structural, Elastic, and Deformation Energetics

Table 7.4 compares lattice and elastic constants computed from MS-MEAM with those computed from Zhou and Ackland EAM potentials. In addition, comparisons have been made to DFT and known experimental values. Overall, the MS-MEAM results

underestimate the DFT and experimental hcp lattice constant *a* within 0.076 Å and 0.031 Å, respectively. In contrast, the Zhou and Ackland EAMs are much closer to DFT and experiment. However, MS-MEAM predicts a *c*/*a* ratio to within .003 Å and .005 Å of DFT and experiment, respectively, which is much better than the other two EAMs and MEAM. It is noted below Table 7.4 that the lattice constants were measured at an unspecified temperature less than 900^{o}C, and therefore a comparison of lattice constants computed at 0 K to those measured experimentally at or near 0 K is not possible. The DFT lattice constants may thus be the better benchmark by which comparisons can be made with the EAMs in this chapter. As for the elastic constants, MS-MEAM predicts C11, C12, C33, C44, and C66, and the bulk modulus within 10% of DFT and experiment. However, MS-MEAM overestimates C13, respectively. The source of this derivation may lie within the contribution by the 2nd angular density, and is thus related to the choice of 2D-hex to derive this density. In addition, MS-MEAM outperforms the Zhou and Ackland EAMs for the computed values of C11, C33, C66, and the bulk modulus with regard to DFT and experiment. It is noted below Table 7.4 that the elastic constants and bulk modulus were measured at a temperature of 4 K. Although not exactly at 0 K as with the DFT and EAM elastic constants, these experimental elastic constants provide a qualitative benchmark with which to compare the elastic constants computed from DFT and the EAMs.

Table 7.5 compares surface and stacking fault energies computed from MS-MEAM with those computed from Zhou and Ackland EAM potentials. In addition, comparisons have been made to DFT and known experimental values. With regard to stacking faults and the twin boundary energies, MS-MEAM outperforms the Zhou and

Ackland EAMs, yielding energetics closest to DFT and experiment. This is to be expected because the stacking faults are related to the hcp and fcc energy difference, which is expected to be exact within MS-MEAM due to fitting of the fcc and hcp equilibrium energies. However, MS-MEAM suffers with regard to surface energetics, being consistent with the Zhou and Ackland EAMs. This deficiency is likely related to how the screening functions were fitted, since surface energetics rely heavily upon 2NN interactions.

Table 7.6 compares vacancy and self-interstitial energetics computed from MS-MEAM with those computed from Zhou and Ackland EAM potentials. In addition, comparisons have been made to DFT. MS-MEAM underestimates and overestimates the vacancy formation and migration energies, respectively. This may be due to the presence of the dampening function applied to the 3rd angular density, since a vacancy may require contributions from all angular densities. The other EAMs perform in line with DFT. On the other hand, the MS-MEAM computes some self-interstitial energies consistent with DFT, including the split, and octahedral self-interstitials. The MS-MEAM tetrahedral self-interstitial deviates from the split self-interstitial by 0.22 eV, unlike DFT, which predicts that the split self-interstitial relaxes to the tetrahedral self-interstitial. Finally, MS-MEAM overestimates all three basal self-interstitials. The self-interstitials are dependent on 2NN interactions and therefore directly dependent on the screening functions. The constraint that the screening functions for the pair potential and the symmetric density are equal to each other for $0 < C < 2$ may have affected the accuracy of the basal self-interstitials, in comparison to DFT. This is suggested because preliminary computations showed that fitting the screening functions to Trigonal

pathway, within the range of $0.5 < C < 1.5$, caused MS-MEAM computations of self-interstitials to be too stable with regard to hcp. The Zhou and Ackland EAMs overestimate the self-interstitial energies with regard to DFT. For the Zhou EAMs, the basal crowd-ion and octahedral self-interstitials appear energetically degenerate, but they do maintain the basal crowd-ion and octahedral configurations. The same can be said for the basal tetrahedral and the crowd-ion self-interstitials. However, for the Ackland EAM, the octahedral self-interstitial relaxed to the basal octahedral configuration.

7.5 Conclusions

In this study, a MS-MEAM potential was constructed for Ti using first-principles DFT data from the VASP code. The binding curves, equilibrium energies, transformation pathways, and various energetic properties for known solid-state structures were computed with MS-MEAM, as well as the Zhou and Ackland EAMs, and compared to each other and DFT. This work shows the ability of MS-MEAM to replicate DFT data very well, and produces the correct hierarchy of energetic stabilities between solid-state structures, with the exception of oDC10 having been predicted as more stable than bcc as well as the DC structure being more stable than predicted by VASP. Also, MS-MEAM can reproduce transformation pathways very well, particularly the Bain, Trigonal, and oDC pathways. The lattice and elastic constants predicted by MS-MEAM are consistent with DFT and experiment, particularly the bulk modulus, C11, C33, and C66. MS-MEAM was shown to outperform the Zhou and Ackland EAMs in the accuracy of stacking fault behavior, but it yielded results consistent with both EAMs. Finally, MS-MEAM deviated

in accuracy for vacancy formation and migration energies, but it showed some consistency in self-interstitial energies with regard to DFT self-interstitial energies.

This was the second application of MS-MEAM, the first of which involved Cu, an fcc stable material. Recommended future work should involve an MS-MEAM application with Fe, which is a bcc stable material. Any future applications of MS-MEAM involving an hcp stable material, such as Zr or Hf, would be expected to face the same challenges that were present in this MS-MEAM involving Ti. Such challenges include fitting the screening functions to yield accuracy self-interstitial formation energies, and applying any necessary dampening functions to any of the angular functions to correct binding curvature behavior, like with the zigzag structure. Also, a new disorder model should be investigated, that may allow for better fitting of, at least, 2NN interactions, so that the correct order of stability between oDC10 and bcc is maintained while simultaneously replicating the behavior of the transformation pathways. Indeed, this model has confirmed that modeling 2NN interactions is sufficient for deformation energetics, given the MS-MEAM self-interstitial energies that match DFT self-interstitial energies. Although the MS-MEAM surface energies, which rely on 2NN interactions, were found lacking compared to DFT and experiment, the deviation in those results could be attributed more to the fitting procedure of the screening functions and the choice of reference structures for the MS-MEAM functions. In any case, this application of MS-MEAM with Ti has shed light on the challenges of developing an hcp-stable MS-MEAM potential and has illustrated to work well in computing energetics for multiple structures as well as structural, elastic, and deformation energetics for hcp Ti.

Table 7.1: Symmetry factors for structures analyzed in this study. The following are variables to be considered: Z_1 is the number of 1NNs; s_1, s_2, and s_3 are the symmetry factors for the first, second, and third angular densities, respectively; Z_2 is the number of 2NNs; *a* is the ratio of the 2NN to 1NN distance; and *C* is screening parameter for the 2NNs. Available reference structures are listed with asterisks.

Structure	Z_1	s^1	s^2	s^3	Z_2	*a*	*C*
fcc*	12	0	0	0	6	√2	1
hcp*	12	0	0	1/3	6	√2	1
o-DC10	10	0	7/24	27/32	4	√(3/2)	5/3
bcc	8	0	0	0	6	√(4/3)	2
SC*	6	0	0	0	12	√2	1
2D-hex*	6	0	6	0	6	√3	1/3
DC*	4	0	0	32/9	12	√(8/3)	1/2
2D-sq	4	0	8/3	0	4	√2	1
beam	4	3	19/6	4/9	2	√3	1/3
graphene	3	0	3/2	9/4	6	√3	1/3
zigzag	2	8/3	8/9	183/386	2	√(4/3)	2
line*	2	0	8/3	0	2	2	0
dimer*	1	1	2/3	2/5	0	-	-

Table 7.2: Selected reference structures and transformation pathways that correspond to the MEAM functions

Reference	Structure	Path	MEAM Function
SC/fcc	X		$\rho_i^{a0}(r_{ij})$
fcc	X		$\phi(r_{ij})$
hcp or DC	X		$\Upsilon^3(r_{ij})$
line or 2D-hex	X		$\Upsilon^2(r_{ij})$
dimer	X		$\Upsilon^1(r_{ij})$
Bain		X	S_{ikj}^{ϕ}
Trigonal		X	$S_{ikj}^{\rho^0}$
2D		X	$S_{ikj}^{\rho^2}$

Table 7.3: Scaled equilibrium energies and nearest neighbor distances for selected structures; all E_{eq} and r_{NN} are unitless.

Structure	VASP		MS-MEAM		EAM (Zhou)		EAM (Ackland)	
	E_{eq}	r_{NN}	E_{eq}	r_{NN}	E_{eq}	r_{NN}	E_{eq}	r_{NN}
fcc	**6.5455**	**2.8938**	**4.8089**	**2.8939**	**4.8639**	**2.9379**	**4.8391**	**2.9505**
hcp	-1.0085	1.0061	-1.0084	1.0003	-1.0013	0.9968	-1.0028	1.0055
hcp (ideal c/a)	-1.0082	0.9994	-1.0081	1.0089	-1.0013	0.9194	-1.0022	0.9972
bcc	-0.9937	0.9683	-0.9922	0.9685	-0.9972	0.9703	-0.9935	0.9576
o-DC10	-0.9915	0.9781	-0.9963	0.9871	-0.9883	0.9841	-0.9869	0.9760
SC	-0.8916	0.9039	-0.8512	0.8870	-0.8892	0.9369	-0.9097	0.9317
2D-hex	-0.7270	0.9218	-0.6516	0.9289	-0.7257	0.9460	-0.7766	0.6657
2D-sq	-0.7017	0.8637	-0.6037	0.8706	-0.6714	0.9103	-0.7766	0.9577
zigzag	-0.6622	0.8300	-0.9159	0.9799	-0.7239	0.8917	-0.7340	0.9340
DC	-0.6515	0.8180	-0.6685	0.7845	-0.5238	0.8706	-0.6253	0.8567
beam	-0.6483	0.8510	-0.6218	0.8494	0.5923	0.9065	-0.6754	0.9396
graphene	-0.5446	0.8057	-0.6909	0.9800	-0.2502	0.8006	-0.6219	0.8865
line	-0.4809	0.7390	-0.2500	0.8120	-0.3662	0.8431	-0.4969	0.9034
dimer	-0.4162	0.6650	-0.2885	0.7925	-0.2412	0.8073	-0.3999	0.8738

Table 7.4: Computations of lattice and elastic constants from selected EAMs, DFT, and experiment.

hcp (non-ideal c/a)	MS-MEAM	EAM (Zhou)	EAM (Ackland)	DFT	Ref	Expt.	Ref
a (Å)	2.920	2.941	2.967	2.996	175	2.951[a]	176
c/a	1.591	1.623	1.592	1.588	175	1.587[a]	176
c11 (GPa)	165.2	160.8	190.0	183.4	175	176.1[b]	177
c12 (GPa)	76.2	74.0	76.6	84.6	175	86.9[b]	177
c33 (GPa)	192.4	203.2	217.1	204.9	175	190.5[b]	177
c13 (GPa)	88.9	70.0	76.1	63.8	175	68.3[b]	177
c44 (GPa)	51.8	34.8	50.1	48.8	175	50.8[b]	177
c66 (GPa)	44.5	43.4	56.7	49.4	175	44.6[b]	177
Bulk modulus (GPa)	114.4	105.9	117.2	110.2	175	109.7[b]	177

a) Values were measured at an unspecified temperature less than 900^{o}C
b) Values were measured at 4^{o}K

Table 7.5: Computations of surface and stacking fault energies from selected EAMs, DFT, and experiment.

hcp (non-ideal c/a)	MS-MEAM	EAM (Zhou)	EAM (Ackland)	DFT	Ref	Expt.	Ref
Intrinsic(1) stacking fault (mJ/m^2)	132.3	121.2	75.9	148.6	175	-	-
Intrinsic(2) stacking fault (mJ/m^2)	239.6	138.3	112.9	259.1	175	290	178
Extrinsic stacking fault (mJ/m^2)	376.1	280.0	195.8	353.1	175	-	-
Twin boundary (0001)[11-20] (mJ/m^2)	190.3	29.1	68.3	233.2	179	-	-
Basal surface (0001) (mJ/m^2)	1178	1290	1007	1936	180	2100	181
Prismatic surface (10-10) (mJ/m^2)	1477	1533	1203	2448	180	1920	182
Prismatic surface (11-20) (mJ/m^2)	1348	1373	1070	1872	180	-	-

Table 7.6: Computations of vacancy and self-interstitial energies from selected EAMs, DFT, and experiment.

hcp (non-ideal c/a)	MS-MEAM	EAM (Zhou)	EAM (Ackland)	DFT	Ref	Expt.	Ref
Vacancy formation (eV)	1.23	1.69	1.45	1.97	49	-	-
Vacancy migration (eV)	3.29	3.09	2.67	-	-	-	-
Crowd-ion self-interstitial (eV)	2.65	3.74(1)	3.34(0)		49	-	-
Octahedral self-interstitial (eV)	2.35	3.70(7)	→ Basal O	2.13	49	-	-
Split self-interstitial (eV)	2.73	3.71(0)	3.66(3)	2.48	49	-	-
Tetrahedral self-interstitial (eV)	2.95	3.73(9)	→ Basal T	→ Split	49	-	-
Basal octahedral self-interstitial (eV)	4.17	3.75(2)	3.11(3)	2.25	49	-	-
Basal crowd-ion self-interstitial (eV)	3.04	3.70(3)	3.07(3)	→ Basal O	49	-	-
Basal tetrahedral self-interstitial (eV)	3.73	3.74(1)	3.10(9)	→ Basal O	49	-	-

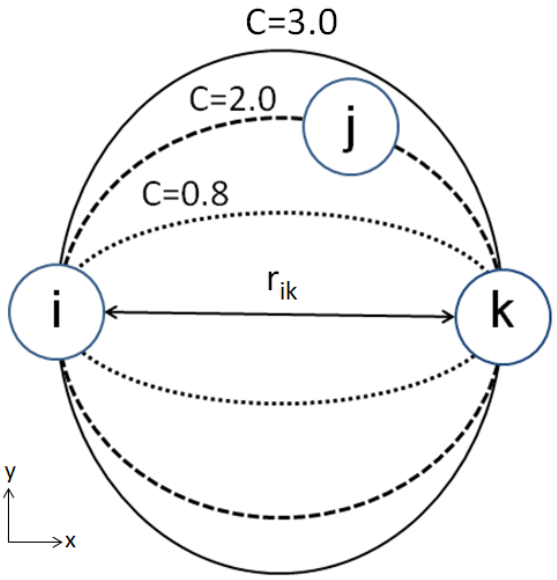

Figure 7.1: The screening ellipse described by Equation [4]. Screening between atoms *i* and *k* occurs by the presence of atom *j*, depending on the value of C. At C=0.8, atom *i* does not see atom *j*. However, at C=2.0 and greater, the atom *j* becomes present and modifies the pair interaction between atoms *i* and *k*.

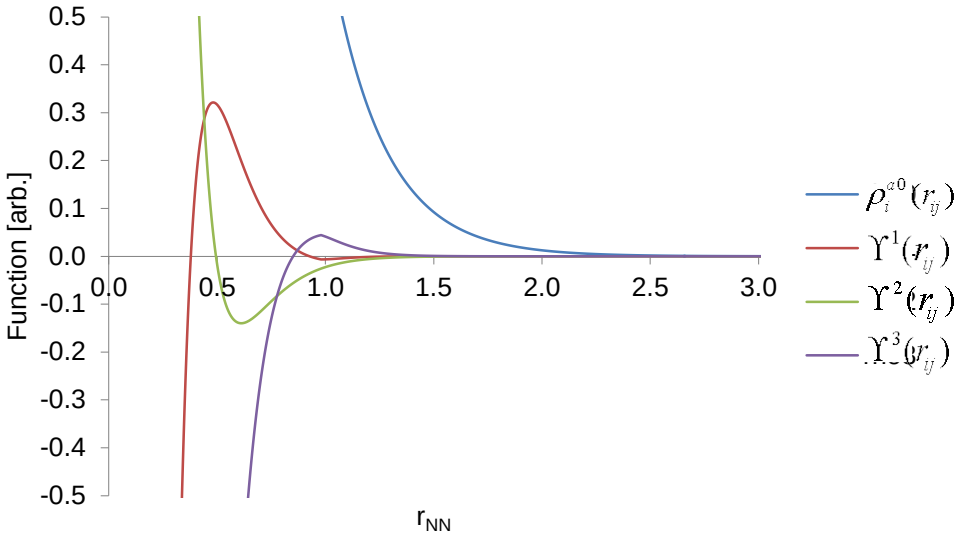

Figure 7.2: The symmetric and angular densities.

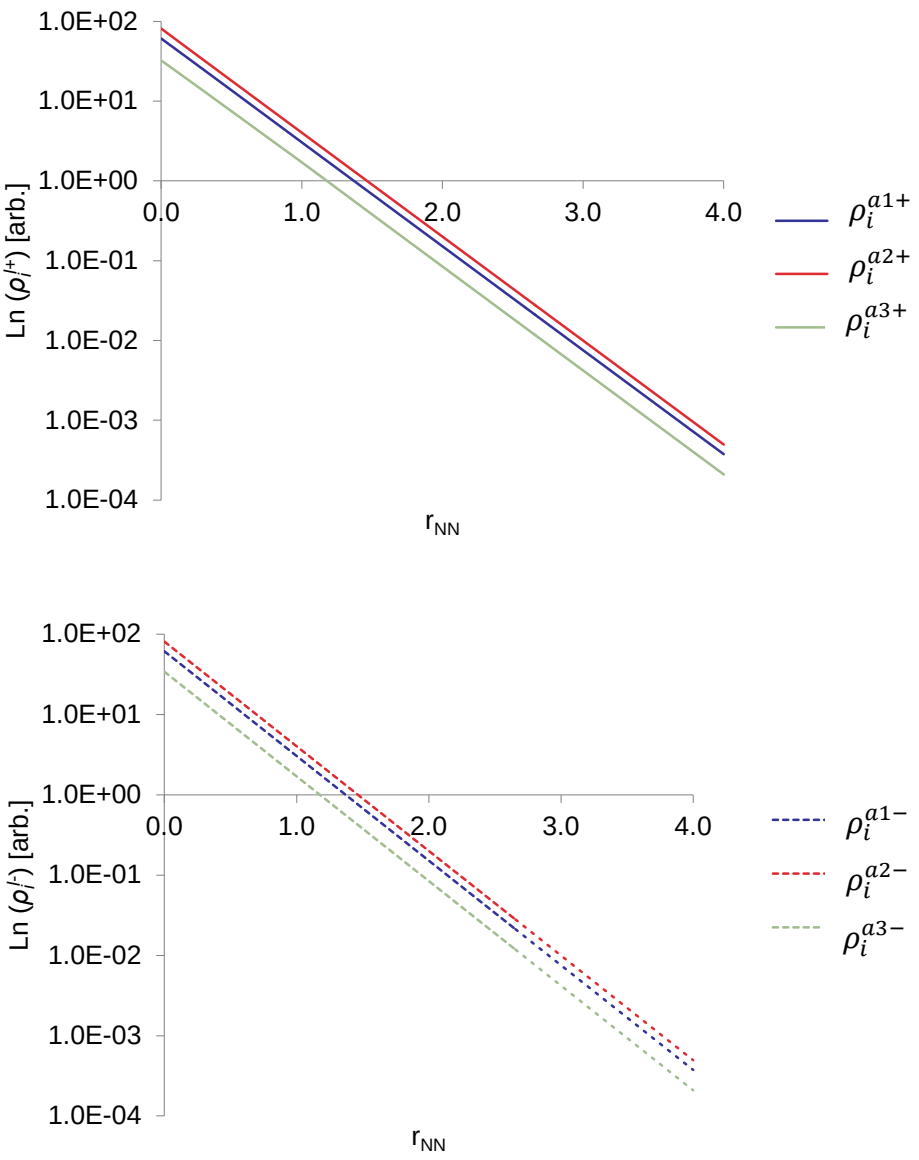

Figure 7.3: Logarithmic plots for the partial positive (a) and negative (b) densities. Both sets of partial densities appear similar, only because for each *l*, a $\Upsilon^l\left(r_{ij}^{low} = r_{NN} = 0.0\right)$ and $\kappa = 6$ were used for the construction of these functions in Equations [18] and [19].

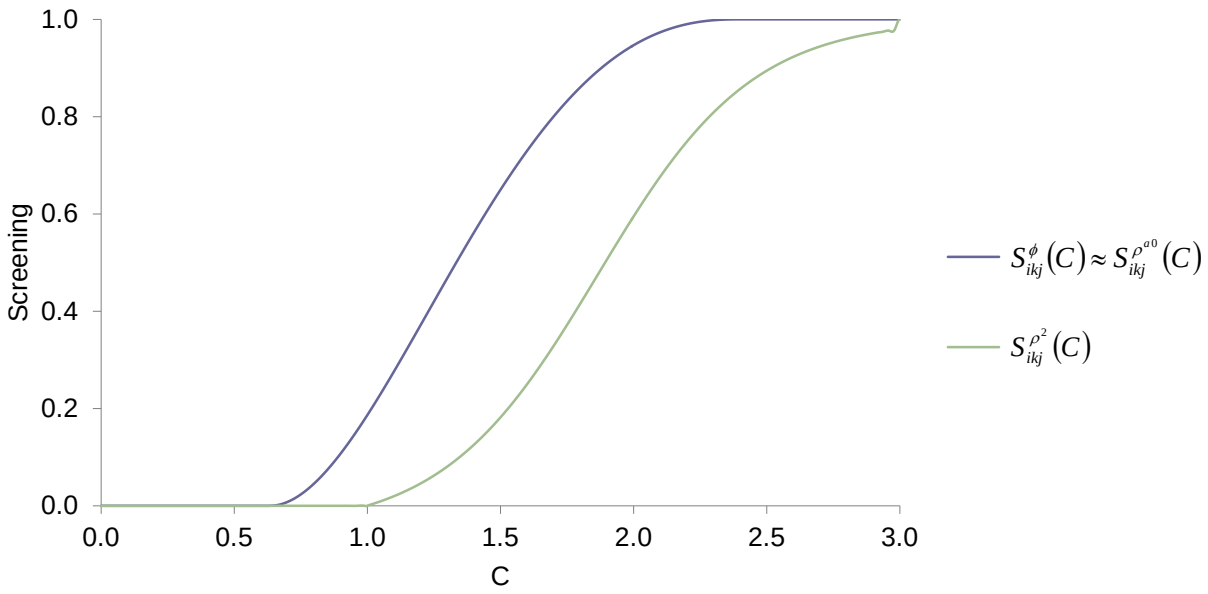

Figure 7.4: The screening functions; the S_{ijk}^{ϕ} function is equal to the $S_{ijk}^{\rho^{a0}}$ function below C = 2 and is approximately equal to the $S_{ijk}^{\rho^{a0}}$ function to the six decimal place. The $S_{ijk}^{\rho^{a2}}$ function is applied to the other angular densities.

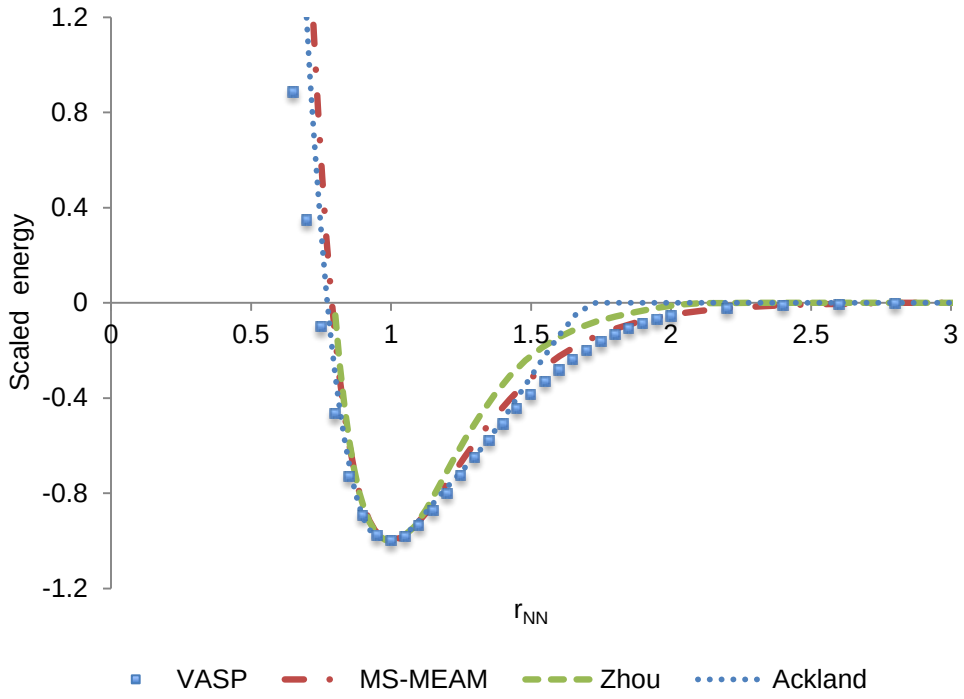

Figure 7.5: The fcc binding curves computed with VASP, MS-MEAM, and the Zhou and Ackland EAMs.

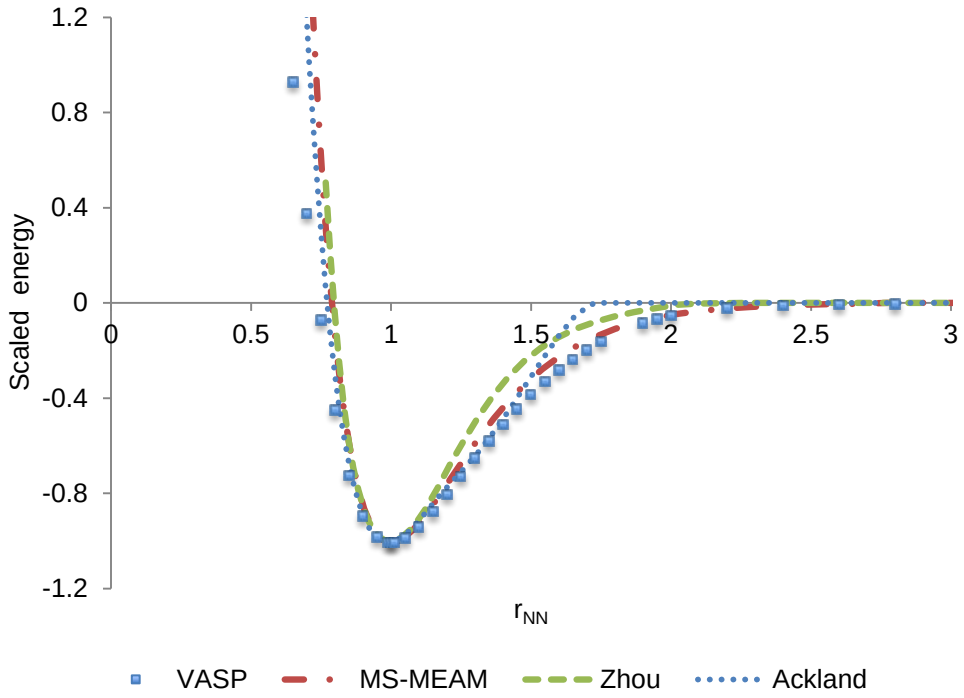

Figure 7.6: The hcp binding curves computed with VASP, MS-MEAM, and the Zhou and Ackland EAMs.

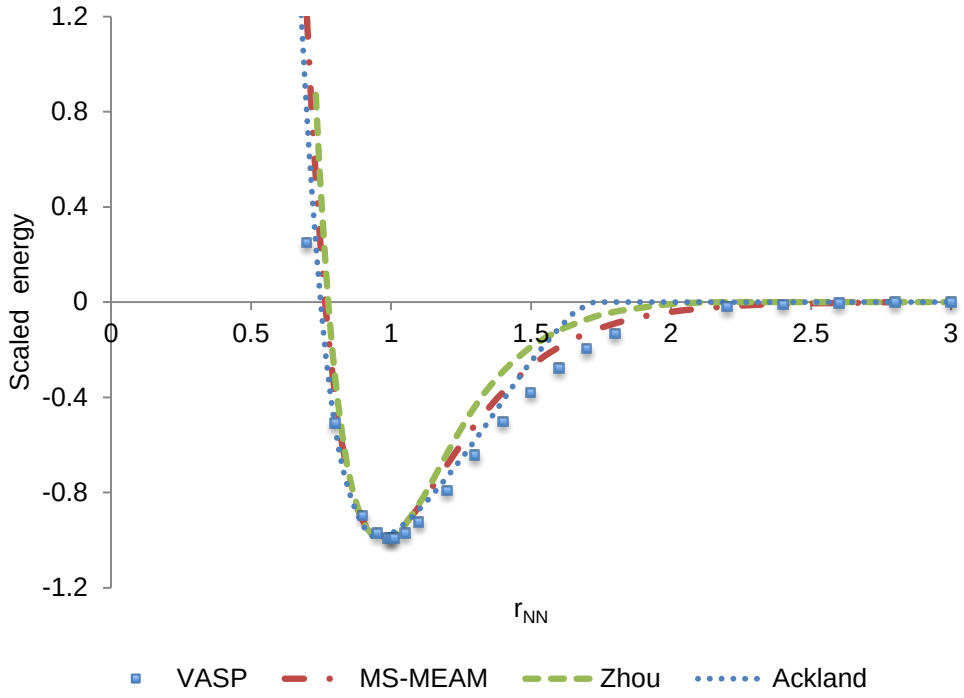

Figure 7.7: The bcc binding curves computed with VASP, MS-MEAM, and the Zhou and Ackland EAMs.

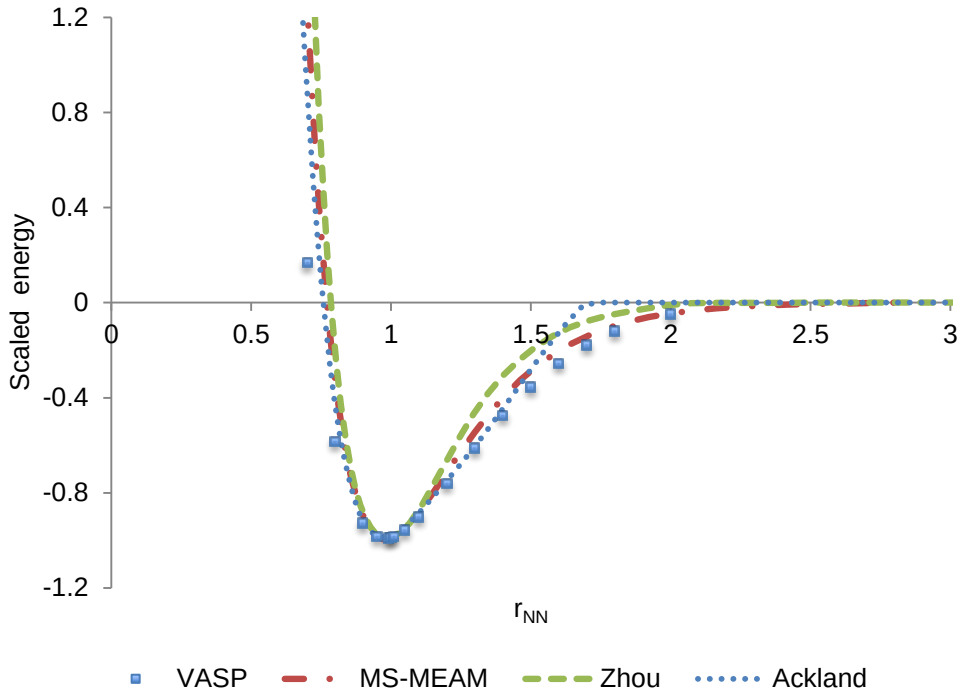

Figure 7.8: The oDC10 binding curves computed with VASP, MS-MEAM, and the Zhou and Ackland EAMs.

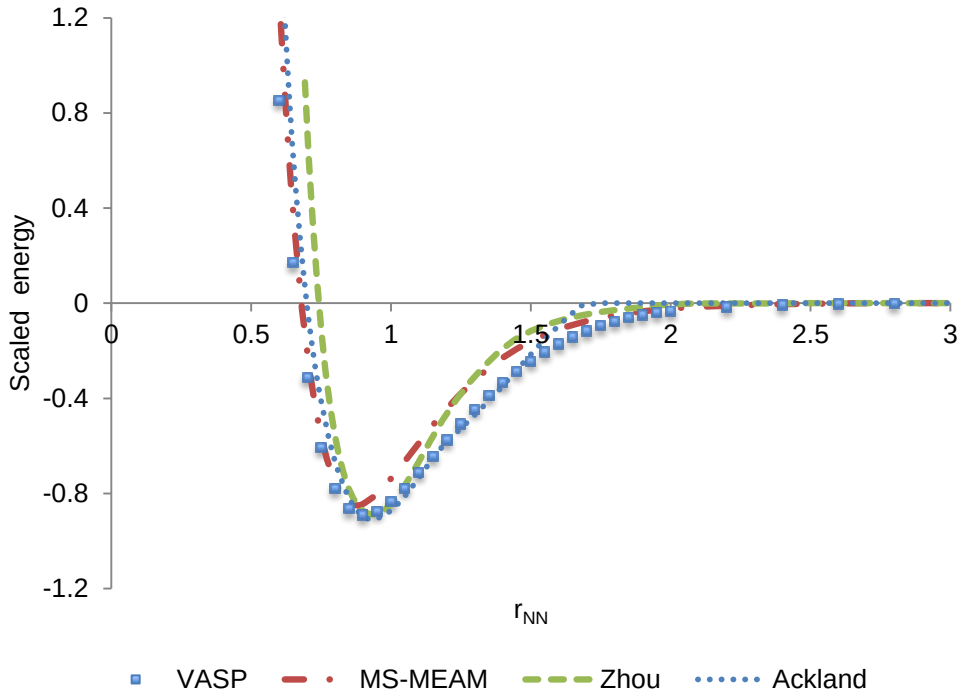

Figure 7.9: The SC binding curves computed with VASP, MS-MEAM, and the Zhou and Ackland EAMs.

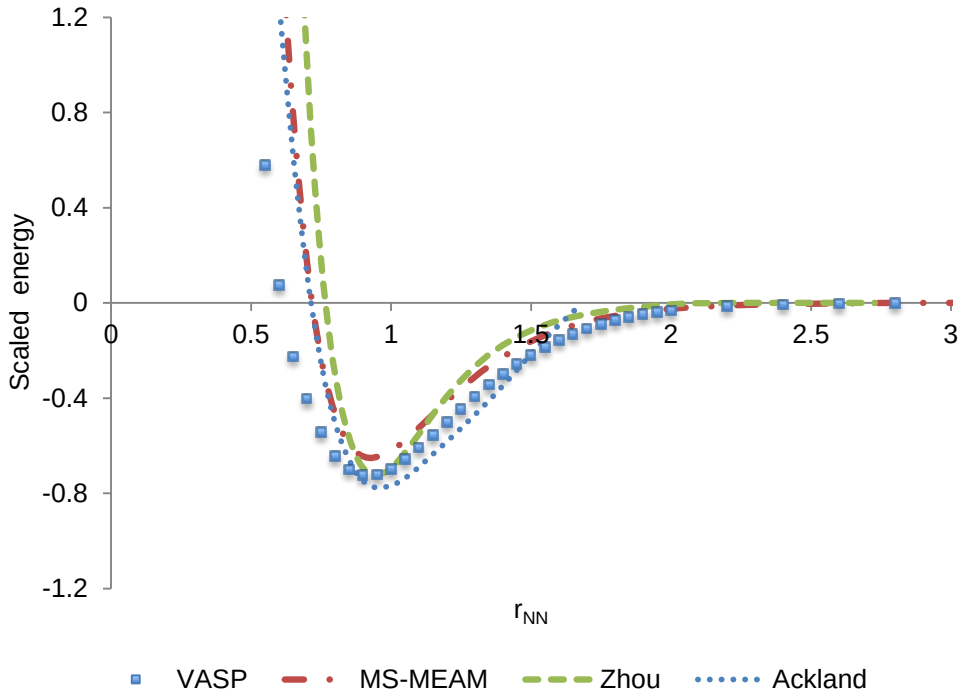

Figure 7.10: The 2D-hex binding curves computed with VASP, MS-MEAM, and the Zhou and Ackland EAMs.

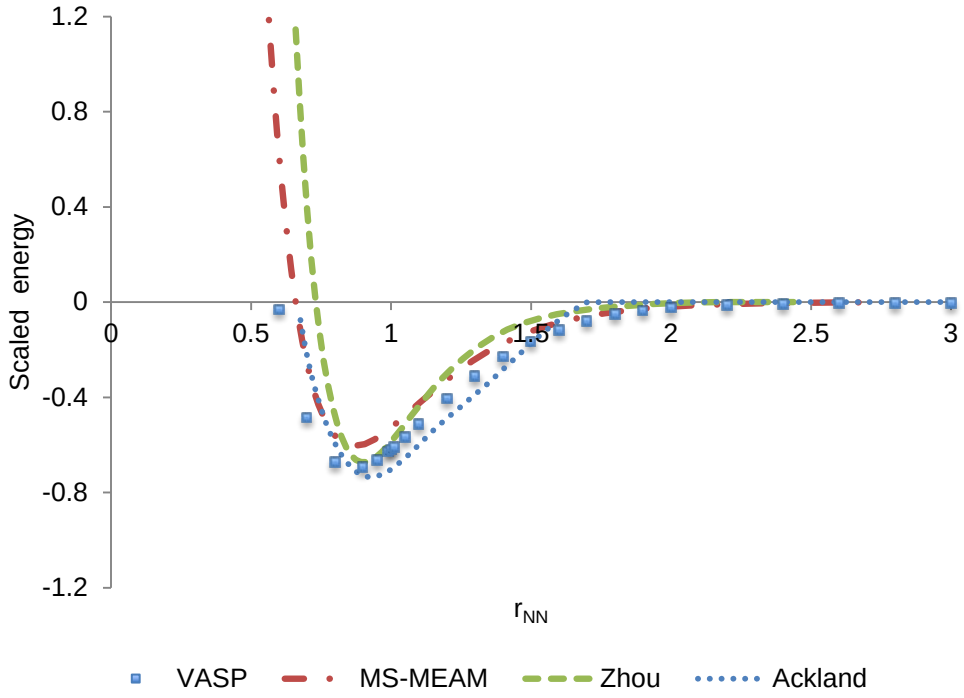

Figure 7.11: The 2D-sq binding curves computed with VASP, MS-MEAM, and the Zhou and Ackland EAMs.

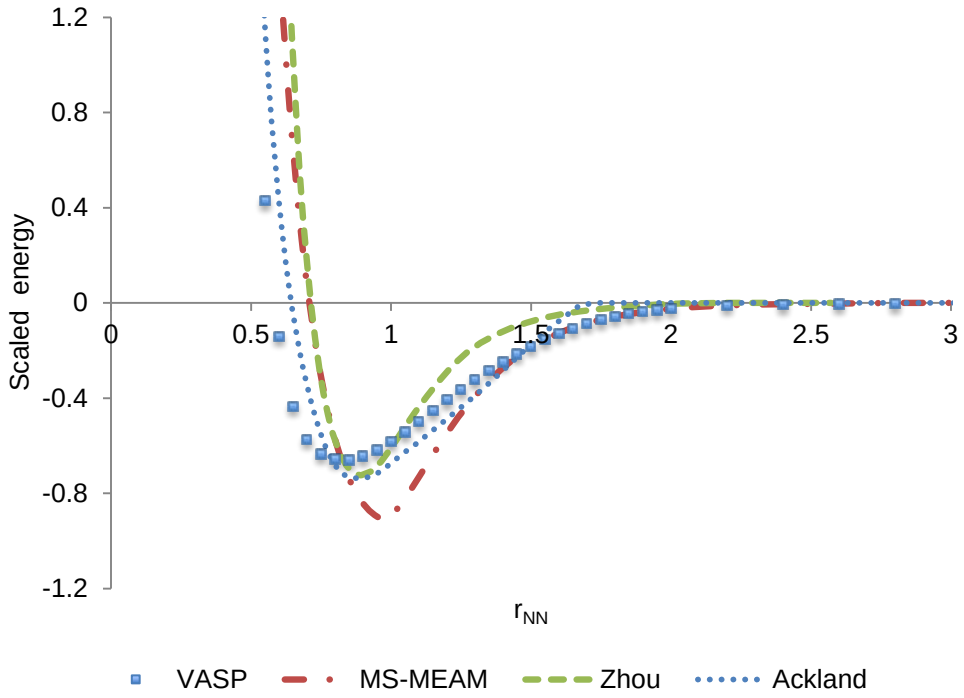

Figure 7.12: The DC binding curves computed with VASP, MS-MEAM, and the Zhou and Ackland EAMs.

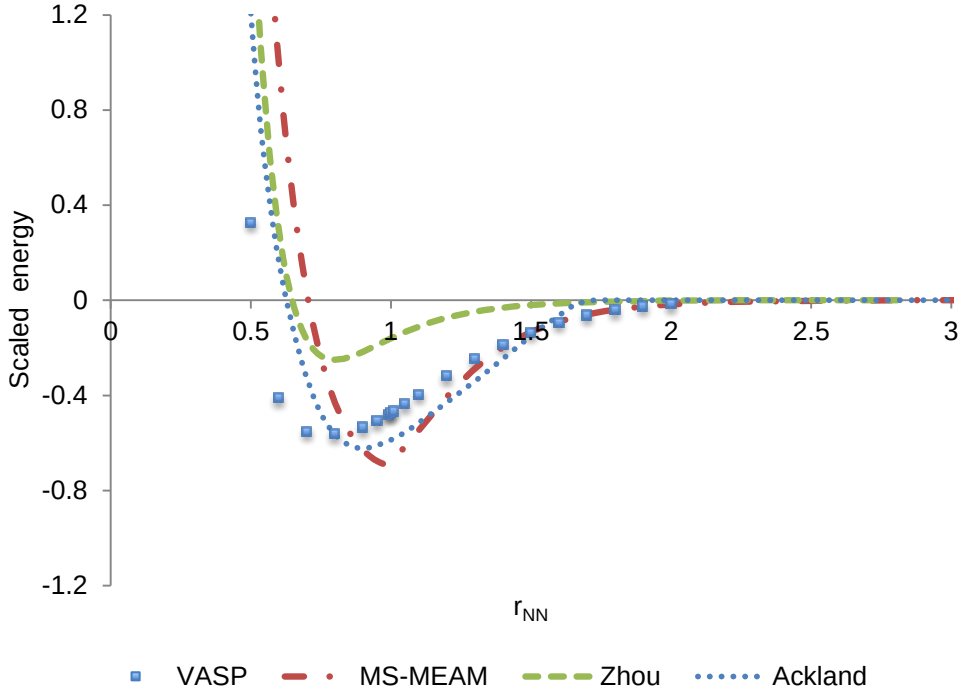

Figure 7.13: The graphene binding curves computed with VASP, MS-MEAM, and the Zhou and Ackland EAMs.

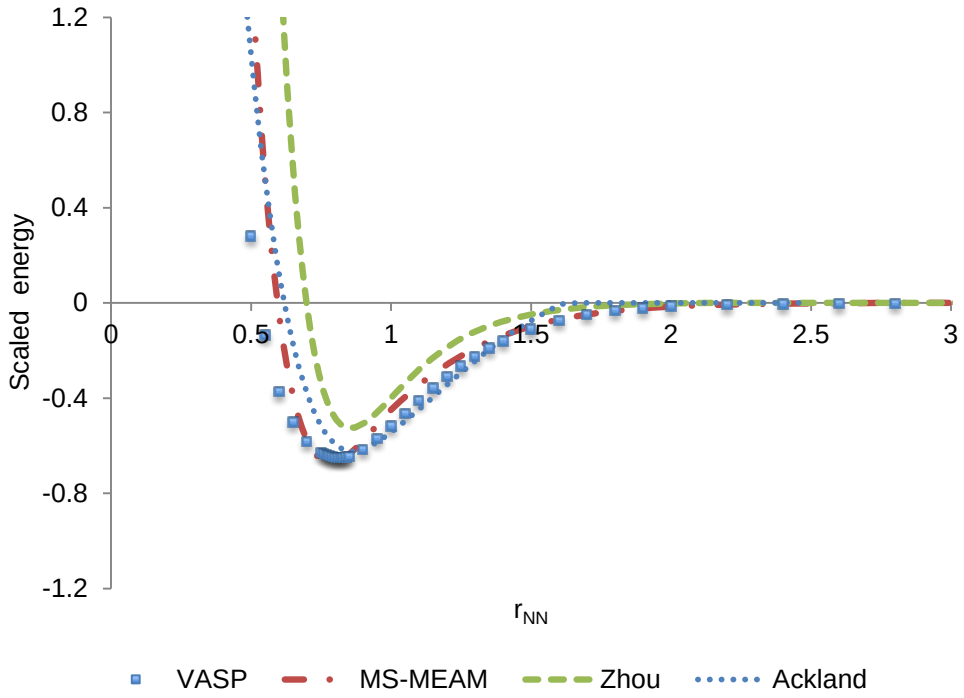

Figure 7.14: The zigzag binding curves computed with VASP, MS-MEAM, and the Zhou and Ackland EAMs.

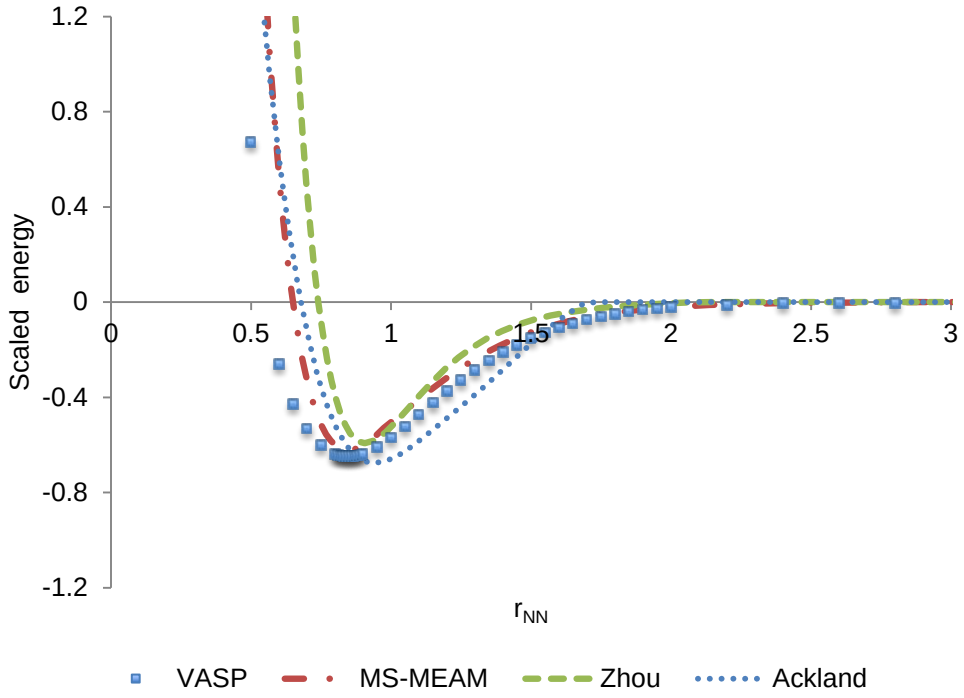

Figure 7.15: The beam binding curves computed with VASP, MS-MEAM, and the Zhou and Ackland EAMs.

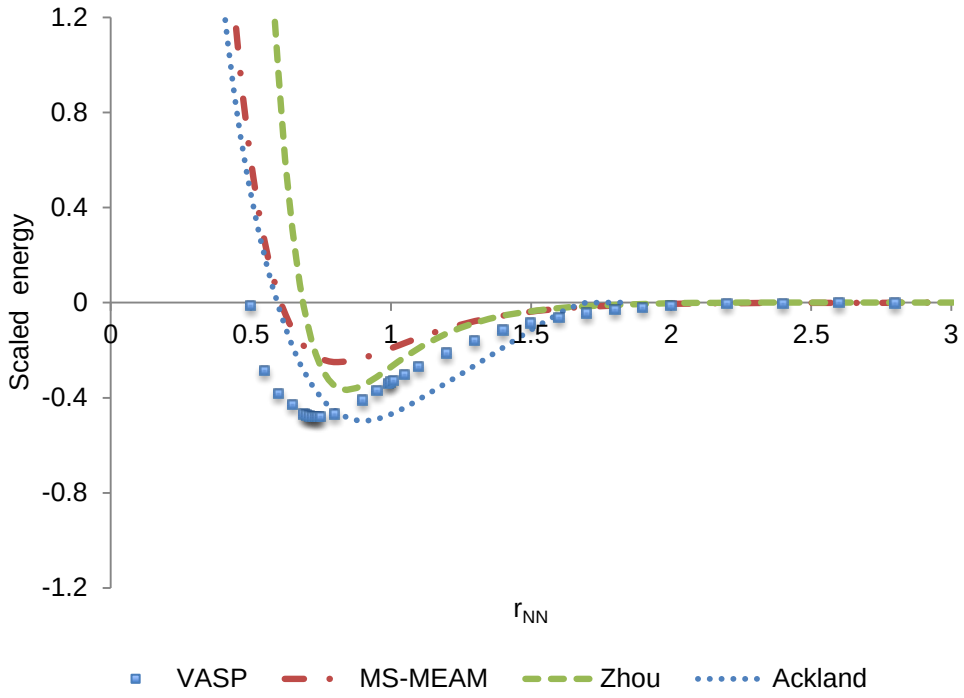

Figure 7.16: The line binding curves computed with VASP, MS-MEAM, and the Zhou and Ackland EAMs.

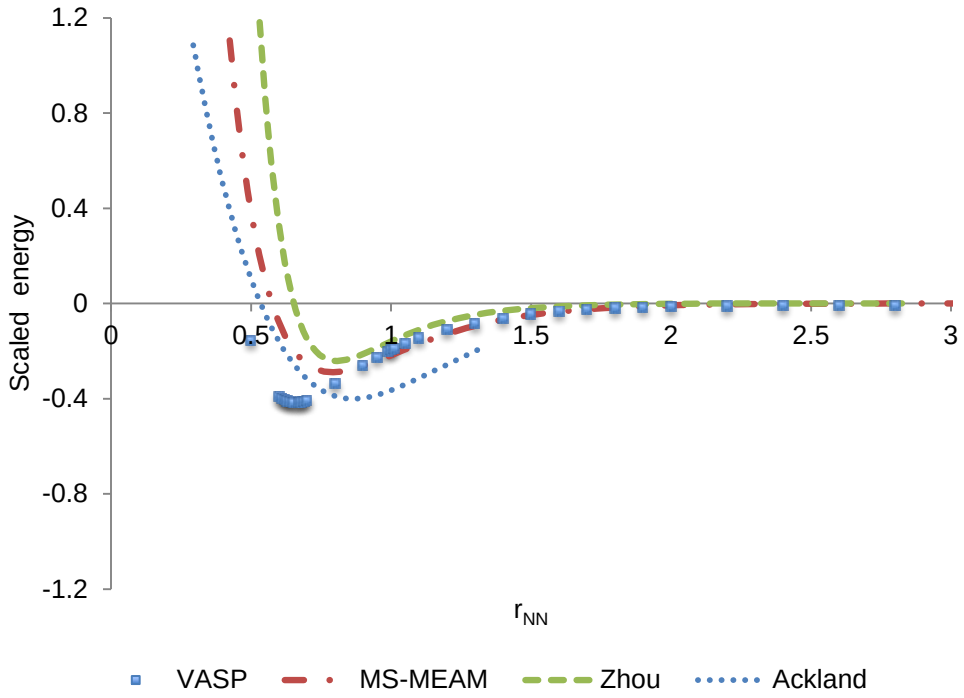

Figure 7.17: The dimer binding curves computed with VASP, MS-MEAM, and the Zhou and Ackland EAMs.

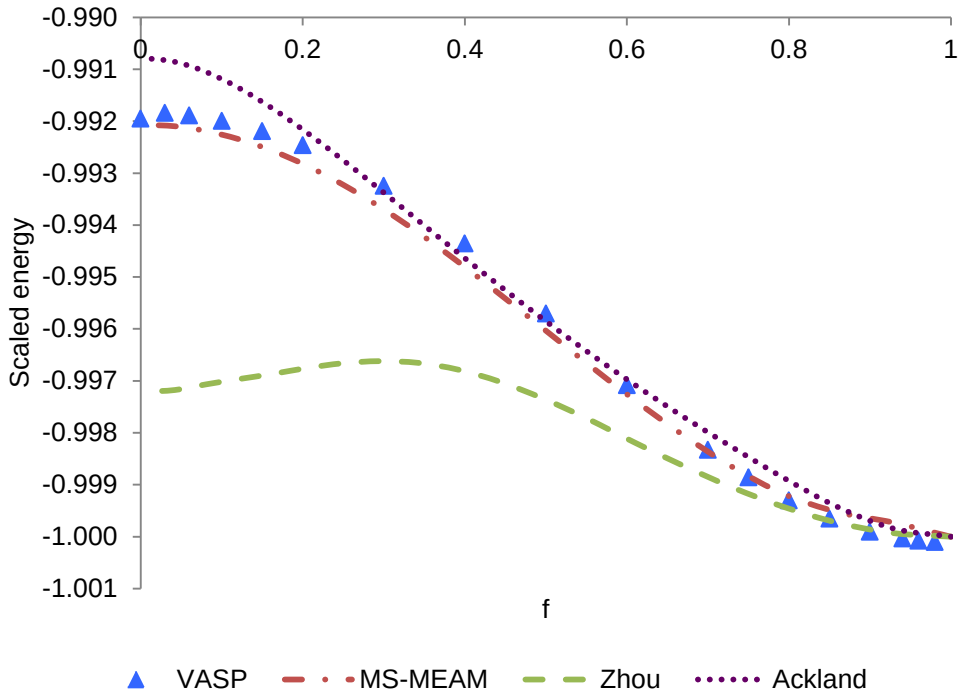

Figure 7.18: The Bain transformation pathway computed with VASP, MS-MEAM, and the Zhou and Ackland EAMs, as a function of the fractional deformation, *f*.

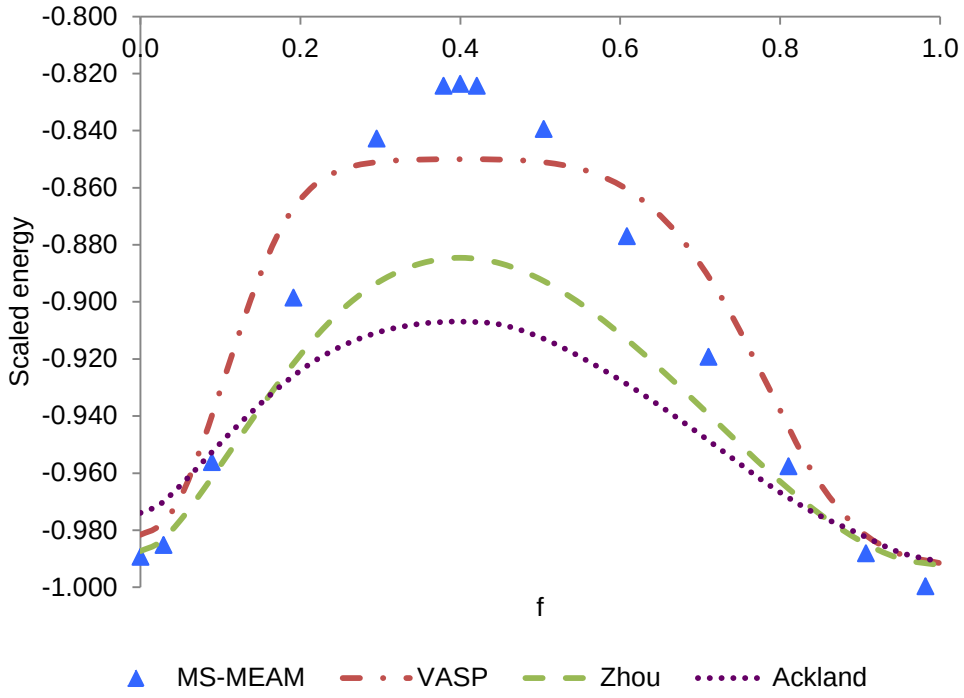

Figure 7.19: The Trigonal transformation pathway computed with VASP, MS-MEAM, and the Zhou and Ackland EAMs, as a function of the fractional deformation, *f*.

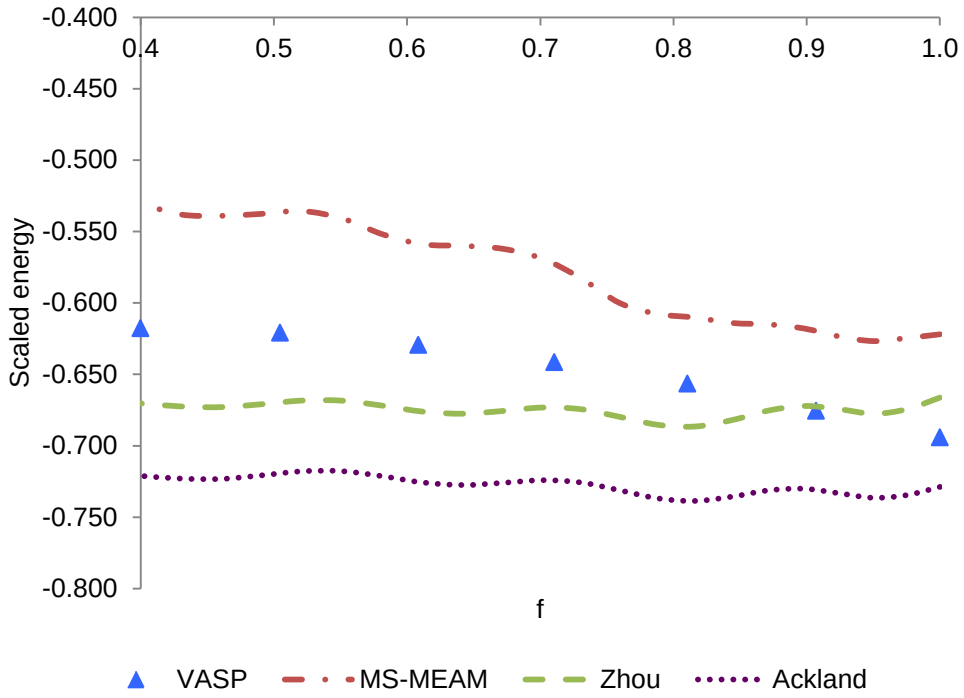

Figure 7.20: The 2D transformation pathway computed with VASP, MS-MEAM, and the Zhou and Ackland EAMs, as a function of the fractional deformation, *f*.

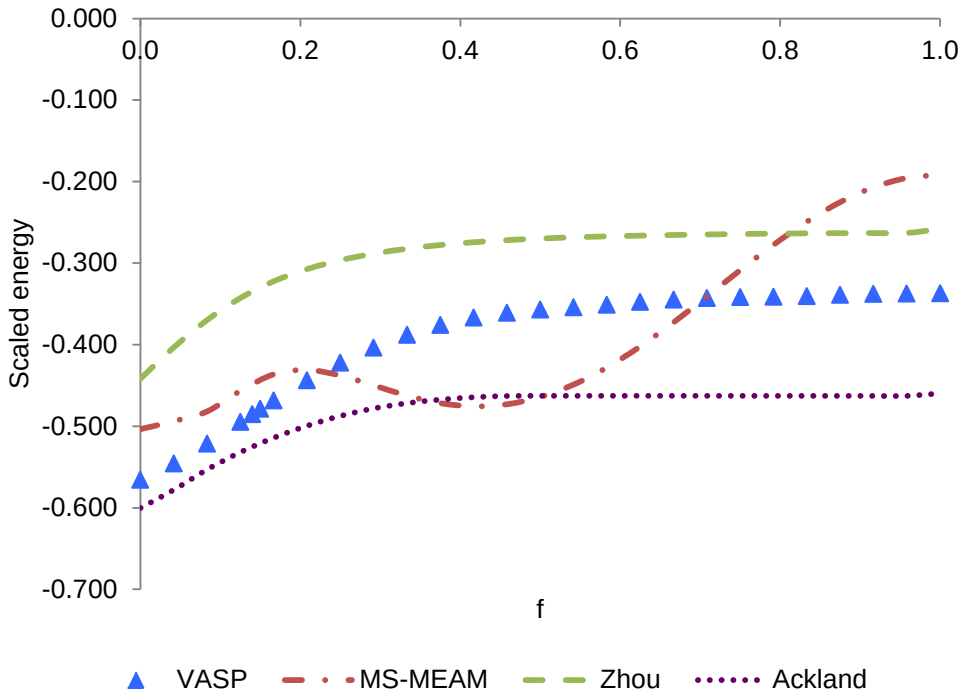

Figure 7.21: The Zigzag transformation pathway computed with VASP, MS-MEAM, and the Zhou and Ackland EAMs, as a function of the fractional deformation, *f*.

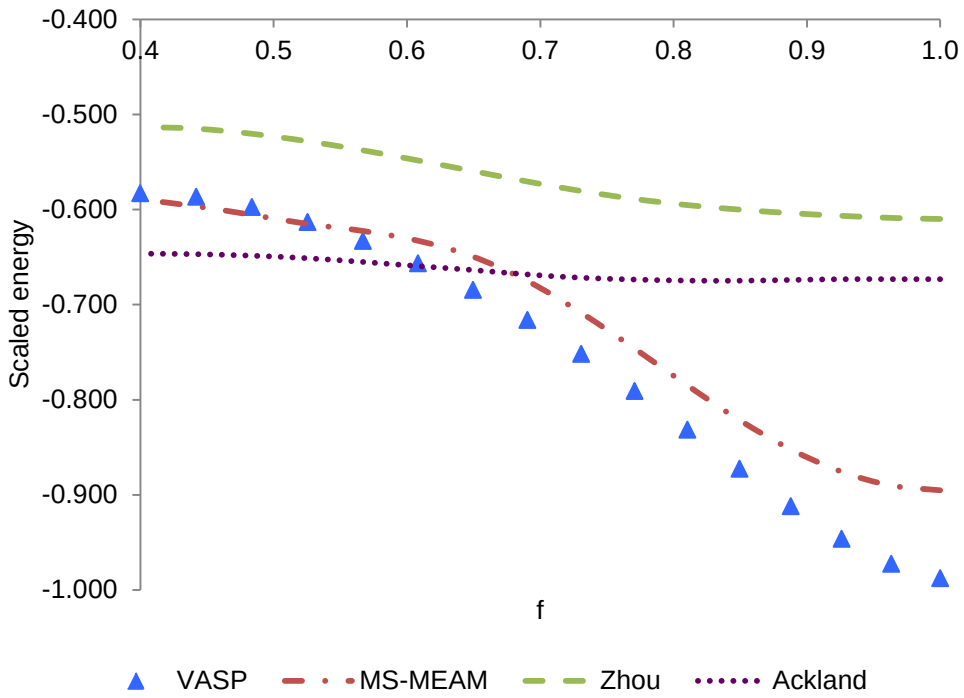

Figure 7.22: The oDC transformation pathway computed with VASP, MS-MEAM, and the Zhou and Ackland EAMs, as a function of the fractional deformation, *f*.

CHAPTER 8

CONCLUDING REMARKS

In this dissertation, the foundation of quantum chemistry has been reviewed. This includes topics such as the Schrödinger equation, the Born-Oppenheimer approximation, and the variational principle. Also, ab initio methodologies that are employed in solving the Schrödinger equation have been briefly examined. These methodologies include the Hartree-Fock (HF) approximation, many-body perturbation theory (MBPT), configuration interaction (CI), coupled cluster (CC) theory, complete active space self-consistent field theory (CASSCF), and density functional theory (DFT). Finally, basis functions and various types of basis sets, with which a wavefunction is expanded in ab initio methodologies, were reviewed.

Topics in solid-state physics were investigated. A brief summary of fourteen types of crystal structures was observed. Also, the topic of translational invariance that is associated with crystal lattices was mathematically developed, as well as the corresponding reciprocal lattice that exists inversely of real space. The electronic structure theory of crystals and types of chemical bonding that occurs was reviewed. Finally, the necessity of kpoint sampling in reciprocal space was illustrated as a means of measuring the energetics of crystal structures.

A study of nickel carbides was executed using plane-wave DFT, with emphasis on Ni_2C due to the scarcity of data on this crystal. It was determined that the most stable crystal structure of Ni_2C exits within an orthorhombic lattice. Also, computations were done that reaffirmed the most stable form of Ni_3C existed within a hexagonal lattice. A face cubic centered form of NiC was assumed, and computed lattice constants

were in agreement within 0.2 Å of previously reported simulations. The calculated formation energies (kcal mol^{-1}) of NiC, Ni_2C, and Ni_3C are 48.6, 7.9 and 6.4, respectively, which illustrates that Ni_2C could be a metastable nickel carbide.

Next, the performance and accuracy of correlation consistent basis sets that were reoptimized for first row atoms using the B3LYP and BLYP functionals was studied. Computations of formation enthalpies, combustion enthalpies, and atomization energies were computed and compared to those done with Dunning's correlation consistent sets. The chapter demonstrates that for the B3LYP and BLYP functionals, the reoptimized sets recover enthalpies greater than 1 kcal mol^{-1}, even at the quadruple- and quintuple-ζ levels. Also, while the double- and triple-ζ reoptimized sets require the same CPU demands of Dunning's correlation consistent sets, the quadruple- and quintuple-ζ reduce the CPU requirements in half or more in comparison.

The fragment Hamiltonian (FH) method, a semi-empirical atomistic potential, was investigated and applied to Ni. Using VASP computations, a set of binding curves for reference structures were used to derive the pair potential and parameterize the embedding functional and the one-electron hopping energy. The FH method was able to predict the VASP fcc and sc binding curves almost exactly and it predicts the other structures approximately well. Also, it is able to predict properties such as the fcc elastic constants, the vacancy formation energy, and the unstable stacking fault energy. However, the FH method is deficient at predicting fcc surface energies and the stable stacking fault energy. To improve the predictability of the method, angular functions need to be added to the background density. Also, second nearest-neighbor interactions should to be included to better describe surface reconstruction.

Finally, a Ti semi-empirical atomistic potential was developed with the multi-state modified embedded atom method (MS-MEAM). Unlike the previous incantation of MEAM, MS-MEAM uses multiple reference crystal structures and implements the MS-MEAM densities by solving for functionals rather fitting to parameters. In comparison to Ti EAMs produced by Zhou and Ackland, MS-MEAM provides a better, almost exact, fit to binding curves of multiple crystal structures and transformation pathways between crystals structures. The lattice and elastic constants predicted by MS-MEAM are consistent with DFT and experiment. MS-MEAM was shown to outperform the Zhou and Ackland EAMs in the accuracy of stacking fault behavior, but it performed on par with both EAMs. Finally, MS-MEAM deviated in accuracy for vacancy formation and migration energies, but it showed some consistency in self-interstitial energies with regard to DFT self-interstitial energies.

APPENDIX A

SUPPLEMENTAL MATERIAL FOR THE CORRELATION CONSISTENT BASIS SETS OPTIMIZED FOR DENSITY FUNCTIONAL THEORY

Table A.1. Comparisons between B3LYP total energies (E_h) computed with the cc-pV*n*Z, cc-pV*n*Z[rc](tr), and cc-pV*n*Z-B3LYP basis sets at geometries optimized with B3LYP/cc-pVTZ. The cc-pV*n*Z[rc](tr) and cc-pV*n*Z-B3LYP basis sets are listed as energy differences (mE_h) from the cc-pV*n*Z sets.

	cc-pV*n*Z				cc-pV*n*Z[rc](tr)				cc-pV*n*Z-B3LYP			
Molecule	D	T	Q	5	ΔD	ΔT	ΔQ	Δ5	ΔD	ΔT	ΔQ	Δ5
H_2	-1.173361	-1.180000	-1.180535	-1.180688	-2.584	-0.040	0.001	0.004	-2.175	-0.008	0.025	0.011
CH	-38.483326	-38.494823	-38.497573	-38.498705	-3.307	-0.644	-0.532	-0.110	-3.224	-0.810	-0.538	-0.077
NH	-55.221145	-55.240454	-55.245176	-55.246990	-4.265	-0.680	-0.550	-0.123	-4.883	-1.534	-0.921	-0.213
OH	-75.730770	-75.762434	-75.770519	-75.773484	-4.638	-0.703	-0.552	-0.138	-6.126	-2.358	-1.327	-0.340
FH	-100.435530	-100.483586	-100.495816	-100.500115	-5.075	-0.746	-0.557	-0.133	-7.853	-2.941	-1.551	-0.409
CN	-92.717585	-92.744003	-92.750825	-92.752910	-6.562	-1.368	-0.905	-0.098	-6.121	-1.304	-0.867	-0.060
CO	-113.321208	-113.357252	-113.366748	-113.369447	-6.462	-1.409	-0.829	-0.099	-5.954	-1.419	-0.653	-0.049
N_2	-109.532872	-109.568426	-109.576976	-109.579759	-7.024	-1.380	-0.923	-0.036	-6.368	-1.566	-1.081	-0.158
NO	-129.899462	-129.938788	-129.949589	-129.953030	-5.143	-1.491	-0.820	-0.037	-4.884	-1.738	-0.837	-0.115
O_2	-150.330512	-150.376647	-150.389626	-150.393766	-3.595	-1.541	-0.818	-0.131	-2.211	-1.662	-0.428	-0.141
F_2	-199.513234	-199.586401	-199.604880	-199.610802	-5.605	-1.532	-1.098	-0.233	-5.607	-1.548	-1.119	-0.295
CH_2 (triplet)	-39.151677	-39.167038	-39.170045	-39.171179	-4.659	-0.674	-0.479	-0.092	-3.824	-0.891	-0.553	-0.091
CH_2 (singlet)	-39.133578	-39.149995	-39.153392	-39.154707	-4.893	-0.672	-0.473	-0.076	-4.295	-0.743	-0.443	-0.020
NH_2	-55.875998	-55.901454	-55.907248	-55.909500	-6.007	-0.711	-0.490	-0.081	-5.705	-1.774	-0.988	-0.212
H_2O	-76.420470	-76.459839	-76.469642	-76.473327	-6.282	-0.738	-0.483	-0.088	-6.753	-2.983	-1.616	-0.402
CCH (linear)	-76.609099	-76.635492	-76.640945	-76.642751	-7.244	-1.317	-0.951	-0.188	-5.979	-1.176	-0.933	-0.188
HCN	-93.429758	-93.461365	-93.468616	-93.470755	-7.797	-1.430	-0.882	-0.140	-6.631	-1.630	-0.857	-0.126
HCO	-113.859154	-113.897410	-113.907309	-113.910370	-6.617	-1.447	-0.801	-0.083	-6.278	-1.672	-0.709	-0.068
CO_2	-188.598266	-188.660569	-188.676606	-188.681145	-9.394	-2.204	-1.231	-0.182	-9.248	-2.179	-0.928	-0.090
N_2O	-184.678220	-184.735189	-184.750093	-184.754553	-7.763	-2.304	-1.228	-0.137	-6.179	-1.907	-0.988	-0.144
NO_2	-205.091020	-205.154201	-205.172063	-205.177502	-6.194	-2.362	-1.072	0.039	-5.233	-2.643	-0.869	-0.018
O_3	-225.425915	-225.499057	-225.519558	-225.526101	-4.603	-2.402	-1.013	-0.100	-2.948	-3.169	-0.593	-0.174
CH_3	-39.837481	-39.857233	-39.860517	-39.861726	-6.456	-0.700	-0.442	-0.053	-4.927	-0.987	-0.519	-0.053
NH_3	-56.553849	-56.584728	-56.591417	-56.594138	-7.780	-0.746	-0.404	-0.019	-6.356	-2.014	-1.003	-0.154
C_2H_2	-77.332661	-77.363544	-77.369320	-77.371200	-8.409	-1.328	-0.925	-0.218	-6.589	-1.496	-0.942	-0.229
H_2CO	-114.507349	-114.549386	-114.559647	-114.562830	-7.567	-1.470	-0.761	-0.051	-7.099	-1.812	-0.711	-0.050
NCCN	-185.667858	-185.722434	-185.735880	-185.739851	-12.519	-2.900	-1.809	-0.335	-10.258	-2.426	-1.575	-0.262

Molecule	cc-pV*n*Z				cc-pV*n*Z[rc](tr)				cc-pV*n*Z-B3LYP			
	D	T	Q	5	ΔD	ΔT	ΔQ	Δ5	ΔD	ΔT	ΔQ	Δ5
BF_3	-324.569330	-324.696365	-324.725487	-324.734079	-9.828	-2.911	-1.668	-0.285	-10.618	0.688	-0.673	-0.271
NF_3	-354.096077	-354.222700	-354.255673	-354.266035	-7.896	-3.224	-1.740	-0.214	-8.582	-4.248	-1.789	-0.377
CH_4	-40.515990	-40.538215	-40.541479	-40.542567	-7.824	-0.732	-0.361	-0.008	-5.249	-0.824	-0.299	0.018
C_2H_3	-77.905043	-77.934623	-77.940473	-77.942540	-8.863	-1.372	-0.866	-0.077	-6.962	-1.419	-0.887	-0.067
H_2COH	-115.062658	-115.108542	-115.119533	-115.123333	-8.427	-1.505	-0.787	-0.058	-7.222	-2.275	-1.119	-0.188
CH_3O	-115.053850	-115.097410	-115.107754	-115.111194	-8.126	-1.482	-0.787	-0.069	-7.664	-2.089	-0.958	-0.146
CH_2CO (ketene)	-152.611462	-152.663881	-152.676302	-152.680039	-11.116	-2.166	-1.236	-0.161	-8.958	-1.937	-0.993	-0.116
HCOOH	-189.773006	-189.840629	-189.857715	-189.862916	-10.397	-2.284	-1.092	-0.059	-9.995	-2.942	-1.131	-0.099
CH_2F_2	-238.989268	-239.081798	-239.104406	-239.111577	-9.280	-2.248	-1.292	-0.099	-10.406	-2.033	-1.330	-0.191
CHF_3	-338.249275	-338.373925	-338.404765	-338.414354	-10.333	-3.031	-1.708	-0.108	-11.190	-1.586	-1.412	-0.158
CF_4	-437.506218	-437.661624	-437.700315	-437.712204	-11.314	-3.838	-2.114	-0.107	-10.584	-0.774	-1.351	-0.106
C_2H_4	-78.590734	-78.623163	-78.629166	-78.631281	-10.144	-1.401	-0.834	-0.032	-7.568	-1.483	-0.843	-0.016
H_3COH	-115.722385	-115.772227	-115.783750	-115.787600	-9.628	-1.521	-0.731	-0.037	-8.359	-2.460	-1.082	-0.179
H_2NNH_2	-111.866539	-111.915839	-111.927478	-111.931630	-11.119	-1.607	-0.705	-0.027	-9.392	-3.156	-1.390	-0.180
CH_3CN	-132.760938	-132.806810	-132.817081	-132.820215	-12.600	-2.180	-1.250	-0.154	-10.173	-2.275	-1.189	-0.113
CH_3CO	-153.188755	-153.241615	-153.254636	-153.258679	-11.291	-2.224	-1.130	-0.073	-9.622	-2.353	-1.016	-0.081
CH_2CHF	-177.831443	-177.898205	-177.913666	-177.918712	-11.016	-2.191	-1.271	-0.064	-9.397	-1.648	-1.133	-0.081
HCOCOH (glyoxal)	-227.835233	-227.909797	-227.929411	-227.935283	-12.273	-3.017	-1.504	-0.077	-11.701	-3.119	-1.193	-0.018
CF_3CN	-430.476103	-430.621307	-430.657736	-430.668738	-14.687	-4.558	-2.541	-0.258	-12.899	-1.960	-1.761	-0.177
C_2F_4	-475.534748	-475.701834	-475.744240	-475.757580	-13.454	-4.606	-2.494	-0.103	-12.522	-1.150	-1.612	-0.125
CH_3NH_2	-95.857517	-95.900005	-95.909189	-95.912424	-11.505	-1.536	-0.687	0.001	-8.923	-2.299	-0.994	-0.080
CH_3CCH	-116.659057	-116.703629	-116.712305	-116.715131	-12.954	-2.067	-1.279	-0.232	-9.670	-2.093	-1.226	-0.216
CH_2CCH_2 (allene)	-116.663416	-116.706516	-116.715079	-116.717969	-12.573	-2.090	-1.292	-0.171	-9.431	-2.025	-1.215	-0.153
C_3H_4 (cyclopropene)	-116.624031	-116.665646	-116.674336	-116.677156	-11.932	-2.184	-1.250	-0.156	-8.926	-1.771	-1.170	-0.148
CH_3CHO	-153.837727	-153.893494	-153.906668	-153.910714	-12.131	-2.246	-1.097	-0.039	-10.160	-2.356	-0.947	0.001
C_2H_4O (oxirane)	-153.791992	-153.848867	-153.862130	-153.866523	-10.939	-2.281	-1.157	-0.023	-9.516	-2.288	-1.188	-0.080
CH_2CHCN	-170.841362	-170.897362	-170.910050	-170.914064	-14.946	-2.865	-1.704	-0.169	-12.099	-2.678	-1.582	-0.121
CH_3NO_2	-245.026948	-245.109413	-245.131277	-245.137976	-11.532	-3.155	-1.265	0.068	-10.698	-3.936	-1.193	0.056
CH_3ONO	-245.025100	-245.105046	-245.125715	-245.132126	-11.626	-3.155	-1.342	0.000	-8.938	-3.335	-1.093	-0.018
CH_3COF	-253.108295	-253.198295	-253.220458	-253.227176	-13.822	-3.029	-1.547	-0.078	-12.392	-2.554	-1.272	-0.051

Molecule	cc-pV*n*Z				cc-pV*n*Z[rc](tr)				cc-pV*n*Z-B3LYP			
	D	T	Q	5	ΔD	ΔT	ΔQ	Δ5	ΔD	ΔT	ΔQ	Δ5
C_2H_6	-79.828718	-79.864272	-79.870473	-79.872501	-12.094	-1.479	-0.694	-0.005	-8.254	-1.407	-0.582	0.044
C_2H_4NH (aziridine)	-133.924943	-133.974949	-133.986255	-133.989997	-12.878	-2.340	-1.150	-0.033	-10.161	-2.403	-1.194	-0.043
CH_3CH_2O	-154.367296	-154.424575	-154.437802	-154.442031	-12.411	-2.246	-1.093	-0.061	-10.559	-2.588	-1.098	-0.071
$HCOOCH_3$	-229.075153	-229.156130	-229.175802	-229.181809	-14.309	-3.046	-1.341	-0.011	-12.691	-3.322	-1.150	-0.011
CH_3COOH	-229.099827	-229.181190	-229.201208	-229.207267	-14.979	-3.061	-1.447	-0.052	-12.937	-3.458	-1.328	-0.056
CH_3CHCH_2	-117.911037	-117.956842	-117.965780	-117.968818	-14.413	-2.146	-1.149	-0.017	-10.419	-2.044	-1.080	0.027
C_3H_6 (cyclopropane)	-117.897233	-117.942669	-117.951599	-117.954546	-14.077	-2.253	-1.175	-0.030	-10.121	-1.793	-1.057	0.013
CH_3CH_2OH	-155.042698	-155.105957	-155.120253	-155.124822	-13.919	-2.281	-1.047	-0.032	-11.299	-2.921	-1.174	-0.085
CH_3OCH_3	-155.028834	-155.089819	-155.103305	-155.107648	-13.177	-2.296	-0.978	0.009	-10.111	-2.457	-0.919	-0.018
CH_3CONH_2	-209.226159	-209.302896	-209.321385	-209.327154	-16.653	-3.053	-1.429	-0.013	-14.450	-3.926	-1.602	-0.059
C_4H_4O (furan)	-230.036403	-230.108696	-230.126486	-230.132319	-14.990	-3.710	-1.833	0.021	-11.536	-2.974	-1.589	0.061
$(CH_3)_2CH$	-118.478332	-118.524863	-118.533980	-118.537028	-15.086	-2.208	-1.085	-0.006	-10.657	-2.091	-1.002	0.043
$(CH_3)_2NH$	-135.165822	-135.219956	-135.231668	-135.235496	-15.156	-2.325	-0.963	0.022	-11.308	-2.689	-1.057	-0.006
$CH_3CH_2NH_2$	-135.176151	-135.231397	-135.243310	-135.247193	-15.724	-2.297	-1.008	0.006	-11.557	-2.726	-1.127	-0.011
$CH_2CHCHCH_2$ (trans-2-butene)	-156.000134	-156.055883	-156.067400	-156.071373	-16.592	-2.801	-1.597	-0.025	-12.335	-2.541	-1.523	0.024
C_4H_6 (methyl-cyclopropane)	-155.968167	-156.023504	-156.035081	-156.038908	-16.285	-2.937	-1.600	-0.117	-12.039	-2.461	-1.476	-0.090
C_4H_6 (bicyclo[1.1.0]butane)	-155.953395	-156.006225	-156.017928	-156.021711	-15.258	-3.028	-1.561	-0.065	-11.185	-2.106	-1.395	-0.023
C_4H_6 (cyclobutene)	-155.979400	-156.031613	-156.043165	-156.046945	-15.405	-2.978	-1.477	-0.052	-11.320	-2.490	-1.354	0.004
C_4H_6 (dimethylacetylene)	-155.983503	-156.041599	-156.053091	-156.056854	-17.500	-2.786	-1.649	-0.252	-12.622	-2.569	-1.495	-0.201
CH_3COCH_3	-193.163826	-193.233233	-193.249338	-193.254270	-16.702	-3.015	-1.423	-0.036	-13.097	-3.001	-1.200	0.032
C_4H_5N (pyrrole)	-210.182366	-210.248974	-210.265340	-210.270882	-16.858	-3.696	-1.851	0.045	-13.182	-3.488	-1.922	0.045
C_3H_8	-119.143380	-119.192302	-119.201483	-119.204456	-16.289	-2.227	-1.011	-0.002	-11.118	-2.011	-0.869	0.058
C_5H_5N (pyridine)	-248.298708	-248.373110	-248.391696	-248.397772	-18.975	-4.407	-2.239	0.066	-15.019	-3.779	-2.097	0.125
C_4H_8 (isobutylene)	-157.230574	-157.289913	-157.301840	-157.305782	-18.692	-2.898	-1.450	-0.003	-13.170	-2.615	-1.306	0.066
$C_2H_5OCH_3$	-194.348778	-194.423344	-194.439640	-194.444772	-17.543	-3.049	-1.295	0.012	-13.140	-2.970	-1.097	0.037
C_6H_6 (benzene)	-232.262132	-232.333355	-232.350024	-232.355799	-19.912	-4.232	-2.342	0.055	-15.095	-3.308	-2.186	0.126
$(CH_3)_3N$	-174.475766	-174.542023	-174.556396	-174.560953	-18.938	-3.119	-1.229	0.027	-13.640	-3.260	-1.211	0.044

Molecule	cc-pV*n*Z				cc-pV*n*Z[rc](tr)				cc-pV*n*Z-B3LYP			
	D	T	Q	5	ΔD	ΔT	ΔQ	Δ5	ΔD	ΔT	ΔQ	Δ5
C_5H_8 (spiropentane)	-195.276600	-195.344431	-195.359000	-195.363699	-20.176	-3.774	-1.901	-0.069	-14.702	-2.810	-1.681	-0.025
C_4H_{10} (butane)	-158.457887	-158.520170	-158.532333	-158.536212	-20.479	-2.978	-1.323	0.004	-14.052	-2.630	-1.146	0.071
				MAD	11.250	2.213	1.164	0.083	9.248	2.221	1.122	0.108
				MSD	-11.250	-2.213	-1.164	-0.075	-9.248	-2.205	-1.122	-0.087

Table A.2. Comparisons between B3LYP complete basis set limit energies (E_h) computed with the cc-pV*n*Z, cc-pV*n*Z[rc](tr), and cc-pV*n*Z-B3LYP basis sets at fixed geometries optimized with B3LYP/cc-pVTZ. The cc-pV*n*Z[rc](tr) and cc-pV*n*Z-B3LYP basis sets are listed as energy differences (mE_h) from the cc-pV*n*Z sets. The different extrapolation schemes are denoted as: the Peterson exponential formula (P), Schwartz cubic formula (S3), and Schwartz quartic formula (S4).

	cc-pV*n*Z			cc-pV*n*Z[rc](tr)			cc-pV*n*Z-B3LYP		
Molecule	P	S3	S4	ΔP	ΔS3	ΔS4	ΔP	ΔS3	ΔS4
H_2	-1.180801	-1.180848	-1.180601	0.010	0.143	0.056	0.019	0.141	0.067
CH	-38.499261	-38.497955	-38.497440	-0.168	-0.245	-0.348	-0.096	-0.294	-0.395
NH	-55.247972	-55.245757	-55.244890	-0.179	-0.211	-0.346	-0.183	-0.619	-0.770
OH	-75.775198	-75.771378	-75.769944	-0.186	-0.202	-0.350	-0.245	-1.007	-1.194
FH	-100.502745	-100.497056	-100.494885	-0.172	-0.190	-0.352	-0.242	-1.200	-1.442
CN	-92.754441	-92.751377	-92.750186	-0.136	-0.416	-0.626	-0.105	-0.394	-0.590
CO	-113.371621	-113.367397	-113.365768	-0.087	-0.408	-0.616	0.045	-0.359	-0.554
N_2	-109.581639	-109.577877	-109.576299	-0.093	-0.376	-0.602	-0.213	-0.578	-0.778
NO	-129.955431	-129.950365	-129.948561	-0.006	-0.487	-0.653	-0.003	-0.618	-0.774
O_2	-150.396652	-150.390493	-150.388363	-0.062	-0.631	-0.742	0.163	-0.615	-0.686
F_2	-199.614891	-199.606573	-199.603287	-0.289	-0.647	-0.819	-0.345	-0.683	-0.854
CH_2 (triplet)	-39.171803	-39.170591	-39.169936	-0.121	-0.148	-0.298	-0.091	-0.295	-0.416
CH_2 (singlet)	-39.155407	-39.153965	-39.153256	-0.107	-0.125	-0.283	-0.025	-0.152	-0.292
NH_2	-55.910697	-55.908076	-55.906953	-0.110	-0.079	-0.275	-0.146	-0.672	-0.851
H_2O	-76.475384	-76.470775	-76.469002	-0.104	-0.072	-0.276	-0.254	-1.300	-1.505
CCH (linear)	-76.643936	-76.641753	-76.640621	-0.247	-0.409	-0.639	-0.278	-0.433	-0.620
HCN	-93.472391	-93.469385	-93.468002	-0.142	-0.370	-0.621	-0.057	-0.490	-0.703
HCO	-113.912585	-113.908118	-113.906392	-0.049	-0.395	-0.609	0.076	-0.450	-0.655
CO_2	-188.684818	-188.677780	-188.674982	-0.123	-0.668	-0.969	0.094	-0.524	-0.827
N_2O	-184.757919	-184.751218	-184.748644	-0.053	-0.780	-1.028	-0.054	-0.661	-0.858
NO_2	-205.181527	-205.173142	-205.170226	0.185	-0.770	-0.972	0.326	-0.867	-1.039
O_3	-225.530659	-225.520945	-225.517571	0.119	-0.909	-1.055	0.500	-1.132	-1.230
CH_3	-39.86241	-39.86128	-39.86047	-0.068	-0.021	-0.233	-0.018	-0.234	-0.394
NH_3	-56.59549	-56.59251	-56.59116	-0.011	0.070	-0.188	-0.038	-0.695	-0.897

	cc-pV*n*Z			cc-pV*n*Z[rc](tr)			cc-pV*n*Z-B3LYP		
Molecule	P	S3	S4	ΔP	ΔS3	ΔS4	ΔP	ΔS3	ΔS4
C_2H_2	-77.37246	-77.37034	-77.36904	-0.257	-0.345	-0.614	-0.221	-0.518	-0.726
H_2CO	-114.56512	-114.56063	-114.55876	0.001	-0.319	-0.567	0.129	-0.440	-0.674
NCCN	-185.74289	-185.73707	-185.73464	-0.333	-0.973	-1.370	-0.294	-0.843	-1.167
BF_3	-324.74065	-324.72858	-324.72302	-0.214	-1.068	-1.378	-0.776	0.513	0.175
NF_3	-354.27338	-354.25838	-354.25266	-0.097	-1.285	-1.531	0.051	-1.655	-1.924
CH_4	-40.54326	-40.54235	-40.54146	0.015	0.096	-0.164	0.099	-0.055	-0.231
C_2H_3	-77.94378	-77.94146	-77.94020	-0.104	-0.258	-0.546	-0.088	-0.391	-0.615
H_2COH	-115.12570	-115.12078	-115.11874	-0.009	-0.291	-0.567	-0.047	-0.782	-1.012
CH_3O	-115.11345	-115.10890	-115.10697	-0.024	-0.306	-0.571	0.011	-0.621	-0.869
CH_2CO (ketene)	-152.68283	-152.67754	-152.67523	-0.124	-0.546	-0.906	-0.031	-0.496	-0.787
HCOOH	-189.86675	-189.85918	-189.85615	0.065	-0.537	-0.878	0.210	-0.804	-1.132
CH_2F_2	-239.11659	-239.10663	-239.10251	-0.074	-0.680	-0.979	-0.233	-0.591	-0.924
CHF_3	-338.42123	-338.40763	-338.40207	-0.059	-1.025	-1.356	-0.381	-0.417	-0.774
CF_4	-437.72086	-437.70380	-437.69686	-0.023	-1.376	-1.736	-0.549	-0.148	-0.483
C_2H_4	-78.63255	-78.63031	-78.62894	-0.046	-0.162	-0.495	-0.008	-0.340	-0.587
H_3COH	-115.79011	-115.78512	-115.78292	0.038	-0.197	-0.514	0.031	-0.757	-1.027
H_2NNH_2	-111.93411	-111.92889	-111.92671	0.082	-0.122	-0.491	0.081	-1.034	-1.336
CH_3CN	-132.82251	-132.81827	-132.81628	-0.124	-0.465	-0.874	-0.028	-0.603	-0.933
CH_3CO	-153.26158	-153.25586	-153.25350	0.016	-0.483	-0.853	0.108	-0.587	-0.902
CH_2CHF	-177.92210	-177.91545	-177.91251	-0.056	-0.537	-0.895	-0.159	-0.414	-0.717
HCOCOH (glyoxal)	-227.93971	-227.93087	-227.92749	0.059	-0.819	-1.219	0.293	-0.752	-1.138
CF_3CN	-430.67693	-430.66088	-430.65439	-0.149	-1.619	-2.085	-0.463	-0.569	-0.980
C_2F_4	-475.76702	-475.74798	-475.74048	0.014	-1.633	-2.062	-0.586	-0.256	-0.653
CH_3NH_2	-95.91438	-95.91051	-95.90866	0.091	-0.059	-0.441	0.105	-0.603	-0.895
CH_3CCH	-116.71702	-116.71373	-116.71184	-0.235	-0.446	-0.865	-0.181	-0.626	-0.936
CH_2CCH_2 (allene)	-116.71982	-116.71647	-116.71463	-0.185	-0.459	-0.866	-0.145	-0.591	-0.894
C_3H_4 (cyclopropene)	-116.67906	-116.67558	-116.67379	-0.123	-0.507	-0.894	-0.193	-0.520	-0.806
CH_3CHO	-153.91366	-153.90802	-153.90557	0.064	-0.416	-0.815	0.207	-0.500	-0.836
C_2H_4O (oxirane)	-153.86942	-153.86366	-153.86115	0.060	-0.514	-0.873	0.004	-0.634	-0.943
CH_2CHCN	-170.91687	-170.91154	-170.90909	-0.164	-0.717	-1.201	-0.115	-0.764	-1.154

	cc-pV*n*Z			cc-pV*n*Z[rc](tr)			cc-pV*n*Z-B3LYP		
Molecule	P	S3	S4	ΔP	ΔS3	ΔS4	ΔP	ΔS3	ΔS4
CH_3NO_2	-245.14288	-245.13292	-245.12918	0.336	-0.768	-1.150	0.596	-1.049	-1.407
CH_3ONO	-245.13675	-245.12742	-245.12381	0.244	-0.815	-1.198	0.412	-0.951	-1.247
CH_3COF	-253.23215	-253.22248	-253.21847	0.038	-0.746	-1.197	0.058	-0.568	-0.974
C_2H_6	-79.87384	-79.87171	-79.87024	0.065	-0.010	-0.412	0.146	-0.158	-0.433
C_2H_4NH (aziridine)	-133.99246	-133.98765	-133.98546	0.069	-0.419	-0.842	0.063	-0.621	-0.953
CH_3CH_2O	-154.44495	-154.43930	-154.43679	0.048	-0.406	-0.814	0.143	-0.633	-0.980
$HCOOCH_3$	-229.18622	-229.17768	-229.17408	0.198	-0.623	-1.095	0.378	-0.740	-1.162
CH_3COOH	-229.21176	-229.20303	-229.19941	0.115	-0.642	-1.134	0.293	-0.851	-1.278
CH_3CHCH_2	-117.97074	-117.96729	-117.96534	0.022	-0.257	-0.732	0.069	-0.422	-0.764
C_3H_6 (cyclopropane)	-117.95648	-117.95305	-117.95112	0.031	-0.327	-0.790	-0.005	-0.355	-0.686
CH_3CH_2OH	-155.12797	-155.12196	-155.11919	0.101	-0.299	-0.759	0.191	-0.730	-1.101
CH_3OCH_3	-155.11061	-155.10500	-155.10235	0.174	-0.308	-0.745	0.236	-0.533	-0.868
CH_3CONH_2	-209.33127	-209.32323	-209.31983	0.150	-0.518	-1.067	0.290	-1.013	-1.488
C_4H_4O (furan)	-230.13622	-230.12828	-230.12505	0.174	-0.964	-1.455	0.116	-0.829	-1.205
$(CH_3)_2CH$	-118.53900	-118.53549	-118.53351	0.079	-0.210	-0.709	0.134	-0.389	-0.741
$(CH_3)_2NH$	-135.23806	-135.23323	-135.23089	0.197	-0.189	-0.693	0.243	-0.582	-0.956
$CH_3CH_2NH_2$	-135.24980	-135.24491	-135.24252	0.152	-0.168	-0.691	0.215	-0.606	-0.988
$CH_2CHCHCH_2$ (trans-2-butene)	-156.07384	-156.06917	-156.06677	-0.018	-0.505	-1.049	-0.011	-0.630	-1.032
C_4H_6 (methyl-cyclopropane)	-156.04143	-156.03675	-156.03437	-0.052	-0.603	-1.135	-0.101	-0.648	-1.037
C_4H_6 (bicyclo[1.1.0]butane)	-156.02428	-156.01940	-156.01710	0.038	-0.660	-1.160	-0.111	-0.529	-0.891
C_4H_6 (cyclobutene)	-156.04947	-156.04464	-156.04237	0.075	-0.600	-1.106	0.044	-0.621	-0.990
C_4H_6 (dimethylacetylene)	-156.05936	-156.05493	-156.05246	-0.231	-0.549	-1.118	-0.168	-0.696	-1.103
CH_3COCH_3	-193.25787	-193.25107	-193.24802	0.123	-0.509	-1.060	0.291	-0.614	-1.048
C_4H_5N (pyrrole)	-210.27444	-210.26706	-210.26408	0.176	-0.846	-1.399	0.086	-1.024	-1.452
C_3H_8	-119.20646	-119.20309	-119.20103	0.123	-0.116	-0.657	0.187	-0.281	-0.651
C_5H_5N (pyridine)	-248.40186	-248.39349	-248.39016	0.206	-1.083	-1.705	0.145	-1.042	-1.532
C_4H_8 (isobutylene)	-157.30837	-157.30370	-157.30117	0.097	-0.350	-0.967	0.151	-0.510	-0.944
$C_2H_5OCH_3$	-194.44838	-194.4417	-194.43847	0.233	-0.405	-0.987	-0.337	0.562	0.999
C_6H_6 (benzene)	-232.35939	-232.35202	-232.34888	0.092	-1.012	-1.662	0.038	0.917	1.406
$(CH_3)_3N$	-174.56412	-174.55825	-174.55538	0.296	-0.315	-0.946	0.371	-0.665	-1.119

	cc-pV*n*Z			cc-pV*n*Z[rc](tr)			cc-pV*n*Z-B3LYP		
Molecule	P	S3	S4	ΔP	ΔS3	ΔS4	ΔP	ΔS3	ΔS4
C_5H_8 (spiropentane)	-195.36690	-195.36095	-195.35802	0.077	-0.733	-1.395	-0.053	-0.652	-1.130
C_4H_{10} (butane)	-158.53888	-158.53428	-158.53165	0.186	-0.220	-0.900	0.237	-0.402	-0.869
			MAD	0.116	0.502	0.864	0.179	0.617	0.908
			MSD	-0.006	-0.495	-0.863	0.000	-0.567	-0.846

Table A.3. Comparisons between BLYP total energies (E_h) computed with the cc-pV*n*Z, cc-pV*n*Z[rc](tr), and cc-pV*n*Z-BLYP basis sets at fixed geometries optimized with B3LYP/cc-pVTZ. The cc-pV*n*Z[rc](tr) and cc-pV*n*Z-B3LYP basis sets are listed as energy differences (mE_h) from the cc-pV*n*Z sets.

	cc-pV*n*Z				cc-pV*n*Z[rc](tr)				cc-pV*n*Z-BLYP			
Molecule	D	T	Q	5	ΔD	ΔT	ΔQ	Δ5	ΔD	ΔT	ΔQ	Δ5
H_2	-1.161788	-1.169578	-1.170143	-1.170301	-3.688	-0.051	0.001	0.005	-3.030	-0.025	0.027	0.014
CH	-38.464240	-38.477400	-38.480485	-38.481965	-4.934	-1.058	-0.847	-0.191	-4.948	-1.450	-0.931	-0.181
NH	-55.201474	-55.223161	-55.228442	-55.230736	-6.264	-1.117	-0.875	-0.215	-7.565	-2.507	-1.470	-0.374
OH	-75.713510	-75.748388	-75.757351	-75.760984	-7.014	-1.163	-0.885	-0.245	-9.792	-3.749	-2.099	-0.564
FH	-100.419183	-100.471408	-100.484880	-100.490034	-7.831	-1.233	-0.900	-0.246	-12.483	-4.737	-2.506	-0.733
CN	-92.706754	-92.735569	-92.742879	-92.745494	-9.628	-2.246	-1.556	-0.296	-9.035	-2.303	-1.563	-0.271
CO	-113.304715	-113.343454	-113.353642	-113.356893	-9.727	-2.329	-1.475	-0.309	-9.015	-2.514	-1.352	-0.286
N_2	-109.517108	-109.555679	-109.564898	-109.568319	-10.411	-2.261	-1.596	-0.245	-9.422	-2.700	-1.896	-0.444
NO	-129.888811	-129.930996	-129.942664	-129.946817	-8.274	-2.429	-1.506	-0.267	-8.174	-3.046	-1.721	-0.430
O_2	-150.325879	-150.374464	-150.388388	-150.393269	-6.417	-2.508	-1.533	-0.389	-5.131	-2.920	-1.350	-0.475
F_2	-199.508255	-199.585714	-199.605499	-199.612397	-9.308	-2.504	-1.814	-0.488	-9.949	-3.288	-2.142	-0.638
CH_2 (triplet)	-39.123764	-39.141328	-39.144692	-39.146137	-6.877	-1.080	-0.760	-0.174	-5.953	-1.524	-0.906	-0.202
CH_2 (singlet)	-39.107547	-39.126359	-39.130155	-39.131818	-7.150	-1.080	-0.758	-0.150	-6.566	-1.436	-0.785	-0.135
NH_2	-55.851333	-55.879761	-55.886204	-55.888981	-8.593	-1.151	-0.796	-0.168	-8.928	-2.918	-1.542	-0.394
H_2O	-76.398186	-76.441276	-76.452112	-76.456553	-9.253	-1.212	-0.803	-0.192	-11.031	-4.663	-2.473	-0.657
CCH (linear)	-76.581812	-76.610833	-76.616767	-76.619057	-10.488	-2.143	-1.542	-0.374	-8.818	-2.161	-1.560	-0.381
HCN	-93.405433	-93.440063	-93.447943	-93.450565	-11.307	-2.306	-1.469	-0.331	-9.787	-2.686	-1.477	-0.325
HCO	-113.838346	-113.879593	-113.890244	-113.893872	-10.096	-2.366	-1.426	-0.287	-9.684	-2.832	-1.405	-0.299
CO_2	-188.578485	-188.644463	-188.661570	-188.666858	-14.382	-3.620	-2.164	-0.512	-14.184	-3.816	-1.922	-0.465
N_2O	-184.667430	-184.727507	-184.743455	-184.748719	-12.350	-3.711	-2.212	-0.477	-10.262	-3.466	-2.029	-0.519
NO_2	-205.085482	-205.151969	-205.171189	-205.177585	-10.617	-3.826	-2.090	-0.317	-9.709	-4.510	-2.082	-0.481
O_3	-225.435398	-225.510961	-225.532884	-225.540544	-8.498	-3.879	-2.087	-0.495	-6.987	-5.121	-2.041	-0.686
CH_3	-39.803249	-39.825879	-39.829504	-39.830991	-9.352	-1.102	-0.710	-0.128	-7.472	-1.576	-0.838	-0.152
NH_3	-56.522579	-56.556946	-56.564369	-56.567699	-10.987	-1.188	-0.686	-0.096	-10.104	-3.256	-1.569	-0.304
C_2H_2	-77.297389	-77.331363	-77.337686	-77.340023	-12.090	-2.137	-1.474	-0.404	-9.588	-2.526	-1.527	-0.428
H_2CO	-114.477235	-114.522787	-114.533827	-114.537553	-11.453	-2.388	-1.361	-0.247	-10.897	-2.963	-1.359	-0.271
NCCN	-185.635149	-185.694456	-185.709004	-185.713858	-18.559	-4.643	-2.996	-0.720	-15.482	-4.256	-2.752	-0.655

	cc-pV*n*Z				cc-pV*n*Z[rc](tr)				cc-pV*n*Z-BLYP			
Molecule	D	T	Q	5	ΔD	ΔT	ΔQ	Δ5	ΔD	ΔT	ΔQ	Δ5
BF_3	-324.531474	-324.662658	-324.693463	-324.703083	-16.130	-4.873	-2.868	-0.724	-15.956	-2.855	-1.816	-0.743
NF_3	-354.081257	-354.213179	-354.248320	-354.260201	-14.240	-5.203	-3.115	-0.722	-15.881	-7.096	-3.510	-1.044
CH_4	-40.474988	-40.500649	-40.504208	-40.505495	-11.329	-1.136	-0.603	-0.075	-8.111	-1.295	-0.527	-0.068
C_2H_3	-77.861105	-77.894257	-77.900682	-77.903241	-12.918	-2.198	-1.428	-0.241	-10.459	-2.491	-1.481	-0.256
H_2COH	-115.022811	-115.072615	-115.084541	-115.089025	-12.688	-2.416	-1.381	-0.250	-11.625	-3.792	-1.933	-0.449
CH_3O	-115.013172	-115.061220	-115.072579	-115.076690	-12.408	-2.382	-1.365	-0.252	-12.356	-3.507	-1.718	-0.403
CH_2CO (ketene)	-152.571209	-152.627865	-152.641229	-152.645655	-16.521	-3.499	-2.114	-0.448	-13.700	-3.495	-1.893	-0.440
HCOOH	-189.735891	-189.808148	-189.826558	-189.832629	-15.903	-3.714	-2.009	-0.374	-15.764	-4.877	-2.202	-0.480
CH_2F_2	-238.947575	-239.045786	-239.070036	-239.078247	-14.975	-3.681	-2.226	-0.424	-16.839	-4.126	-2.454	-0.609
CHF_3	-338.206932	-338.337954	-338.370870	-338.381769	-17.272	-4.990	-2.993	-0.569	-18.815	-4.159	-2.824	-0.697
CF_4	-437.462487	-437.624786	-437.665871	-437.679280	-19.534	-6.336	-3.755	-0.708	-18.949	-3.662	-2.991	-0.766
C_2H_4	-78.538594	-78.574988	-78.581532	-78.584109	-14.687	-2.224	-1.386	-0.187	-11.270	-2.512	-1.402	-0.192
H_3COH	-115.673648	-115.728245	-115.740823	-115.745349	-14.415	-2.429	-1.291	-0.217	-13.368	-3.997	-1.852	-0.440
H_2NNH_2	-111.818485	-111.872799	-111.885656	-111.890679	-16.073	-2.524	-1.280	-0.203	-15.001	-5.092	-2.290	-0.451
CH_3CN	-132.707695	-132.758525	-132.769718	-132.773532	-18.431	-3.472	-2.095	-0.417	-15.352	-3.790	-2.051	-0.398
CH_3CO	-153.139380	-153.197078	-153.211188	-153.216001	-17.064	-3.579	-2.001	-0.351	-15.088	-4.049	-1.973	-0.412
CH_2CHF	-177.780119	-177.851738	-177.868324	-177.874174	-16.735	-3.533	-2.166	-0.350	-14.664	-3.396	-2.071	-0.416
HCOCOH (glyoxal)	-227.788332	-227.868183	-227.889311	-227.896196	-18.968	-4.882	-2.710	-0.475	-18.335	-5.356	-2.443	-0.454
CF_3CN	-430.424338	-430.576761	-430.615649	-430.628224	-24.000	-7.428	-4.428	-0.922	-21.818	-5.087	-3.554	-0.870
C_2F_4	-475.485233	-475.659483	-475.704597	-475.719695	-22.871	-7.539	-4.430	-0.793	-21.807	-4.673	-3.561	-0.897
CH_3NH_2	-95.798473	-95.845906	-95.856007	-95.859886	-16.689	-2.409	-1.215	-0.153	-13.949	-3.744	-1.667	-0.293
CH_3CCH	-116.595209	-116.644681	-116.654158	-116.657625	-18.831	-3.291	-2.082	-0.490	-14.486	-3.530	-2.039	-0.497
CH_2CCH_2 (allene)	-116.601490	-116.649242	-116.658587	-116.662121	-18.254	-3.330	-2.116	-0.418	-14.010	-3.485	-2.024	-0.425
C_3H_4 (cyclopropene)	-116.559332	-116.605576	-116.615082	-116.618524	-17.637	-3.449	-2.061	-0.406	-13.572	-3.232	-1.964	-0.415
CH_3CHO	-153.779179	-153.840167	-153.854424	-153.859180	-18.247	-3.590	-1.941	-0.307	-15.851	-3.988	-1.810	-0.300
C_2H_4O (oxirane)	-153.732394	-153.794128	-153.808530	-153.813725	-16.747	-3.624	-2.017	-0.294	-15.085	-4.074	-2.168	-0.410
CH_2CHCN	-170.778067	-170.839630	-170.853447	-170.858368	-21.876	-4.568	-2.854	-0.516	-18.044	-4.655	-2.732	-0.489
CH_3NO_2	-244.982127	-245.069948	-245.093531	-245.101349	-18.506	-5.047	-2.491	-0.352	-17.865	-6.392	-2.610	-0.437
CH_3ONO	-244.982237	-245.067369	-245.089611	-245.097143	-18.439	-5.045	-2.590	-0.430	-15.397	-5.611	-2.488	-0.517
CH_3COF	-253.049812	-253.146082	-253.169893	-253.177659	-21.374	-4.899	-2.737	-0.483	-19.752	-4.854	-2.510	-0.510

	cc-pV*n*Z				cc-pV*n*Z[rc](tr)				cc-pV*n*Z-BLYP			
Molecule	D	T	Q	5	ΔD	ΔT	ΔQ	Δ5	ΔD	ΔT	ΔQ	Δ5
C_2H_6	-79.759085	-79.799743	-79.806543	-79.808964	-17.697	-2.299	-1.181	-0.145	-12.833	-2.336	-1.043	-0.123
C_2H_4NH (aziridine)	-133.853420	-133.908815	-133.921210	-133.925728	-19.121	-3.656	-1.978	-0.277	-15.890	-4.174	-2.080	-0.336
CH_3CH_2O	-154.297941	-154.361371	-154.375924	-154.380952	-18.807	-3.569	-1.907	-0.317	-16.960	-4.404	-2.014	-0.381
$HCOOCH_3$	-229.010779	-229.097698	-229.118896	-229.125896	-21.750	-4.903	-2.504	-0.402	-19.773	-5.551	-2.388	-0.458
CH_3COOH	-229.033254	-229.121057	-229.142722	-229.149819	-22.756	-4.923	-2.612	-0.441	-20.586	-5.854	-2.599	-0.512
CH_3CHCH_2	-117.830372	-117.881808	-117.891584	-117.895269	-21.039	-3.386	-1.944	-0.243	-15.837	-3.513	-1.854	-0.225
C_3H_6 (cyclopropane)	-117.813575	-117.864729	-117.874526	-117.878107	-20.788	-3.514	-1.965	-0.252	-15.648	-3.288	-1.826	-0.249
CH_3CH_2OH	-154.965354	-155.035023	-155.050669	-155.056044	-20.804	-3.609	-1.846	-0.286	-17.995	-4.835	-2.095	-0.401
CH_3OCH_3	-154.953392	-155.020073	-155.034690	-155.039760	-19.764	-3.637	-1.788	-0.249	-16.067	-4.110	-1.776	-0.327
CH_3CONH_2	-209.149057	-209.232459	-209.252536	-209.259341	-24.708	-4.873	-2.559	-0.372	-22.262	-6.408	-2.866	-0.483
C_4H_4O (furan)	-229.952631	-230.030404	-230.049686	-230.056665	-22.804	-5.907	-3.276	-0.426	-18.211	-5.515	-3.013	-0.398
$(CH_3)_2CH$	-118.388182	-118.441000	-118.451058	-118.454756	-22.202	-3.460	-1.847	-0.225	-16.665	-3.596	-1.755	-0.209
$(CH_3)_2NH$	-135.079031	-135.139389	-135.152207	-135.156756	-22.196	-3.630	-1.737	-0.208	-17.565	-4.377	-1.868	-0.290
$CH_3CH_2NH_2$	-135.088711	-135.150441	-135.163536	-135.168160	-22.980	-3.589	-1.778	-0.222	-18.158	-4.548	-1.952	-0.292
$CH_2CHCHCH_2$ (trans-2-butene)	-155.909281	-155.971074	-155.983636	-155.988493	-24.176	-4.444	-2.698	-0.338	-18.433	-4.509	-2.606	-0.315
C_4H_6 (methyl-cyclopropane)	-155.874646	-155.936297	-155.949000	-155.953674	-24.051	-4.619	-2.665	-0.426	-18.457	-4.423	-2.515	-0.436
C_4H_6 (bicyclo[1.1.0]butane)	-155.857083	-155.915929	-155.928777	-155.933391	-22.806	-4.726	-2.629	-0.375	-17.475	-4.058	-2.414	-0.367
C_4H_6 (cyclobutene)	-155.884906	-155.943131	-155.955831	-155.960441	-22.974	-4.672	-2.532	-0.361	-17.611	-4.427	-2.371	-0.325
C_4H_6 (dimethylacetylene)	-155.891003	-155.955837	-155.968367	-155.972955	-25.586	-4.416	-2.711	-0.585	-19.248	-4.387	-2.528	-0.565
CH_3COCH_3	-193.076337	-193.152649	-193.170148	-193.175973	-25.026	-4.792	-2.511	-0.379	-20.573	-5.112	-2.283	-0.350
C_4H_5N (pyrrole)	-210.086265	-210.158871	-210.176697	-210.183410	-25.039	-5.847	-3.263	-0.371	-20.228	-6.150	-3.346	-0.398
C_3H_8	-119.045101	-119.100686	-119.110786	-119.114350	-23.896	-3.465	-1.740	-0.215	-17.316	-3.408	-1.556	-0.193
C_5H_5N (pyridine)	-248.191001	-248.272266	-248.292601	-248.300037	-28.323	-6.979	-3.934	-0.427	-22.937	-6.761	-3.720	-0.372
C_4H_8 (isobutylene)	-157.121131	-157.187703	-157.200773	-157.205548	-27.359	-4.560	-2.488	-0.303	-20.239	-4.528	-2.294	-0.259
$C_2H_5OCH_3$	-194.244631	-194.326585	-194.344305	-194.350322	-26.244	-4.808	-2.347	-0.319	-20.807	-5.033	-2.144	-0.341
C_6H_6 (benzene)	-232.142525	-232.220820	-232.239058	-232.246156	-29.530	-6.717	-4.015	-0.416	-22.962	-6.199	-3.775	-0.348
$(CH_3)_3N$	-174.360994	-174.434676	-174.450406	-174.455843	-27.794	-4.859	-2.253	-0.282	-21.171	-5.306	-2.218	-0.323

	cc-pV*n*Z				cc-pV*n*Z[rc](tr)				cc-pV*n*Z-BLYP			
Molecule	D	T	Q	5	ΔD	ΔT	ΔQ	Δ5	ΔD	ΔT	ΔQ	Δ5
C_5H_8 (spiropentane)	-195.151117	-195.226946	-195.242984	-195.248719	-30.059	-5.896	-3.207	-0.447	-22.924	-5.264	-2.954	-0.451
C_4H_{10} (butane)	-158.330909	-158.401427	-158.414828	-158.419484	-30.074	-4.635	-2.293	-0.279	-21.880	-4.508	-2.060	-0.256
				MAD	16.627	3.486	1.986	0.340	14.140	3.790	1.986	0.391
				MSD	-16.627	-3.486	-1.986	-0.340	-14.140	-3.790	-1.986	-0.391

Table A.4. Comparisons between BLYP complete basis set limit energies (E_h) computed with the cc-pV*n*Z, cc-pV*n*Z[rc](tr), and cc-pV*n*Z-BLYP basis sets at fixed geometries optimized with B3LYP/cc-pVTZ. The cc-pV*n*Z[rc](tr) and cc-pV*n*Z-B3LYP basis sets are listed as energy differences (mE_h) from the cc-pV*n*Z sets. The different extrapolation schemes are denoted as: the Peterson exponential formula (P), Schwartz cubic formula (S3), and Schwartz quartic formula (S4).

	cc-pV*n*Z			cc-pV*n*Z[rc](tr)			cc-pV*n*Z-B3LYP		
Molecule	P	S3	S4	ΔP	ΔS3	ΔS4	ΔP	ΔS3	ΔS4
H_2	-1.170430	-1.173468	-1.172030	0.012	0.206	0.082	0.026	0.188	0.085
CH	-38.482553	-38.486565	-38.483817	-0.270	-0.427	-0.579	-0.188	-0.580	-0.733
NH	-55.231792	-55.238382	-55.233840	-0.288	-0.385	-0.582	-0.302	-1.034	-1.267
OH	-75.762830	-75.773286	-75.765929	-0.305	-0.370	-0.592	-0.403	-1.602	-1.901
FH	-100.492873	-100.508602	-100.497596	-0.294	-0.350	-0.599	-0.453	-1.973	-2.356
CN	-92.747072	-92.755866	-92.749821	-0.364	-0.828	-1.130	-0.330	-0.875	-1.158
CO	-113.359175	-113.370957	-113.362804	-0.310	-0.824	-1.131	-0.174	-0.874	-1.159
N_2	-109.570283	-109.582274	-109.574253	-0.340	-0.781	-1.110	-0.516	-1.166	-1.454
NO	-129.949342	-129.961779	-129.952798	-0.259	-0.939	-1.198	-0.313	-1.284	-1.535
O_2	-150.396297	-150.410424	-150.400018	-0.343	-1.131	-1.324	-0.195	-1.307	-1.460
F_2	-199.616706	-199.640340	-199.624083	-0.568	-1.096	-1.380	-0.620	-1.487	-1.787
CH_2 (triplet)	-39.146812	-39.152595	-39.149046	-0.211	-0.280	-0.500	-0.172	-0.542	-0.730
CH_2 (singlet)	-39.132574	-39.138664	-39.134834	-0.191	-0.254	-0.483	-0.086	-0.408	-0.620
NH_2	-55.890273	-55.899150	-55.893265	-0.206	-0.211	-0.488	-0.235	-1.119	-1.398
H_2O	-76.458774	-76.471788	-76.462729	-0.212	-0.203	-0.502	-0.395	-1.995	-2.332
CCH (linear)	-76.620302	-76.629759	-76.623858	-0.451	-0.767	-1.096	-0.457	-0.882	-1.154
HCN	-93.452306	-93.463351	-93.456223	-0.334	-0.728	-1.087	-0.218	-0.943	-1.253
HCO	-113.896209	-113.908768	-113.900101	-0.258	-0.788	-1.108	-0.118	-0.961	-1.269
CO_2	-188.670725	-188.690954	-188.677112	-0.441	-1.290	-1.743	-0.225	-1.260	-1.712
N_2O	-184.752255	-184.770405	-184.757731	-0.406	-1.446	-1.831	-0.417	-1.440	-1.756
NO_2	-205.181837	-205.201201	-205.186959	-0.180	-1.483	-1.815	-0.102	-1.817	-2.118
O_3	-225.545317	-225.567174	-225.550956	-0.301	-1.692	-1.950	-0.059	-2.240	-2.448
CH_3	-39.831732	-39.839546	-39.835079	-0.148	-0.104	-0.408	-0.086	-0.425	-0.666
NH_3	-56.569160	-56.580026	-56.572956	-0.088	-0.013	-0.374	-0.079	-1.135	-1.456
C_2H_2	-77.341370	-77.352765	-77.345949	-0.446	-0.656	-1.039	-0.372	-0.960	-1.259

	cc-pV*n*Z			cc-pV*n*Z[rc](tr)			cc-pV*n*Z-B3LYP		
Molecule	P	S3	S4	ΔP	ΔS3	ΔS4	ΔP	ΔS3	ΔS4
H_2CO	-114.539982	-114.554191	-114.544719	-0.189	-0.676	-1.044	-0.036	-0.904	-1.255
NCCN	-185.717071	-185.735509	-185.723157	-0.726	-1.752	-2.332	-0.661	-1.698	-2.178
BF_3	-324.710022	-324.751634	-324.724537	-0.593	-1.927	-2.428	-0.682	-0.908	-1.411
NF_3	-354.267933	-354.307644	-354.279781	-0.612	-2.236	-2.671	-0.508	-3.015	-3.499
CH_4	-40.506257	-40.515435	-40.510457	-0.046	0.062	-0.312	0.051	-0.152	-0.420
C_2H_3	-77.904572	-77.915514	-77.908818	-0.277	-0.548	-0.964	-0.224	-0.815	-1.148
H_2COH	-115.091554	-115.107007	-115.096645	-0.196	-0.619	-1.028	-0.219	-1.404	-1.770
CH_3O	-115.079131	-115.094159	-115.084191	-0.199	-0.620	-1.020	-0.162	-1.172	-1.566
CH_2CO (ketene)	-152.648613	-152.666477	-152.654752	-0.405	-1.081	-1.608	-0.284	-1.165	-1.601
HCOOH	-189.836711	-189.858889	-189.843751	-0.229	-1.122	-1.632	-0.065	-1.617	-2.122
CH_2F_2	-239.083578	-239.114001	-239.093518	-0.385	-1.264	-1.738	-0.518	-1.449	-1.980
CHF_3	-338.389057	-338.429467	-338.402078	-0.499	-1.884	-2.425	-0.766	-1.508	-2.098
CF_4	-437.688418	-437.738397	-437.704439	-0.595	-2.514	-3.121	-1.052	-1.426	-2.014
C_2H_4	-78.585470	-78.597731	-78.590453	-0.209	-0.416	-0.893	-0.129	-0.721	-1.084
H_3COH	-115.748058	-115.765293	-115.754014	-0.124	-0.475	-0.945	-0.115	-1.333	-1.760
H_2NNH_2	-111.893365	-111.910228	-111.898937	-0.083	-0.398	-0.924	-0.020	-1.754	-2.233
CH_3CN	-132.775986	-132.792337	-132.781920	-0.383	-0.940	-1.531	-0.246	-1.204	-1.694
CH_3CO	-153.219095	-153.237019	-153.225002	-0.249	-0.997	-1.546	-0.141	-1.281	-1.764
CH_2CHF	-177.877770	-177.900378	-177.885576	-0.344	-1.062	-1.597	-0.385	-1.131	-1.596
HCOCOH (glyoxal)	-227.900898	-227.925082	-227.908251	-0.319	-1.610	-2.214	-0.027	-1.697	-2.286
CF_3CN	-430.636898	-430.683737	-430.651811	-0.786	-2.925	-3.672	-0.998	-1.959	-2.638
C_2F_4	-475.729652	-475.782742	-475.746126	-0.649	-2.981	-3.693	-1.146	-1.838	-2.515
CH_3NH_2	-95.862009	-95.877284	-95.867584	-0.046	-0.281	-0.830	0.018	-1.094	-1.546
CH_3CCH	-116.659652	-116.676132	-116.666172	-0.489	-0.880	-1.482	-0.394	-1.204	-1.662
CH_2CCH_2 (allene)	-116.664096	-116.679875	-116.670227	-0.436	-0.912	-1.497	-0.341	-1.186	-1.629
C_3H_4 (cyclopropene)	-116.620566	-116.635684	-116.626286	-0.363	-0.963	-1.529	-0.378	-1.104	-1.534
CH_3CHO	-153.862329	-153.881606	-153.869000	-0.183	-0.892	-1.483	0.010	-1.114	-1.628
C_2H_4O (oxirane)	-153.816824	-153.836226	-153.823446	-0.198	-1.016	-1.555	-0.229	-1.359	-1.839
CH_2CHCN	-170.861353	-170.880972	-170.868307	-0.522	-1.402	-2.099	-0.406	-1.605	-2.176
CH_3NO_2	-245.106570	-245.132970	-245.114405	-0.062	-1.566	-2.161	0.211	-2.115	-2.691

	cc-pV*n*Z			cc-pV*n*Z[rc](tr)			cc-pV*n*Z-B3LYP		
Molecule	P	S3	S4	ΔP	ΔS3	ΔS4	ΔP	ΔS3	ΔS4
CH_3ONO	-245.102034	-245.127853	-245.109931	-0.174	-1.634	-2.224	-0.018	-1.995	-2.485
CH_3COF	-253.182955	-253.212853	-253.192787	-0.338	-1.484	-2.169	-0.257	-1.494	-2.127
C_2H_6	-79.810431	-79.824451	-79.816406	-0.057	-0.170	-0.753	0.049	-0.415	-0.836
C_2H_4NH (aziridine)	-133.928385	-133.946022	-133.934625	-0.160	-0.863	-1.484	-0.098	-1.284	-1.795
CH_3CH_2O	-154.384129	-154.404247	-154.391163	-0.182	-0.843	-1.453	-0.035	-1.287	-1.835
$HCOOCH_3$	-229.130592	-229.157693	-229.139612	-0.157	-1.348	-2.051	0.052	-1.655	-2.295
CH_3COOH	-229.154631	-229.181913	-229.163617	-0.238	-1.348	-2.083	-0.008	-1.802	-2.465
CH_3CHCH_2	-117.897337	-117.914473	-117.904122	-0.200	-0.636	-1.321	-0.093	-0.949	-1.462
C_3H_6 (cyclopropane)	-117.880203	-117.897245	-117.886947	-0.179	-0.704	-1.380	-0.164	-0.886	-1.391
CH_3CH_2OH	-155.059466	-155.081726	-155.067404	-0.119	-0.703	-1.382	0.035	-1.402	-1.985
CH_3OCH_3	-155.042947	-155.064399	-155.050737	-0.050	-0.739	-1.385	0.041	-1.139	-1.660
CH_3CONH_2	-209.263753	-209.289819	-209.272494	-0.175	-1.170	-1.972	0.043	-1.967	-2.686
C_4H_4O (furan)	-230.060810	-230.084724	-230.068466	-0.265	-1.900	-2.630	-0.219	-1.942	-2.520
$(CH_3)_2CH$	-118.456903	-118.474520	-118.463894	-0.118	-0.549	-1.275	-0.008	-0.885	-1.427
$(CH_3)_2NH$	-135.159529	-135.179101	-135.166785	0.001	-0.558	-1.287	0.101	-1.155	-1.728
$CH_3CH_2NH_2$	-135.170997	-135.191029	-135.178436	-0.044	-0.518	-1.272	0.107	-1.207	-1.798
$CH_2CHCHCH_2$ (trans-2-butene)	-155.991126	-156.011294	-155.998738	-0.344	-1.101	-1.882	-0.249	-1.423	-2.014
C_4H_6 (methyl-cyclopropane)	-155.956386	-155.976503	-155.963967	-0.345	-1.186	-1.962	-0.325	-1.406	-1.995
C_4H_6 (bicyclo[1.1.0]butane)	-155.936159	-155.955064	-155.943005	-0.253	-1.263	-1.999	-0.326	-1.284	-1.842
C_4H_6 (cyclobutene)	-155.963167	-155.981863	-155.969929	-0.209	-1.195	-1.939	-0.162	-1.364	-1.930
C_4H_6 (dimethylacetylene)	-155.975634	-155.997179	-155.984111	-0.558	-1.104	-1.927	-0.447	-1.400	-2.013
CH_3COCH_3	-193.179839	-193.204117	-193.188391	-0.182	-1.110	-1.923	0.059	-1.387	-2.056
C_4H_5N (pyrrole)	-210.187188	-210.209510	-210.194341	-0.237	-1.722	-2.528	-0.201	-2.148	-2.791
C_3H_8	-119.116537	-119.135347	-119.124240	-0.058	-0.406	-1.192	0.047	-0.707	-1.274
C_5H_5N (pyridine)	-248.304393	-248.329270	-248.312252	-0.287	-2.157	-3.066	-0.191	-2.310	-3.042
C_4H_8 (isobutylene)	-157.208345	-157.230377	-157.216932	-0.183	-0.859	-1.751	-0.047	-1.187	-1.844
$C_2H_5OCH_3$	-194.354211	-194.380730	-194.363979	-0.050	-0.961	-1.819	0.111	-1.293	-1.972
C_6H_6 (benzene)	-232.249972	-232.274426	-232.258192	-0.399	-2.025	-2.973	-0.365	-2.137	-2.867
$(CH_3)_3N$	-174.459275	-174.483177	-174.468139	0.038	-0.837	-1.749	0.169	-1.380	-2.072

C_5H_8 (spiropentane)	-195.252178	-195.276785	-195.261318	-0.265	-1.445	-2.420	-0.316	-1.577	-2.312
C_4H_{10} (butane)	-158.422401	-158.446019	-158.431852	-0.050	-0.641	-1.629	0.063	-0.997	-1.713
			MAD	0.274	1.005	1.546	0.248	1.313	1.775
			MSD	-0.273	-0.999	-1.544	-0.221	-1.308	-1.773

Table A.5. Comparisons of CPU savings for B3LYP total energy calculations computed with the cc-pV*n*Z[rc](tr) and cc-pV*n*Z-B3LYP basis sets as a percent ratio of the cc-pV*n*Z basis sets, using fixed geometries optimized with B3LYP/cc-pVTZ.

Molecule	B3LYP cc-pV*n*Z[rc](tr)				B3LYP cc-pV*n*Z-B3LYP			
	vdz	vtz	vqz	v5z	vdz	vtz	vqz	v5z
H_2	0.00%	0.00%	44.12%	62.50%	0.00%	0.00%	41.18%	62.50%
CH	-4.00%	0.00%	41.06%	57.69%	0.00%	-2.13%	41.72%	58.37%
NH	-3.85%	-2.08%	41.45%	57.83%	0.00%	0.00%	41.45%	58.04%
OH	-4.00%	0.00%	41.06%	57.69%	0.00%	-2.13%	41.72%	58.37%
FH	0.00%	-2.86%	44.35%	60.84%	0.00%	-5.71%	44.35%	60.57%
CN	4.76%	-0.99%	41.18%	59.05%	-4.76%	-1.98%	41.94%	59.93%
CO	-3.23%	-1.41%	45.69%	61.66%	-6.45%	1.41%	45.69%	60.90%
N_2	0.00%	-2.08%	45.41%	58.82%	0.00%	0.00%	45.87%	59.54%
NO	5.13%	1.12%	48.24%	60.55%	2.56%	1.12%	48.24%	60.31%
O_2	-4.35%	-1.96%	46.22%	57.52%	-4.35%	-1.96%	45.33%	58.14%
F_2	0.00%	0.00%	45.97%	58.64%	4.76%	0.00%	44.55%	57.07%
CH_2 (triplet)	0.00%	0.71%	48.15%	67.46%	-1.79%	1.43%	48.46%	67.10%
CH_2 (singlet)	0.00%	-2.27%	51.55%	69.80%	0.00%	1.14%	51.55%	69.54%
NH_2	-1.96%	-1.65%	49.15%	68.39%	1.96%	-0.83%	48.98%	68.48%
H_2O	-5.71%	-4.71%	52.32%	70.61%	2.86%	-3.53%	52.11%	70.57%
CCH (linear)	0.00%	1.59%	47.57%	62.52%	14.29%	17.14%	57.11%	70.17%
HCN	-2.13%	0.76%	52.12%	64.54%	-2.13%	4.55%	52.69%	64.96%
HCO	3.30%	0.00%	49.75%	66.31%	2.20%	-0.38%	49.68%	66.02%
CO_2	0.00%	-0.69%	52.40%	62.98%	-2.38%	-0.69%	52.05%	63.59%
N_2O	1.49%	1.33%	51.91%	63.08%	1.49%	-0.44%	51.25%	62.88%
NO_2	0.00%	0.22%	47.31%	62.83%	0.00%	-0.22%	49.94%	62.72%
O_3	1.05%	0.00%	50.19%	64.61%	1.05%	-0.29%	50.09%	64.66%
CH_3	2.04%	2.33%	54.92%	70.91%	-14.29%	0.78%	54.92%	70.98%
NH_3	0.00%	7.28%	56.14%	73.17%	1.92%	7.95%	53.73%	73.26%
C_2H_2	2.50%	3.68%	58.20%	67.64%	5.00%	1.47%	59.17%	67.55%

Molecule	B3LYP cc-pV*n*Z[rc](tr)				B3LYP cc-pV*n*Z-B3LYP			
	vdz	vtz	vqz	v5z	vdz	vtz	vqz	v5z
H_2CO	-1.79%	4.95%	57.42%	69.35%	-3.57%	3.30%	57.51%	69.57%
NCCN	-1.43%	0.60%	55.48%	64.00%	0.00%	0.30%	55.52%	64.09%
BF_3	-1.20%	0.25%	53.62%	64.35%	-3.61%	-0.50%	52.86%	63.19%
NF_3	-0.63%	0.43%	51.60%	64.25%	-0.63%	-0.58%	50.95%	63.80%
CH_4	-1.64%	0.00%	58.94%	74.03%	-6.56%	0.00%	59.05%	71.60%
C_2H_3	-0.65%	0.32%	56.04%	68.37%	0.00%	0.16%	55.93%	69.75%
H_2COH	0.85%	2.91%	54.06%	69.21%	0.00%	2.82%	54.26%	69.13%
CH_3O	-2.04%	1.58%	56.19%	68.54%	-0.68%	2.11%	56.38%	70.09%
CH_2CO (ketene)	-0.98%	0.00%	55.70%	67.03%	0.00%	-0.66%	55.68%	67.19%
HCOOH	0.00%	-3.39%	55.69%	69.15%	1.85%	-4.07%	55.60%	68.94%
CH_2F_2	0.00%	0.00%	56.20%	69.50%	-4.08%	1.07%	55.09%	68.40%
CHF_3	-2.79%	-2.75%	53.79%	66.89%	-3.35%	-2.75%	53.53%	66.59%
CF_4	5.29%	-2.76%	53.12%	64.96%	4.81%	-3.38%	53.00%	64.16%
C_2H_4	-1.85%	-0.35%	64.17%	71.48%	0.00%	0.35%	64.17%	71.43%
H_3COH	0.83%	0.17%	59.94%	71.16%	-7.50%	-0.67%	59.99%	71.13%
H_2NNH_2	0.00%	-0.19%	58.54%	72.36%	0.00%	0.66%	58.59%	72.29%
CH_3CN	0.61%	0.11%	57.43%	69.01%	1.22%	0.32%	55.36%	69.05%
CH_3CO	-0.78%	2.22%	57.28%	68.87%	0.78%	1.84%	56.82%	68.88%
CH_2CHF	4.43%	-5.46%	56.08%	67.96%	4.93%	-5.93%	55.93%	67.96%
HCOCOH (glyoxal)	-0.70%	-3.58%	55.81%	68.03%	2.82%	0.49%	55.69%	69.83%
CF_3CN	0.28%	-0.90%	52.43%	64.75%	0.85%	-1.61%	51.59%	63.95%
C_2F_4	3.66%	-0.50%	55.22%	64.43%	3.05%	-2.43%	53.34%	63.23%
CH_3NH_2	-0.68%	0.00%	60.00%	71.94%	-1.35%	-0.24%	60.16%	71.98%
CH_3CCH	0.45%	-0.36%	57.76%	68.51%	0.45%	3.20%	58.17%	68.91%
CH_2CCH_2 (allene)	-0.70%	-0.12%	59.25%	68.16%	-5.63%	0.96%	60.82%	68.66%
C_3H_4 (cyclopropene)	-0.70%	-0.69%	59.35%	70.27%	0.70%	0.14%	61.54%	70.39%
CH_3CHO	0.88%	0.00%	59.04%	70.27%	0.88%	-0.28%	58.90%	70.33%

Molecule	B3LYP cc-pV*n*Z[rc](tr)				B3LYP cc-pV*n*Z-B3LYP			
	vdz	vtz	vqz	v5z	vdz	vtz	vqz	v5z
C_2H_4O (oxirane)	3.50%	-1.96%	60.31%	71.37%	1.40%	-2.09%	60.44%	71.46%
CH_2CHCN	0.28%	0.23%	57.43%	69.06%	-1.11%	0.77%	57.38%	69.52%
CH_3NO_2	-1.61%	-0.05%	56.35%	71.47%	-1.61%	-0.24%	56.39%	71.44%
CH_3ONO	0.00%	3.23%	56.22%	72.74%	0.19%	3.64%	56.41%	72.82%
CH_3COF	0.68%	0.40%	57.27%	68.89%	1.02%	0.60%	57.09%	68.81%
C_2H_6	2.04%	0.72%	64.31%	73.09%	2.04%	0.72%	64.36%	73.02%
C_2H_4NH (aziridine)	0.84%	-0.06%	60.44%	71.32%	0.84%	0.00%	60.26%	71.53%
CH_3CH_2O	2.45%	0.60%	60.96%	72.16%	1.40%	0.64%	60.88%	72.07%
$HCOOCH_3$	0.00%	0.69%	57.43%	73.12%	0.31%	0.83%	57.38%	72.99%
CH_3COOH	-0.79%	0.22%	56.56%	69.22%	0.26%	4.63%	58.52%	69.91%
CH_3CHCH_2	-1.46%	-0.19%	61.12%	72.07%	0.29%	0.23%	60.85%	72.13%
C_3H_6 (cyclopropane)	-1.10%	-0.07%	63.45%	72.64%	0.55%	-0.82%	63.57%	73.45%
CH_3CH_2OH	2.45%	0.60%	60.96%	72.16%	1.40%	0.64%	60.88%	72.07%
CH_3OCH_3	-1.23%	2.91%	60.88%	72.15%	1.23%	2.79%	60.95%	72.26%
CH_3CONH_2	1.06%	-5.38%	58.80%	75.87%	9.69%	-5.81%	58.51%	75.92%
C_4H_4O (furan)	0.45%	0.54%	58.11%	70.29%	1.81%	0.70%	58.41%	70.53%
$(CH_3)_2CH$	-0.43%	0.40%	82.58%	75.29%	1.41%	1.20%	59.42%	75.63%
$(CH_3)_2NH$	9.00%	-2.04%	61.37%	75.87%	9.49%	-2.54%	61.44%	76.45%
$CH_3CH_2NH_2$	-0.29%	0.10%	62.55%	73.34%	0.29%	-0.37%	62.13%	73.36%
$CH_2CHCHCH_2$ (trans-2-butene)	0.88%	-0.37%	80.68%	71.77%	8.30%	1.34%	80.81%	72.40%
C_4H_6 (methyl-cyclopropane)	1.05%	0.00%	61.30%	72.16%	-4.20%	-0.12%	61.86%	72.52%
C_4H_6 (bicyclo[1.1.0]butane)	-0.38%	-0.66%	61.81%	72.28%	1.52%	1.04%	61.66%	72.61%
C_4H_6 (cyclobutene)	0.00%	-0.08%	61.76%	71.98%	0.74%	0.83%	63.65%	71.96%
C_4H_6 (dimethylacetylene)	1.32%	0.71%	60.40%	72.27%	0.44%	3.79%	61.08%	72.30%
CH_3COCH_3	0.21%	4.74%	61.72%	72.98%	1.24%	4.52%	61.66%	73.12%
C_4H_5N (pyrrole)	0.74%	0.44%	60.24%	70.72%	0.00%	1.03%	60.72%	71.18%
C_3H_8	-1.25%	0.50%	62.75%	73.83%	1.00%	-0.16%	62.75%	73.81%

C_5H_5N (pyridine)	0.00%	0.82%	59.20%	70.73%	1.32%	1.66%	59.63%	71.12%
C_4H_8 (isobutylene)	-0.95%	-0.08%	63.72%	72.46%	0.79%	0.26%	63.84%	73.42%
$C_2H_5OCH_3$	0.46%	-1.24%	59.11%	71.32%	2.01%	0.88%	59.42%	71.70%
C_6H_6 (benzene)	-0.54%	0.77%	62.92%	70.93%	0.66%	6.29%	63.14%	72.62%
$(CH_3)_3N$	0.46%	-0.13%	62.69%	73.20%	1.15%	-0.08%	62.75%	73.74%
C_5H_8 (spiropentane)	-1.09%	-0.50%	63.48%	74.17%	1.21%	0.82%	63.77%	74.20%
C_4H_{10} (butane)	-0.68%	0.20%	62.62%	73.71%	0.14%	2.13 %	63.02%	74.11%

Table A.6. Comparisons of CPU savings for BLYP total energy calculations computed with the cc-pV*n*Z[rc](tr) and cc-pV*n*Z-BLYP basis sets as a percent ratio of the cc-pV*n*Z basis sets, using fixed geometries optimized with B3LYP/cc-pVTZ.

	cc-pV*n*Z[rc](tr)				cc-pV*n*Z-BLYP			
Molecule	D	T	Q	5	D	T	Q	5
H_2	-10.00%	-7.69%	41.67%	58.03%	0.00%	-7.69%	44.12%	61.36%
CH	0.00%	0.00%	40.79%	57.77%	0.00%	0.00%	42.36%	58.03%
NH	-3.70%	0.00%	41.67%	58.03%	3.70%	2.00%	40.79%	57.77%
OH	0.00%	0.00%	45.45%	60.60%	0.00%	0.00%	42.36%	58.03%
FH	0.00%	0.00%	43.01%	59.79%	0.00%	-2.86%	45.45%	60.05%
CN	-2.50%	0.00%	44.34%	61.45%	-7.50%	3.23%	43.01%	61.52%
CO	-3.23%	-1.37%	46.33%	58.52%	-3.23%	0.00%	44.98%	61.28%
N_2	-5.00%	-4.26%	45.24%	57.81%	0.00%	0.00%	46.33%	60.22%
NO	-8.57%	-4.94%	43.44%	58.21%	-8.57%	-3.70%	42.86%	57.54%
O_2	0.00%	-3.85%	46.45%	58.63%	0.00%	-1.92%	43.44%	57.84%
F_2	0.00%	2.08%	47.58%	66.94%	0.00%	0.00%	45.50%	57.71%
CH_2 (triplet)	-1.89%	-1.53%	51.64%	71.47%	0.00%	0.00%	47.23%	67.13%
CH_2 (singlet)	2.56%	0.00%	49.64%	67.62%	0.00%	1.08%	51.41%	71.36%
NH_2	0.00%	-0.84%	51.63%	70.76%	1.89%	0.84%	50.00%	67.90%
H_2O	0.00%	0.00%	49.43%	63.17%	-2.78%	-1.11%	51.63%	70.09%
CCH (linear)	-1.72%	0.00%	52.95%	64.40%	-1.72%	-0.63%	50.19%	63.27%
HCN	-4.44%	-2.36%	51.46%	66.72%	0.00%	-3.94%	54.07%	64.33%
HCO	0.00%	8.47%	52.69%	62.82%	-1.18%	8.47%	51.22%	66.82%
CO_2	-2.38%	-3.55%	51.06%	62.94%	-4.76%	-2.13%	52.22%	63.75%
N_2O	-1.59%	0.00%	48.69%	64.13%	-3.17%	-0.93%	50.83%	62.81%
NO_2	-0.86%	-4.58%	51.61%	65.55%	-1.72%	-4.83%	46.45%	62.87%
O_3	1.06%	-0.63%	37.12%	66.00%	-1.06%	-0.63%	50.32%	65.02%
CH_3	-2.04%	0.00%	54.49%	70.93%	-1.02%	-2.19%	74.38%	79.21%
NH_3	-2.17%	0.00%	55.76%	74.27%	-4.35%	0.00%	54.34%	71.07%
C_2H_2	-2.08%	0.00%	57.42%	67.28%	-2.08%	0.00%	55.65%	75.51%
H_2CO	-5.41%	0.00%	56.72%	68.84%	-2.70%	2.26%	59.98%	67.00%
NCCN	-3.70%	5.88%	55.37%	63.82%	-3.70%	5.35%	56.89%	69.59%

Molecule	cc-pV*n*Z[rc](tr)				cc-pV*n*Z-BLYP			
	D	T	Q	5	D	T	Q	5
BF_3	-2.94%	-2.17%	53.97%	64.18%	-2.94%	-1.55%	55.73%	63.87%
NF_3	0.00%	2.78%	50.84%	64.34%	4.71%	1.77%	52.81%	63.43%
CH_4	-0.65%	0.77%	58.34%	74.32%	-9.80%	0.31%	50.51%	63.68%
C_2H_3	-3.17%	-2.67%	56.70%	67.29%	-1.59%	-1.78%	58.40%	74.28%
H_2COH	-1.37%	1.02%	54.52%	68.87%	-2.05%	0.68%	56.37%	70.18%
CH_3O	1.20%	1.84%	54.03%	67.39%	1.99%	2.23%	51.38%	68.69%
CH_2CO (ketene)	-0.69%	-3.32%	55.72%	67.36%	0.00%	-3.14%	54.61%	68.67%
HCOOH	0.94%	2.81%	53.79%	69.50%	0.00%	3.46%	56.16%	67.59%
CH_2F_2	-0.60%	2.18%	54.49%	68.59%	0.00%	0.68%	53.79%	69.46%
CHF_3	3.09%	1.30%	55.63%	66.93%	1.03%	2.07%	55.48%	68.16%
CF_4	0.00%	0.55%	53.09%	65.37%	-0.52%	-3.75%	55.55%	67.52%
C_2H_4	0.49%	-2.59%	63.72%	71.33%	1.47%	-2.34%	53.03%	64.84%
H_3COH	0.00%	-1.40%	59.62%	73.10%	0.00%	-1.75%	64.04%	71.47%
H_2NNH_2	-0.81%	2.65%	58.34%	71.89%	0.81%	3.15%	59.75%	73.18%
CH_3CN	-1.04%	0.11%	57.60%	69.01%	-1.56%	-8.54%	58.25%	71.91%
CH_3CO	0.61%	0.22%	56.42%	68.77%	0.00%	0.43%	57.31%	69.11%
CH_2CHF	-1.24%	2.72%	57.21%	68.65%	-0.41%	2.55%	56.26%	70.70%
HCOCOH (glyoxal)	-4.08%	0.00%	56.26%	67.89%	-2.04%	0.00%	56.96%	68.61%
CF_3CN	1.44%	0.12%	50.29%	65.10%	0.72%	0.49%	56.09%	70.22%
C_2F_4	1.38%	1.83%	54.88%	63.61%	1.38%	-2.78%	49.80%	64.35%
CH_3NH_2	1.84%	-0.33%	61.38%	71.92%	-1.23%	-2.50%	52.72%	62.49%
CH_3CCH	-0.70%	-0.24%	57.92%	70.59%	0.00%	-1.21%	61.27%	71.97%
CH_2CCH_2 (allene)	-1.44%	-0.38%	59.36%	69.98%	0.48%	3.23%	58.17%	71.06%
C_3H_4 (cyclopropene)	-1.30%	-2.09%	58.98%	70.21%	0.00%	0.37%	60.85%	70.32%
CH_3CHO	-1.39%	-0.27%	59.13%	70.51%	-0.69%	-0.54%	61.58%	70.23%
C_2H_4O (oxirane)	-9.35%	-0.61%	61.18%	71.73%	-7.94%	-0.23%	59.25%	70.58%
CH_2CHCN	-0.68%	3.70%	57.52%	70.05%	0.68%	7.28%	62.20%	71.86%
CH_3NO_2	-0.58%	-0.84%	56.41%	69.85%	1.16%	-0.19%	57.22%	70.42%
CH_3ONO	-6.40%	2.53%	56.08%	71.16%	-6.18%	2.76%	56.32%	69.71%
CH_3COF	0.18%	-2.92%	57.25%	68.95%	2.03%	-0.06%	56.14%	71.07%

Molecule	cc-pV*n*Z[rc](tr)				cc-pV*n*Z-BLYP			
	D	T	Q	5	D	T	Q	5
C_2H_6	0.35%	0.05%	63.95%	72.92%	1.76%	-4.53%	57.11%	68.87%
C_2H_4NH (aziridine)	0.00%	-1.17%	60.34%	70.92%	1.05%	-1.61%	64.21%	73.14%
CH_3CH_2O	-0.83%	0.37%	61.36%	73.03%	-0.41%	-0.56%	60.12%	71.07%
$HCOOCH_3$	-1.37%	-0.14%	57.08%	70.41%	0.68%	-0.64%	61.26%	73.02%
CH_3COOH	1.22%	-2.73%	60.02%	70.03%	2.14%	-2.28%	57.15%	70.52%
CH_3CHCH_2	0.27%	2.28%	62.43%	71.26%	0.54%	2.17%	59.97%	70.05%
C_3H_6 (cyclopropane)	0.57%	-0.41%	63.03%	72.41%	0.28%	-0.69%	62.22%	71.59%
CH_3CH_2OH	-0.56%	-0.15%	61.36%	73.03%	-5.06%	-0.45%	63.04%	72.79%
CH_3OCH_3	-1.37%	-0.14%	60.89%	71.87%	0.68%	-0.64%	61.26%	73.02%
CH_3CONH_2	0.90%	0.13%	59.81%	71.51%	0.90%	-0.17%	61.10%	72.17%
C_4H_4O (furan)	2.24%	2.71%	60.20%	71.34%	3.51%	2.18%	57.78%	71.40%
$(CH_3)_2CH$	2.13%	4.17%	60.64%	72.22%	3.05%	4.33%	60.13%	71.69%
$(CH_3)_2NH$	0.44%	-0.38%	60.90%	74.28%	0.00%	-0.66%	62.16%	72.37%
$CH_3CH_2NH_2$	-1.59%	-0.06%	62.74%	73.16%	0.18%	-0.46%	60.72%	74.25%
$CH_2CHCHCH_2$ (trans-2-butene)	-0.60%	-0.61%	63.25%	71.17%	0.00%	-0.47%	62.66%	73.28%
C_4H_6 (methyl-cyclopropane)	0.66%	2.51%	61.54%	71.94%	0.99%	4.19%	63.33%	71.49%
C_4H_6 (bicyclo[1.1.0]butane)	-0.34%	0.00%	61.69%	71.96%	0.68%	0.29%	61.52%	72.24%
C_4H_6 (cyclobutene)	0.00%	-2.05%	61.56%	71.66%	0.78%	0.57%	61.51%	72.51%
C_4H_6 (dimethylacetylene)	-0.36%	-0.37%	60.25%	72.38%	0.00%	-0.12%	61.81%	72.01%
CH_3COCH_3	-0.42%	0.71%	60.32%	71.98%	1.67%	3.59%	60.69%	72.74%
C_4H_5N (pyrrole)	1.69%	4.03%	60.19%	70.69%	7.84%	3.81%	60.20%	71.04%
C_3H_8	-1.68%	2.61%	62.93%	73.88%	0.24%	-0.09%	60.59%	71.11%
C_5H_5N (pyridine)	0.51%	2.59%	60.14%	71.49%	0.51%	2.13%	62.91%	73.96%
C_4H_8 (isobutylene)	1.44%	-0.04%	64.31%	73.57%	3.21%	0.77%	61.47%	71.96%
$C_2H_5OCH_3$	0.25%	0.21%	60.84%	72.32%	2.03%	0.69%	64.11%	73.73%
C_6H_6 (benzene)	5.44%	-0.11%	62.85%	71.20%	1.51%	1.84%	61.28%	72.58%
$(CH_3)_3N$	0.00%	0.10%	62.54%	73.51%	0.42%	5.42%	63.24%	72.74%
C_5H_8 (spiropentane)	-0.85%	-0.58%	63.55%	73.64%	-0.85%	-0.41%	62.37%	73.88%
C_4H_{10} (butane)	0.00%	0.45%	62.47%	73.36%	2.27%	0.98%	63.58%	73.79%

Tables A.7: Hydrogen cc-pVDZ-B3LYP
(4*s*1*p*) → [2*s*1*p*]

s	Exponent	Coefficient	Coefficient
	1.2412060E+01	2.1987109E-02	-
	1.8911710E+00	1.5073329E-01	-
	4.2468271E-01	4.8584667E-01	-
	1.1006130E-01	4.8957333E-01	1.0000000E+00

p	Exponent	Coefficient
	9.8827060E-01	1.0000000E+00

Tables A.8: Hydrogen cc-pVTZ-B3LYP
(5*s*2*p*1*d*) → [3*s*2*p*1*d*]

s	Exponent	Coefficient	Coefficient	Coefficient
	3.3638981E+01	6.3580722E-03	-	-
	5.1757202E+00	4.7122482E-02	-	-
	1.1737961E+00	2.0877273E-01	-	-
	3.1995761E-01	5.0213146E-01	1.0000000E+00	-
	9.3408182E-02	3.8866943E-01	-	1.0000000E+00

p	Exponent	Coefficient	Coefficient
	1.7460300E+00	1.0000000E+00	-
	4.8582710E-01	-	1.0000000E+00

d	Exponent	Coefficient
	1.0570000E+00	1.0000000E+00

Tables A.9: Hydrogen cc-pVQZ-B3LYP

(6*s*3*p*2*d*) → [4*s*3*p*2*d*]

s	Exponent	Coefficient	Coefficient	Coefficient	Coefficient
	8.2845871E+01	2.1339275E-03	-	-	-
	1.2242850E+01	1.6309276E-02	-	-	-
	2.8669810E+00	7.7692658E-02	-	-	-
	8.1378722E-01	2.5703800E-01	1.0000000E+00	-	-
	2.5508261E-01	4.9218780E-01	-	1.0000000E+00	-
	8.1797399E-02	3.0990607E-01	-	-	1.0000000E+00

p	Exponent	Coefficient	Coefficient	Coefficient
	2.3636190E+00	1.0000000E+00	-	-
	7.7487650E-01	-	1.0000000E+00	-
	3.1704410E-01	-	-	1.0000000E+00

d	Exponent	Coefficient	Coefficient
	2.0620000E+00	1.0000000E+00	-
	6.6200000E-01	-	1.0000000E+00

Tables A.10: Hydrogen cc-pV5Z-B3LYP
(8*s*4*p*3*d*) → [5*s*4*p*3*d*]

s	Exponent	Coefficient	Coefficient	Coefficient	Coefficient	Coefficient
	4.0170740E+02	2.9168426E-04	-	-	-	-
	6.0258839E+01	2.2934561E-03	-	-	-	-
	1.3698810E+01	1.1750787E-02	-	-	-	-
	3.9292610E+00	4.7781955E-02	-	-	-	-
	1.2702980E+00	1.5066747E-01	1.0000000E+00	-	-	-
	4.6678180E-01	3.0907935E-01	-	1.0000000E+00	-	-
	1.8542220E-01	4.1817626E-01	-	-	1.0000000E+00	-
	6.9170877E-02	2.1666324E-01	-	-	-	1.0000000E+00

p	Exponent	Coefficient	Coefficient	Coefficient	Coefficient
	4.5567800E+00	1.0000000E+00	-	-	-
	1.7439500E+00	-	1.0000000E+00	-	-
	5.9312240E-01	-	-	1.0000000E+00	-
	2.5541990E-01	-	-	-	1.0000000E+00

d	Exponent	Coefficient	Coefficient	Coefficient
	2.9500000E+00	1.0000000E+00	-	-
	1.2060000E+00	-	1.0000000E+00	-
	4.9300000E-01	-	-	1.0000000E+00

Tables A.11: Hydrogen cc-pVDZ-BLYP
(4*s*1*p*) → [2*s*1*p*]

s	Exponent	Coefficient	Coefficient
	1.2201100E+01	2.2905463E-02	-
	1.8670670E+00	1.5558469E-01	-
	4.1831961E-01	4.8881057E-01	-
	1.0611300E-01	4.8493332E-01	1.0000000E+00

p	Exponent	Coefficient
	1.0122660E+00	1.0000000E+00

Tables A.12: Hydrogen cc-pVTZ-BLYP
(5*s*2*p*1*d*) → [3*s*2*p*1*d*]

s	Exponent	Coefficient	Coefficient	Coefficient
	3.3608871E+01	6.4998353E-03	-	-
	5.1799650E+00	4.8004787E-02	-	-
	1.1782560E+00	2.1132055E-01	-	-
	3.1820601E-01	5.0147569E-01	1.0000000E+00	-
	9.0442330E-02	3.8991678E-01	-	1.0000000E+00

p	Exponent	Coefficient	Coefficient
	1.6859790E+00	1.0000000E+00	-
	4.5488730E-01	-	1.0000000E+00

d	Exponent	Coefficient
	1.0570000E+00	1.0000000E+00

Tables A.13: Hydrogen cc-pVQZ-BLYP
(6*s*3*p*2*d*) → [4*s*3*p*2*d*]

s	Exponent	Coefficient	Coefficient	Coefficient	Coefficient
	8.2880318E+01	2.1794455E-03	-	-	-
	1.2201580E+01	1.6747758E-02	-	-	-
	2.8710539E+00	7.8731902E-02	-	-	-
	8.1936961E-01	2.5789666E-01	1.0000000E+00	-	-
	2.5389409E-01	4.9095026E-01	-	1.0000000E+00	-
	7.8964889E-02	3.1321308E-01	-	-	1.0000000E+00

p	Exponent	Coefficient	Coefficient	Coefficient
	2.4171850E+00	1.0000000E+00	-	-
	7.4448520E-01	-	1.0000000E+00	-
	3.3070400E-01	-	-	1.0000000E+00

d	Exponent	Coefficient	Coefficient
	2.0620000E+00	1.0000000E+00	-
	6.6200000E-01	-	1.0000000E+00

Tables A.14: Hydrogen cc-pV5Z-BLYP
(8*s*4*p*3*d*) → [5*s*4*p*3*d*]

s	Exponent	Coefficient	Coefficient	Coefficient	Coefficient	Coefficient
	4.0151651E+02	2.9608700E-04	-	-	-	-
	6.0282291E+01	2.3560671E-03	-	-	-	-
	1.3678970E+01	1.1910522E-02	-	-	-	-
	3.9430830E+00	4.9121302E-02	-	-	-	-
	1.2619240E+00	1.5386097E-01	1.0000000E+00	-	-	-
	4.6835271E-01	3.0276006E-01	-	1.0000000E+00	-	-
	1.8628730E-01	4.1290429E-01	-	-	1.0000000E+00	-
	6.7738377E-02	2.2791709E-01	-	-	-	1.0000000E+00

p	Exponent	Coefficient	Coefficient	Coefficient	Coefficient
	4.5160570E+00	1.0000000E+00	-	-	-
	1.7120260E+00	-	1.0000000E+00	-	-
	6.4894090E-01	-	-	1.0000000E+00	-
	2.4576360E-01	-	-	-	1.0000000E+00

d	Exponent	Coefficient	Coefficient	Coefficient
	2.9500000E+00	1.0000000E+00	-	-
	1.2060000E+00	-	1.0000000E+00	-
	4.9300000E-01	-	-	1.0000000E+00

Tables A.15: Boron cc-pVDZ-B3LYP
(9*s*4*p*1*d*) → [3*s*2*p*1*d*]

s	Exponent	Coefficient	Coefficient	Coefficient
	4.5590122E+03	7.0625549E-04	-1.3031314E-04	-
	6.8574048E+02	5.4174908E-03	-1.0194045E-03	-
	1.5703960E+02	2.7350210E-02	-5.0788256E-03	-
	4.4697289E+01	1.0240930E-01	-2.0418540E-02	-
	1.4454290E+01	2.7554917E-01	-5.7880044E-02	-
	5.0587292E+00	4.5117405E-01	-1.3390805E-01	-
	1.8290790E+00	2.9533142E-01	-1.2050352E-01	-
	3.3823901E-01	2.0503862E-04	5.5276555E-01	-
	1.0300980E-01	-2.0092893E-02	5.7198256E-01	1.0000000E+00

p	Exponent	Coefficient	Coefficient
	5.9131131E+00	4.1037280E-02	-
	1.2285089E+00	2.1467604E-01	-
	3.3493650E-01	5.0746548E-01	-
	9.0326183E-02	4.7005835E-01	1.0000000E+00

d	Exponent	Coefficient
	3.7196890E-01	1.0000000E+00

Tables A.16: Boron cc-pVTZ-B3LYP
(10*s*5*p*2*d*1*f*) → [4*s*3*p*2*d*1*f*]

s	Exponent	Coefficient	Coefficient	Coefficient	Coefficient
	5.4690811E+03	5.6282867E-04	-1.0965834E-04	-	-
	8.1930280E+02	4.3468606E-03	-8.4578840E-04	-	-
	1.8661459E+02	2.2292368E-02	-4.4025541E-03	-	-
	5.2601479E+01	8.6284287E-02	-1.7434314E-02	-	-
	1.6903191E+01	2.4276984E-01	-5.3899508E-02	-	-
	5.8885241E+00	4.3682471E-01	-1.1976314E-01	-	-
	2.1250510E+00	3.4353051E-01	-1.5663539E-01	-	-
	5.5424601E-01	3.6768679E-02	1.5904182E-01	1.0000000E+00	-
	2.3228960E-01	-2.3251612E-02	5.9095871E-01	-	-
	8.2305819E-02	-5.0759790E-03	3.8369474E-01	-	1.0000000E+00

p	Exponent	Coefficient	Coefficient	Coefficient
	1.1831730E+01	1.4783619E-02	-	-
	2.6927240E+00	8.4723905E-02	-	-
	7.6203239E-01	2.9261130E-01	-	-
	2.3831390E-01	4.9864087E-01	1.0000000E+00	-
	7.2421558E-02	3.5369256E-01	-	1.0000000E+00

d	Exponent	Coefficient	Coefficient
	1.6293090E+00	1.0000000E+00	-
	3.2426380E-01	-	1.0000000E+00

f	Exponent	Coefficient
	1.0918700E+00	1.0000000E+00

Tables A.17: Boron cc-pVQZ-B3LYP
(11*s*6*p*3*d*2*f*) → [5*s*4*p*3*d*2*f*]

s	Exponent	Coefficient	Coefficient	Coefficient	Coefficient	Coefficient
	2.3888811E+04	8.9485045E-05	-1.7520508E-05	-	-	-
	3.5718059E+03	6.9297972E-04	-1.3563778E-04	-	-	-
	8.1743732E+02	3.6045567E-03	-7.0792175E-04	-	-	-
	2.3033279E+02	1.5200527E-02	-3.0015826E-03	-	-	-
	7.4467194E+01	5.2274294E-02	-1.0555740E-02	-	-	-
	2.6910509E+01	1.4242513E-01	-3.0164218E-02	-	-	-
	1.0420780E+01	2.9756871E-01	-7.1380116E-02	-	-	-
	4.1872492E+00	4.0388069E-01	-1.2753461E-01	-	-	-
	1.6912110E+00	2.3677310E-01	-1.2126037E-01	-	-	-
	4.7579369E-01	1.3298037E-02	2.7724627E-01	1.0000000E+00	-	-
	1.9025511E-01	-1.5669564E-02	5.7989645E-01	-	1.0000000E+00	-
	7.2394997E-02	-4.2121359E-03	2.8794819E-01	-	-	1.0000000E+00

p	Exponent	Coefficient	Coefficient	Coefficient	Coefficient
	2.2321720E+01	5.5234209E-03	-	-	-
	5.0870490E+00	3.8115785E-02	-	-	-
	1.4859760E+00	1.4204226E-01	-	-	-
	5.1174313E-01	3.4154892E-01	1.0000000E+00	-	-
	1.7934319E-01	4.5827946E-01	-	1.0000000E+00	-
	6.0589369E-02	2.6387382E-01	-	-	1.0000000E+00

d	Exponent	Coefficient	Coefficient	Coefficient
	2.8268320E+00	1.0000000E+00	-	-
	1.0070220E+00	-	1.0000000E+00	-
	2.5726550E-01	-	-	1.0000000E+00

f	Exponent	Coefficient	Coefficient
	2.0270050E+00	1.0000000E+00	-

	6.8428770E-01	-	1.0000000E+00

Tables A.18: Boron cc-pV5Z-B3LYP
(12*s*8*p*4*d*3*f*) → [6*s*5*p*4*d*3*f*]

s	Exponent	Coefficient	Coefficient	Coefficient	Coefficient	Coefficient	Coefficient
	6.8263461E+04	2.3974646E-05	-4.6903774E-06	-	-	-	-
	1.0270900E+04	1.8572812E-04	-3.6565889E-05	-	-	-	-
	2.3352100E+03	9.7728195E-04	-1.9084406E-04	-	-	-	-
	6.6376233E+02	4.0632919E-03	-8.0490467E-04	-	-	-	-
	2.1735960E+02	1.4551631E-02	-2.8593589E-03	-	-	-	-
	7.8628777E+01	4.4583518E-02	-9.0901721E-03	-	-	-	-
	3.1029160E+01	1.1355940E-01	-2.3566175E-02	-	-	-	-
	1.2963590E+01	2.3478347E-01	-5.5097044E-02	-	-	-	-
	5.6305680E+00	3.5146031E-01	-9.7014844E-02	-	-	-	-
	2.5308690E+00	3.0084702E-01	-1.2721422E-01	-	-	-	-
	1.1608480E+00	9.8510981E-02	-5.0712183E-02	1.0000000E+00	-	-	-
	4.3603089E-01	-2.2028843E-03	3.3858997E-01	-	1.0000000E+00	-	-
	1.7163040E-01	-1.0888292E-02	5.6842232E-01	-	-	1.0000000E+00	
	6.7188501E-02	-4.3088146E-03	2.3993392E-01	-	-	-	1.0000000E+00

p	Exponent	Coefficient	Coefficient	Coefficient	Coefficient	Coefficient
	6.6826492E+01	9.2647062E-04	-	-	-	-
	1.5692400E+01	6.9455337E-03	-	-	-	-
	4.9460492E+00	3.3170499E-02	-	-	-	-
	1.7439700E+00	1.0039590E-01	-	-	-	-
	7.0212650E-01	2.3306432E-01	1.0000000E+00	-	-	-
	2.9572889E-01	3.5276070E-01	-	1.0000000E+00	-	-
	1.2312730E-01	3.6165169E-01	-	-	1.0000000E+00	-
	4.8172291E-02	1.6369157E-01	-	-	-	1.0000000E+00

d	Exponent	Coefficient	Coefficient	Coefficient	Coefficient
	4.6446800E+00	1.0000000E+00	-	-	-
	1.7836430E+00	-	1.0000000E+00	-	-
	7.4798890E-01	-	-	1.0000000E+00	-
	2.0552200E-01	-	-	-	1.0000000E+00

f	Exponent	Coefficient	Coefficient	Coefficient
	2.9419710E+00	1.0000000E+00	-	-
	1.2040080E+00	-	1.0000000E+00	-
	4.9249340E-01	-	-	1.0000000E+00

Tables A.19: Boron cc-pVDZ-BLYP
(9*s*4*p*1*d*) → [3*s*2*p*1*d*]

s	Exponent	Coefficient	Coefficient	Coefficient
	4.5637329E+03	7.0603652E-04	-1.3662707E-04	-
	6.8804230E+02	5.4120044E-03	-1.0648854E-03	-
	1.5719650E+02	2.7466083E-02	-5.3554927E-03	-
	4.4646679E+01	1.0286691E-01	-2.1394247E-02	-
	1.4433520E+01	2.7562091E-01	-6.0900267E-02	-
	5.0437899E+00	4.4973758E-01	-1.3779560E-01	-
	1.8132060E+00	2.9500079E-01	-1.2145973E-01	-
	3.3870369E-01	3.6065117E-03	5.5808216E-01	-
	1.0162900E-01	-1.6840037E-02	5.6846762E-01	1.0000000E+00

p	Exponent	Coefficient	Coefficient
	5.9083881E+00	4.2006265E-02	-
	1.2325470E+00	2.1610248E-01	-
	3.3641389E-01	5.0595051E-01	-

	8.8356487E-02	4.7429815E-01	1.0000000E+00

d	Exponent	Coefficient
	3.7161550E-01	1.0000000E+00

Tables A.20: Boron cc-pVTZ-BLYP
(10*s*5*p*2*d*1*f*) → [4*s*3*p*2*d*1*f*]

s	Exponent	Coefficient	Coefficient	Coefficient	Coefficient
	5.4645962E+03	5.6453317E-04	-1.1440166E-04	-	-
	8.1921283E+02	4.3629566E-03	-8.8136218E-04	-	-
	1.8630080E+02	2.2434672E-02	-4.6115159E-03	-	-
	5.2462742E+01	8.6834662E-02	-1.8192196E-02	-	-
	1.6851761E+01	2.4336247E-01	-5.6327172E-02	-	-
	5.8674278E+00	4.3536675E-01	-1.2325900E-01	-	-
	2.1104310E+00	3.4224918E-01	-1.5765980E-01	-	-
	5.5421591E-01	3.8604066E-02	1.6250180E-01	1.0000000E+00	-
	2.3230889E-01	-2.0762630E-02	5.9049016E-01	-	-
	8.0977388E-02	-3.3881185E-03	3.8277510E-01	-	1.0000000E+00

p	Exponent	Coefficient	Coefficient	Coefficient
	1.1846890E+01	1.5189775E-02	-	-
	2.6960080E+00	8.5799210E-02	-	-
	7.6649129E-01	2.9292917E-01	-	-
	2.3959820E-01	4.9444887E-01	1.0000000E+00	-
	7.0510551E-02	3.6237738E-01	-	1.0000000E+00

d	Exponent	Coefficient	Coefficient
	1.0781610E+00	1.0000000E+00	-
	2.8910640E-01	-	1.0000000E+00

f	Exponent	Coefficient
	1.0918480E+00	1.0000000E+00

Tables A.21: Boron cc-pVQZ-BLYP
(11*s*6*p*3*d*2*f*) → [5*s*4*p*3*d*2*f*]

s	Exponent	Coefficient	Coefficient	Coefficient	Coefficient	Coefficient
	2.3969650E+04	8.9294430E-05	-1.8171560E-05	-	-	-
	3.5779451E+03	6.9593010E-04	-1.4123347E-04	-	-	-
	8.1466681E+02	3.6347557E-03	-7.4276538E-04	-	-	-
	2.3017500E+02	1.5192654E-02	-3.1065103E-03	-	-	-
	7.4702339E+01	5.2218765E-02	-1.0982544E-02	-	-	-
	2.6958561E+01	1.4266098E-01	-3.1205252E-02	-	-	-
	1.0431390E+01	2.9661784E-01	-7.4393161E-02	-	-	-
	4.1860061E+00	4.0248621E-01	-1.2920719E-01	-	-	-
	1.6812680E+00	2.3780507E-01	-1.2338728E-01	-	-	-
	4.7813600E-01	1.5203206E-02	2.8096163E-01	1.0000000E+00	-	-
	1.9014920E-01	-1.3225527E-02	5.7885462E-01	-	1.0000000E+00	-
	7.1022108E-02	-2.9914335E-03	2.8807974E-01	-	-	1.0000000E+00

p	Exponent	Coefficient	Coefficient	Coefficient	Coefficient
	2.2321341E+01	5.6252419E-03	-	-	-
	5.0915322E+00	3.9119355E-02	-	-	-
	1.4820290E+00	1.4455424E-01	-	-	-
	5.1149988E-01	3.4036085E-01	1.0000000E+00	-	-
	1.8084720E-01	4.4677413E-01	-	1.0000000E+00	-
	5.9693009E-02	2.7940378E-01	-	-	1.0000000E+00

d	Exponent	Coefficient	Coefficient	Coefficient

	2.8268220E+00	1.0000000E+00	-	-
	1.0069710E+00	-	1.0000000E+00	-
	2.5701540E-01	-	-	1.0000000E+00

f	Exponent	Coefficient	Coefficient
	2.0270100E+00	1.0000000E+00	-
	6.8426990E-01	-	1.0000000E+00

Tables A.22: Boron cc-pV5Z-BLYP
(12*s*8*p*4*d*3*f*) → [6*s*5*p*4*d*3*f*]

s	Exponent	Coefficient	Coefficient	Coefficient	Coefficient	Coefficient	Coefficient
	6.8177430E+04	2.3993012E-05	-4.8673023E-06	-	-	-	-
	1.0290110E+04	1.8627854E-04	-3.8094953E-05	-	-	-	-
	2.3359380E+03	9.7751955E-04	-1.9778071E-04	-	-	-	-
	6.6372443E+02	4.0954626E-03	-8.4333523E-04	-	-	-	-
	2.1673010E+02	1.4606483E-02	-2.9706082E-03	-	-	-	-
	7.8717453E+01	4.4634506E-02	-9.4682015E-03	-	-	-	-
	3.1019890E+01	1.1391910E-01	-2.4426637E-02	-	-	-	-
	1.2968880E+01	2.3417850E-01	-5.7279866E-02	-	-	-	-
	5.6291628E+00	3.4987926E-01	-9.9484600E-02	-	-	-	-
	2.5304339E+00	2.9878470E-01	-1.2706874E-01	-	-	-	-
	1.1608710E+00	1.0154132E-01	-5.2948371E-02	1.0000000E+00	-	-	-
	4.3603590E-01	-4.4075350E-04	3.4483972E-01	-	1.0000000E+00	-	-
	1.7184700E-01	-8.4920833E-03	5.5783468E-01	-	-	1.0000000E+00	
	6.7012258E-02	-3.3855324E-03	2.4666615E-01	-	-	-	1.0000000E+00

p	Exponent	Coefficient	Coefficient	Coefficient	Coefficient	Coefficient
	6.6826492E+01	9.4249839E-04	-	-	-	-
	1.5692460E+01	7.0785256E-03	-	-	-	-

	4.9460492E+00	3.4172457E-02	-	-	-	-
	1.7439260E+00	1.0122474E-01	-	-	-	-
	7.0216191E-01	2.3584385E-01	1.0000000E+00	-	-	-
	2.9570991E-01	3.4871924E-01	-	1.0000000E+00	-	-
	1.2313970E-01	3.5055098E-01	-	-	1.0000000E+00	-
	4.8116110E-02	1.8073842E-01	-	-	-	1.0000000E+00

d	Exponent	Coefficient	Coefficient	Coefficient	Coefficient
	4.6447310E+00	1.0000000E+00	-	-	-
	1.7836400E+00	-	1.0000000E+00	-	-
	7.4794820E-01	-	-	1.0000000E+00	-
	2.0532830E-01	-	-	-	1.0000000E+00

f	Exponent	Coefficient	Coefficient	Coefficient
	2.9419750E+00	1.0000000E+00	-	-
	1.2040150E+00	-	1.0000000E+00	-
	4.9247910E-01	-	-	1.0000000E+00

Tables A.23: Carbon cc-pVDZ-B3LYP
(9*s*4*p*1*d*) → [3*s*2*p*1*d*]

s	Exponent	Coefficient	Coefficient	Coefficient
	6.6486338E+03	7.0101517E-04	-1.3046099E-04	-
	1.0028500E+03	5.3728353E-03	-1.0260957E-03	-
	2.2910390E+02	2.7264800E-02	-5.0963596E-03	-
	6.5118240E+01	1.0249297E-01	-2.0874389E-02	-
	2.1090860E+01	2.7743122E-01	-5.8912318E-02	-
	7.4328299E+00	4.5205471E-01	-1.4047322E-01	-
	2.7216671E+00	2.9255077E-01	-1.1474977E-01	-
	5.2354407E-01	-3.0745864E-03	5.6076521E-01	-

	1.5456089E-01	-2.2747638E-02	5.6838429E-01	1.0000000E+00

p	Exponent	Coefficient	Coefficient
	9.2682571E+00	4.2837888E-02	-
	1.9636370E+00	2.2483097E-01	-
	5.3505683E-01	5.1133424E-01	-
	1.4136700E-01	4.6015173E-01	1.0000000E+00

d	Exponent	Coefficient
	5.5646300E-01	1.0000000E+00

Tables A.24: Carbon cc-pVTZ-B3LYP
(10*s*5*p*2*d*1*f*) → [4*s*3*p*2*d*1*f*]

s	Exponent	Coefficient	Coefficient	Coefficient	Coefficient
	8.1998330E+03	5.3891051E-04	-1.0647176E-04	-	-
	1.2351310E+03	4.1459310E-03	-8.2037441E-04	-	-
	2.8092709E+02	2.1381332E-02	-4.2774742E-03	-	-
	7.8977242E+01	8.3589807E-02	-1.7223451E-02	-	-
	2.5338800E+01	2.3916627E-01	-5.3907499E-02	-	-
	8.8426418E+00	4.3780375E-01	-1.2379430E-01	-	-
	3.2017801E+00	3.4899575E-01	-1.5955921E-01	-	-
	8.4506941E-01	3.5639793E-02	1.8864039E-01	1.0000000E+00	-
	3.4018040E-01	-2.5375042E-02	5.9589183E-01	-	-
	1.1842740E-01	-6.1905622E-03	3.5771450E-01	-	1.0000000E+00

p	Exponent	Coefficient	Coefficient	Coefficient
	1.8585180E+01	1.5242425E-02	-	-
	4.2075620E+00	9.1386922E-02	-	-
	1.2047840E+00	3.0456644E-01	-	-

	3.7612081E-01	4.9642140E-01	1.0000000E+00	-
	1.1178160E-01	3.4334862E-01	-	1.0000000E+00

d	Exponent	Coefficient	Coefficient
	1.6771810E+00	1.0000000E+00	-
	4.0582580E-01	-	1.0000000E+00

f	Exponent	Coefficient
	1.0918660E+00	1.0000000E+00

Tables A.25: Carbon cc-pVQZ-B3LYP
(11*s*6*p*3*d*2*f*) → [5*s*4*p*3*d*2*f*]

s	Exponent	Coefficient	Coefficient	Coefficient	Coefficient	Coefficient
	3.4040641E+04	9.1886977E-05	-1.8228708E-05	-	-	-
	5.0847231E+03	7.0706534E-04	-1.4076701E-04	-	-	-
	1.1661980E+03	3.7004668E-03	-7.3525734E-04	-	-	-
	3.2721420E+02	1.5588205E-02	-3.1389331E-03	-	-	-
	1.0616190E+02	5.3442549E-02	-1.0919464E-02	-	-	-
	3.8310299E+01	1.4652207E-01	-3.1938866E-02	-	-	-
	1.4892060E+01	3.0242813E-01	-7.4121580E-02	-	-	-
	6.0751328E+00	3.9925990E-01	-1.3317238E-01	-	-	-
	2.5037551E+00	2.3050894E-01	-1.1570054E-01	-	-	-
	7.4023932E-01	1.1419312E-02	2.8852820E-01	1.0000000E+00	-	-
	2.8842789E-01	-1.7612198E-02	5.8111459E-01	-	1.0000000E+00	-
	1.0633340E-01	-5.5624070E-03	2.8239435E-01	-	-	1.0000000E+00

p	Exponent	Coefficient	Coefficient	Coefficient	Coefficient
	3.4934502E+01	5.6659826E-03	-	-	-
	7.8840389E+00	4.0827349E-02	-	-	-

	2.3090489E+00	1.5567358E-01	-	-	-
	7.9023570E-01	3.5711381E-01	1.0000000E+00	-	-
	2.7416131E-01	4.5102370E-01	-	1.0000000E+00	-
	9.0506360E-02	2.4643981E-01	-	-	1.0000000E+00

d	Exponent	Coefficient	Coefficient	Coefficient
	2.8369890E+00	1.0000000E+00	-	-
	9.6801980E-01	-	1.0000000E+00	-
	3.3463990E-01	-	-	1.0000000E+00

f	Exponent	Coefficient	Coefficient
	2.0270190E+00	1.0000000E+00	-
	6.8429680E-01	-	1.0000000E+00

Tables A.26: Carbon cc-pV5Z-B3LYP
(12*s*8*p*4*d*3*f*) → [6*s*5*p*4*d*3*f*]

s	Exponent	Coefficient	Coefficient	Coefficient	Coefficient	Coefficient	Coefficient
	9.6770961E+04	2.4940788E-05	-4.9541613E-06	-	-	-	-
	1.4367300E+04	1.9410405E-04	-3.8780290E-05	-	-	-	-
	3.2980320E+03	1.0059986E-03	-1.9951361E-04	-	-	-	-
	9.3554413E+02	4.2479183E-03	-8.5392373E-04	-	-	-	-
	3.0522681E+02	1.5074411E-02	-3.0115377E-03	-	-	-	-
	1.1169190E+02	4.5277003E-02	-9.3897283E-03	-	-	-	-
	4.4262810E+01	1.1670753E-01	-2.4745915E-02	-	-	-	-
	1.8430071E+01	2.4259788E-01	-5.8668822E-02	-	-	-	-
	7.9993539E+00	3.5957456E-01	-1.0318566E-01	-	-	-	-
	3.5723939E+00	2.9654470E-01	-1.3599050E-01	-	-	-	-
	1.6166070E+00	8.3544999E-02	-2.3840379E-02	1.0000000E+00	-	-	-
	6.4481860E-01	-6.1539141E-03	3.5640711E-01	-	1.0000000E+00	-	-

	2.5544599E-01	-1.2535532E-02	5.5260056E-01	-	-	1.0000000E+00	
	9.8235287E-02	-5.3302548E-03	2.3303716E-01	-	-	-	1.0000000E+00

p	Exponent	Coefficient	Coefficient	Coefficient	Coefficient	Coefficient
	1.0122230E+02	9.4794785E-04	-	-	-	-
	2.4469601E+01	7.1373656E-03	-	-	-	-
	7.7507539E+00	3.4547169E-02	-	-	-	-
	2.7690101E+00	1.0724649E-01	-	-	-	-
	1.1075180E+00	2.4717979E-01	1.0000000E+00	-	-	-
	4.5429429E-01	3.6890689E-01	-	1.0000000E+00	-	-
	1.8243331E-01	3.5085264E-01	-	-	1.0000000E+00	-
	6.9417886E-02	1.4323646E-01	-	-	-	1.0000000E+00

d	Exponent	Coefficient	Coefficient	Coefficient	Coefficient
	4.6470020E+00	1.0000000E+00	-	-	-
	1.8129960E+00	-	1.0000000E+00	-	-
	7.0701030E-01	-	-	1.0000000E+00	-
	2.7571750E-01	-	-	-	1.0000000E+00

f	Exponent	Coefficient	Coefficient	Coefficient
	2.9419700E+00	1.0000000E+00	-	-
	1.2040020E+00	-	1.0000000E+00	-
	4.9250140E-01	-	-	1.0000000E+00

Tables A.27: Carbon cc-pVDZ-BLYP
(9*s*4*p*1*d*) → [3*s*2*p*1*d*]

s	Exponent	Coefficient	Coefficient	Coefficient
	6.6486338E+03	7.0270186E-04	-1.3566023E-04	-
	1.0028500E+03	5.3844168E-03	-1.0653595E-03	-
	2.2910390E+02	2.7348211E-02	-5.3049233E-03	-
	6.5118240E+01	1.0266523E-01	-2.1633789E-02	-
	2.1090860E+01	2.7736300E-01	-6.1153639E-02	-
	7.4328299E+00	4.4904143E-01	-1.4325106E-01	-
	2.7216671E+00	2.9400158E-01	-1.1495226E-01	-
	5.2354407E-01	3.8493099E-04	5.6108564E-01	-
	1.5456089E-01	-2.0601783E-02	5.6770635E-01	1.0000000E+00

p	Exponent	Coefficient	Coefficient
	9.3124428E+00	4.3481793E-02	-
	1.9594210E+00	2.2811316E-01	-
	5.3103769E-01	5.1239675E-01	-
	1.3711810E-01	4.6018630E-01	1.0000000E+00

d	Exponent	Coefficient
	5.5593220E-01	1.0000000E+00

Tables A.28: Carbon cc-pVTZ-BLYP
(10*s*5*p*2*d*1*f*) → [4*s*3*p*2*d*1*f*]

s	Exponent	Coefficient	Coefficient	Coefficient	Coefficient
	8.1975518E+03	5.4128206E-04	-1.1027027E-04	-	-
	1.2301310E+03	4.1836975E-03	-8.5240678E-04	-	-
	2.7950650E+02	2.1566462E-02	-4.4515636E-03	-	-
	7.8671051E+01	8.4057614E-02	-1.7816603E-02	-	-
	2.5271980E+01	2.3949064E-01	-5.5774763E-02	-	-
	8.8196735E+00	4.3665585E-01	-1.2656692E-01	-	-
	3.1839609E+00	3.4810460E-01	-1.6053683E-01	-	-
	8.4544581E-01	3.7009943E-02	1.9189657E-01	1.0000000E+00	-
	3.4044999E-01	-2.3397608E-02	5.9432095E-01	-	-
	1.1696250E-01	-4.9867756E-03	3.5794875E-01	-	1.0000000E+00

p	Exponent	Coefficient	Coefficient	Coefficient
	1.8416040E+01	1.5551971E-02	-	-
	4.2464280E+00	9.1225274E-02	-	-
	1.2103710E+00	3.0708599E-01	-	-
	3.7466809E-01	4.9466932E-01	1.0000000E+00	-
	1.0846360E-01	3.4792987E-01	-	1.0000000E+00

d	Exponent	Coefficient	Coefficient
	1.6770600E+00	1.0000000E+00	-
	4.0542980E-01	-	1.0000000E+00

f	Exponent	Coefficient
	1.0918580E+00	1.0000000E+00

Tables A.29: Carbon cc-pVQZ-BLYP
(11*s*6*p*3*d*2*f*) → [5*s*4*p*3*d*2*f*]

s	Exponent	Coefficient	Coefficient	Coefficient	Coefficient	Coefficient
	3.4137148E+04	9.1394424E-05	-1.8689203E-05	-	-	-
	5.1123340E+03	7.0738641E-04	-1.4496713E-04	-	-	-
	1.1644060E+03	3.7206276E-03	-7.6248130E-04	-	-	-
	3.2703720E+02	1.5631214E-02	-3.2377243E-03	-	-	-
	1.0620830E+02	5.3444263E-02	-1.1268768E-02	-	-	-
	3.8452110E+01	1.4572483E-01	-3.2614887E-02	-	-	-
	1.4958870E+01	3.0141124E-01	-7.6391615E-02	-	-	-
	6.0807528E+00	3.9929533E-01	-1.3483205E-01	-	-	-
	2.4901440E+00	2.3153390E-01	-1.1756561E-01	-	-	-
	7.4279302E-01	1.2642108E-02	2.9280242E-01	1.0000000E+00	-	-
	2.8781840E-01	-1.5598548E-02	5.7997668E-01	-	1.0000000E+00	-
	1.0457910E-01	-4.6084519E-03	2.8182605E-01	-	-	1.0000000E+00

p	Exponent	Coefficient	Coefficient	Coefficient	Coefficient
	3.4918308E+01	5.7200138E-03	-	-	-
	7.9044399E+00	4.1677747E-02	-	-	-
	2.2997360E+00	1.5779272E-01	-	-	-
	7.9144478E-01	3.5408095E-01	1.0000000E+00	-	-
	2.7622929E-01	4.4327471E-01	-	1.0000000E+00	-
	8.9251392E-02	2.5980884E-01	-	-	1.0000000E+00

d	Exponent	Coefficient	Coefficient	Coefficient
	2.8369790E+00	1.0000000E+00	-	-
	9.6803960E-01	-	1.0000000E+00	-
	3.3428590E-01	-	-	1.0000000E+00

f	Exponent	Coefficient	Coefficient
	2.0270340E+00	1.0000000E+00	-

	6.8429050E-01	-	1.0000000E+00

Tables A.30: Carbon cc-pV5Z-BLYP
(12*s*8*p*4*d*3*f*) → [6*s*5*p*4*d*3*f*]

s	Exponent	Coefficient	Coefficient	Coefficient	Coefficient	Coefficient	Coefficient
	9.6771133E+04	2.4956653E-05	-5.1026568E-06	-	-	-	-
	1.4367220E+04	1.9518865E-04	-4.0190051E-05	-	-	-	-
	3.2887190E+03	1.0103441E-03	-2.0612538E-04	-	-	-	-
	9.3604858E+02	4.2486377E-03	-8.8071806E-04	-	-	-	-
	3.0547720E+02	1.5114916E-02	-3.1039440E-03	-	-	-	-
	1.1147640E+02	4.5710832E-02	-9.7810738E-03	-	-	-	-
	4.4057121E+01	1.1737505E-01	-2.5554659E-02	-	-	-	-
	1.8397280E+01	2.4164295E-01	-6.0442109E-02	-	-	-	-
	7.9913960E+00	3.5888073E-01	-1.0526872E-01	-	-	-	-
	3.5530930E+00	2.9631504E-01	-1.3691884E-01	-	-	-	-
	1.6000590E+00	8.4130250E-02	-2.4266269E-02	1.0000000E+00	-	-	-
	6.4607638E-01	-5.2452944E-03	3.6148816E-01	-	1.0000000E+00	-	-
	2.5452739E-01	-1.0621125E-02	5.4919392E-01	-	-	1.0000000E+00	
	9.6793666E-02	-4.5677442E-03	2.3354894E-01	-	-	-	1.0000000E+00

p	Exponent	Coefficient	Coefficient	Coefficient	Coefficient	Coefficient
	1.0123270E+02	9.6351979E-04	-	-	-	-
	2.4475330E+01	7.2001866E-03	-	-	-	-
	7.7623711E+00	3.5428647E-02	-	-	-	-
	2.7650931E+00	1.0767310E-01	-	-	-	-
	1.1093270E+00	2.4926101E-01	1.0000000E+00	-	-	-
	4.5345721E-01	3.6458263E-01	-	1.0000000E+00	-	-
	1.8299110E-01	3.4270200E-01	-	-	1.0000000E+00	-
	6.9074348E-02	1.5842751E-01	-	-	-	1.0000000E+00

d	Exponent	Coefficient	Coefficient	Coefficient	Coefficient
	4.6470830E+00	1.0000000E+00	-	-	-
	1.8129980E+00	-	1.0000000E+00	-	-
	7.0702040E-01	-	-	1.0000000E+00	-
	2.7543110E-01	-	-	-	1.0000000E+00

f	Exponent	Coefficient	Coefficient	Coefficient
	2.9420000E+00	1.0000000E+00	-	-
	1.2040000E+00	-	1.0000000E+00	-
	4.9250660E-01	-	-	1.0000000E+00

Tables A.31: Nitrogen cc-pVDZ-B3LYP
(9*s*4*p*1*d*) → [3*s*2*p*1*d*]

s	Exponent	Coefficient	Coefficient	Coefficient
	8.9787969E+03	7.1348820E-04	-1.3366426E-04	-
	1.3553910E+03	5.4467754E-03	-1.0515427E-03	-
	3.1009671E+02	2.7707139E-02	-5.2078003E-03	-
	8.7724503E+01	1.0505009E-01	-2.1734716E-02	-
	2.8344910E+01	2.8419772E-01	-6.1030697E-02	-
	1.0041000E+01	4.5279646E-01	-1.4663322E-01	-
	3.7270000E+00	2.8232339E-01	-1.0582105E-01	-
	7.4073982E-01	-5.8971294E-03	5.6801879E-01	-
	2.1390229E-01	-2.3723492E-02	5.6330252E-01	1.0000000E+00

p	Exponent	Coefficient	Coefficient
	1.3299790E+01	4.4065077E-02	-
	2.8540161E+00	2.3187968E-01	-
	7.7738369E-01	5.1324368E-01	-

	2.0246071E-01	4.5400947E-01	1.0000000E+00

d	Exponent	Coefficient
	8.1618300E-01	1.0000000E+00

Tables A.32: Nitrogen cc-pVTZ-B3LYP
(10*s*5*p*2*d*1*f*) → [4*s*3*p*2*d*1*f*]

s	Exponent	Coefficient	Coefficient	Coefficient	Coefficient
	1.1350960E+04	5.2971294E-04	-1.0568530E-04	-	-
	1.7169640E+03	4.0717921E-03	-8.1563933E-04	-	-
	3.8838971E+02	2.1236842E-02	-4.2871400E-03	-	-
	1.0868880E+02	8.3380133E-02	-1.7438555E-02	-	-
	3.4923641E+01	2.3899291E-01	-5.4492142E-02	-	-
	1.2252450E+01	4.3803272E-01	-1.2702075E-01	-	-
	4.4638271E+00	3.4907481E-01	-1.5961167E-01	-	-
	1.1908530E+00	3.4030724E-02	2.0851718E-01	1.0000000E+00	-
	4.6536320E-01	-2.6044190E-02	5.9878105E-01	-	-
	1.5939739E-01	-6.6342331E-03	3.4076115E-01	-	1.0000000E+00

p	Exponent	Coefficient	Coefficient	Coefficient
	2.5654869E+01	1.6445685E-02	-	-
	5.8601451E+00	9.8478526E-02	-	-
	1.7096090E+00	3.1456867E-01	-	-
	5.3541690E-01	4.9277264E-01	1.0000000E+00	-
	1.5733640E-01	3.3336201E-01	-	1.0000000E+00

d	Exponent	Coefficient	Coefficient
	1.6540000E+00	1.0000000E+00	-
	4.6853100E-01	-	1.0000000E+00

f	Exponent	Coefficient
	1.0919070E+00	1.0000000E+00

Tables A.33: Nitrogen cc-pVQZ-B3LYP
(11*s*6*p*3*d*2*f*) → [5*s*4*p*3*d*2*f*]

s	Exponent	Coefficient	Coefficient	Coefficient	Coefficient	Coefficient
	4.5971559E+04	9.3016191E-05	-1.8632716E-05	-	-	-
	6.8796592E+03	7.2214025E-04	-1.4551102E-04	-	-	-
	1.5635060E+03	3.7994327E-03	-7.6160493E-04	-	-	-
	4.4162439E+02	1.5712138E-02	-3.2079942E-03	-	-	-
	1.4510970E+02	5.2975763E-02	-1.0915007E-02	-	-	-
	5.2816349E+01	1.4592664E-01	-3.2392312E-02	-	-	-
	2.0489519E+01	3.0650041E-01	-7.6006986E-02	-	-	-
	8.3355360E+00	4.0133619E-01	-1.3883339E-01	-	-	-
	3.4531479E+00	2.2537220E-01	-1.0984296E-01	-	-	-
	1.0433640E+00	9.3909036E-03	3.0295950E-01	1.0000000E+00	-	-
	3.9762250E-01	-1.8350402E-02	5.8202779E-01	-	1.0000000E+00	-
	1.4324480E-01	-6.0270200E-03	2.7103159E-01	-	-	1.0000000E+00

p	Exponent	Coefficient	Coefficient	Coefficient	Coefficient
	4.9909950E+01	5.7322797E-03	-	-	-
	1.1397110E+01	4.1519981E-02	-	-	-
	3.3696361E+00	1.6068016E-01	-	-	-
	1.1519600E+00	3.6153904E-01	1.0000000E+00	-	-
	3.9687279E-01	4.4767416E-01	-	1.0000000E+00	-
	1.2829320E-01	2.4421334E-01	-	-	1.0000000E+00

d	Exponent	Coefficient	Coefficient	Coefficient

	2.8370000E+00	1.0000000E+00	-	-
	9.6800000E-01	-	1.0000000E+00	-
	3.3466500E-01	-	-	1.0000000E+00

f	Exponent	Coefficient	Coefficient
	2.0270000E+00	1.0000000E+00	-
	6.8431500E-01	-	1.0000000E+00

Tables A.34: Nitrogen cc-pV5Z-B3LYP
(12*s*8*p*4*d*3*f*) → [6*s*5*p*4*d*3*f*]

s	Exponent	Coefficient	Coefficient	Coefficient	Coefficient	Coefficient	Coefficient
	1.2877860E+05	2.5771253E-05	-5.1777733E-06	-	-	-	-
	1.9167180E+04	2.0062948E-04	-4.0488798E-05	-	-	-	-
	4.4029102E+03	1.0341251E-03	-2.0758419E-04	-	-	-	-
	1.2538840E+03	4.3592402E-03	-8.8476721E-04	-	-	-	-
	4.0786450E+02	1.5599378E-02	-3.1589807E-03	-	-	-	-
	1.4849780E+02	4.7088139E-02	-9.8691275E-03	-	-	-	-
	5.8867748E+01	1.2004390E-01	-2.5942067E-02	-	-	-	-
	2.4714291E+01	2.4649288E-01	-6.0740199E-02	-	-	-	-
	1.0774640E+01	3.6495480E-01	-1.0830541E-01	-	-	-	-
	4.7695551E+00	2.9440451E-01	-1.4108780E-01	-	-	-	-
	2.1015611E+00	7.1274772E-02	3.0306315E-03	1.0000000E+00	-	-	-
	8.6011910E-01	-9.2923306E-03	3.8036889E-01	-	1.0000000E+00	-	-
	3.4142551E-01	-1.2964862E-02	5.3555387E-01	-	-	1.0000000E+00	
	1.3050070E-01	-5.4461136E-03	2.1506655E-01	-	-	-	1.0000000E+00

p	Exponent	Coefficient	Coefficient	Coefficient	Coefficient	Coefficient
	1.4655740E+02	9.5061655E-04	-	-	-	-
	3.4817341E+01	7.3148557E-03	-	-	-	-

	1.1218160E+01	3.4745742E-02	-	-	-	-
	4.0470052E+00	1.1116327E-01	-	-	-	-
	1.6096570E+00	2.5473422E-01	1.0000000E+00	-	-	-
	6.5166938E-01	3.7464330E-01	-	1.0000000E+00	-	-
	2.5670439E-01	3.4530139E-01	-	-	1.0000000E+00	-
	9.5331967E-02	1.3629605E-01	-	-	-	1.0000000E+00

d	Exponent	Coefficient	Coefficient	Coefficient	Coefficient
	4.6470000E+00	1.0000000E+00	-	-	-
	1.8130000E+00	-	1.0000000E+00	-	-
	7.0700000E-01	-	-	1.0000000E+00	-
	2.7572400E-01	-	-	-	1.0000000E+00

f	Exponent	Coefficient	Coefficient	Coefficient
	2.9420000E+00	1.0000000E+00	-	-
	1.2040000E+00	-	1.0000000E+00	-
	4.9250700E-01	-	-	1.0000000E+00

Tables A.35: Nitrogen cc-pVDZ-BLYP
(9*s*4*p*1*d*) → [3*s*2*p*1*d*]

s	Exponent	Coefficient	Coefficient	Coefficient
	8.9695957E+03	7.1399874E-04	-1.3822455E-04	-
	1.3571140E+03	5.4597179E-03	-1.0871688E-03	-
	3.0914621E+02	2.7937405E-02	-5.4308851E-03	-
	8.7348160E+01	1.0572384E-01	-2.2531131E-02	-
	2.8230631E+01	2.8478149E-01	-6.3334391E-02	-
	9.9987898E+00	4.5132345E-01	-1.4939983E-01	-
	3.7014830E+00	2.8158024E-01	-1.0611400E-01	-
	7.4233907E-01	-3.6988810E-03	5.7088447E-01	-

	2.1205850E-01	-2.1340664E-02	5.6178766E-01	1.0000000E+00

p	Exponent	Coefficient	Coefficient
	1.3124790E+01	4.5614768E-02	-
	2.8081100E+00	2.3756948E-01	-
	7.6377690E-01	5.1409656E-01	-
	1.9547050E-01	4.5071974E-01	1.0000000E+00

d	Exponent	Coefficient
	8.1536680E-01	1.0000000E+00

Tables A.36: Nitrogen cc-pVTZ-BLYP
(10*s*5*p*2*d*1*f*) → [4*s*3*p*2*d*1*f*]

s	Exponent	Coefficient	Coefficient	Coefficient	Coefficient
	1.1383780E+04	5.2934047E-04	-1.0832716E-04	-	-
	1.7161930E+03	4.0930831E-03	-8.4006443E-04	-	-
	3.8739819E+02	2.1342780E-02	-4.4212192E-03	-	-
	1.0859080E+02	8.3550259E-02	-1.7888913E-02	-	-
	3.4912350E+01	2.3901367E-01	-5.5976640E-02	-	-
	1.2244330E+01	4.3696702E-01	-1.2925270E-01	-	-
	4.4478431E+00	3.4891453E-01	-1.6066165E-01	-	-
	1.1934670E+00	3.5205487E-02	2.1075651E-01	1.0000000E+00	-
	4.6598330E-01	-2.4323931E-02	5.9740460E-01	-	-
	1.5770170E-01	-5.6633363E-03	3.4162703E-01	-	1.0000000E+00

p	Exponent	Coefficient	Coefficient	Coefficient
	2.5592310E+01	1.6748354E-02	-	-
	5.8556528E+00	9.9756517E-02	-	-

	1.6997590E+00	3.1899261E-01	-	-
	5.2794981E-01	4.9140105E-01	1.0000000E+00	-
	1.5157160E-01	3.3410421E-01	-	1.0000000E+00

d	Exponent	Coefficient	Coefficient
	1.6540000E+00	1.0000000E+00	-
	4.6806250E-01	-	1.0000000E+00

f	Exponent	Coefficient
	1.0919070E+00	1.0000000E+00

Tables A.37: Nitrogen cc-pVQZ-BLYP
(11*s*6*p*3*d*2*f*) → [5*s*4*p*3*d*2*f*]

s	Exponent	Coefficient	Coefficient	Coefficient	Coefficient	Coefficient
	4.5956621E+04	9.3019516E-05	-1.9108938E-05	-	-	-
	6.9006040E+03	7.2129292E-04	-1.4893513E-04	-	-	-
	1.5630291E+03	3.8192887E-03	-7.8539480E-04	-	-	-
	4.4128531E+02	1.5727583E-02	-3.2891200E-03	-	-	-
	1.4526120E+02	5.3074807E-02	-1.1220963E-02	-	-	-
	5.2784180E+01	1.4627136E-01	-3.3227209E-02	-	-	-
	2.0494360E+01	3.0537885E-01	-7.7844545E-02	-	-	-
	8.3417444E+00	3.9979586E-01	-1.3986649E-01	-	-	-
	3.4452369E+00	2.2687732E-01	-1.1136784E-01	-	-	-
	1.0459610E+00	1.0532610E-02	3.0658612E-01	1.0000000E+00	-	-
	3.9644331E-01	-1.6682882E-02	5.8143926E-01	-	1.0000000E+00	-
	1.4087071E-01	-5.1911236E-03	2.7008244E-01	-	-	1.0000000E+00

p	Exponent	Coefficient	Coefficient	Coefficient	Coefficient
	4.9984119E+01	5.8010500E-03	-	-	-

	1.1371170E+01	4.2406365E-02	-	-	-
	3.3662341E+00	1.6093948E-01	-	-	-
	1.1596670E+00	3.5941043E-01	1.0000000E+00	-	-
	3.9732170E-01	4.4567594E-01	-	1.0000000E+00	-
	1.2518691E-01	2.5249264E-01	-	-	1.0000000E+00

d	Exponent	Coefficient	Coefficient	Coefficient
	2.8370000E+00	1.0000000E+00	-	-
	9.6800000E-01	-	1.0000000E+00	-
	3.3433030E-01	-	-	1.0000000E+00

f	Exponent	Coefficient	Coefficient
	2.0270000E+00	1.0000000E+00	-
	6.8431500E-01	-	1.0000000E+00

Tables A.38: Nitrogen cc-pV5Z-BLYP
(12*s*8*p*4*d*3*f*) → [6*s*5*p*4*d*3*f*]

s	Exponent	Coefficient	Coefficient	Coefficient	Coefficient	Coefficient	Coefficient
	1.2868870E+05	2.5870962E-05	-5.3256886E-06	-	-	-	-
	1.9171180E+04	2.0047415E-04	-4.1492771E-05	-	-	-	-
	4.4017852E+03	1.0409255E-03	-2.1399475E-04	-	-	-	-
	1.2531570E+03	4.3442813E-03	-9.0472028E-04	-	-	-	-
	4.1010120E+02	1.5535895E-02	-3.2198797E-03	-	-	-	-
	1.4873360E+02	4.7276478E-02	-1.0169927E-02	-	-	-	-
	5.8947369E+01	1.1990115E-01	-2.6486758E-02	-	-	-	-
	2.4704880E+01	2.4760683E-01	-6.2740646E-02	-	-	-	-
	1.0719220E+01	3.6535528E-01	-1.1043286E-01	-	-	-	-
	4.7367449E+00	2.9205018E-01	-1.4154504E-01	-	-	-	-
	2.0913470E+00	7.1979165E-02	3.9500371E-03	1.0000000E+00	-	-	-

	8.6074942E-01	-8.4621077E-03	3.8375616E-01	-	1.0000000E+00	-	-
	3.3994359E-01	-1.1329014E-02	5.3337133E-01	-	-	1.0000000E+00	
	1.2839830E-01	-4.8189741E-03	2.1491843E-01	-	-	-	1.0000000E+00

p	Exponent	Coefficient	Coefficient	Coefficient	Coefficient	Coefficient
	1.4664510E+02	9.6142362E-04	-	-	-	-
	3.4817612E+01	7.3877485E-03	-	-	-	-
	1.1220740E+01	3.5474818E-02	-	-	-	-
	4.0417418E+00	1.1160848E-01	-	-	-	-
	1.6117110E+00	2.5630531E-01	1.0000000E+00	-	-	-
	6.5075850E-01	3.7078810E-01	-	1.0000000E+00	-	-
	2.5718701E-01	3.3863023E-01	-	-	1.0000000E+00	-
	9.5033541E-02	1.4955582E-01	-	-	-	1.0000000E+00

d	Exponent	Coefficient	Coefficient	Coefficient	Coefficient
	4.6470000E+00	1.0000000E+00	-	-	-
	1.8130000E+00	-	1.0000000E+00	-	-
	7.0700000E-01	-	-	1.0000000E+00	-
	2.7544830E-01	-	-	-	1.0000000E+00

f	Exponent	Coefficient	Coefficient	Coefficient
	2.9420000E+00	1.0000000E+00	-	-
	1.2040000E+00	-	1.0000000E+00	-
	4.9250700E-01	-	-	1.0000000E+00

Tables A.39: Oxygen cc-pVDZ-B3LYP
(9*s*4*p*1*d*) → [3*s*2*p*1*d*]

s	Exponent	Coefficient	Coefficient	Coefficient
	1.1798660E+04	7.1741920E-04	-1.3535086E-04	-
	1.7495540E+03	5.6068925E-03	-1.0901673E-03	-
	3.9689871E+02	2.8610215E-02	-5.4197651E-03	-
	1.1248200E+02	1.0756321E-01	-2.2502417E-02	-
	3.6567211E+01	2.8836462E-01	-6.2867731E-02	-
	1.3054590E+01	4.5285603E-01	-1.5061191E-01	-
	4.8974042E+00	2.7502850E-01	-1.0161837E-01	-
	1.0104361E+00	-8.1593404E-03	5.6929636E-01	-
	2.9045519E-01	-2.5238205E-02	5.6397718E-01	1.0000000E+00

p	Exponent	Coefficient	Coefficient
	1.7175920E+01	4.8253734E-02	-
	3.7285700E+00	2.4862967E-01	-
	1.0064189E+00	5.2791333E-01	-
	2.5233969E-01	4.2787829E-01	1.0000000E+00

d	Exponent	Coefficient
	1.1689680E+00	1.0000000E+00

Tables A.40: Oxygen cc-pVTZ-B3LYP
(10*s*5*p*2*d*1*f*) → [4*s*3*p*2*d*1*f*]

s	Exponent	Coefficient	Coefficient	Coefficient	Coefficient
	1.5381630E+04	5.1346497E-04	-1.0321473E-04	-	-
	2.2889790E+03	4.0036985E-03	-8.0757763E-04	-	-
	5.1859460E+02	2.0727480E-02	-4.2178407E-03	-	-
	1.4562720E+02	8.1441663E-02	-1.7156079E-02	-	-
	4.6880260E+01	2.3536062E-01	-5.4212991E-02	-	-
	1.6486919E+01	4.3678802E-01	-1.2775806E-01	-	-
	6.0363078E+00	3.5389021E-01	-1.6292593E-01	-	-
	1.6761320E+00	3.6326975E-02	1.9552691E-01	1.0000000E+00	-
	6.5045780E-01	-2.7446005E-02	6.0247934E-01	-	-
	2.1984050E-01	-8.1570940E-03	3.5242295E-01	-	1.0000000E+00

p	Exponent	Coefficient	Coefficient	Coefficient
	3.2896969E+01	1.8240677E-02	-	-
	7.5222449E+00	1.0958789E-01	-	-
	2.2027731E+00	3.3531865E-01	-	-
	6.7874008E-01	4.9992222E-01	1.0000000E+00	-
	1.9159320E-01	3.0094203E-01	-	1.0000000E+00

d	Exponent	Coefficient	Coefficient
	1.6922840E+00	1.0000000E+00	-
	4.7055710E-01	-	1.0000000E+00

f	Exponent	Coefficient
	1.1374240E+00	1.0000000E+00

Tables A.41: Oxygen cc-pVQZ-B3LYP
(11*s*6*p*3*d*2*f*) → [5*s*4*p*3*d*2*f*]

s	Exponent	Coefficient	Coefficient	Coefficient	Coefficient	Coefficient
	6.1546770E+04	9.0980786E-05	-1.8379726E-05	-	-	-
	9.1624521E+03	7.0879818E-04	-1.4414421E-04	-	-	-
	2.0906541E+03	3.6945634E-03	-7.4662000E-04	-	-	-
	5.9137000E+02	1.5395009E-02	-3.1735576E-03	-	-	-
	1.9242700E+02	5.2951325E-02	-1.1005475E-02	-	-	-
	6.9491814E+01	1.4664270E-01	-3.2964762E-02	-	-	-
	2.7008841E+01	3.0625680E-01	-7.7039383E-02	-	-	-
	1.1065400E+01	4.0054929E-01	-1.4107850E-01	-	-	-
	4.6156340E+00	2.2564539E-01	-1.0989009E-01	-	-	-
	1.4366500E+00	9.2113316E-03	2.9893798E-01	1.0000000E+00	-	-
	5.4742920E-01	-1.9722473E-02	5.8390456E-01	-	1.0000000E+00	-
	1.9566029E-01	-6.9787386E-03	2.7588034E-01	-	-	1.0000000E+00

p	Exponent	Coefficient	Coefficient	Coefficient	Coefficient
	6.4132172E+01	6.3735973E-03	-	-	-
	1.4564340E+01	4.6422146E-02	-	-	-
	4.3254399E+00	1.7772520E-01	-	-	-
	1.4690100E+00	3.8105544E-01	1.0000000E+00	-	-
	4.9513051E-01	4.4607487E-01	-	1.0000000E+00	-
	1.5358301E-01	2.1071422E-01	-	-	1.0000000E+00

d	Exponent	Coefficient	Coefficient	Coefficient
	2.8370220E+00	1.0000000E+00	-	-
	9.6800290E-01	-	1.0000000E+00	-
	3.3466950E-01	-	-	1.0000000E+00

f	Exponent	Coefficient	Coefficient
	2.4753770E+00	1.0000000E+00	-

	5.8638400E-01	-	1.0000000E+00

Tables A.42: Oxygen cc-pV5Z-B3LYP
(12*s*8*p*4*d*3*f*) → [6*s*5*p*4*d*3*f*]

s	Exponent	Coefficient	Coefficient	Coefficient	Coefficient	Coefficient	Coefficient
	1.6404241E+05	2.6653055E-05	-5.4081097E-06	-	-	-	-
	2.4535650E+04	2.0707591E-04	-4.2189069E-05	-	-	-	-
	5.5779888E+03	1.0925028E-03	-2.2154993E-04	-	-	-	-
	1.5809480E+03	4.5478097E-03	-9.3200256E-04	-	-	-	-
	5.1781403E+02	1.6267175E-02	-3.3308368E-03	-	-	-	-
	1.8697050E+02	4.9876861E-02	-1.0575793E-02	-	-	-	-
	7.3999977E+01	1.2510999E-01	-2.7479814E-02	-	-	-	-
	3.1338720E+01	2.5180468E-01	-6.3513860E-02	-	-	-	-
	1.3783680E+01	3.6610574E-01	-1.1183384E-01	-	-	-	-
	6.1527009E+00	2.8504390E-01	-1.4215016E-01	-	-	-	-
	2.7313261E+00	6.5275438E-02	1.9612705E-02	1.0000000E+00	-	-	-
	1.1294430E+00	-1.0660388E-02	3.8968834E-01	-	1.0000000E+00	-	-
	4.5371810E-01	-1.3985751E-02	5.2603847E-01	-	-	1.0000000E+00	
	1.7420180E-01	-5.7918807E-03	2.0717429E-01	-	-	-	1.0000000E+00

p	Exponent	Coefficient	Coefficient	Coefficient	Coefficient	Coefficient
	1.9756190E+02	9.5632422E-04	-	-	-	-
	4.6784321E+01	7.6798745E-03	-	-	-	-
	1.4699250E+01	3.8308568E-02	-	-	-	-
	5.2098398E+00	1.2582576E-01	-	-	-	-
	2.0318661E+00	2.7991390E-01	1.0000000E+00	-	-	-
	8.0135423E-01	3.8899496E-01	-	1.0000000E+00	-	-
	3.0572709E-01	3.2559833E-01	-	-	1.0000000E+00	-
	1.0996910E-01	1.0306729E-01	-	-	-	1.0000000E+00

d	Exponent	Coefficient	Coefficient	Coefficient	Coefficient
	4.6470000E+00	1.0000000E+00	-	-	-
	1.8130000E+00	-	1.0000000E+00	-	-
	7.0700000E-01	-	-	1.0000000E+00	-
	2.7600000E-01	-	-	-	1.0000000E+00

f	Exponent	Coefficient	Coefficient	Coefficient
	2.9422060E+00	1.0000000E+00	-	-
	1.2039920E+00	-	1.0000000E+00	-
	4.9250120E-01	-	-	1.0000000E+00

Tables A.43: Oxygen cc-pVDZ-BLYP
(9*s*4*p*1*d*) → [3*s*2*p*1*d*]

s	Exponent	Coefficient	Coefficient	Coefficient
	1.1728890E+04	7.2168512E-04	-1.3975654E-04	-
	1.7558890E+03	5.5567119E-03	-1.1077949E-03	-
	4.0147290E+02	2.8193422E-02	-5.4830564E-03	-
	1.1383810E+02	1.0650358E-01	-2.2791777E-02	-
	3.6909611E+01	2.8680509E-01	-6.4194746E-02	-
	1.3133260E+01	4.5242131E-01	-1.5223251E-01	-
	4.9002318E+00	2.7776784E-01	-1.0352600E-01	-
	1.0120341E+00	-6.1632334E-03	5.7232928E-01	-
	2.8723460E-01	-2.3281777E-02	5.6249386E-01	1.0000000E+00

p	Exponent	Coefficient	Coefficient
	1.7007170E+01	4.9610980E-02	-
	3.6814110E+00	2.5352550E-01	-
	9.9186552E-01	5.2838016E-01	-

	2.4447019E-01	4.2543858E-01	1.0000000E+00

d	Exponent	Coefficient
	0.1167797D+01	1.0000000E+00

Tables A.44: Oxygen cc-pVTZ-BLYP
(10*s*5*p*2*d*1*f*) → [4*s*3*p*2*d*1*f*]

s	Exponent	Coefficient	Coefficient	Coefficient	Coefficient
	1.5222680E+04	5.1730452E-04	-1.0601152E-04	-	-
	2.2941040E+03	3.9916001E-03	-8.1961660E-04	-	-
	5.2146521E+02	2.0530837E-02	-4.2614457E-03	-	-
	1.4766360E+02	7.9849489E-02	-1.7095881E-02	-	-
	4.7711140E+01	2.3174982E-01	-5.4402553E-02	-	-
	1.6729429E+01	4.3553907E-01	-1.2845625E-01	-	-
	6.0837612E+00	3.5864052E-01	-1.6552375E-01	-	-
	1.6975610E+00	3.8773462E-02	1.9114482E-01	1.0000000E+00	-
	6.5661442E-01	-2.6448902E-02	6.0368961E-01	-	-
	2.1830390E-01	-7.4144718E-03	3.5664016E-01	-	1.0000000E+00

p	Exponent	Coefficient	Coefficient	Coefficient
	3.2614529E+01	1.8719204E-02	-	-
	7.4688230E+00	1.1159462E-01	-	-
	2.1802950E+00	3.4009996E-01	-	-
	6.6752100E-01	4.9775630E-01	1.0000000E+00	-
	1.8462750E-01	3.0069128E-01	-	1.0000000E+00

d	Exponent	Coefficient	Coefficient
	1.6924260E+00	1.0000000E+00	-
	4.7010470E-01	-	1.0000000E+00

f	Exponent	Coefficient
	1.1433350E+00	1.0000000E+00

Tables A.45: Oxygen cc-pVQZ-BLYP
(11*s*6*p*3*d*2*f*) → [5*s*4*p*3*d*2*f*]

s	Exponent	Coefficient	Coefficient	Coefficient	Coefficient	Coefficient
	6.1157969E+04	9.0646441E-05	-1.8660194E-05	-	-	-
	9.2343037E+03	7.0879969E-04	-1.4681954E-04	-	-	-
	2.0761960E+03	3.7479529E-03	-7.7201735E-04	-	-	-
	5.8819769E+02	1.5494043E-02	-3.2527808E-03	-	-	-
	1.9158830E+02	5.3305954E-02	-1.1295009E-02	-	-	-
	6.9313583E+01	1.4670922E-01	-3.3575431E-02	-	-	-
	2.7026110E+01	3.0466878E-01	-7.8253657E-02	-	-	-
	1.1093000E+01	3.9884260E-01	-1.4132829E-01	-	-	-
	4.6176472E+00	2.2772428E-01	-1.1186457E-01	-	-	-
	1.4475230E+00	1.0296348E-02	2.9855433E-01	1.0000000E+00	-	-
	5.4930937E-01	-1.8464534E-02	5.8367532E-01	-	1.0000000E+00	-
	1.9364040E-01	-6.3916259E-03	2.7853429E-01	-	-	1.0000000E+00

p	Exponent	Coefficient	Coefficient	Coefficient	Coefficient
	6.4179428E+01	6.4354488E-03	-	-	-
	1.4539610E+01	4.7355056E-02	-	-	-
	4.2934432E+00	1.8063635E-01	-	-	-
	1.4562510E+00	3.8328767E-01	1.0000000E+00	-	-
	4.8711690E-01	4.4277015E-01	-	1.0000000E+00	-
	1.4787871E-01	2.1301608E-01	-	-	1.0000000E+00

d	Exponent	Coefficient	Coefficient	Coefficient

	2.8370860E+00	1.0000000E+00	-	-
	0.9680087D+00	-	1.0000000E+00	-
	3.3433620E-01	-	-	1.0000000E+00

f	Exponent	Coefficient	Coefficient
	2.4514500E+00	1.0000000E+00	-
	5.9685110E-01	-	1.0000000E+00

Tables A.46: Oxygen cc-pV5Z-BLYP
(12*s*8*p*4*d*3*f*) → [6*s*5*p*4*d*3*f*]

s	Exponent	Coefficient	Coefficient	Coefficient	Coefficient	Coefficient	Coefficient
	1.6559830E+05	2.6539095E-05	-5.4839015E-06	-	-	-	-
	2.4449189E+04	2.0931130E-04	-4.3464966E-05	-	-	-	-
	5.5849590E+03	1.0811363E-03	-2.2316269E-04	-	-	-	-
	1.5930031E+03	4.5403587E-03	-9.4869989E-04	-	-	-	-
	5.1717950E+02	1.6377088E-02	-3.4117857E-03	-	-	-	-
	1.8722701E+02	4.9709342E-02	-1.0752690E-02	-	-	-	-
	7.4027382E+01	1.2598494E-01	-2.8121136E-02	-	-	-	-
	3.1175880E+01	2.5341177E-01	-6.5446302E-02	-	-	-	-
	1.3725170E+01	3.6327291E-01	-1.1205329E-01	-	-	-	-
	6.1558042E+00	2.8276804E-01	-1.4242376E-01	-	-	-	-
	2.7580111E+00	6.7750841E-02	1.8229326E-02	1.0000000E+00	-	-	-
	1.1388390E+00	-9.7184591E-03	3.8818705E-01	-	1.0000000E+00	-	-
	4.5638749E-01	-1.2795168E-02	5.2474564E-01	-	-	1.0000000E+00	
	1.7322829E-01	-5.4298150E-03	2.1229413E-01	-	-	-	1.0000000E+00

p	Exponent	Coefficient	Coefficient	Coefficient	Coefficient	Coefficient
	1.9736420E+02	9.6692424E-04	-	-	-	-
	4.6944439E+01	7.6579913E-03	-	-	-	-

	1.4880660E+01	3.8079772E-02	-	-	-	-
	5.2754841E+00	1.2496073E-01	-	-	-	-
	2.0527790E+00	2.7994791E-01	1.0000000E+00	-	-	-
	8.0855709E-01	3.8502932E-01	-	1.0000000E+00	-	-
	3.0822429E-01	3.2376239E-01	-	-	1.0000000E+00	-
	1.1070540E-01	1.1484668E-01	-	-	-	1.0000000E+00

d	Exponent	Coefficient	Coefficient	Coefficient	Coefficient
	4.6470140E+00	1.0000000E+00	-	-	-
	1.8130020E+00	-	1.0000000E+00	-	-
	7.0700030E-01	-	-	1.0000000E+00	-
	2.7572400E-01	-	-	-	1.0000000E+00

f	Exponent	Coefficient	Coefficient	Coefficient
	2.9422300E+00	1.0000000E+00	-	-
	1.2039910E+00	-	1.0000000E+00	-
	4.9250110E-01	-	-	1.0000000E+00

Tables A.47: Fluorine cc-pVDZ-B3LYP
(9*s*4*p*1*d*) → [3*s*2*p*1*d*]

s	Exponent	Coefficient	Coefficient	Coefficient
	1.4697140E+04	7.3076540E-04	-1.3875370E-04	-
	2.2089670E+03	5.6110676E-03	-1.0996147E-03	-
	5.0415540E+02	2.8582653E-02	-5.4487376E-03	-
	1.4266679E+02	1.0817848E-01	-2.2847423E-02	-
	4.6293789E+01	2.9090616E-01	-6.4074315E-02	-
	1.6553471E+01	4.5367128E-01	-1.5392448E-01	-
	6.2435460E+00	2.7119830E-01	-9.8295495E-02	-
	1.3170930E+00	-9.4454801E-03	5.7001507E-01	-

	3.7649080E-01	-2.6071291E-02	5.6440830E-01	1.0000000E+00

p	Exponent	Coefficient	Coefficient
	2.2098789E+01	4.9723499E-02	-
	4.8357172E+00	2.5429654E-01	-
	1.3007070E+00	5.2935314E-01	-
	3.2038110E-01	4.2368305E-01	1.0000000E+00

d	Exponent	Coefficient
	1.4516520E+00	1.0000000E+00

Tables A.48: Fluorine cc-pVTZ-B3LYP
(10*s*5*p*2*d*1*f*) → [4*s*3*p*2*d*1*f*]

s	Exponent	Coefficient	Coefficient	Coefficient	Coefficient
	1.9613721E+04	5.1184918E-04	-1.0367771E-04	-	-
	2.9132510E+03	3.9847703E-03	-8.0991676E-04	-	-
	6.6431458E+02	2.0387251E-02	-4.1811168E-03	-	-
	1.8804840E+02	7.9552375E-02	-1.6889820E-02	-	-
	6.0880939E+01	2.3097932E-01	-5.3632371E-02	-	-
	2.1477011E+01	4.3463236E-01	-1.2789671E-01	-	-
	7.8850141E+00	3.5965964E-01	-1.6610585E-01	-	-
	2.2574270E+00	3.9124530E-02	1.8338394E-01	1.0000000E+00	-
	8.6726660E-01	-2.8076384E-02	6.0465026E-01	-	-
	2.8925949E-01	-9.1639413E-03	3.6401656E-01	-	1.0000000E+00

p	Exponent	Coefficient	Coefficient	Coefficient
	4.2248070E+01	1.8764539E-02	-	-
	9.6949158E+00	1.1341477E-01	-	-
	2.8512480E+00	3.4013686E-01	-	-

	8.7383598E-01	4.9822864E-01	1.0000000E+00	-
	2.4234390E-01	2.9785183E-01	-	1.0000000E+00

d	Exponent	Coefficient	Coefficient
	2.0093220E+00	1.0000000E+00	-
	4.6528050E-01	-	1.0000000E+00

f	Exponent	Coefficient
	1.5652790E+00	1.0000000E+00

Tables A.49: Fluorine cc-pVQZ-B3LYP
(11*s*6*p*3*d*2*f*) → [5*s*4*p*3*d*2*f*]

s	Exponent	Coefficient	Coefficient	Coefficient	Coefficient	Coefficient
	7.4382430E+04	9.6304415E-05	-1.9629273E-05	-	-	-
	1.1219010E+04	7.3685625E-04	-1.5131678E-04	-	-	-
	2.5599250E+03	3.8958560E-03	-7.9428084E-04	-	-	-
	7.1829102E+02	1.6247539E-02	-3.3857636E-03	-	-	-
	2.3554730E+02	5.4719679E-02	-1.1485649E-02	-	-	-
	8.5932426E+01	1.4964938E-01	-3.4173068E-02	-	-	-
	3.3714180E+01	3.0840328E-01	-7.8770429E-02	-	-	-
	1.3958640E+01	3.9675122E-01	-1.4340201E-01	-	-	-
	5.8864379E+00	2.2124071E-01	-1.0651373E-01	-	-	-
	1.8758260E+00	8.6679971E-03	2.9922959E-01	1.0000000E+00	-	-
	7.1419370E-01	-2.0108502E-02	5.8263546E-01	-	1.0000000E+00	-
	2.5409430E-01	-7.4661514E-03	2.7850860E-01	-	-	1.0000000E+00

p	Exponent	Coefficient	Coefficient	Coefficient	Coefficient
	8.0992828E+01	6.6890717E-03	-	-	-
	1.8557550E+01	4.8325166E-02	-	-	-

	5.5748782E+00	1.8264100E-01	-	-	-
	1.9000950E+00	3.8250640E-01	1.0000000E+00	-	-
	6.3804263E-01	4.4200867E-01	-	1.0000000E+00	-
	1.9491901E-01	2.1043797E-01	-	-	1.0000000E+00

d	Exponent	Coefficient	Coefficient	Coefficient
	2.8371680E+00	1.0000000E+00	-	-
	9.6799950E-01	-	1.0000000E+00	-
	3.3466220E-01	-	-	1.0000000E+00

f	Exponent	Coefficient	Coefficient
	2.5111880E+00	1.0000000E+00	-
	6.3981820E-01	-	1.0000000E+00

Tables A.50: Fluorine cc-pV5Z-B3LYP
(12*s*8*p*4*d*3*f*) → [6*s*5*p*4*d*3*f*]

s	Exponent	Coefficient	Coefficient	Coefficient	Coefficient	Coefficient	Coefficient
	2.1095959E+05	2.6157988E-05	-5.3611434E-06	-	-	-	-
	3.1725631E+04	2.0214228E-04	-4.1559833E-05	-	-	-	-
	7.2227158E+03	1.0662948E-03	-2.1851146E-04	-	-	-	-
	2.0344659E+03	4.5130742E-03	-9.3288504E-04	-	-	-	-
	6.6487939E+02	1.5907457E-02	-3.2932742E-03	-	-	-	-
	2.4291029E+02	4.8286203E-02	-1.0320735E-02	-	-	-	-
	9.5896873E+01	1.2417057E-01	-2.7608689E-02	-	-	-	-
	4.0308048E+01	2.5221413E-01	-6.4162947E-02	-	-	-	-
	1.7728609E+01	3.6590460E-01	-1.1357617E-01	-	-	-	-
	7.9332662E+00	2.8697267E-01	-1.4371353E-01	-	-	-	-
	3.5109439E+00	6.5899171E-02	2.4146389E-02	1.0000000E+00	-	-	-
	1.4595860E+00	-1.1371299E-02	3.9087820E-01	-	1.0000000E+00	-	-

	5.8760703E-01	-1.4350056E-02	5.2319288E-01	-	-	1.0000000E+00	
	2.2489180E-01	-6.0588014E-03	2.0705710E-01	-	-	-	1.0000000E+00

p	Exponent	Coefficient	Coefficient	Coefficient	Coefficient	Coefficient
	2.4084151E+02	1.0697782E-03	-	-	-	-
	5.7367779E+01	8.3667208E-03	-	-	-	-
	1.8460791E+01	4.0125165E-02	-	-	-	-
	6.6633720E+00	1.3023357E-01	-	-	-	-
	2.6164970E+00	2.8302950E-01	1.0000000E+00	-	-	-
	1.0332370E+00	3.8569552E-01	-	1.0000000E+00	-	-
	3.9318919E-01	3.2106936E-01	-	-	1.0000000E+00	-
	1.3993430E-01	1.0507691E-01	-	-	-	1.0000000E+00

d	Exponent	Coefficient	Coefficient	Coefficient	Coefficient
	4.6469620E+00	1.0000000E+00	-	-	-
	1.8130010E+00	-	1.0000000E+00	-	-
	7.0700200E-01	-	-	1.0000000E+00	-
	2.7572400E-01	-	-	-	1.0000000E+00

f	Exponent	Coefficient	Coefficient	Coefficient
	2.9422760E+00	1.0000000E+00	-	-
	1.2039800E+00	-	1.0000000E+00	-
	4.9251020E-01	-	-	1.0000000E+00

Tables A.51: Fluorine cc-pVDZ-BLYP
(9*s*4*p*1*d*) → [3*s*2*p*1*d*]

s	Exponent	Coefficient	Coefficient	Coefficient
	1.4578420E+04	7.3477940E-04	-1.4287976E-04	-
	2.2145530E+03	5.5916505E-03	-1.1214693E-03	-
	5.0583649E+02	2.8490778E-02	-5.5631418E-03	-
	1.4341930E+02	1.0756336E-01	-2.3217330E-02	-
	4.6552841E+01	2.8958264E-01	-6.5297045E-02	-
	1.6621691E+01	4.5277753E-01	-1.5546569E-01	-
	6.2459030E+00	2.7336124E-01	-9.9745199E-02	-
	1.3178240E+00	-7.6082647E-03	5.7305694E-01	-
	3.7211201E-01	-2.4115507E-02	5.6275088E-01	1.0000000E+00

p	Exponent	Coefficient	Coefficient
	2.1886480E+01	5.1017027E-02	-
	4.7792430E+00	2.5887612E-01	-
	1.2827719E+00	5.3015804E-01	-
	3.1094769E-01	4.2090270E-01	1.0000000E+00

d	Exponent	Coefficient
	0.1450208D+01	1.0000000E+00

Tables A.52: Fluorine cc-pVTZ-BLYP
(10*s*5*p*2*d*1*f*) → [4*s*3*p*2*d*1*f*]

s	Exponent	Coefficient	Coefficient	Coefficient	Coefficient
	1.9705570E+04	5.0996285E-04	-1.0522683E-04	-	-
	2.9155291E+03	4.0033688E-03	-8.2865771E-04	-	-
	6.6128247E+02	2.0577800E-02	-4.2995797E-03	-	-
	1.8702139E+02	8.0209896E-02	-1.7338978E-02	-	-
	6.0508671E+01	2.3239358E-01	-5.5032834E-02	-	-
	2.1329580E+01	4.3493894E-01	-1.3023229E-01	-	-
	7.8115711E+00	3.5752088E-01	-1.6609183E-01	-	-
	2.2226479E+00	3.8430985E-02	1.9416694E-01	1.0000000E+00	-
	8.5169357E-01	-2.6659787E-02	6.0395771E-01	-	-
	2.8214121E-01	-7.9623209E-03	3.5597143E-01	-	1.0000000E+00

p	Exponent	Coefficient	Coefficient	Coefficient
	4.1544460E+01	1.9450402E-02	-	-
	9.5700884E+00	1.1600222E-01	-	-
	2.8119221E+00	3.4522867E-01	-	-
	8.5712898E-01	4.9632716E-01	1.0000000E+00	-
	2.3324990E-01	2.9584700E-01	-	1.0000000E+00

d	Exponent	Coefficient	Coefficient
	2.0093520E+00	1.0000000E+00	-
	4.6490480E-01	-	1.0000000E+00

f	Exponent	Coefficient
	1.5410140E+00	1.0000000E+00

Tables A.53: Fluorine cc-pVQZ-BLYP
(11*s*6*p*3*d*2*f*) → [5*s*4*p*3*d*2*f*]

s	Exponent	Coefficient	Coefficient	Coefficient	Coefficient	Coefficient
	7.5563180E+04	9.5495176E-05	-1.9796464E-05	-	-	-
	1.1121780E+04	7.5501320E-04	-1.5767061E-04	-	-	-
	2.5288091E+03	3.9234059E-03	-8.1344735E-04	-	-	-
	7.2076978E+02	1.6069733E-02	-3.4056846E-03	-	-	-
	2.3691240E+02	5.4601721E-02	-1.1652390E-02	-	-	-
	8.6133087E+01	1.4992315E-01	-3.4791790E-02	-	-	-
	3.3698608E+01	3.0880773E-01	-8.0315135E-02	-	-	-
	1.3931450E+01	3.9564687E-01	-1.4411551E-01	-	-	-
	5.8674679E+00	2.2149217E-01	-1.0749914E-01	-	-	-
	1.8860900E+00	9.3385261E-03	2.9997200E-01	1.0000000E+00	-	-
	7.1432030E-01	-1.8818129E-02	5.8258319E-01	-	1.0000000E+00	-
	2.5089979E-01	-6.8496424E-03	2.7979553E-01	-	-	1.0000000E+00

p	Exponent	Coefficient	Coefficient	Coefficient	Coefficient
	8.1395630E+01	6.7063887E-03	-	-	-
	1.8607540E+01	4.8859626E-02	-	-	-
	5.5670338E+00	1.8436699E-01	-	-	-
	1.8926539E+00	3.8476604E-01	1.0000000E+00	-	-
	6.2967420E-01	4.4048959E-01	-	1.0000000E+00	-
	1.8790171E-01	2.1208106E-01	-	-	1.0000000E+00

d	Exponent	Coefficient	Coefficient	Coefficient
	2.8373160E+00	1.0000000E+00	-	-
	9.6800430E-01	-	1.0000000E+00	-
	3.3432990E-01	-	-	1.0000000E+00

f	Exponent	Coefficient	Coefficient
	2.5952650E+00	1.0000000E+00	-

	6.2915030E-01	-	1.0000000E+00

Tables A.54: Fluorine cc-pV5Z-BLYP
(12*s*8*p*4*d*3*f*) → [6*s*5*p*4*d*3*f*]

s	Exponent	Coefficient	Coefficient	Coefficient	Coefficient	Coefficient	Coefficient
	2.1119041E+05	2.6017064E-05	-5.4210445E-06	-	-	-	-
	3.1793080E+04	2.0369384E-04	-4.2596850E-05	-	-	-	-
	7.1996172E+03	1.0636119E-03	-2.2153385E-04	-	-	-	-
	2.0522200E+03	4.4616833E-03	-9.3826838E-04	-	-	-	-
	6.6629187E+02	1.6051641E-02	-3.3766553E-03	-	-	-	-
	2.4204420E+02	4.8589386E-02	-1.0570062E-02	-	-	-	-
	9.5752159E+01	1.2414236E-01	-2.8022196E-02	-	-	-	-
	4.0331551E+01	2.5114027E-01	-6.5147929E-02	-	-	-	-
	1.7780140E+01	3.6401200E-01	-1.1379936E-01	-	-	-	-
	7.9455628E+00	2.8807494E-01	-1.4518107E-01	-	-	-	-
	3.5112410E+00	6.7324311E-02	2.4660738E-02	1.0000000E+00	-	-	-
	1.4619730E+00	-1.0830996E-02	3.9141864E-01	-	1.0000000E+00	-	-
	5.8693522E-01	-1.3107544E-02	5.2127606E-01	-	-	1.0000000E+00	
	2.2227550E-01	-5.6350017E-03	2.0927414E-01	-	-	-	1.0000000E+00

p	Exponent	Coefficient	Coefficient	Coefficient	Coefficient	Coefficient
	2.4199600E+02	1.0769049E-03	-	-	-	-
	5.7323631E+01	8.4405504E-03	-	-	-	-
	1.8559669E+01	4.0140022E-02	-	-	-	-
	6.7378550E+00	1.2835400E-01	-	-	-	-
	2.6570561E+00	2.8167248E-01	1.0000000E+00	-	-	-
	1.0435510E+00	3.8632470E-01	-	1.0000000E+00	-	-
	3.9088219E-01	3.2396278E-01	-	-	1.0000000E+00	-
	1.3500559E-01	1.0959807E-01	-	-	-	1.0000000E+00

d	Exponent	Coefficient	Coefficient	Coefficient	Coefficient
	4.6469480E+00	1.0000000E+00	-	-	-
	1.8130000E+00	-	1.0000000E+00	-	-
	7.0700230E-01	-	-	1.0000000E+00	-
	2.7544830E-01	-	-	-	1.0000000E+00

f	Exponent	Coefficient	Coefficient	Coefficient
	2.9564030E+00	1.0000000E+00	-	-
	1.2031960E+00	-	1.0000000E+00	-
	4.9245110E-01	-	-	1.0000000E+00

APPENDIX B

TRANSFORMATION PATHWAYS FOR THE MULTI-STATE MODIFIED EMBEDDED ATOM METHOD

The transformation pathways listed in Table 7.2 are used for the derivation of the screening functions for the pair potential, the symmetric and angular densities. The Bain,[53] Trigonal,[183] and 2D[166] pathways are required to solve for the screening functions. The Bain pathway links the fcc and bcc pathways by modifying the ratio of the *c* and *a* lattice vectors, as shown in Figure B.1. For fcc, $c/a = \sqrt{2}$, and for bcc, $c/a = 1$. The fractional deformation along the Bain path is given by:

$$f = \left(\frac{c}{a}\right)^2 - 1 \qquad [B.1]$$

For each point along the Bain path, the following functions both apply for the screening parameters:

$$C_1^{Bain} = 2 + f \qquad [B.2]$$

$$C_2^{Bain} = \frac{2}{1+f} \qquad [B.3]$$

At $c/a = 1$, for bcc, $f = 0$, and $C_1^{Bain} = C_2^{Bain} = 2$, in agreement with Table 1. However, with $c/a = \sqrt{2}$, for fcc, $f = 1$, and thus $C_1^{Bain} = 3.0$ and $C_2^{Bain} = 1.0$. The latter screening parameter is in agreement with Table 1 for fcc; however, $C_1^{Bain} = 3.0$ also correctly applies to fcc because $f = 1$. Also, as in Table 7.2, the 2NN to 1NN distance ratio for fcc is large enough that the 2NNs contribute negligibly to the total energy, despite that the screening ellipse from Equation [7.4] and [7.5] is at its largest.

The 2D pathway links a two-dimensional hexagonal plane (2D-hex) to a two-dimensional square plane (2D-sq) through the deformation of the angle, θ, between

nearest neighbor atoms. This is illustrated in Figure B.2. At $\theta = 60^o$, the two-dimensional structure is a hexagonal plane, and at $\theta = 90^o$, it is a square plane. The fractional deformation is a function of the angle:

$$f = \frac{2}{5}[1 + 3\cos\theta] \quad [B.4]$$

Two screening parameters are applicable for the 2D pathway:

$$C_1^{2D} = \frac{1 + \cos\theta}{1 - \cos\theta} = \frac{4 + 5f}{8 - 5f} \quad [B.5]$$

$$C_2^{2D} = \frac{1}{C_1^{2D}} \quad [B.6]$$

In Table 7.1, the screening parameters for 2D-sq are $C_1^{2D} = C_2^{2D} = 1$. For 2D-hex, $C_1^{2D} = 1/3$, which is in agreement with Table 1; however, Equation [7.29] allows that $C_2^{2D} = 3$. This produces a large screening ellipse, but the 2NN to 1NN distance ratio 2D-hex is $\sqrt{3}$ and thus indicates a negligible contribution to the total energy by the 2NN atoms.

The Trigonal pathway[183] links the bcc and fcc structures through a different deformation route that intersects the SC structure, as shown in Figure B.3. It can be described as a constant volume deformation of a bcc lattice. If the bcc lattice is oriented such that the *x*, *y*, and *z* axes are oriented in the [110], [112], and [111] directions, respectively, then the transformation pathway can be described by the following equations:

$$a = a_o\sqrt{2}p^{(-1/3)} \quad [B.7]$$

$$b = a_o\sqrt{6}p^{(-1/3)} \quad [B.8]$$

$$c = a_o \frac{\sqrt{3}}{2} p^{(-1/3)} \quad [B.9]$$

The equations for *a*, *b*, and *c* correspond to the deformation of the bcc lattice on the *x*, *y*, and *z* axes, respectively. The constant, a_o, corresponds to the bcc lattice constant. The values of *p* = 1, 2, or 4 are used to specify the bcc, SC, and fcc lattice structures, respectively, on the pathway. The angle, *θ*, between nearest neighbor atoms can be related to *p* by the following:

$$\cos\theta = \frac{p^2 - 4}{p^2 + 8} \quad [B.10]$$

Thus bcc, SC, and fcc structures can be described as having angles of 109.47°, 90°, and 60°, respectively. With *f* as described by Equation [B.4], the relevant screening parameters for the Trigonal pathway are given as well:

$$C_1^{trig} = \frac{1 - \cos\theta}{1 + 2\cos\theta} = \frac{8 - 5f}{2 + 10f} \quad [B.11]$$

$$C_2^{trig} = \frac{\cos\theta - 1}{2\cos\theta} = \frac{8 - 5f}{4 - 10f} \quad [B.12]$$

$$C_3^{trig} = C_2^{2D} \quad [B.13]$$

$$C_4^{trig} = C_1^{2D} \quad [B.14]$$

With the increasing variety and interchangeability of the screening parameters for the Trigonal and 2D pathways, a table of screening parameters is illustrated on Figure B.4, in which Equations [B.2]-[B.3] and [B.11]-[B.12] are plotted.

Approximately between ten and twenty total energy data points along each pathway, at constant fcc volume, were calculated using VASP 4.6. The fcc dissociation

energy, which is the total *E/atom* for fcc at r_{NN} = 4.0, was subtracted from each data point, followed by division of each data point by the fcc cohesive energy to maintain consistency with the reference binding curves, such that the resulting minimum fcc binding energy, at the fcc volume r_{ij} = 1.0, is -1.0 eV. The Bain pathway is fitted with respect to the fractional deformation parameter, *f*, with the equation:

$$E_{fit}^{Bain} = a_1 + a_2 \cos(\pi \cdot f) \quad \text{[B.15]}$$

The variables *f, a_2, and a_1* are set such that a_1 equals the bcc cohesive energy, which occurs at *f* = 0, and a_2 = | -1 – a_1 |, so that at *f* =1, E_{fit}^{Bain} = *-1* eV. The 2D pathway can be fitted with respect to the angle between atoms, *θ,* with the equation:

$$E_{fit}^{2D} = a_6 + \left(\frac{\theta - 90}{30}\right)^2 (a_6 - a_5) + \left(\frac{\theta - 60}{30}\right) \sum_{i=1}^{4} a_i \left(\frac{\theta}{100}\right)^{i-1} \quad \text{[B.16]}$$

The variables are optimized such that a_6 and a_5 are constrained to the 2D-hex and 2D-sq binding energies and the remaining variables are optimized to fit the pathway between the endpoints. Finally, the Trigonal pathway can also be fitted with respect to the angle between atoms, *θ,* with the equation:

$$E_{fit}^{trig} = -1 + a_6(p-4)^4(p-1)^2 + \sum_{i=1}^{5} a_i(-1)^{i-1}\left(p^i - 4^i\right) \quad \text{[B.17]}$$

$$p = \sqrt{\frac{8\cos(\theta\pi/180) + 2}{1 - \cos(\theta\pi/180)}} \quad \text{[B.18]}$$

For this fit, no constraints should be imposed on the variables. Equation [B.17] was constructed such that at *p* = 4, which corresponds to fcc, the fit equals -1 eV.

Two more pathways are introduced because they involve structures that are listed in Table 7.1, but not yet introduced. Both pathways are not implemented in the determination of MS-MEAM function, but they are evaluated in the Results section to gauge the predictive capability of MS-MEAM. The first applied pathway is the orthorhombic diamond cubic (oDC) pathway, which mandates an orthorhombic transformation of the DC structure. The oDC pathway transforms the DC structure, with four 1NNs, into the oDC10 structure, with 10 1NNs. The constant-volume transformation is a function of θ, and has a range of $60^o \leq \theta \leq 90^o$. For DC, the angle between 1NN atoms is $\theta = 90^o$, and for oDC10, which is illustrated in Figure B.5, the angle between 1NN atoms is $\theta = 60^o$. The deformations that occur on the lattice are given:

$$\delta_x = \omega(\theta)\sin(\theta)\left[1-\cos(\theta)\right] \quad \text{[B.19]}$$

$$\delta_y = \omega(\theta)[1-\cos(\theta)/2] \quad \text{[B.20]}$$

$$\delta_z = \omega(\theta)\sqrt{3-{\delta_x}^2-{\delta_y}^2} \quad \text{[B.21]}$$

At each angle, the $\omega(\theta)$ is solved so that volume is constant for each deformation on the pathway:

$$\omega(\theta) = \delta_x\delta_y\delta_z \quad \text{[B.22]}$$

The second applied pathway is the Zigzag pathway. It is a low-coordination deformation characterized by involved an infinite zigzag structure. Starting with angle between the atoms being $\theta = 60^{o,}$, the beam structure is present. The angle is increased, through $\theta = 70.53^o$, at which the zigzag structure exists, towards an infinite line structure,

which is present at $\theta = 180^{o}$. Figure B.6 depicts mechanism of the transformation with the following functions

$$\zeta_x = 2\sin(\theta) \quad [B.23]$$

$$\zeta_y = \cos\left(\frac{\theta}{2}\right) \quad [B.24]$$

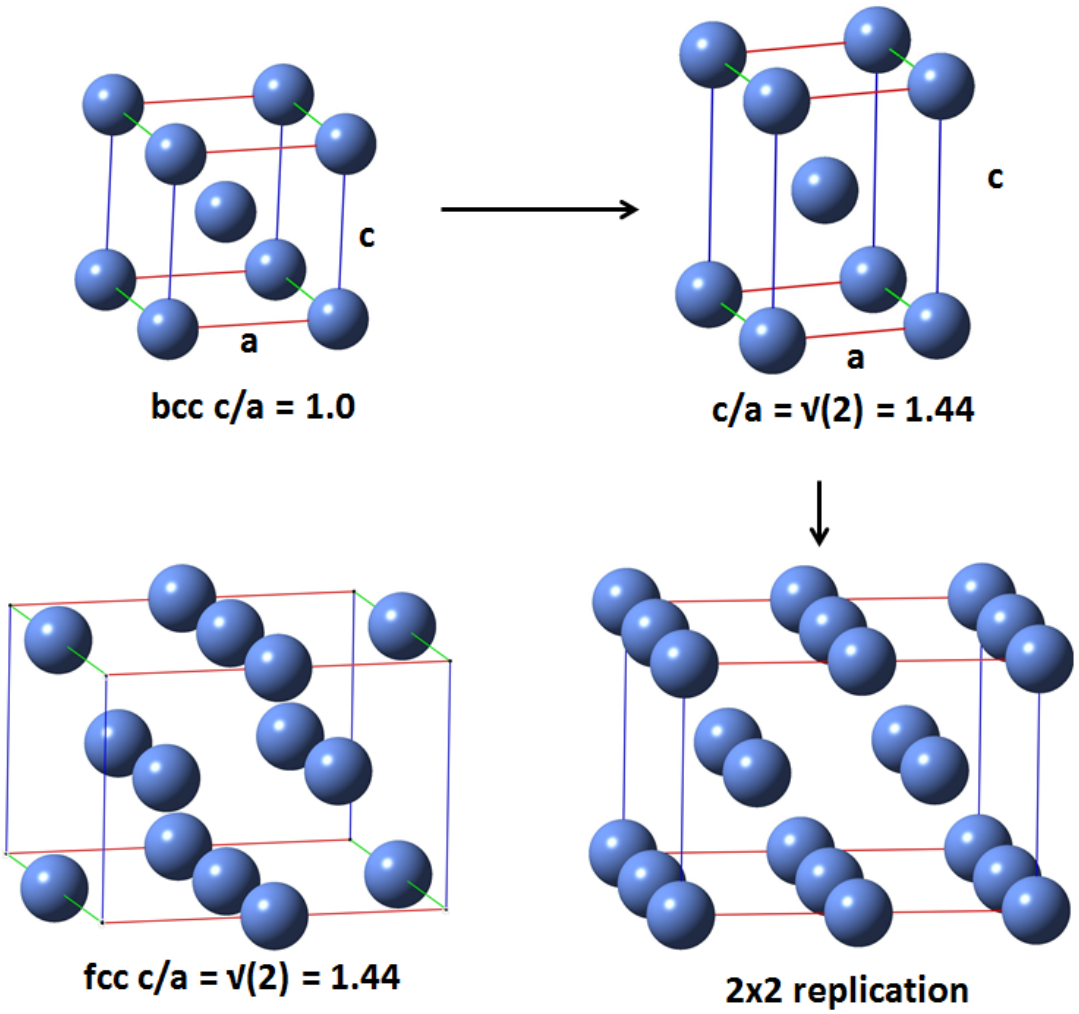

Figure B.1: The Bain transformation pathway. Top-left: the bcc cell has a c/a ratio of 1.0. Top-right: the transformation occurs causing the c/a ratio to be 1.44. However, the fcc cell here is not obvious due to periodic boundary conditions. Bottom-right: the top-right cell is replicated in directions orthogonal to the c axis to produce the fcc structure. Bottom-left: the corner atoms are whited-out, *only to illustrate the fcc structure in the 2x2 replication*.

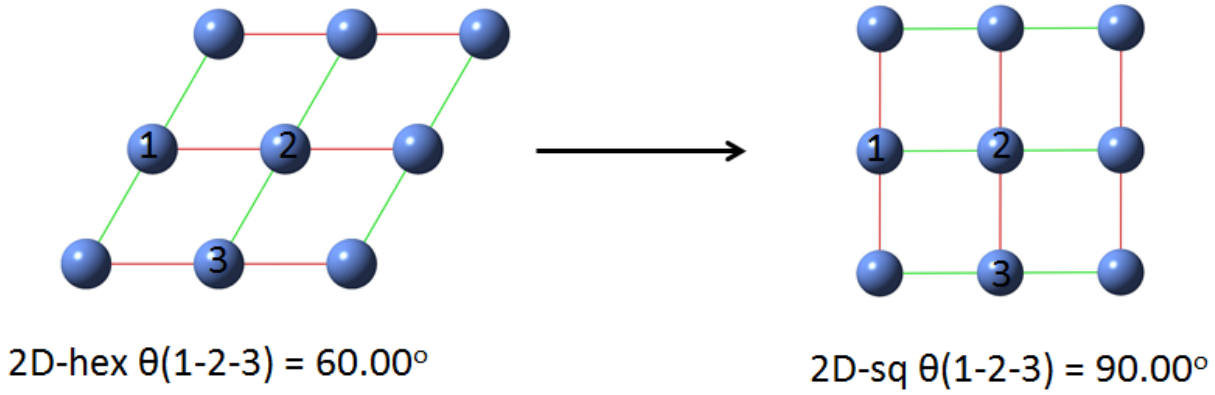

Figure B.2: The 2D transformation pathway. The 2D-hex and 2D-sq structures have angles of 60.00° and 90.00°, respectively.

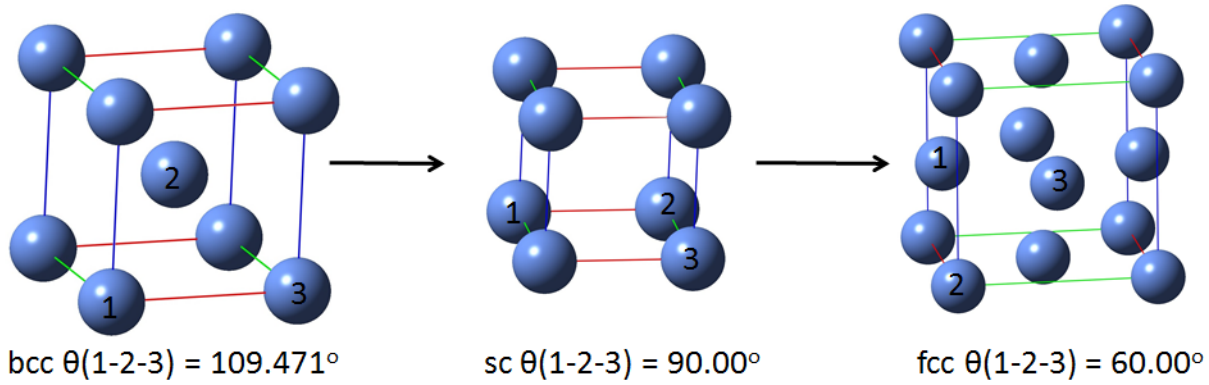

Figure B.3: The Trigonal transformation pathway. The bcc, SC, and fcc structures have angles of 109.471°, 90.00°, and 60.00°, respectively.

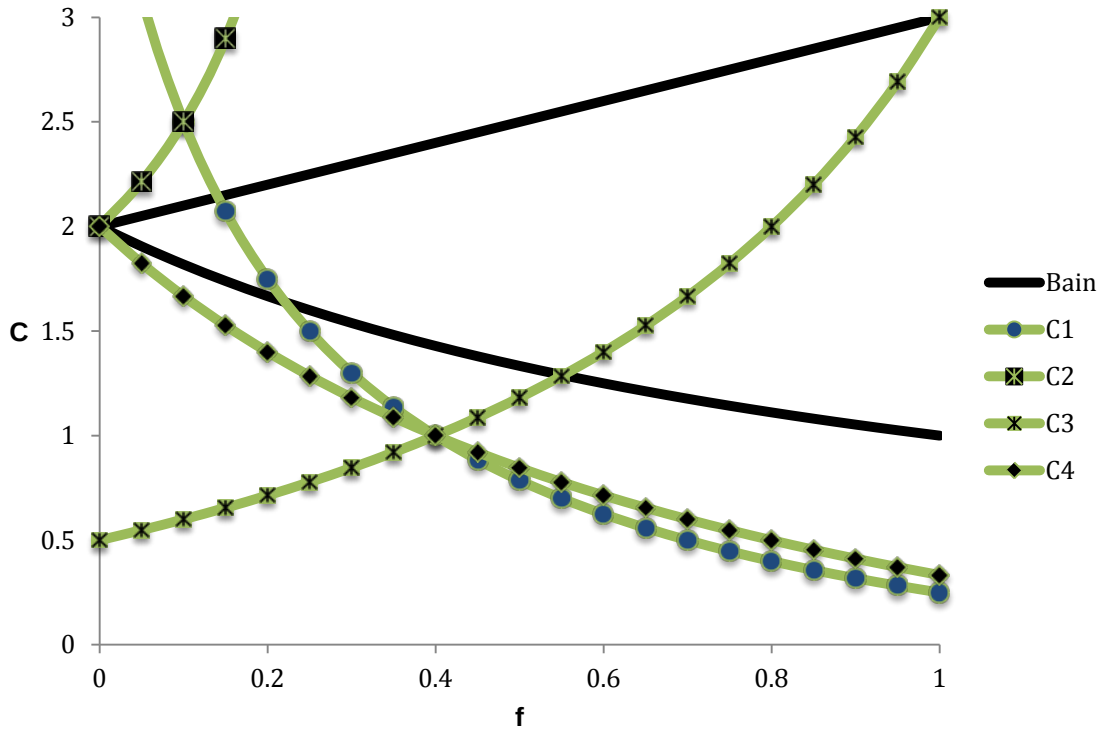

Figure B.4: The screening parameters for Bain, Trigonal, and 2D pathways from Equations [B.3]-[B.4] and [B.11]-[B.14]. Further, Equations [B.13]-[B.14], for C_3 and C_4 of the Trigonal pathway, are the same as Equations [B.5]-[B.6] for the C_1 and C_2 of the 2D pathway.

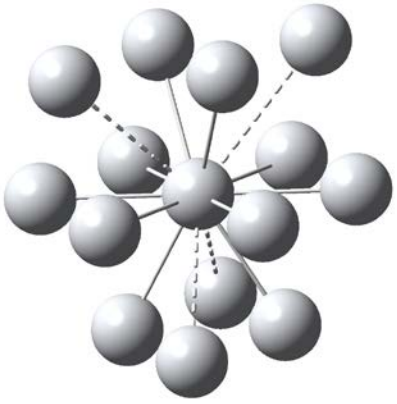

Figure B.5: The oDC10 structure. The 1NN atoms are illustrated with solid bonds, and 2NN atoms are illustrated with dashed bonds.

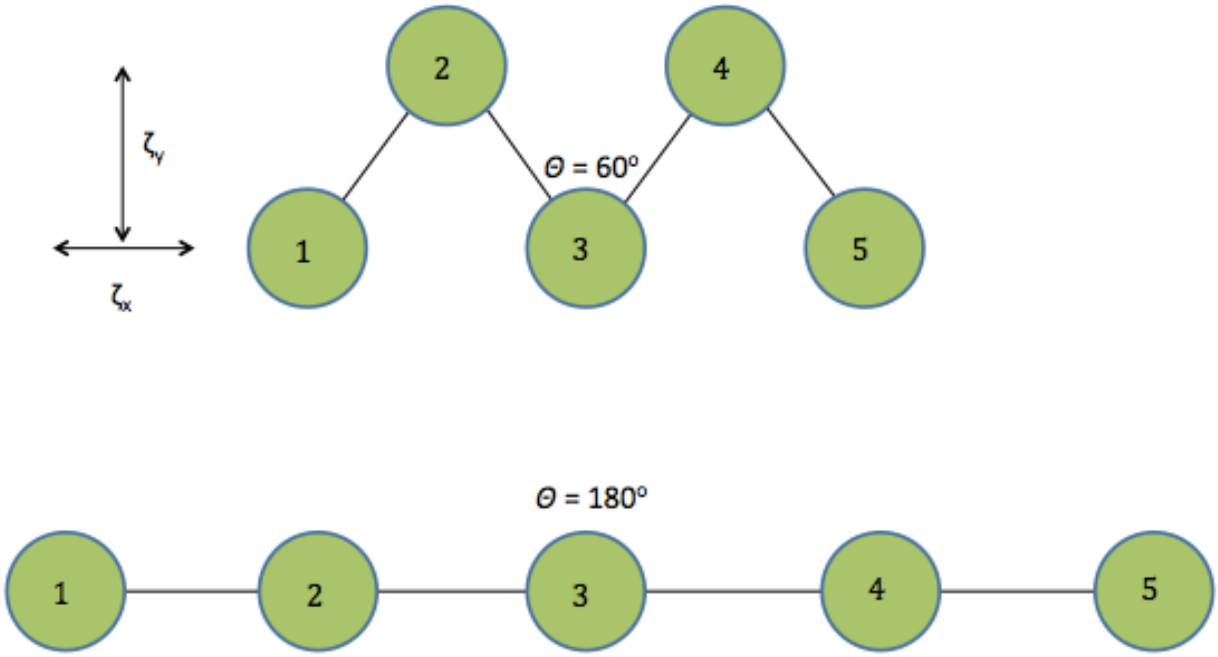

Figure B.6: The Zigzag pathway. The beam (top) and line (bottom) structures are illustrated.

REFERENCES

(1) Schrödinger, E. *Phys. Rev.* **1926**, *28*, 1049.

(2) Born, M.; Oppenheimer, J. R. *Ann. Phys. (Leipzig)* **1927**, *84*, 457.

(3) Pauli, W. *Z. Physik* **1925**, *31*, 765.

(4) Slater, J. C. *Phys. Rev.* **1929**, *34*, 1293.

(5) Szabo, A.; Ostlund, N. S. *Modern Quantum Chemistry: Introduction to Advanced Electronic Structure Theory*; McGraw Hill Inc.: New York, 1996.

(6) Slater, J. C. *Phys. Rev.* **1930**, *35*, 210.

(7) Hartree, D. R.; Hartree, W. *Proc. Roy. Soc.* **1935**, *A150*.

(8) Fock, V. *Z. Physik* **1930**, *61*, 126.

(9) Hall, G. G. *P. R. Soc. London.* **1951**, *205*, 541.

(10) Roothaan, C. C. J. *Rev. Mod. Phys.* **1951**, *23*, 69.

(11) Schrödinger, E. *Ann. Phys. (Berlin)* **1926**, *80*, 437.

(12) Møller, C.; Plesset, S. M. *Phys. Rev.* **1934**, *46*, 618.

(13) Pople, J. A.; Seeger, R.; Krishnan, R. *Int. J. Quantum Chem.* **177**, *14*, 545.

(14) Handy, N. C. *Chem. Phys. Lett.* **1980**, *74*, 280.

(15) Langhoff, S. R.; Davidson, E. R. *Int. J. Quantum Chem.* **1974**, *8*, 61.

(16) Bartlett, R. J. *Ann. Rev. Phys. Chem.* **1981**, *32*, 359.

(17) Jensen, F. *Introduction to Computational Chemistry*; 2nd Edition ed.; John Wiley & Sons Ltd.: West Sussex, 2007.

(18) Paldus, J. In *Methods in Computational Molecular Physics*; Wilson, S., Dickerson, H. F., Eds.; Plenum Press: New York, 1992.

(19) Paldus, J.; Li, X. In *Advances in Chemical Physics*; Prigogine, I., Rice, S., Eds.; John Wiley & Sons Ltd., 1999; Vol. 110.

(20) Roos, B. O.; Taylor, P. R. *Chem. Phys.* **1980**, *48*, 157.

(21) Pauncz, R. *The Symmetric Group in Quantum Chemistry*; CRC: Boca Raton, FL, 1995.

(22) Andersson, K.; Malmqvist, P. Å.; Roos, B. O.; Sadlej, A. J.; Wolinski, K. *J. Chem. Phys.* **1990**, *94*, 5483.

(23) Werner, H. J. *Mol. Phys.* **1996**, *89*, 645.

(24) Werner, H. J.; Knowles, P. J. *Theor. Chim. Acta.* **1990**, *78*, 175.

(25) Werner, H. J.; Knowles, P. J. *J. Chem. Phys.* **1988**, *89*, 5803.

(26) Knowles, P. J.; Wener, H. J. *Chem. Phys. Lett.* **1988**, *145*, 514.

(27) Laidig, W. D.; Bartlett, R. J. *Chem. Phys. Lett.* **1984**, *104*, 424.

(28) Hohenberg, P.; Kohn, W. *Phys. Rev.* **1964**, *136*, B864.

(29) Kohn, W.; Sham, L. J. *Phys. Rev.* **1965**, *140*, A1133.

(30) Levine, I. R. *Quantum Chemistry*; 5th ed.; Prentive Hall, Inc.: Upper Saddle River, NJ, 2000.

(31) Parr, R. G.; Yang, W. *Density Functional Theory of Atoms and Molecules*; Oxford University Press: Oxford, 1989.

(32) Dirac, P. A. M. *Proc. Cambridge Phil. Soc.* **1930**, *26*, 376.

(33) Perdew, J. P.; Wang, Y. *Phys. Rev. B* **1992**, *45*, 13244.

(34) Perdew, J. P.; Chevary, J. A.; Vosko, S. H.; Jackson, K. A.; Pederson, M. R.; Singh, D. J.; Fiolhais, C. *Phys. Rev. B* **1992**, *46*, 6671.

(35) Perdew, J. P.; Burke, K.; Ernzerhof, M. *Phys. Rev. Lett.* **1997**, *78*, 1396.

(36) Perdew, J. P.; Burke, K.; Ernzerhof, M. *Phys. Rev. Lett.* **1996**, *77*, 3865.

(37) Becke, A. D. *J. Chem. Phys.* **1993**, *98*, 5648.

(38) Becke, A. D. *Phys. Rev. A* **1988**, *38*, 3098.

(39) Vosko, S. H.; Wilk, L.; Nusair, M. *Can. J. Phys.* **1980**, *58*, 1200.

(40) Lee, C.; Yang, W.; Parr, R. G. *Phys. Rev. B* **1988**, *37*, 785.

(41) Slater, J. C. *Phys. Rev.* **1930**, *36*, 57.

(42) Boys, S. F. *Proc. R. Soc. A* **1950**, *200*, 542.

(43) Dunning Jr., T. H. *J. Chem. Phys.* **1988**, *90*, 15.

(44) Kendall, R. A.; Dunning Jr., T. H.; Harrison, R. J. *J. Chem. Phys.* **1992**, *96*, 6796.

(45) Cox, P. A. *The Electronic Structure of Chemistry of Solids*; Oxford: New York, 1987.

(46) *Handbook of Metal Elements*; Walker, P.; Tarn, W. H., Eds.; CRC Press: Boca Raton, 1991.

(47) Furlani, E. P. *Permanent Magnet and Electromechanical Devices: Materials, Analysis, and Applications*; Academic Press: San Diego, 2001.

(48) Johnson, R. A.; Oh, D. J. *J. Mater. Res.* **1989**, *4*, 1195.

(49) Raji, A. T.; Scandolo, S.; Mazzarello, R.; Nsengiyumva, S.; Härting, M.; Britton, D. T. *Philos. Mag.* **2009**, *89*, 1629.

(50) Methfessel, M.; Paxton, A. T. *Phys. Rev. B* **1989**, *40*, 3616

(51) Miessler, G. L.; Tarr, D. A. *Inorganic Chemistry*; Prentice Hall: New York, 2003.

(52) "Semiconductor Theory." < http://simple-semiconductors.com/ >.

(53) Bain, E. C.; Dunkirk, N. Y. *T. Am. I. Min. Met. Eng.* **1924**, *70*, 1.

(54) Kittel, C. *Introduction to Solid State Physics*; 7th ed.; Wiley: New Delhi, 2004.

(55) Alvarez, L.; Guillard, T.; Sauvajol, J. L.; Flamant, G.; Lapaze, D. *Chem. Phys. Lett.* **2001**, *342*, 7.

(56) Amara, H.; Roussel, J. M.; Bichara, C.; Gaspard, J. P.; Ducastelle, F. *Phys. Rev. B* **2009**, *79*, 014109.

(57) Dommele, S. V.; Romero-Izquirdo, A.; Byrdson, R.; Jong, K. P. d.; Bitter, J. H. *Carbon* **2008**, *46*, 138.

(58) Moors, M.; Amara, H.; Bocarme, T. V.; Bichara, C. *ACS Nano* **2009**, *3*, 511.

(59) Shibuta, Y.; Maruyama, S. *Comput. Mater. Sci.* **2007**, *39*, 842.

(60) Xiao, W.; Baskes, M. I.; Cho, K. *Surf. Sci.* **2009**, *603*, 1985.

(61) Browning, L. C.; DeWitt, T. W.; Emmett, P. H. *J. Am. Chem. Soc.* **1950**, *72*, 4211.

(62) Jiang, C.; Srinivasan, S. G.; Caro, A.; Maoly, S. A. *J. Appl. Phys.* **2008**, *103*, 043502.

(63) Browning, L. C.; Emmett, P. H. *J. Am. Chem. Soc.* **1952**, *74*, 1680.

(64) Jacobson, B.; Westgren, A. *Z. Phys. Chem.* **1933**, *B20*, 361.

(65) Lv, Z. Q.; Sun, S. H.; Jiang, P.; Wang, B. Z.; Fu, W. T. *Comput. Mater. Sci.* **2008**, *42*, 692.

(66) Premkumar, P. A.; Turchanin, A.; Bahlawane, N. *Chem. Mater.* **2007**, *19*, 6206.

(67) Kraposhin, V. S. *Int. J Non-Equilib. Proc.* **1998**, *10*, 333.

(68) Kraposhin, V. S.; Shakhlevich, K. V. *Poverkhnost* **1990**, 139.

(69) Nagakura, S. *J. Phys. Soc. Japan* **1957**, *12*, 482.

(70) Nagakura, S. *J. Phys. Soc. Japan* **1958**, *13*, 1005.

(71) Struis, J. R. P. W.; Bachelin, D.; Ludwig, C.; Wokaun, A. *J. Phys. Chem. C* **2009**, *113*, 2443.

(72) Goto, Y.; Taniguchi, K.; Omata, T.; Otsuka-Yao-Matsuo, S.; Ohashi, N.; Udea, S.; Yoshikawa, H.; Yamashita, Y.; Oohashi, H.; Kobayashi, K. *Chem. Mater.* **2008**, *20*, 4156.

(73) Paduani, C. *J. Phys.: Condens. Matter* **2008**, *20*, 225014.

(74) Haglund, J.; Grimvall, G.; Jarlborg, T.; Guillermet, A. F. *Phys. Rev. B* **1991**, *43*, 14400.

(75) Haglund, J.; Guillermet, A. F.; Grimvall, G.; Korling, M. *Phys. Rev. B* **1993**, *48*, 11685.

(76) Cheng-Bin, L.; Ming-Kai, L.; Dong, Y.; Fu-Qing, L.; Xiang-Jun, F. *Chin.. Phys.* **2005**, *14*, 2287.

(77) Zhang, Y.; Li, J.; Zhou, L.; Xiang, S. *Solid State Commun.* **2002**, *121*, 411.

(78) Bannerjee, R. 2009; UNT, personal communication.

(79) Guillermet, A. F.; Grimvall, G. *J. Phys. Chem. Solids* **1992**, *53*, 105.

(80) Kresse, G.; Furthmüller, J. *Phys. Rev. B* **1996**, *54*, 11169.

(81) Kresse, G.; Hafner, J. *Phys. Rev. B* **1993**, *47*, 558.

(82) Kresse, G.; Hafner, J. *Phys. Rev. B* **1994**, *49*, 14251.

(83) Kresse, G.; Hafner, J. *Comput. Mater. Sci.* **1996**, *6*, 15.

(84) Kresse, G.; Joubert, D. *Phys. Rev. B* **1999**, *59*, 1758.

(85) Reeber, R.; Wang, K. *J. Electron. Mater.* **1996**, *25*, 63.

(86) Wyckoff, R. W. G. *Crystal Structres*; Wiley: New York, 1963.

(87) Hull, A. W. *Phys. Rev.* **1917**, *10*, 661.

(88) He, X.; Kong, L. T.; Liu, B. X. *J. Appl. Phys.* **2005**, *97*, 106107.

(89) Hemenger, P.; Weik, H. *Acta Crystallogr.* **1965**, *19*, 690.

(90) Wright, J. G.; Goddard, J. *Phil. Mag.* **1965**, *11*, 485.

(91) Koniger, A.; Hammerl, C.; Zeitler, M.; Rauschenbach, B. *Phys. Rev. B* **1997**, *55*, 8143.

(92) Nagakura, S. *J. Phys. Soc. Japan* **1961**, *16*, 1213.

(93) Belogurov, S.; Berzgunov, M.; Petrov, A. *Latv. PSR Zinat. Akad Vestis Fiz. Teh. Zinat. Ser. (USSR)* **1988**, 120.

(94) Brossonneau, L.; Kacheva, A.; Senocq, F.; Kang, J. K.; Rhee, S. W.; Gleizes, A.; Vahlas, C. *J. Physique* **1999**, *9*, 597.

(95) Leng, Y.; Xie, L.; Liao, F.; Zheng, J.; Li, X. *Thermochimica. Acta* **2008**, *473*, 14.

(96) Leslie-Pelecky, D. L.; Zhang, X. Q.; Kim, S. H.; Bonder, M.; Rieke, R. D. *Chem. Mater.* **1998**, *10*, 164.

(97) Yue, L.; Sabiryanov, R.; Kirkpatrick, E. M.; Leslie-Pelecky, D. L. *Phys. Rev. B* **2000**, *62*, 8969.

(98) Shein, I. R.; Medvedeva, N. I.; Ivanovskii, A. L. *Physica B* **2006**, *371*, 126.

(99) Ruhl, R. C.; Cohen, M. *Scr. Metall.* **1967**, *1*, 73.

(100) Zhu, Y. A.; Dai, Y. C.; Chen, D.; Yuan, W. K. *Carbon* **2007**, *45*, 21.

(101) Hohenberg, P.; Kohn, W. *Phys Rev* **1964**, *136*, B864.

(102) Koch, W.; Holthausen, M. C. *A Chemist's Guide to Density Functional Theory*; Wiley-VCH: Weinheim, Germany, 2002.

(103) Parr, R. G.; Weitao, Y. *Density Functional Theory of Atoms and Molecules*; Oxford University Press: New York, New York, 1989.

(104) Dunning Jr., T. H. *J Chem Phys* **1989**, *90*, 1007.

(105) Kohn, W.; Sham, L. J. *Phys Rev* **1965**, *140*, A1133.

(106) Peterson, K. A.; Woon, D. E.; Dunning, T. H. *J Chem Phys* **1994**, *100*, 7410.

(107) Wang, N. X.; Venkatesh, K.; Wilson, A. K. *J Phys Chem A* **2006**, *110*, 779.

(108) Wilson, A. K.; Dunning, T. H. *J Chem Phys* **1997**, *106*, 8718.

(109) Woon, D. E.; Dunning, T. H. *J Chem Phys* **1993**, *98*, 1358.

(110) Woon, D. E.; Dunning, T. H. *J Chem Phys* **1995**, *103*, 4572.

(111) Wang, N. X. Ph.D dissertation, University of North Texas, 2005.

(112) Wang, N. X.; Wilson, A. K. *J Chem Phys A* **2003**, *107*, 6720.

(113) Wang, N. X.; Wilson, A. K. *J Chem Phys A* **2004**, *121*, 7632.

(114) Wang, N. X.; Wilson, A. K. *Mol Phys* **2005**, *103*, 345.

(115) Wang, N. X.; Wilson, A. K. *J Chem Phys A* **2005**, *109*, 7187.

(116) Prascher, B. P. Ph.D dissertation, University of North Texas, 2009.

(117) Prascher, B. P.; Wilson, A. K. *Mol Phys* **2007**, *105*, 2899.

(118) Prascher, B. P.; WIlson, B. R.; Wilson, A. K. *J Chem Phys* **2007**, *127*, 124110.

(119) Jensen, F. *J Chem Phys* **2001**, *115*, 9113.

(120) Jensen, F. *J Chem Phys* **2002**, *116*, 7372.

(121) Jensen, F. *J Chem Phys* **2003**, *118*, 2459.

(122) Jensen, F. *Chem Phys Lett* **2005**, *402*, 510.

(123) Jensen, F. *J Chem Phys* **2005**, *122*, 74111.

(124) Jensen, F. *Theor Chem Acc* **2013**, *132*, 1380.

(125) Lehtola, S.; Manninen, P.; Hamalainen, K. *J Chem Phys* **2013**, *138*, 044109.

(126) Caillie, C. V.; Amos, R. D. *Chem Phys Lett* **2000**, *316*, 159.

(127) Minami, T.; Ito, S.; Nanako, M. *Int J Quantum Chem* **2012**, *113*, 252.

(128) Capano, G.; Penfold, T. J.; Besley, N. A.; Milne, C. J.; Reinhard, M.; Rittmann-Frank, H.; P. Glatzel; Abela, R.; Rothlisberger, U.; Chergui, M.; Tavernelli, I. *Chem Phys Lett* **2013**, *in press*.

(129) Izgorodina, E. I.; Brittain, D. R. B.; Hodgson, J. L.; Krenske, E. H.; Lin, C. Y.; Namazian, M.; Coote, M. L. *Phys Org Chem* **2007**, *111*, 10754.

(130) Tentscher, P. R.; Arey, J. S. *J Chem Theory Comput* **2013**, *9*, 1568.

(131) Montero-Campillo, M. M.; Lamsabhi, A. M.; Mo, O.; Yanez, M. *Theor Chem Acc* **2013**, *132*, 1328.

(132) Jursic, B. S. *J Mol Struct* **2000**, *499*, 137.

(133) Lu, L.; H. Hu; Hou, H.; Wang, N. *Comput Theor Chem* **2013**, *1015*, 64.

(134) Ciriaco, F.; Mavelli, F.; Cassidei, L. *Comput Theor Chem* **2013**, *1*, 60.

(135) Barone, V.; Orlandini, L.; Adamo, C. *Chem Phys Lett* **1994**, *231*, 295.

(136) Johnson, E. R.; Salamone, M.; Bietti, M.; DiLabio, G. A. *J Phys Chem* **2013**, *117*, 947.

(137) Auzmendi-Murua, I.; Charaya, S.; Bozzelli, J. W. *J Phys Chem* **2013**, *117*, 378.

(138) Zhou, M. 2011; University of North Texas.

(139) Lee, C.; Yang, W.; Parr, R. G. *Phys Rev B* **1987**, *37*, 785.

(140) Vosko, S. H.; Wilk, L.; Nusair, M. *Can J Phys* **1980**, *58*, 785.

(141) Press, W. H.; Flannery, B. P.; Teukolsky, S. A.; Vetterling, W. T. *Numerical Recipes in FORTRAN 77: The Art of Scientific Computing*; 3rd ed.; Cambridge University Press, 2007.

(142) Schwartz, C. *Phys Rev* **1962**, *126*, 1015.

(143) Werner, H. J.; Knowles, P. J.; Lindh, R.; Manby, F. R.; Schutz, M.; Amos, R. D.; Bernhardsson, A.; Berning, A.; Celani, P.; Cooper, D. L.; Deegan, M. J. O.; Dobbyn, A. J.; Eckert, F.; Hampel, C.; Hetzer, G.; Korona, T.; Lloyd, A. W.; McNicholas, S. J.; Meyer, W.; Mura, M. E.; Nicklass, A.; Palmieri, P.; Pitzer, R.; Rauhut, G.; Schumann, U.; Stoll, H.; Stone, A. J.; Tarroni, R.; Thorsteinsson, T. Molpro. versions 2002.1 and 2002.6.

(144) Diego, H. P.; de Piedale, M. E. M.; Dennis, T. J. S.; Hare, J. P.; Kroto, H. W.; Taylor, R.; Walton, D. R. M. *J Chem Soc Faraday* **1993**, *98*, 3541.

(145) Steele, W. V.; Chirico, R. D.; Smith, N. K.; Billups, W. E.; Elmore, P. R.; Wheeler, A. E. *J Phys Chem* **1992**, *96*, 4731.

(146) Beckhaus, H. D.; Verevkin, S.; Ruchardt, C.; Deidrich, F.; Thilgun, C.; Meer, H. U.; Hohn, H.; Muller, W. *Agnew Chem Int Ed Engl* **1994**, *33*, 996.

(147) Baskes, M. I. *Phys. Rev. B* **1992**, *46*, 2727.

(148) Baskes, M. I.; Srinivasan, S. G.; Valone, S. M.; Hoagland, R. *Phys. Rev. B* **2007**, *75*, 094113.

(149) Dongare, A. M.; Neurock, M.; Zhigilei, L. V. *Phys. Rev. B* **2009**, *80*, 184106.

(150) Finnis, M. W.; Sinclair, J. E. *Phil. Mag. A* **1984**, *50*, 45.

(151) Foiles, S. M.; Baskes, M.; Daw, M. S. *Phys. Rev. B* **1986**, *33*, 7983.

(152) Foiles, S. M. *Phys. Rev. B* **1985**, *32*, 7685.

(153) Daw, M. S.; Baskes, M. *Phys. Rev. B* **1984**, *29*, 6443.

(154) Mishin, Y.; Mehl, M. J.; Papaconstantopoulos, D. A.; Voter, A. F.; Kress, J. D. *Phys. Rev. B* **2001**, *63*, 224106.

(155) Valone, S. M.; Atlas, S. R.; Baskes, M. I. *Model. Simul. Mater. Sc.* **2013**, *Submitted*.

(156) Valone, S. M. *J. Theor. Comput. Chem.* **2011**, *7*, 2253.

(157) Perdew, J. P.; Chevary, J. A.; Vosko, S. H.; Jackson, K. A.; Pederson, M. R.; Singh, D. J.; Foilhais, C. *Phys. Rev. B* **1993**, *48*, 4973.

(158) Perdew, J. P.; Chevary, J. A.; Vosko, S. H.; Jackson, K. A.; Pederson, M. R.; Singh, D. J.; Foilhais, C. *Phys. Rev. B* **1992**, *46*, 6671.

(159) Simmons, G.; Wang, H. *Single Crystal Elastic Constants and Calculated Aggregate Properties: A Handbook*; 2nd ed.; Cambridge, MA: MIT Press, 1971.

(160) Baskes, M. I. *Mater. Chem. Phys.* **1997**, *50*, 152.

(161) Ackland, G. J.; Mendelev, M. I.; Srolovitz, D. J.; Han, S.; Barashev, A. V. *J. Phys-Condens. Mat.* **2004**, *16*, S2629.

(162) Oh, D. J.; Johnson, R. A. *J. Mater. Res.* **1988**, *3*, 471.

(163) Baskes, M. I. *Phys. Rev. Lett.* **1987**, *59*, 2666.

(164) Baskes, M. I.; Johnson, R. A. *Modell. Simul. Mater. Sci. Eng.* **1994**, *2*, 147.

(165) Rose, J. H.; Smith, J. R.; Guinea, F.; Ferrante, J. *Phys. Rev. B* **1984**, *29*, 7983.

(166) Baskes, M. I.; Srinivasan, S. G.; Valone, S.; Hoagland, R. *Phys. Rev. B* **2007**, *75*, 094113.

(167) Valone, S. M.; Baskes, M. I.; Rudin, S. P. *J. Nucl. Mater,* **2012**, *422*, 20.

(168) Zhou, X.; Johnson, R.; Wadley, H. *Phys. Rev. B* **2004**, *69*, 144113.

(169) Ackland, G. J. *Philos. Mag. A* **1992**, *66*, 917.

(170) Lee, B. J.; Baskes, M. I. *Phys. Rev. B* **2000**, *62*, 8564.

(171) Kresse, G.; Hafner, J. *Phys. Rev. B* **1993**, *47*, 588.

(172) Blochl, P. E. *Phys. Rev. B* **1994**, *50*, 17953.

(173) Nelder, J. A.; Mead, R. *Comput. J.* **1965**, *7*, 308.

(174) Hafner, J. *J. Comput. Chem* **2008**, *29*, 2044.

(175) Benoit, M.; Tarrat, N.; Morillo, J. *Modell. Simul. Mater. Sci. Eng.* **2013**, *21*, 015009.

(176) *Structure of metals: crystallographic methods, principles, and data.*; Barret, C. S.; Massalski, T. B., Eds.; McGraw-Hill, 1966.

(177) FIsher, E. S.; Renken, C. J. *Phys. Rev.* **1964**, *135*, A482.

(178) Legrand, P. B. *Philos. Mag. B* **1984**, *49*, 171.

(179) Lane, N. J.; Simak, S. I.; Mikhaylushkin, A. S.; Abrikosov, I. A.; Hultman, L.; Barsoum, M. W. *Phys. Rev. B* **2011**, *84*, 184101.

(180) Hennig, R. G.; Lenosky, T. J.; Rudin, S. P.; Wilkins, J. W. *Phys. Rev. B* **2008**, *78*, 054121.

(181) de Boer, F. R.; Boom, R.; Mattens, W. C. M.; Miedema, A. R.; Niessen, A. K. *Cohesion in Metals: Transition Metal Alloys* Elsevier Science: North Holland, 1989.

(182) Tyson, W. R.; Miller, W. A. *Surf. Sci.* **1977**, *62*, 267.

(183) Paidar, V.; Wang, L. G.; Sob, M.; Vitek, V. *Modell. Simul. Mater. Sci. Eng.* **1999**, *7*, 369.